TRANSIENTS FROM RARE, VIOLENT STELLAR DEATHS

A Dissertation

Submitted to the Faculty

of

Purdue University

by

Adithan Kathirgamaraju

In Partial Fulfillment of the

Requirements for the Degree

of

Doctor of Philosophy

August 2019

Purdue University

West Lafayette, Indiana

THE PURDUE UNIVERSITY GRADUATE SCHOOL
STATEMENT OF DISSERTATION APPROVAL

Dr. Dimitrios Giannios, Chair

    Department of Physics and Astronomy

Dr. Martin Kruczenski

    Department of Physics and Astronomy

Dr. Matthew L. Lister

    Department of Physics and Astronomy

Dr. Maxim Lyutikov

    Department of Physics and Astronomy

Approved by:

    Dr. John P. Finley

        Head of the Department of Physics and Astronomy

ACKNOWLEDGMENTS

I would like to express my sincere gratitude towards my advisor Dimitrios Giannios, his guidance throughout my graduate career has made this dissertation into a reality. My time as a Ph.D. student at Purdue has been a pleasant experience thanks to his benevolence and assistance. I am extremely thankful for my mentors, Rodolfo Barniol Duran and Sasha Tchekhovskoy, for their encouragement and patience when showing me the ropes at the start of new research projects.

Thanks to all my mentors, professors and teachers during my time as a high school and undergraduate student. A special thanks to my high school math and physics teachers for sparking my interest in the natural sciences.

Thanks to all my friends and colleagues, especially the Sri Lankan community at Purdue, for their unconditional help and for all the laughs we shared. My time at Purdue would have been much less lively without the fun gatherings and extra curricular activities I was able to part take in with you all.

Thanks to my sister, brother in law and cousins for their endless support. Above all, I would like to thank my parents, who have my utmost gratitude. Their unrelenting self sacrifices in order to prioritize my education and ensure I have the opportunities to pursue my passion is what made all this possible.

TABLE OF CONTENTS

LIST OF TABLES

LIST OF FIGURES

Figure   Page

Figure   Page

ABSTRACT

Kathirgamaraju, Adithan Ph.D., Purdue University, August 2019. Transients from Rare, Violent Stellar Deaths. Major Professor: Dimitrios Giannios.

Some of the brightest and most energetic events in the Universe are associated with the death of stars. These stellar deaths power transient electromagnetic emission which are routinely observed on Earth. This dissertation presents our research on various such transients. Its topics includes, supernova remnants, kilonovae, gamma-ray bursts (GRBs): The "long" type produced from core-collapse supernovae and the "short" type associated with neutron star merger events. It also focuses on the disruption of stars by the tidal forces of supermassive black holes i.e., tidal disruption events (TDEs). We model the emission from these transients and compare them to observations in order to draw a number of conclusions and make predictions for future detections. For example, we find that the non-thermal emission from supernovae and kilonovae associated with GRBs can produce long term emission which may be detected as a re-brightening in the overall emission. The sharp cut off observed in some TDE flares can be caused by a pre-existing accretion disk present around a supermassive black hole, which is expected in active galactic nuclei. Our work successfully predicted the nature of the very first electromagnetic detection from a neutron star merger, and was able to reproduce the emission that had been observed for more than one hundred days after the merger. This dissertation also provides frameworks on how the observable features of these transients can be leveraged to probe the properties of the progenitor system and their environment.

1. INTRODUCTION

In this report, we investigate a variety of astrophysical phenomena that produce short lived (relative to cosmological timescales) emission. These phenomena are usually associated with violent and energetic events such as stellar explosions (supernovae), stars that get ripped apart due to the gravitational forces of black holes (tidal disruption events) and binary mergers involving neutron stars. We model the transient emission produced in these events in order to understand what properties and physical processes we can discern about the system and its environment from observations. In this chapter we briefly introduce the various transients that are studied in this dissertation.

1.1 Long gamma-ray bursts and their associated supernovae

Supernovae (SNe) are catastrophic explosions that occur at the end of a star's life. During some SNe, the inner core of a star collapses and the outer layers of a star are ejected (these are classified as core collapse SNe). The collapsed core forms a compact object, either a black hole (BH) or a neutron star (NS), which is surrounded by remnant stellar material. SNe power various electromagnetic (EM) transients, for example, the ejected stellar envelopes undergo radioactive decay releasing thermal emission and the interaction between the ejected material and its surroundings can shock and energize the external medium producing non-thermal emission. For certain types of core-collapse SN, there can be additional transients powered by the accretion and rotation of the remnant compact object. Accretion of stellar material onto the compact object can launch highly relativistic and collimated outflows of plasma called jets. Jets produced in stellar deaths emit two distinct types of electromagnetic signals, one is a burst of X-rays and gamma rays (lasting a few seconds to minutes) termed

the prompt emission, which originates from within the jet. The other is a longer lived (months to years) emission termed the afterglow and is emitted by external material that is shocked and energized by the jet as it propagates. The prompt and afterglow emission constitute the phenomenon known as a gamma-ray burst (GRB). GRBs whose prompt emission lasts longer than ~ 2 seconds are classified as long GRBs, and are thought to be associated with core-collapse SNe. In chapter 3 we model the various EM transients from a core-collapse SNe and its accompanying long GRB. In chapter 4, we apply these models to observations in order to constraint the properties of the SNe ejecta and the environment of observed long GRBs.

1.2 Neutron star mergers

Two neutron stars in a close orbit around each other emit gravitational waves which transfers gravitational potential energy out of the binary system. This causes the orbit of the system to shrink until eventually, the two NSs merge. The tidal interactions between the NSs and their coalescence unbinds and ejects some material over a broad angular distribution. This material undergoes radioactive decay which powers the thermal transient termed the kilonova (KN). Following the merger, the coalesced NSs form a compact object which will be surrounded by a torus of remnant material. Accretion of this material onto the compact object can launch jets which also produces its own emission. It was long suspected that jets from NS mergers produced short GRBs, which are a subclass of GRBs whose prompt emission lasts less than 2 seconds. NS mergers are therefore a unique class of transients since they can produce detectable signals in both gravitational and EM waves. In chapter 5, we model the emission associated with the jet of a NS merger and assess which EM signals are likely to be detected from a NS merger. In chapter 6, we present the observations of the first detected NS merger (GW170817), which matched the predictions of our previous work. In chapter 7, we utilize numerical simulations and semi-analytic methods to reproduce the observations of GW170817, which further

substantiates our theory on the origin of the EM emission in GW170817. In chapter 8, we study the emission associated with the KN of GW170817, which may be detected in the years to come.

1.3 Tidal disruption events

The centers of galaxies are believed to harbor supermassive black holes (SMBHs) which are more than a million times the mass of our Sun. When stars approach too close to a SMBH, the tidal forces from the BH can exceed the self-gravity of the star, which can unbind and tear the star apart. This phenomenon is known as a tidal disruption event (TDE), the disrupted star forms a stream of stellar material, a part of which falls back to the SMBH and is eventually accreted. This process powers EM transients produced by the circularization and formation of an accretion disk around the SMBH, and by jets launched during the accretion of this material onto the SMBH. In chapter 9, we give a brief introduction to the theory of TDEs. In chapter 10, we investigate how the presence of a pre-existing accretion disk surrounding the SMBH could affect the emission in TDEs. Such pre-existing disks are expected to be present in the center of galaxies, especially those which harbor active galactic nuclei. We demonstrate how some peculiar properties observed in TDEs could be explained by the presence of a pre-existing disk.

2. SYNCHROTRON RADIATION IN A FORWARD SHOCK

As highlighted in the introduction, all the transients investigated in this thesis are powered by outflows of plasma. These outflows propagate through an external medium much faster than the sound speed, which drives a shock wave through the external medium. A majority of our work studies the synchrotron emission produced by the shocked external medium (i.e., the forward shock). We study emission from forward shocks produced in various astrophysical contexts, ranging from highly collimated, ultra-relativistic shock waves driven by jets (e.g., GRB afterglows), to spherical, non/mildly-relativistic shocks driven by SN or KN ejecta (see fig. 2.1). In this chapter we lay out the foundation and physical principles used to calculate the synchrotron emission from a forward shock, in particular how we can model its spectrum and light curve (flux vs. time). A more comprehensive report on this topic can be found in [1–4].

2.1 Shock jump conditions

A shock sweeps up, compresses and energizes the external material it propagates through. As a result, the shock front forms a contact discontinuity where quantities (such as internal energy and density) of the shocked and unshocked material have different values. From the conservation of mass, momentum and energy across a shock, we can find expressions which relate quantities of the unshocked fluid to quantities of the shocked fluid, these expressions are commonly referred to as the shock jump conditions. To obtain these expressions we first start with the energy-momentum tensor for a perfect fluid (neglecting viscosity)

$$T^{\mu\nu} = (\rho c^2 + e + p)u^\mu u^\nu + g^{\mu\nu}p, \tag{2.1}$$

"afterglow" produced
by synchrotron emission
from particles accelerated
at the shock front

GRB jet and
associated shock

SN shock front
sweeps up ISM

θ_j

Synchrotron emission
radiated by particles
accelerated at the shock
front
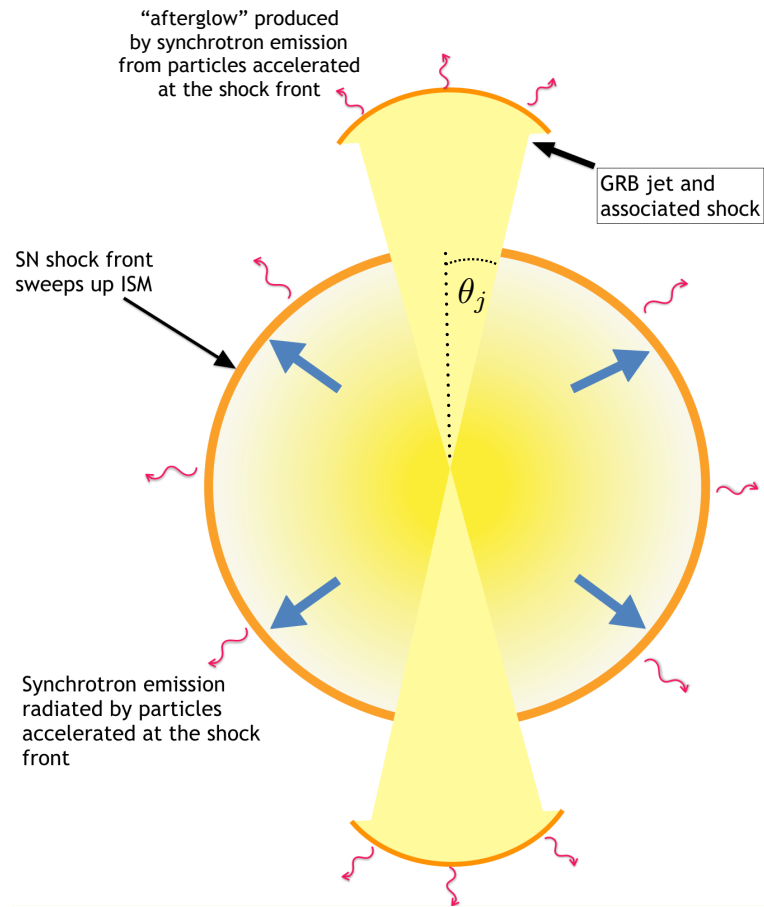
Fig. 2.1. Diagram illustrating the forward shock driven by the GRB jet (with half opening angle θ_j) and the SN ejecta. Particles swept by the shock radiate via synchrotron emission. The emission from the shock associated with the jet is called the GRB afterglow.

where ρ is mass density, e is the internal energy density, p is the pressure, u^μ is the 4-velocity and $g^{\mu\nu}$ is the metric tensor. We will use a flat spacetime throughout this chapter. Next, we assume a one directional fluid flow perpendicular to the shock front

and equate the mass flux ($\gamma\rho\beta$), momentum flux (T^{ii}) and energy flux (T^{0i}) of the shocked and unshocked material, which yields [1]

$$\gamma_1\rho_1\beta_1 = \gamma_0\rho_0\beta_0 \tag{2.2}$$

$$\gamma_1^2\beta_1^2 w_1 + p_1 = \gamma_0^2\beta_0^2 w_0 + p_0 \tag{2.3}$$

$$\gamma_1^2\beta_1 w_1 = \gamma_0^2\beta_0 w_0, \tag{2.4}$$

where γ, β are the Lorentz factor and velocity of the fluid respectively (measured in the frame of the shock front) and $w = \rho c^2 + e + p$ (measured in the rest frame of the fluid). Quantities with subscripts "0" and "1" are associated with the unshocked and shocked fluid respectively. We use the equation of state for an ideal gas given by $p = (\kappa - 1)e$, where κ is the adiabatic index ranging from 4/3 for relativistic fluids, to 5/3 for non-relativistic, monatomic fluids. In all our applications, the unshocked medium is cold, so we can neglect the pressure in this medium in comparison to its rest mass (i.e. $w_1 \approx \rho_1 c^2$). Under these assumptions, the jump conditions can be simplified to give (e.g., [4,5])

$$\frac{\rho_1}{\rho_0} = \frac{\kappa\Gamma + 1}{\kappa + 1} \tag{2.5}$$

$$e_1 = (\Gamma - 1)\rho_1 c^2, \tag{2.6}$$

with Γ the bulk Lorentz factor of the shocked fluid in the frame of the unshocked fluid. The unshocked fluid is at rest with respect to the observer for our purposes, therefore Γ is also the Lorentz factor of the shocked fluid as seen by the observer. We will approximate equation (2.5) as $\rho_1 \approx 4\Gamma\rho_0$, which is valid for strong shocks in the highly relativistic and non-relativistic cases e.g., [1,6].

The densities involved in these shocks are small, making the mean free path of particle-particle collisions much larger than the scale of the system. Therefore, these shocks are not mediated by collisions (i.e., they are collisionless shocks). Rather, they are believed to be mediated by charged particles interacting with self-generated electromagnetic fields e.g., [7,8]. However, many aspects of collisionless shocks e.g., generation of the electromagnetic fields and acceleration of particles at the shock are

not well understood from first principles. In afterglow modeling, these uncertainties are commonly incorporated as microphysical parameters (e.g., [9]). One such parameter is ϵ_B, which denotes the energy density in the magnetic fields of the shocked fluid as a fraction of the internal energy density (e_1), which is obtained from the shock jump conditions (2.5, 2.6),

$$\frac{B'^2}{8\pi} = \epsilon_B e_1 = \epsilon_B (\Gamma - 1) n_1 m_p c^2. \tag{2.7}$$

Here B$'$ is the magnetic field in the frame of the shocked fluid, m_p is the mass of a proton. To obtain the last equality, we have used $\rho_1 = n_1 m_p$, with n_1 the number density of the shocked fluid. Similarly, ϵ_e is another microphysical parameter which denotes the energy density in the shocked electrons as a fraction of the internal energy density,

$$n_1 \gamma_e m_e c^2 = \epsilon_e e_1 = \epsilon_e (\Gamma - 1) n_1 m_p c^2, \tag{2.8}$$

where γ_e is the Lorentz factor of an electron within the shocked fluid (in the frame of the shocked fluid) and m_e is the electron mass. The accelerated electrons are assumed to have a power law distribution in energy (see equations 2.23–2.26).

2.2 Dynamics of the blast wave

The forward shock associated with the GRB afterglow and SNR are driven by a blast wave of stellar material. We derive expressions relating the energy (E), radius (R) and speed (βc) of the blast, to the observer time (t) for the relativistic and non-relativistic cases. These relations are needed to calculate the light curves of the resulting emission. The blast wave is assumed to have a spherical geometry and we employ spherical coordinates (r, θ, ϕ), we take the number density of the external medium (n_0) to be uniform. We will assume the blast wave moves radially outwards and its properties are independent of the ϕ coordinate, however the calculations done below can be easily extended to include a ϕ dependency. Assume the shocked external medium is concentrated in a thin shell at a radius R from the center of explosion and

consider a small region of the this shell at an arbitrary polar angle θ and denote the total number of protons in the shocked medium as N. The bulk kinetic energy of the shocked medium in this region is

$$
\begin{aligned}
E(\theta) = \Gamma(\Gamma - 1)m_p c^2 N &= \Gamma(\Gamma - 1)m_p c^2 \int n_0 R^2 dR d\Omega \\
&= \Gamma(\Gamma - 1)n_0 m_p c^2 \frac{R^3}{3} \int d\Omega,
\end{aligned}
\tag{2.9}
$$

where Ω is the solid angle subtended by the blast wave and n_0 is the number density of the external medium (assumed to be constant for our applications). The additional factor of gamma in the above equation takes into account the motion of particles in shocked fluid frame. Therefore, the energy per solid angle is

$$
\frac{dE}{d\Omega} = \Gamma(\Gamma - 1)n_0 m_p c^2 \frac{R^3}{3}.
\tag{2.10}
$$

In calculations below, we will often use the isotropic equivalent energy (E_{iso}) given by $E_{\mathrm{iso}} = 4\pi dE/d\Omega$. From 2.9, we see that the energy is proportional to Γ^2 for relativistic cases ($\Gamma \gg 1$) and β^2 for non-relativistic cases ($\beta \ll 1$). We can therefore express the energy as $E \propto (\beta\Gamma)^2$ which accurately captures the dynamics during the relativistic and non-relativistic phases. This expression simplifies a lot of the calculations. The energy in the forward shocked is supplied by the ejected material which drives the shock as it propagates through the external medium (e.g., the jet or SN ejecta), the total energy of this ejecta will be an input parameter, and, assuming no energy losses, we will take this total energy as a constant throughout the evolution of the blast wave. In general, we will model the energy of the ejecta having a power law distribution in 4-velocity ($\beta\Gamma$) and an arbitrary angular distribution (θ), which is supported by theory [10, 11] and observations [12]. Therefore, the energy of the ejecta can be expressed as

$$
E \propto (\beta\Gamma)^{-\alpha},
\tag{2.11}
$$

normalized to the total energy of the ejecta at some minimum 4-velocity $\beta_0\Gamma_0$, the angular distribution is implicitly accounted for. From (2.9) and (2.11), we get

$$
R^3 \propto (\beta\Gamma)^{-(\alpha+2)}
\tag{2.12}
$$

Take a small portion of the blast wave at an angle θ, ϕ (the observer and jet lie along the plane of $\phi = 0°$), with this portion moving radially outward at velocity β at an angle ω with respect to the line of sight of the observer. Suppose this portion emits two photons a distance dr apart, the time interval at which an observer receives these photons is [4, 13]

$$\frac{dt}{1+z} = \frac{dr}{\beta c}(1 - \beta \cos \omega), \tag{2.13}$$

with z the redshift to the source and ω in terms of θ, ϕ and observing angle θ_{obs} is given by

$$\cos \omega = \cos \theta \cos \theta_{\mathrm{obs}} + \sin \theta \sin \theta_{\mathrm{obs}} \cos \phi, \tag{2.14}$$

see figure 5.4.1 for the geometry used. Using (2.12) and (2.13), we can relate the velocity and radius of the blast wave to the observer time. By fixing dt, we can find which parts of the blast wave (over different radii and angles) contribute to the emission at a given observed time.

For $\omega \ll 1$, these dynamic quantities can be expressed analytically for the highly relativistic and non-relativistic cases. For a highly relativistic blast wave, the observer time can be approximated as (e.g., [14])

$$t \approx \frac{R}{2c\Gamma^2}, \tag{2.15}$$

where we use $1/\beta \approx 1 + 1/2\Gamma^2$ when $\Gamma \gg 1$.

From equations (2.9), (2.12),(2.15), using $\beta\Gamma \approx \Gamma$ for the highly relativistic case, we obtain

$$t \propto \begin{cases} \Gamma^{-\frac{8+\alpha}{3}} \\ E^{\frac{8+\alpha}{3\alpha}} \quad \text{relativistic phase} \\ R^{\frac{8+\alpha}{2+\alpha}}. \end{cases} \tag{2.16}$$

For the non-relativistic phase, using $\beta\Gamma \approx \beta$ when $\Gamma \sim 1$ and $t \approx R/\beta c$ we obtain the dynamic relations

$$
t \propto
\begin{cases}
\beta^{-\frac{5+\alpha}{3}} \\
E^{\frac{5+\alpha}{3\alpha}} & \text{non-relativistic phase} \\
R^{\frac{5+\alpha}{2+\alpha}}.
\end{cases}
\tag{2.17}
$$

When energy injection ceases, all the ejecta travel together and begin to decelerate faster. The dynamics during this phase can be obtained by taking the limit $\alpha \to 0$ in (2.16) if the blast wave is still relativistic (called the Blandford-McKee phase [5]), or (2.17) if the blast wave in non-relativistic (called the Sedov-Taylor phase [15, 16]). For example, the dynamic evolution during the Sedov-Taylor phase is given by

$$
t \propto
\begin{cases}
\beta^{-\frac{5}{3}} & \text{Sedov-Taylor} \\
R^{\frac{5}{2}}, & \text{Phase}
\end{cases}
\tag{2.18}
$$

and E is a constant in time. So the evolution of the blast wave associated with the SN in chronological order is as follows. Initially the blast wave is in the relativistic phase with its dynamics given by (2.16). When $\beta\Gamma \sim 1$, the dynamics transitions to the non-relativistic phase governed by (2.17). Finally, when the energy injection ceases, the blast wave decelerates and is governed by the ST phase (2.18).

2.3 Synchrotron spectrum of electrons in a forward shock

In section 2.1, we obtain properties of the shocked fluid in terms of its velocity and quantities of the unshocked medium. In section 2.2, we relate the velocity of the shock to its radius (or equivalently, to the observer time). Here we combine this information with a time dependent injection of non-thermal particles in a magnetized fluid to calculate the resulting synchrotron spectra.

The synchrotron power emitted from a single electron with Lorentz factor γ varies as $P'_\nu \propto \nu'^{\frac{1}{3}}$ (P_ν is the power per unit frequency or "spectral" power) up to a frequency

$$
\nu'_{syn} \approx \frac{3eB'\gamma^2}{4\pi m_e c},
\tag{2.19}
$$

after which the power the power drops off exponentially (see e.g., [2] for a derivation). Here, e is the charge of an electron, γ is the Lorentz factor of an electron within the shocked fluid. The primed (un-primed) quantities are in the comoving (observer) frame. This frequency can be transformed to the observer frame via the relation $\nu = \delta\nu'$, where δ is the Doppler factor given by

$$\delta = \frac{1}{\Gamma(1 - \beta(\cos\theta\cos\theta_{\text{obs}} + \sin\theta\sin\theta_{\text{obs}}\cos\phi))}, \tag{2.20}$$

where Γ and β are the bulk Lorentz factor and speed of the fluid emitting the radiation (see Fig. 5.4.1 for an illustration of the angles used in the above expression). The total power emitted (in the fluid frame) is [2, 17]

$$P' \approx \frac{4}{3}\sigma_T c\gamma^2 \frac{B'^2}{8\pi}, \tag{2.21}$$

(assuming $\gamma \gg 1$) where B is the magnetic field in the frame of the shocked fluid (2.7) and σ_T is the Thomson cross-section. In the observer frame, $P = \delta^2 P'$. Hence, the peak spectral power per electron is

$$P'_{\nu',max} \approx \frac{2m_e c^2 \sigma_T}{9e} B'. \tag{2.22}$$

In the Diffusive Shock Acceleration model, the number distribution of electrons in the forward shock depends as a power of γ, $dN/d\gamma \propto \gamma^{-p}$ [18, 19]. The spectrum from this distribution of electrons will be proportional to

$$\int_{\gamma_m}^{\gamma_c} P'_{\nu'} \frac{dN}{d\gamma} d\gamma \propto \nu'^{\frac{1-p}{2}} \quad \text{if } \nu' \geq \nu'_m, \tag{2.23}$$

where γ_m is the minimum Lorentz factor of the electron distribution and $\nu_m = \nu_{syn}(\gamma_m)$. For $\nu \leq \nu_m$ the spectrum remains $\propto \nu^{\frac{1}{3}}$. Beyond γ_c the electrons are in the fast cooling regime, discussed in the next paragraph. To obtain γ_m, we first normalize the electron distribution,

$$\int_{\gamma_m}^{\gamma_{\text{max}}} \frac{dN}{d\gamma} d\gamma = \int_{\gamma_m}^{\gamma_{\text{max}}} a\gamma^{-p} = N_e, \tag{2.24}$$

where a is a normalization constant to be determined, γ_{max} is the maximum Lorentz factor in the distribution, N_e is the total number of shocked electrons. We assume

$p > 2$ and $\gamma_{\max} \gg \gamma_m$, as a result, the above integral evaluated at its upper limit $(\gamma_{\max})$ can be ignored. This yields $a = (p-1)N/\gamma_m^{1-p}$. Next we integrate the energy distribution of the electrons and equate it to equation (2.8),

$$\int_{\gamma_m}^{\gamma_c} \gamma m_e c^2 \frac{dN}{d\gamma} d\gamma = \epsilon_e N_p (\Gamma - 1) m_p c^2, \tag{2.25}$$

where N_p is the total number of shocked protons. Assuming $N_e = N_p$, the above equation gives

$$\gamma_m = \frac{p-2}{p-1} \epsilon_e (\Gamma - 1) \frac{m_p}{m_e}. \tag{2.26}$$

Electrons with very high Lorentz factors $\gamma \geq \gamma_c$ with [20]

$$\gamma_c = \frac{6\pi m_e c}{\sigma_T B'^2 t'}, \tag{2.27}$$

will have radiated almost all their energy in the frequency $\nu'_{syn}(\gamma)$. The expression for γ_c can be obtained by equating the synchrotron cooling time $(\gamma m_e c^2/P')$ to the comoving time (t'). The comoving time is related to the blast wave radius by $dt' = dr/(c\beta\Gamma)$. Therefore the spectral power for frequencies larger than $\nu'(\gamma_c) \equiv \nu'_c$ is proportional to

$$P'_{\nu'} \propto \gamma m_e c^2 \frac{dN}{d\gamma} \frac{d\gamma}{d\nu'} \propto \nu'^{-\frac{p}{2}}. \tag{2.28}$$

Here, we have used $\nu \propto \gamma^2$ (see (2.19)). For frequencies below the self-absorption frequency (ν'_a) the emission is similar to that of a blackbody of a fluid with temperature approximately equal to $\gamma_m m_e c^2/3k_b$ (k_b is the Boltzmann constant), hence $F'_{\nu'} \propto \nu'^2$ when $\nu' \leq \nu'_a$. Therefore, the complete synchrotron spectrum for this distribution of electrons is

$$P'_{\nu'} = \begin{cases} P'_{\nu',max} \left(\dfrac{\nu'_a}{\nu'_m} \right)^{\frac{1}{3}} \left(\dfrac{\nu'}{\nu'_a} \right)^2 & \nu' \leq \nu'_a \tag{2.29a} \\[2ex] P'_{\nu',max} \left(\dfrac{\nu'}{\nu'_m} \right)^{\frac{1}{3}} & \nu'_a \leq \nu' \leq \nu'_m \tag{2.29b} \\[2ex] P'_{\nu',max} \left(\dfrac{\nu'}{\nu'_m} \right)^{\frac{1-p}{2}} & \nu'_m \leq \nu' \leq \nu'_c \tag{2.29c} \\[2ex] P'_{\nu',max} \left(\dfrac{\nu'_c}{\nu'_m} \right)^{\frac{1-p}{2}} \left(\dfrac{\nu'}{\nu'_c} \right)^{-\frac{p}{2}} & \nu' \geq \nu'_c. \tag{2.29d} \end{cases}$$
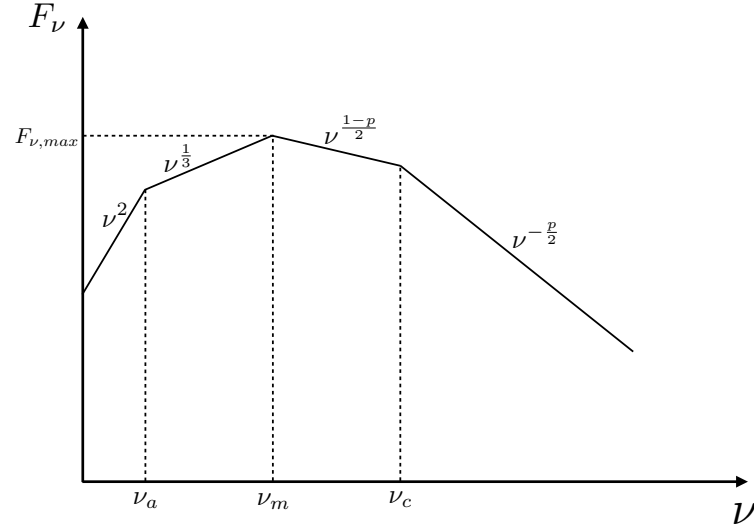
Fig. 2.2. The spectrum of synchrotron emission from a blast wave as given in equation (1.24). This spectrum is valid only if $\nu_a < \nu_m < \nu_c$

In this case the peak will occur at the frequency ν_m (see fig. 2.2). This spectrum is valid only when the characteristic frequencies are in the order $\nu_a < \nu_m < \nu_c$, the spectra and values of the peak flux and characteristic frequencies for every ordering is given in [20].

2.4 Calculating the light curve

With the spectrum and dynamical evolution of the blast wave, we can calculate the light curve of the synchrotron emission in a forward shock, which is the spectral flux density, F_ν (power per unit area per unit frequency), versus the observer time, t. In general, assuming the emission is isotropic in the comoving frame, the spectral flux at a frequency ν for a blast wave at radius R can be calculated using

$$F_\nu(\nu, R) = \frac{1+z}{4\pi D^2} P_\nu(\nu, R) N_e = \frac{1+z}{4\pi D^2} \int \frac{n_0 R^3}{3} \delta^3 P'_{\nu'}(\nu(1+z)/\delta, R) \, d\Omega, \quad (2.30)$$

where D is the distance to the source and $d\Omega$ indicates the integral is carried out over the solid angle of the blast wave. Equation (2.30) is given as a function of the radius R, but using (2.13), we can relate R to the observer time in order to get F_ν in terms of t.

For a general case the integrals of (2.13) and (2.30) need to be done numerically. However, we can obtain analytic approximations for the light curve using the same simplifications as in section 2.2, which were used to obtained analytic expressions for the dynamic quantities (2.16–2.18). Since the analytic approximations of both the spectrum and blast wave evolve as a series of power laws, so will the resulting light curve. The light curve will contain several breaks in its slope depending on which phase the blast wave is in (e.g., relativistic, ST) and which part of the spectrum our observing frequency (ν_{obs}) lies (e.g., $\nu_{obs} \leq \nu_a$ or $\nu_{obs} \geq \nu_c$). In this section we demonstrate how to obtain the slope of the light curve for these different phases assuming we are in the part of the spectrum $\max(\nu_a, \nu_m) \leq \nu_{obs} \leq \nu_c$, which corresponds to equation (2.29c). To calculate the light curve for other cases, we can follow the same steps presented in this chapter but we have to use the spectrum which corresponds to our observing frequency, this general calculation can be found in [21].

The first step is to express all the quantities in equation (2.29c) in terms of dynamic variables. A detailed list for all these expressions (for the relativistic phase) can be found in [20] and will be used here. The dynamic evolution of $F_{\nu,max}$ and ν_m is given by

$$F_{\nu,max} \propto P_{\nu,max} N_e \propto E \propto t^{\frac{3\alpha}{8+\alpha}} \tag{2.31}$$

$$\nu_m \propto t^{-\frac{3}{2}} E^{\frac{1}{2}} \propto t^{-\frac{12}{8+\alpha}} . \tag{2.32}$$

Here, we have used equation (2.16) to express all quantities in terms of time. Using (2.29c), we find

$$F_{\nu_{obs}} = F_{\nu,max} \left(\frac{\nu_{obs}}{\nu_m} \right)^{\frac{1-p}{2}} \propto t^{\frac{3\alpha - 6(p-1)}{8+\alpha}} \nu_{obs}^{\frac{1-p}{2}} . \tag{2.33}$$

This is the light curve during the relativistic phase of the blast wave. Once again this expression applies only if $\nu_m \leq \nu_{obs} \leq \nu_c$. The expression for the characteristic frequencies and peak flux during the non-relativistic phase can be found in [22], where

$$F_{\nu,max} \propto t^{\frac{3}{5}} E^{\frac{4}{5}} \propto t^{\frac{3(\alpha+1)}{5+\alpha}} \tag{2.34}$$

$$\nu_m \propto t^{-3} E \propto t^{-\frac{15}{(5+\alpha)}} . \tag{2.35}$$

Here, we use (2.17) to express all quantities in terms of time, therefore the spectral flux during the non-relativistic phase of the blast wave is

$$F_{\nu_{obs}} \propto t^{\frac{21+6\alpha-15p}{2(5+\alpha)}} \nu_{obs}^{\frac{1-p}{2}} . \tag{2.36}$$

Before the blast wave reaches the ST phase, it enters the deep Newtonian (DN) regime. The DN regime sets in when $\gamma_m \lesssim 2$, after this point in time, a majority of the shocked electrons become non-relativistic and the peak contribution in synchrotron flux will come from electrons with Lorentz factor $\gamma \sim 2$ (instead of γ_m) e.g., [23, 24]. This will alter the slope of the light curve during the non-relativistic and ST phase. The slope of the light curve during the DN regime is calculated in [25] and we will sketch the calculation below.

From equation (2.19), the frequency at which the peak flux is emitted $\nu_{pk} \propto \gamma_{pk}^2 B$ and γ_{pk} remains at a constant value of ~ 2 during the DN regime and $\Gamma \sim 1$ since the DN regime sets in during the non-relativistic phase. Using the non-relativistic version of (2.7), we find $B \propto \beta$. From (2.22), the peak spectral flux is $F_{\nu,pk} \propto BR^3\beta^2 \propto R^3\beta^3$. Using the dynamics of a non-relativistic blast wave (2.17), we can relate these quantities to the observer time

$$\nu_{pk} \propto t^{-\frac{3}{5+\alpha}} \tag{2.37}$$

$$F_{\nu,pk} \propto t^{\frac{3(\alpha-1)}{5+\alpha}} . \tag{2.38}$$

Again, using the fact that $\nu_m \leq \nu_{obs} \leq \nu_c$, the spectrum will be of the form (2.29c), hence

$$F_{\nu_{obs}} \propto t^{\frac{6\alpha-3(1+p)}{2(5+\alpha)}} \nu_{obs}^{\frac{1-p}{2}} . \tag{2.39}$$

This expression provides the slope of the light curve for the non-relativistic phase of the blast wave during the DN regime. When energy injection ceases, the blast wave enters the ST phase, at which point the energy remains constant. Therefore, the slope of the light curve for the ST phase during the DN regime can be obtained by setting $\alpha = 0$ in equation (2.39). Putting it all together, the light curve is of the form $F_\nu \propto t^{-s}\nu^{\frac{1-p}{2}}$, with the slope s given in chronological order for the different phases as

$$
s = \begin{cases}
\frac{6(p-1)-3\alpha}{8+\alpha} & \text{relativistic} \\[2mm]
\frac{15p-21-6\alpha}{2(5+\alpha)} & \text{non-relativistic} \\[2mm]
\frac{3(1+p)-6\alpha}{2(5+\alpha)} & \text{non-relativistic, DN} \\[2mm]
\frac{3(1+p)}{10} & \text{ST, DN}
\end{cases} \tag{2.40}
$$

All the calculations so far have assumed the blast wave is spherical, which is fine when modeling the SN emission. However, the blast wave associated with the afterglow is not spherical but rather a spherical cap of a sector of a sphere (see fig. 2.1). Hence its geometry has to be taken into account when calculating the light curve of the afterglow. The afterglow for on-axis observers will appear spherical until the blast wave decelerates to a Lorentz factor $\Gamma \sim 1/\theta_j$, after which point the light curve will start to decay faster, this phenomenon is known as a "jet-break" [26, 27]. Theories involving the jet-break are not completely in agreement with numerical simulations (e.g., [28–30]). Hence, we do not calculate the post jet-break light curves analytically, the afterglow light curves will be generated either numerically [30] or semi-analytically [31].

3. GRB OFF-AXIS AFTERGLOWS AND THE EMISSION FROM ACCOMPANYING SUPERNOVAE

A. Kathirgamaraju, R. Barniol Duran, and D. Giannios, *Monthly Notices of the Royal Astronomical Society*, 461:1568—1575, September 2016.

Gamma-Ray Burst (GRB) afterglows are likely produced in the shock that is driven as the GRB jet interacts with the external medium. Long duration GRBs are also associated with powerful supernovae (SN). We consider the optical and radio afterglows of long GRBs for both blasts viewed along the jet axis ("on-axis" afterglows) and misaligned observes ("off-axis" afterglows). Comparing the optical emission from the afterglow with that of the accompanying SN, using SN 1998bw as an archetype, we find that only a few percent of afterglows viewed off-axis are brighter than the SN. For observable optical off-axis afterglows the viewing angle is at most twice the half-opening angle of the GRB jet. Radio off-axis afterglows should be detected with upcoming radio surveys within a few hundred Mpc. We propose that these surveys will act as "radio triggers," and that dedicated radio facilities should follow-up these sources. Follow-ups can unveil the presence of the radio supernova remnant, if present. In addition, they can probe the presence of a mildly relativistic component, either associated with the GRB jet or the SN ejecta, expected in these sources.

3.1 Introduction

Gamma-ray burst (GRB) afterglows are likely to be produced in the external forward shock (e.g., [17, 32, 33]). In this framework, the GRB jet interacts with the external medium and drives a relativistic shock, accelerating electrons that radiate via synchrotron emission. The decelerating blast wave, initially highly collimated,

transitions from a relativistic stage to a non-relativistic spherical stage at late times. Hydrodynamical simulations are, nowadays, able to capture this long term evolution of the blast wave and calculate multi-wavelength synchrotron light curves and spectra (e.g., [30]), for observers located along the jet axis ("on-axis" observers) and at a large angle ("off-axis" observers) (e.g., [34–39]). Off-axis afterglows can potentially be observed without the detection of the prompt gamma-ray emission. For this reason, they have been referred to as "orphan afterglows". The detection of orphan afterglows remains elusive to this date (e.g., [40, 41]). Current and upcoming surveys in the optical (e.g., Pan-STARRS1, ZTF, LSST) and radio (e.g., LOFAR, VAST, VLASS, SKA1) have the detection of orphan afterglows among their main objectives.

Long GRBs are also accompanied by supernovae (SNe) of the rare broad-line Ic type. The sample of GRB-associated SNe are quite homogeneous, and the optical SN emission from SN 1998bw serves as an excellent archetype (e.g., [42]). Modeling of the SN optical emission reveals typically very energetic ejecta with kinetic energy of several $\times 10^{52}$ erg, and fairly fast velocity of $\sim 0.1c$ (see, e.g, [43–45], and references therein). The SN "remnant" also drives an external shock, accelerating electrons that radiate via synchrotron emission (e.g., [46–48]). Recently, the emission from this SN remnant (SNR) has been shown to produce a strong radio signal that could potentially be observed ~ 10 yrs after the GRB explosion [49].

Typical GRBs occur at cosmological distances. Current and near-future facilities will be capable of detecting orphan afterglows from much closer distances: just $\sim$ a few hundred Mpc. Therefore, future orphan afterglow observations should increase the number of GRBs detected nearby. This carries the promise of following these afterglows for decades in the radio, and studying the very late stages of the shock, including the potential detection of the onset of the SNR emission.

The main objective of this paper is to calculate the emission that follows the GRB, including the afterglow and the SNR, for an observer located at any angle with respect to the jet axis. We assess the various strategies of detecting an orphan afterglow at different wavelengths, especially optical and radio. In particular, in the optical band,

we compare the expected afterglow emission with the optical emission from the SN itself. We stress, in line with previous work, that radio frequencies constitute the best observing strategy to detect the emission from an orphan afterglow (e.g., [50–58]).

It is likely that the two components that we have mentioned above, the GRB jet and the SN ejecta, are not simply expelled from the central object with a single velocity and a characteristic energy. Instead, the quasi-spherical SN ejecta is thought to be composed of a range of energies that follow a power-law in velocity, with faster parts of the ejecta carrying smaller energies, as expected in hydrodynamical explosions (e.g., [10]). At the same time, a distribution of energies could also be present in the GRB jet (e.g., [59]), or the GRB jet could be surrounded by a slower "sheath" (or "cocoon") of a larger opening angle (e.g., [60]; [61]). These possibilities motivate us to consider the presence of a mildly relativistic component in the ejecta. In this paper we calculate the radiative signatures of such a component.

The paper is organized as follows. In Section 3.2 we describe the emission from the different components that follow the GRB prompt emission. In Section 3.3 we present optical and radio light curves of these components. In Section 3.4 we comment on their potential detection, and briefly discuss observing strategies and rates. We finish with our conclusions in Section 3.5.

3.2   Modeling the emission that follows the GRB

The long-lasting emission that follows the prompt GRB emission has different components: (i) the external forward shock emission that is initially strongly beamed along the direction of propagation of the jet but that gradually turns spherical as the blast slows down; (ii) the quasi-spherical SN optical emission powered by the radioactive decay, and (iii) the quasi-isotropic SNR emission, which is produced by synchrotron emission from electrons accelerated at the SN shock. For completeness, we explore the possible contribution of: (iv) synchrotron emission from an external

forward shock driven by mildly relativistic ejecta. We discuss all of these in the following subsections.

3.2.1 GRB jet afterglow model

Afterglow library

We calculate the GRB afterglow light curves using the "Afterglow library" described in [30] (see, also, [62–66]).[1] The library calculates the synchrotron light curves and spectra (at a given frequency and for a given observer angle with respect to the jet axis) using linear radiative transfer, which includes synchrotron self-absorption. The library uses snapshots of hydrodynamical simulations of GRB jets to generate these light curves. In this paper, we modify the library as described in [25]. This modification allows us to consider the "deep Newtonian" regime, which is relevant for the late time light curves calculation, where most of the shock-heated electrons are non-relativistic, but mildly relativistic particles with Lorentz factor ~ 2 contribute to the bulk of the total electron energy (see, also, [67]).

Baseline: Optical and radio light curve on-axis modeling

We use the sample of optical on-axis GRB afterglow observations found in [68] as a baseline for our study. This comprehensive sample has been extinction-corrected and scaled to a common redshift $z = 1$ and common R-band (~ 2 eV) magnitude. We arrange these observed afterglows in descending order of their brightness at 1 day and then divide them into ten groups. The first group contains the 10% brightest afterglows (9th decile), the second group contains the subsequent 10% brightest afterglows (8th decile) and so on. For each decile, we produce an average optical afterglow light curve so that we can use it to represent that decile. We also calculate the decile's

---

[1]The Afterglow Library (here we use the "Boxfit" code) is publicly available at http://cosmo.nyu.edu/afterglowlibrary.

average isotropic gamma-ray energy, $E_{\gamma,\text{iso}}$, which is the energy released during the prompt GRB phase.

To model the representative afterglow light curve of each decile, we need several parameters: E_{iso}, the isotropic equivalent kinetic energy of the jet; n, the number density of the external medium (assumed constant); the microphysical parameters ϵ_e and ϵ_B, the fraction of energy in the electrons and magnetic field in the shocked fluid, respectively; and p, the power-law index of the electron energy distribution. Although modeling of afterglow data of different GRBs indicates that these parameters are not universal, we first assume a particular set of values (based on recent studies), and later discuss how varying some of these parameters would affect our results (see Section 3.4 and the Appendix).

For each decile, we assume a GRB gamma-ray efficiency of $\sim 20\%$, so that $E_{\text{iso}} \approx 5E_{\gamma,\text{iso}}$ (e.g., [69]), $\epsilon_e \sim 0.1$ [70], $p = 2.4$ [71]. We assume $n = 1$ cm^{-3}, and then find a suitable value of ϵ_B to match the average optical brightness at 1 day for each decile using the Afterglow library, which turns out to be $\sim 10^{-5} - 10^{-4}$ consistent with, e.g., [72], [70], [69]. A large number of afterglow studies seem to point out that ϵ_e is quite constrained to be ~ 0.1 (e.g., [70], see, also, particle-in-cell simulations of [73]). It also seems that the prompt gamma-ray efficiency should not be too high (e.g., [69]). Hence, we investigate below how changing the remaining parameters n and correspondingly ϵ_B, which seem to be the least constrained, affects our conclusions. To illustrate this, we can analytically estimate the optical flux at 1 day, when the optical band is likely to be above the minimum frequency, but below the cooling one. It is given by (e.g., [20])

$$F_\nu \approx (3\text{mJy})\epsilon_{e,-1}^{1.4}\epsilon_{B,-4}^{0.9}E_{\text{iso},53}^{1.4}n_0^{1/2}t_d^{-1}d_{27}^{-2}\nu_{14}^{-0.7}, \tag{3.1}$$

where we have used the parameters mentioned above, t is the observed time since the explosion (in days), we have normalized the luminosity distance d to 300 Mpc, and we have used the common notation $Q_x = Q/10^x$ in c.g.s units. Since we consider nearby sources, we take the redshift to be $1 + z \approx 1$ in our equations. For example, for the 5th decile, $E_{\text{iso},53} \sim 2$, the flux at 1 d (at 300 Mpc) at 2 eV is ~ 5 mJy, and

therefore, $n = 1$ cm^{-3} requires $\epsilon_B \sim 4 \times 10^{-4}$. This value of ϵ_B agrees with the one found using the Afterglow library within a factor of ~ 2.

The final parameter needed is the half-opening angle of the jet, θ_j, which affects the time of the "jet break" (e.g., [26]; [27]). Individual fitting of each of the light curves is needed to do this, which is outside of the scope of this paper. Therefore, we use a simple approach and consider $\theta_j = 0.1$ ($\sim 6°$) and 0.2 ($\sim 11°$), which spans the approximate range of typical opening angles inferred from observations (e.g., [74]; [75] and references therein). We now introduce some terminology that will be used throughout this paper. The afterglows in the 9th decile will be called the "brightest afterglows." We also group the GRBs in the 4th, 5th and 6th deciles together and call these the "average afterglows," since they yield the average optical flux at 1 d of our sample.

Using the parameters described above, we predict the off-axis afterglow in the optical (R-band). We also use these parameters to predict the on-axis and off-axis radio afterglows (at 4.9 GHz, which is a typical observing radio band). Given that radio on-axis afterglows observations are available, we use the average observed radio afterglow light curve in [76] to compare with our predicted on-axis radio afterglows.

3.2.2 SN optical emission

The supernovae accompanying long duration GRBs are very similar in nature. At ~ 10 d after the GRB, the GRB-SNe sample spans only a factor of $\lesssim 4$ in bolometric luminosity [45]. Also, in a systematic study recently done by [42], it was found that SN 1998bw represents a typical supernova that accompanies a GRB. Hence, we will use the derived physical parameters of 1998bw in this paper: a SN ejecta kinetic energy of $E_{\text{SN}} \sim 5 \times 10^{52}$ erg and a velocity of 24,000 km/s, which is $\beta_{\text{SN}} \approx 0.08$ in units of the speed of light (e.g., [77]). The optical data for SN1998bw were obtained from [78].

3.2.3   SN remnant (SNR) radio emission

At very late times, radio emission from the SNR may outshine the GRB after-glow [49]. Therefore, it proves useful to include this component in our late time calculations. We follow the same procedure as in [49] to obtain the SNR light curve for a 1998bw-like SN. To summarize their work, the SNR radio flux is

$$
F_\nu = F_p \begin{cases} t^3 & t < t_{\text{dec,SN}} & \text{(3.2a)} \\ t^{\frac{-3(1+p)}{10}} & t > t_{\text{dec,SN}}, & \text{(3.2b)} \end{cases}
$$

where the deceleration time of the SN ejecta is

$$
t_{\text{dec,SN}} \approx 29 \beta_{\text{SN},-1}^{-5/3} (E_{\text{SN},52.5}/n_0)^{1/3} \, \text{yr}, \tag{3.3}
$$

and the peak flux (in μJy) at observed frequency ν at this time is given by

$$
F_p \approx 440 \, \bar{\epsilon}_{e,-1} \epsilon_{\text{B-SN},-2}^{\frac{1+p}{4}} \beta_{\text{SN},-1}^{\frac{1+p}{2}} E_{\text{SN},52.5} \, n_0^{\frac{1+p}{4}} \nu_{\text{GHz}}^{\frac{1-p}{2}} d_{27}^{-2}, \tag{3.4}
$$

where $\bar{\epsilon}_e \equiv 4\epsilon_e(p-2)/(p-1)$. It is important to note that these results are valid for $\max(\nu_a, \nu_m) < \nu < \nu_c$, where ν_a, ν_m and ν_c are the synchrotron self-absorption, minimum injection and cooling frequencies, respectively. We assume that the SNR emission is quasi-isotropic; therefore, it is observable for any viewing angle.

Since SNR emission from a GRB-accompanying SN has not been observed, the SNR physical parameters remain uncertain. In the following, we will use the same values for density, ϵ_e and p used for our GRB afterglows calculations, and we will use the kinetic energy and velocity of the SN ejecta inferred from 1998bw (see Section 3.2.2). We will use a value of $\epsilon_{\text{B-SN}} \sim 0.01$, inferred for "normal" Ibc young radio SNe (e.g. [79]). Ideally, one could use very late time radio afterglow observations (~ 10 yr) to constrain ϵ_B and other parameters, and use them to calculate the radio SNR emission. This can only be done for one GRB, so here we simply adopt a fixed value of ϵ_B (see [49]). A different choice of parameters would yield different fluxes according to equation (3.4).

3.2.4 Other possible mildly relativistic components

So far we have considered the light curves from two components with distinct energies and distinct velocities: the ultra-relativistic jet and the non-relativistic SN ejecta. Motivated by previous work, we consider the presence of a mildly relativistic component (e.g., [59]) and predict its light curve. This extra component could be related to the GRB jet or the SN ejecta. For simplicity, we will assume that it is associated to the quasi-spherical SN ejecta. We will model the SN ejecta with a continuous kinetic energy distribution as $E \propto (\beta\Gamma)^{-\alpha}$ with $0.1 \leq \beta\Gamma$, α varying from 1 to 5 (observations and theory seem to constrain $\alpha \sim 5$ for typical SNe), and we normalize the total kinetic energy to that of the SN (e.g., [10], [80]). Faster parts of the ejecta, which contain less energy, decelerate at earlier times; slower but more energetic parts catch up with them later on, re-energizing the blast wave. In this scenario, the Lorentz factor and energy of the blast wave are $\Gamma \propto t^{-3/(8+\alpha)}$ and $E \propto t^{3\alpha/(8+\alpha)}$ (e.g., [81]), while in the non-relativistic phase the velocity and energy are $\beta \propto t^{-3/(5+\alpha)}$ and $E \propto t^{3\alpha/(5+\alpha)}$ (see section 2.2). The synchrotron emission from this blast wave yields light curves of the form $F_\nu \propto t^{-s}\nu^{-(p-1)/2}$, with the temporal decay index presented in [21]. During the non-relativistic phase, the blast wave will transition to the deep Newtonian (DN) phase. The DN phase sets in when the minimum Lorentz factor of the shocked electrons drops to $\gamma_{min} \lesssim 2$ [25]. At this stage, the mildly relativistic electrons contribute to the majority of the flux emitted, causing a slight change in the slope of the light curves. The temporal decay indices in order of appearance are

$$
s = \begin{cases}
\dfrac{6(p-1) - 3\alpha}{8 + \alpha} & \text{relativistic phase,} & (3.5\text{a}) \\[2mm]
\dfrac{15p - 21 - 6\alpha}{10 + 2\alpha} & \text{non-relativistic phase,} & (3.5\text{b}) \\[2mm]
\dfrac{3(1 + p) - 6\alpha}{10 + 2\alpha} & \text{deep Newtonian phase.} & (3.5\text{c})
\end{cases}
$$

The transition from the relativistic to the non-relativistic phase occurs at $\beta\Gamma = 1$, and the transition from the non-relativistic to DN phase occurs at a velocity $\beta_{\mathrm{DN}} =$

$0.2\bar{\epsilon}_{e,-1}^{-1/2}$ [25]. We note that for $\alpha \to \infty$, that is, when all energy is concentrated in a single-velocity component of $\sim 0.1c$, then the flux increases as $\propto t^3$ as the blast wave coasts. For $\alpha = 0$, which means constant blast wave energy (no energy injection), one obtains the "usual" temporal flux decay for a decelerating blast wave in the corresponding phases (e.g. [17, 22, 25]). When the slowest component, with $\sim 0.1c$ velocity, catches up with the mildly relativistic component, energy injection ceases and the flux decreases as $\propto t^{-3(1+p)/10}$, see equation (3.2b). This occurs at $t_{\mathrm{dec,SN}}$ given by equation (3.3). Therefore, due to our choice of the kinetic energy normalization of this mildly relativistic component, the radio SNR light curve will exhibit a modified light curve before $t_{\mathrm{dec,SN}}$, but the normalization at $t_{\mathrm{dec,SN}}$ and the light curve beyond this time will remain the same as presented in Section 3.2.3.

As discussed above, the flux of the mildly relativistic component before $t_{\mathrm{dec,SN}}$ is given by $F_\nu = F_p(t/t_{\mathrm{dec,SN}})^{-s}$. When the blast wave is non-relativistic and energy injection proceeds, then s takes the value in equation (3.5b) and the flux (in μJy) is given by

$$F_\nu \approx 440\, \bar{\epsilon}_{e,-1}\, \epsilon_{\mathrm{B\text{-}SN},-2}^{\frac{1+p}{4}}\, \beta_{\mathrm{SN},-2}^{\frac{40+11\alpha+p(\alpha-20)}{10+2\alpha}}\, E_{\mathrm{SN},52.5}^{\frac{3+5p}{10+2\alpha}}\, n_0^{\frac{p(\alpha-5)+5\alpha+19}{20+4\alpha}}\, \nu_{\mathrm{GHz}}^{\frac{1-p}{2}}\, (1+z)^{\frac{p(10-\alpha)-5\alpha-16}{10+2\alpha}} \\ \times d_{27}^{-2} \left(\frac{t}{29\,\mathrm{yr}}\right)^{-s}, \tag{3.6}$$

where we have left the redshift dependence since it is non-trivial. As an example, if we let $\alpha = 5$ and $p = 2.4$ this flux is given by (in μJy)

$$F_\nu \approx 35\, \bar{\epsilon}_{e,-1}\, \epsilon_{\mathrm{B\text{-}SN},-2}^{0.85}\, \beta_{\mathrm{SN},-2}^{2.95}\, E_{\mathrm{SN},52.5}^{0.75}\, n_0^{1.1}\, \nu_{\mathrm{GHz}}^{-0.7}\, d_{27}^{-2}\, t_{\mathrm{yr}}^{0.75}, \tag{3.7}$$

which rises slower than $\propto t^3$.

It is also instructive to determine the time when the decaying flux of the GRB jet component (at this late time it is spherical and in the deep Newtonian regime) is equal to the flux of the SNR (before $t_{\mathrm{dec,SN}}$) as was done in [49]. Setting equation (3.6) equal to the flux of the GRB afterglow (equation (7) in [49]), we obtain the time after which the SNR outshines the GRB afterglow (we will call this the rebrightening time, t_{rb}). As an example, for $\alpha = 5$ and $p = 2.4$, the rebrightening time is

$$t_{rb} \approx (1.8\,\mathrm{yr})\, \beta_{\mathrm{SN},-1}^{-\frac{5}{3}}\, E_{\mathrm{SN},52.5}^{-0.42}\, E_{\mathrm{GRB},51}^{0.76}\, n_0^{-\frac{1}{3}}\, \chi_B^{-0.48}. \tag{3.8}$$

In this expression, E_{GRB} is the true (beaming-corrected) energy of the GRB jet, and $\chi_B \equiv \epsilon_{\mathrm{B\text{-}SN}}/\epsilon_B$.

Taking $\alpha \to \infty$ (i.e. assume no mildly relativistic component) and $p = 2.4$ gives $t_{rb} \sim 9$ yr, which is significantly longer. Therefore, the presence of a mildly relativistic component in the SN ejecta naturally yields a radio SNR flux that exceeds the GRB component at a much earlier time. We note that to obtain equation (3.8), we have used the simplifying assumption that the GRB emission is in the deep Newtonian phase and that the energy injection to the SN ejecta is in the non-relativistic phase. As for the SNR emission, we assume that this mildly relativistic SN-component is quasi-isotropic; therefore, it is observable for any viewing angle.

The results presented in this subsection are valid for $\max(\nu_a, \nu_m) < \nu < \nu_c$. At early times, in the relativistic phase, the characteristic frequencies are larger; therefore the observing frequency could be either below ν_m or ν_a. We use the expressions in [21] (see their equations 18 and 19) to estimate the location of the characteristic frequencies and the expected light curves. Whenever the characteristic frequencies cross the observing band, a sharp break in the radio light curves occurs when $\max(\nu_a, \nu_m) < \nu < \nu_c$. At later times, the light curve transitions to the non-relativistic phase, then to the deep Newtonian phase, and then finally to the time when energy injection ceases (see Fig. 3.2).

3.3   Summary of results

In the following subsections we present the expected optical and radio light curves, respectively, including all different components discussed above.

3.3.1   Optical emission

We have calculated the GRB optical afterglow for each decile for different viewing angles, θ_{v}. We compare this emission with that of the optical emission of SN 1998bw. As an example, the light curves for the "brightest afterglow" and the 5th decile are

shown in Fig. 3.1 (we plot these for $\theta_j = 0.2$). As can be seen, the SN optical emission is brighter than any off-axis afterglow for which the viewing angle is larger than $\theta_{v,crit} \sim 20° \sim 1.7\theta_j$. A similar conclusion holds for $\theta_j = 0.1$ (we obtain $\theta_{v,crit} \sim 15°$).

3.3.2 Radio emission

Using the parameters obtained from matching the optical data at 1 day, we have calculated the GRB radio afterglow for each decile for different viewing angles. As an example, the light curves for the "average afterglow" are shown in the top panel of Fig. 3.2. We plot these for $\theta_j = 0.2$. For $\theta_j = 0.1$ the on-axis radio light curve peaks only a factor of ~ 2 earlier and with similar flux. The $\theta_j = 0.1$ off-axis light curves peak at similar times, although with weaker fluxes by a factor of ~ 4, compared with the $\theta_j = 0.2$ case.

We present the SNR radio emission, and also the possible contribution of a mildly relativistic SN component with $\alpha \approx 5$ (e.g., [80]), in the top panel of Figure 3.2. In the bottom panel of Figure 3.2, we only include the on-axis radio afterglow for the average afterglow, but include several possible distributions for the mildly relativistic SN component: $1 \leq \alpha \leq 5$, and $\alpha \to \infty$, which corresponds to the case where the SN ejecta has a single speed of $\sim 0.1c$ (no mildly relativistic component). As can be seen, allowing for the presence of a mildly relativistic component yields a contribution to the radio flux at earlier times.

Our predicted on-axis average radio light curve (predicted using the parameters obtained from matching the optical data at 1 day) does fairly well in reproducing the early ($<$ month) average radio observations in [76][2]. However, it underpredicts the late time ($>$ months) radio observations. These late time data ($>$ months) in [76] are sparse: their average observed radio afterglow light curve at this stage is dominated

---

[2]As pointed out by Chandra & Frail (2012), the bright radio data at $<$ few days might be the result of an extra component: the reverse shock emission, which should decay quickly afterward and will not affect our radio light curves at late times.
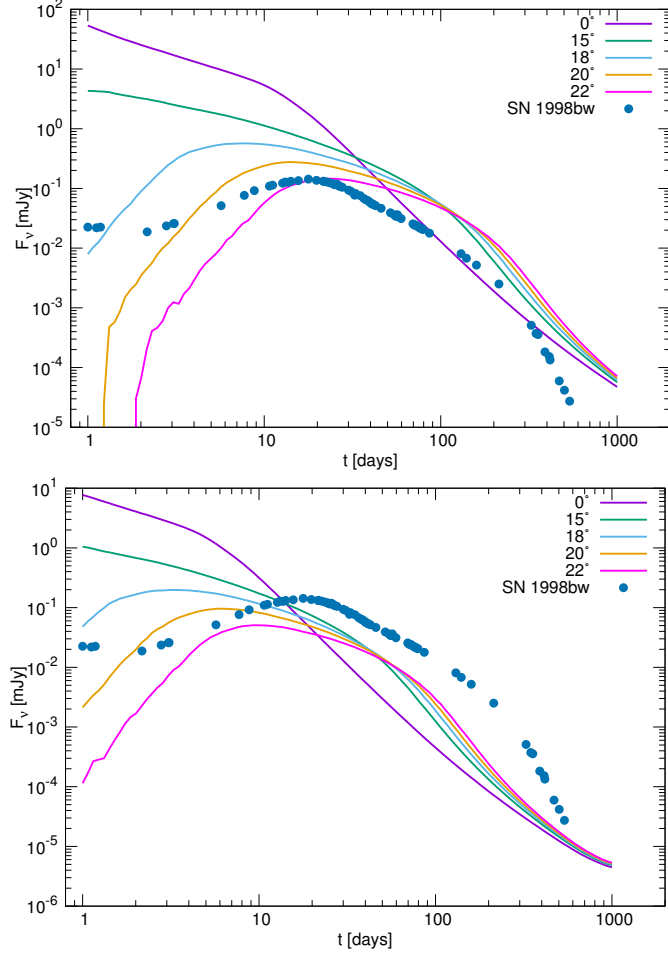
Fig. 3.1. Optical (~ 2 eV) GRB afterglow light curves (lines) and the SN optical emission (points); for the latter we use observations of SN 1998bw, which serves as a typical GRB-accompanying SN. The top panel shows the model for the "brightest" afterglows in our sample, while the bottom panel shows the model for the afterglow observed in the 5th decile. In both panels we show the on-axis and off-axis afterglows (viewing angles are indicated in the legend, peak flux of light curves decreases for larger viewing angles). The SN optical emission outshines the off-axis afterglow emission unless the viewing angle is very close to twice the half-opening angle of the GRB jet. An external density of $n = 1$ cm^{-3} was used (for other parameters, see Section 3.2.1). The source is placed at a distance $d_L = 300$ Mpc. Afterglow light curves are produced with the Afterglow Library ([30]).

only by a few bright long-lived afterglows. However, it does seem that some specific radio afterglows do decay much slower than expected in the simplest external shock model (see, e.g., [82]). We discuss this in the next section.

3.4   Discussion

In Fig. 3.1 we see that the brightest afterglows are visible up to a critical viewing angle of $\theta_{\rm v,crit} \sim 20°$, beyond which the SN emission becomes comparable to the optical afterglow. For fainter optical afterglows, the SN emission outshines the afterglow at early times ($\lesssim 1$ month), but it will still be detectable up to $\theta_{\rm v,crit}$. This pattern is seen for afterglows up to the 5th decile. For optical afterglows in the $\leq 6^{th}$ decile, the critical viewing angle is $< 20°$. Therefore, optimistically, $\sim 50\%$ of afterglows in our sample outshine the optical SN emission as long as the viewing angle is $< \theta_{\rm v,crit}$. From this, we can calculate the solid angle subtended by observers with viewing angle within $\theta_{\rm v,crit}$ and divide this by the total solid angle to find the probability of detecting such afterglows (including the counter jet). We find a small probability of $100 \times 0.5 \int_{0}^{\theta_{\rm v,crit}} sin\theta d\theta \approx 3\%$ to clearly identify the afterglow emission in a GRB associated with a SN. If we consider $\theta_j = 0.1$, this probability decreases to $\sim 2\%$. As mentioned in Section 3.2.1, there are different sets of parameters that could be used to match the optical on-axis fluxes. In the Appendix, we investigate the afterglow light curves in Fig. 1 for different sets of $E_{\rm iso}, n$ and ϵ_B. We find that our conclusions do not change even when considering this degeneracy in the parameters.

In the radio band the afterglow is observable for various viewing angles and for long times as shown in Fig. 3.2. At late times, the radio SNR emission outshines the GRB afterglow [49]. The rebrightening time decreases significantly if the SN ejecta contains a mildly relativistic component. Therefore, the time when the rebrightening occurs can give us important information on the energy distribution of the SN ejecta. The radio SNR emission does depend on the microphysical parameters of the SN
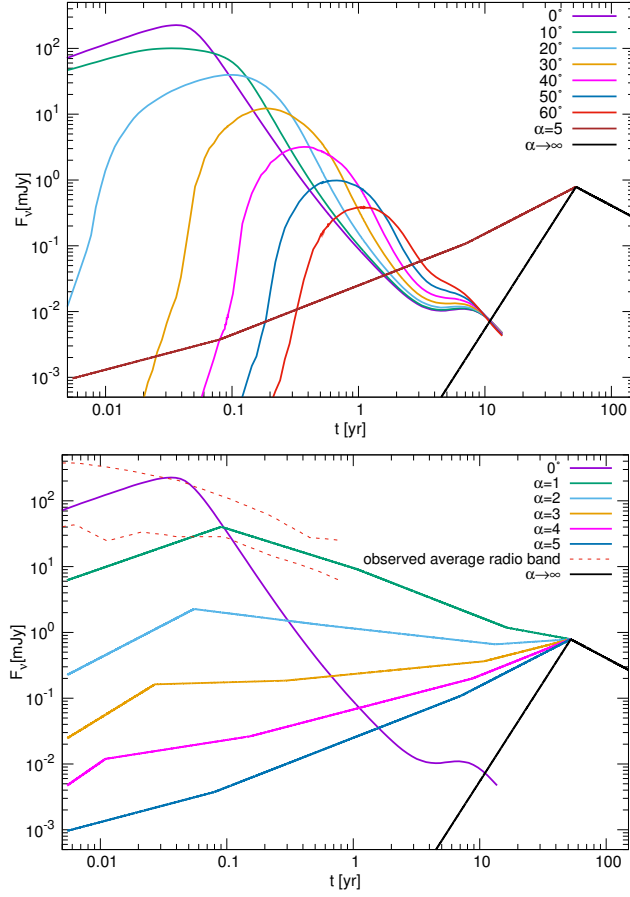
Fig. 3.2. Top panel: Radio (4.9 GHz) GRB afterglow light curves for the "average" afterglow of our sample for various viewing angles (see legend, peak flux of light curves decreases for larger viewing angles). Radio SNR emission, allowing for the presence of a mildly relativistic component in the SN ejecta for different values of α (see legends in both panels, higher values of α correspond to lower fluxes at 1 yr), where the kinetic energy is injected to the blast wave as a function of velocity $\propto (\beta\Gamma)^{-\alpha}$. Bottom panel: The region between the dashed lines indicates the location of the observed on-axis radio afterglows from the sample of [76]. The mildly relativistic component generally shows four breaks in its light curve: the crossing of the minimum synchrotron frequency, the transition to the non-relativistic phase, the transition to the deep Newtonian phase, and the cessation of energy injection (in order of appearance, see Section 3.2.4). An external density of $n = 1$ cm^{-3} was used (for other parameters, see Section 3.2.1), the source is placed at $d_L = 300$ Mpc. Afterglow light curves are produced with the Afterglow Library ([30]). The SNR radio emission is calculated as in [49].

shock. Here, we used microphysical parameters similar to those obtained in young radio SNe (e.g., [79], see discussion in [49]).

For a smaller density by a factor of 10 ($n = 0.1$ cm^{-3}, increasing ϵ_B correspondingly, so that the optical flux at 1 day is matched), the on-axis radio afterglow peaks earlier by a factor of ~ 1.5 and has a similar flux as the $n = 1$ cm^{-3} case. The off-axis radio afterglows peak a factor of $\lesssim 4$ later in time with a factor of $\lesssim 3$ smaller fluxes. Also, for this smaller density, the peak time of the SNR radio emission increases by a factor of ~ 2, which is expected from equation (3.3). This causes the rebrightening time to increase by a factor of ~ 2.

As can be seen in the bottom panel of Fig. 3.2, our on-axis GRB radio afterglow underestimates the late time ($>$ months) average observed radio flux. Although the data used in [76] to construct the late time average light curve are sparse, there *are* some bursts that show a shallow radio light curve. Its origin has been studied by [82], who have considered several possibilities (including time-varying microphysical parameters, and energy injection to the reverse shock, among others), but it is clear that it cannot have an external shock origin in the simplest model. The theoretically calculated radio on-axis afterglows decrease too fast.

In order to account for the observed flat late-time radio curves, we consider a SN ejecta with a mildly relativistic contribution with $\alpha = 1$, which nicely follows the late-time on-axis radio afterglow of [76]. Therefore, we can add both contributions to the radio band: 1. the on-axis GRB afterglow and 2. the (quasi-spherical) mildly relativistic SN ejecta component, to obtain the late time radio on-axis light curve. The precise physical origin of the second component is outside of the scope of this paper (it could be, e.g., a mildly relativistic component from the GRB jet itself, and probably not related to the SN). Nevertheless, at these late times, the component is most likely non-relativistic and quasi-spherical, allowing observers at any angle to detect it. We present the contribution from both components for different viewing angles in Figure 3. In light of this, radio fluxes presented in the top panel of Fig. 3.2 serve as lower limits.
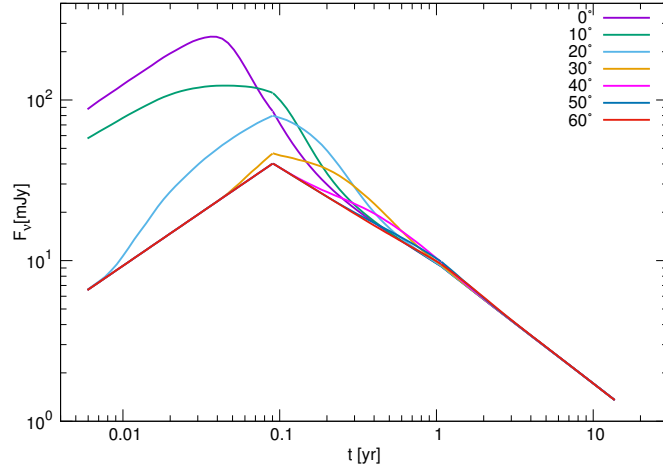
Fig. 3.3. The sum of the "average" radio (4.9 GHz) GRB afterglow light curves (for different viewing angles, see legend, peak flux of light curves decreases for larger viewing angles) and the radio emission from an $\alpha = 1$ mildly relativistic component, which is quasi-spherical (see Fig. 3.2, bottom panel). An external density of $n = 1$ cm^{-3} was used (for other parameters, see Section 3.2.1), the source is placed at $d_L = 300$ Mpc. Afterglow light curves are produced with the Afterglow Library ([30]).

After finding that the $\alpha = 1$ component reproduces the observed late time on-axis afterglow radio data quite well, we investigated the contribution of this component in the optical band, i.e., its contribution to Fig. 3.1. We found that this component outshines the SN optical emission after ~ 3 months. However, for typical cosmological GRBs, which occur at $z \gtrsim 1$, the optical flux from the $\alpha = 1$ component is too weak to be observed. Nearby GRBs ($\lesssim 300$ Mpc) might show a flattening in the optical light curve at ~ 3 months due to the contribution of this $\alpha = 1$ component.

As mentioned above, the vast majority of off-axis optical afterglows are expected to be weaker than the emission from the accompanying SN. This can make the detection of off-axis optical afterglows a more difficult task than previously thought (e.g., [36, 39, 83]), even if they are stronger compared to their host galaxy emission. Optical

off-axis afterglow studies should include the contribution from the SN emission, since the SN-GRB association is firm.

Several radio surveys are coming online in the near future. We briefly mention their potential in detecting radio off-axis afterglows for "average" GRBs in view of our results (these "average" GRBs have isotropic equivalent energy $E_{iso} \sim 10^{53}$ ergs). We consider one of those programs: VAST, which is the ASKAP Survey for Variables and Slow Transients [84]. They have planned several surveys to detect radio transients at ~ 1.4 GHz. The "VAST-Wide" survey has a 1σ rms sensitivity of 0.5 mJy and covers 10^4 deg^2 per day. From Fig. 2, we see that the peak flux at $\theta_{\rm v} \approx 45°$ is ~ 1 mJy for a frequency of 4.9 GHz (the flux at 1.4 GHz would be a factor of ~ 2 larger). Therefore we deduce that this survey will be able to detect afterglows up to a distance of 300 Mpc provided $\theta_{\rm v} \lesssim 45°$. With the covered area of the survey and using the beaming-corrected local GRB rate of[3] ~ 15 Gpc^{-3} yr^{-1}, we expect only ~ 0.4 events per year. The "VAST-Deep Multi-field" survey has a 1σ rms sensitivity of 0.05 mJy and covers 10^4 deg^2 per year. Constraining $\theta_{\rm v} \lesssim 45°$, we expect to detect ~ 13 events per year. Finally, the "VAST-Deep Single field" survey has a 1σ rms sensitivity of 0.05 mJy but covers 30 deg^2 per day, which yields ~ 0.04 events per year (here again we keep the same constraint on $\theta_{\rm v}$). Since these surveys will last for a $\sim$ few years, off-axis radio afterglows should be detected (see [57, 58]). Other radio surveys such as Apertif on WSRT [87], MeerKat [88], surveys with the VLA [89] known as VLASS, SKA1 [90], should also be able to detect orphan afterglows, provided that it is possible to distinguish between them and other slowly evolving radio synchrotron sources.

The calculations in the previous paragraph take into account the afterglow light curves of Fig. 2, which were shown to underestimate the radio flux after a few months. If we consider the presence of a mildly-relativistic quasi-spherical component

---

[3]The local GRB rate is ~ 1 Gpc^{-3} yr^{-1} [85] for events with gamma-ray isotropic luminosities $\gtrsim 10^{50}$ erg/s. For the bursts energies considered in Fig. 3.2, the local rate would be a factor of ~ 3 smaller (see [58]). For $\theta_j = 0.2$, the beaming correction is $2\pi\theta_j^2/(4\pi) \sim \frac{1}{50}$ (e.g., [86]). Therefore, the beaming-corrected local rate is ~ 15 Gpc^{-3} yr^{-1}.

(see Fig. 3), the radio flux of the source for any observing angle is increased by one order of magnitude. Thus even if a modest fraction of GRBs contain such a mildly relativistic component, the number of orphan afterglows detected in the radio would have a significant increase.

Since the nearby population of GRBs is likely to be dominated by low-luminosity GRBs (*ll*GRBs, e.g., [91]), we briefly discuss the detection of *ll*GRBs in regards to upcoming surveys. Even though they are more abundant and roughly isotropic, the afterglows of *ll*GRBs are a couple of orders of magnitude fainter than off-axis long GRBs. This makes them quite hard to detect in upcoming radio surveys; SKA1 is the only survey that will be able to detect them [58]. Nevertheless, detection and very late time follow-up of the radio afterglows of *ll*GRBs should give us insight into the energy distribution of their blast waves and the emergence of the radio SNR [21, 49].

3.5 Conclusions

We have explored the different components present in a long GRB explosion: the GRB jet, the SN ejecta and the possible contribution of a mildly relativistic component. The GRB jet interacts with the external medium and produces an afterglow, which can in principle be detected for different viewing angles without the detection of the prompt gamma-ray emission. The SN ejecta is generally quasi-spherical and produces optical photons detected by observers at any angle.

Using a sample of optical on-axis afterglows, we predict that the vast majority of optical off-axis afterglow will be too weak to be detected in excess of the emission from the accompanying SN. In lines with previous work, radio observations provide the best alternative to detect afterglow without an associated gamma-ray trigger.

Upcoming radio surveys should be able to detect off-axis afterglows within $\sim$ $300 - 500$ Mpc. These radio surveys can act as radio "triggers". We encourage the follow-up of newly found off-axis afterglows with dedicated facilities (e.g., VLA). Follow-ups may discover the emission from the radio SNR that accompany long GRBs

[49]. In addition, they can strongly constrain the energetics of any mildly relativistic component (either associated to the SN ejecta or the GRB jet). Finally, the discovery of nearby GRB sources could help us in identifying their central engines. For example, bright soft gamma-ray repeater-like flares at a location coincident with that of the afterglow could reveal that the GRB is associated with the birth of a magnetar [92].

4. OBSERVATIONAL CONSTRAINTS ON LATE-TIME RADIO REBRIGHTENING OF GRB-SUPERNOVAE

As coauthor, I was partly responsible for the write up of this article ($\sim$ 15%) and provided the analytic expressions which were used to constrain the observed results.

We present a search for late-time rebrightening of radio emission from three supernovae (SNe) with associated gamma-ray bursts (GRBs). It has been previously proposed that the unusually energetic SNe associated with GRBs should enter the Sedov-Taylor phase decades after the stellar explosion, and this SN "remnant" emission will outshine the GRB radio afterglow and be detectable at significant distances. We place deep limits on the radio luminosity of GRB 980425/SN 1998bw, GRB 030329/SN 2003dh and GRB 060218/SN 2006aj, $10 - 18$ years after explosion, with our deepest limit being $L_\nu < 4 \times 10^{26}$ erg s^{-1} Hz^{-1} for GRB 980425/SN 1998bw. We put constraints on the density of the surrounding medium for various assumed values of the microphysical parameters related to the magnetic field and synchrotron-emitting electrons. For GRB 060218/SN 2006aj and GRB 980425/SN 1998bw, these density limits have implications for the density profile of the surrounding medium, while the non-detection of GRB 030329/SN 2003dh implies that its afterglow will not be detectable anymore at GHz frequencies.

4.1 Introduction

Due to the extreme luminosities of gamma-ray bursts (GRBs), releasing $\sim 10^{51}$ erg of kinetic energy on a timescale of seconds, they can be detected out to very large

redshifts and provide a unique way to study physics in extreme conditions e.g., [93–96]. GRBs can emit long-lasting synchrotron emission spanning X-ray to radio frequencies, known as afterglows [97–99]. The radio emission of a GRB, sometimes spanning hours to years after the initial outburst, is dominated by this synchrotron emission produced by the GRB ejecta, which start out as a collimated jet and gradually spread to expand more isotropically e.g., [26, 100]. When the ejecta interact with the ambient medium, they amplify the magnetic field and accelerate particles to relativistic speeds [101]. Radio observations play an essential role in understanding GRB afterglows, as they provide information about the energetics of the explosion, the ambient medium, shock physics, and the relativistic expansion velocity in the jets (for a review, see [102]).

Jets are not the only ejecta expelled in the GRB event; if there is an associated supernova (SN), a spherical outflow is also present. Long-duration GRBs, unlike short GRBs, have been found to have associated SNe and may provide insights into the deaths of massive stars [103, 104]. The SNe associated with GRBs are of Type Ic and feature broad lines in their optical spectra, implying fast moving ejecta with velocities ~ 0.1 times the speed of light c [105, 106]. These broad-line Type Ic SNe display kinetic energies that are ~ 10 times greater than those of GRBs or normal Type Ic SNe ($\sim 10^{52}$ erg; [106–110]).

Although the SN ejecta have a slower maximum velocity, they are much more massive ($\sim 1 - 12$ M$_\odot$, [111–113]) than GRB jets ($\sim 10^{-6}$ M$_\odot$; [114]) and are expected to coast a longer time before decelerating. After the explosion, the SN ejecta will remain in free expansion for a few decades, and will sweep up material from the surrounding medium. The SN ejecta interact with the surrounding medium, accelerating particles to relativistic speeds and amplifying the magnetic field, producing radio synchrotron emission much like in a typical SN remnant [115–117].

This radio emission peaks when the SN has swept up an equivalent mass to the initial ejected mass, at the Sedov-Taylor time [15, 16]. For typical SNe, the Sedov-Taylor time is $\sim 1,000$ years after the explosion (e.g., [118]). The Sedov-Taylor time may be ~ 2 orders of magnitude shorter for the more energetic GRB/SNe, due to

their large expansion velocities [116]. Because of the likeness to typical SN remnants (SNRs), we refer to GRB/SN radio emission on decades-long scales as "SNR emission" throughout the rest of this paper. After peaking at the Sedov-Taylor time, the radio emission will decline throughout the Sedov-Taylor phase, as the SNR blast wave decelerates [116–119].

In the first few years after a GRB/SN explosion, while the SN ejecta coast in a free expansion phase, the GRB shock decelerates from ultra-relativistic to non-relativistic speeds. Around 10 years after the burst, the radio emission from the SN shock approaches the same prominence as the emission from the GRB shock. Ultimately, the SNR emission dominates the total emission due to its higher kinetic energy. [116] and [117] modeled the GRB afterglow and SNR emission, and find that SNRs accompanying nearby GRBs should become detectable with sensitive modern radio telescopes some $\sim$20–50 years after explosion (assuming that the GRB/SN is interacting with a 1 cm^{-3} medium, and is at a nearby distance of z $\lesssim 0.2$; see [116]). Here we present our search for the radio SNRs associated with three nearby, well-studied GRB/SNe: GRB 980425/SN 1998bw, GRB 030329/SN 2003dh, and GRB 060218/SN 2006aj. Radio emission on timescales from days to years has previously been detected in these GRB/SN systems.

Detecting the radio rebrightening of a GRB/SN would mark the first time that we have watched a SN transform into an SNR. Although there have been efforts to detect the radio re-brightening which defines the start of the SNR phase decades after SN explosion (e.g., [120, 121]), this has yet to be done successfully. Our study focuses on sources that should reach the Sedov-Taylor time faster and have higher luminosity, compared to SNe with more typical energetics (i.e. $\sim 10^{51}$ erg). Indeed, GRB/SNe may present some of the best prospects for detecting this rebrightening radio emission, despite being much further away than the SNe in the [120] sample. Detection of the SNR radio emission would also develop our understanding of particle acceleration and magnetic field amplification in $\sim 0.1\,c$ shocks. Finally, the radio rebrightening offers a chance to study the properties of a GRB/SN system, including constraining the

density of the ambient medium and potentially settling if the SNe associated with GRBs truly are extra-energetic.

In Section 4.2, we describe the models for radio SNR emission from a GRB/SN. Section 4.3 introduces our sample of three GRB/SN sources, and the observations of these sources are described in Section 4.4. The results of the observations and analysis are discussed in Section 4.5, and our conclusions are laid out in Section 4.6.

4.2 Models of early SNR radio emission

When we began this study of GRB/SN systems, we followed the predictions by [116] to estimate radio emission from the SN ejecta at the time of our observations ($\sim 10-20$ years after explosion). While our observations were being conducted, more sophisticated models of the SNR emission from GRB/SN systems were published [117]. Within this paper, we use our deep limits and the models of [117], which build on the models of [116, 122], to constrain parameters which determine the SNR radio luminosity. Here we outline the details of the calculations and models of [117]. We discuss the implications of these models with our observational limits in more detail in Section 4.5.

The flux from an SNR reaches a maximum flux density (F_p) at the deceleration time of the SN (t_{dec}; essentially, the Sedov-Taylor time). The equations for these quantities are given in [116] as:

$$t_{\mathrm{dec}} \approx 29 \, \beta_{\mathrm{SN},-1}^{-5/3} \left(E_{\mathrm{SN},52.5}/n_0\right)^{1/3} (1+z) \text{ yr} \tag{4.1}$$

$$\begin{aligned} F_p \approx 440 \, \bar{\epsilon}_{e,-1} \, \epsilon_{\mathrm{B},-2}^{\frac{1+p}{4}} \, \beta_{\mathrm{SN},-1}^{\frac{1+p}{2}} \, E_{\mathrm{SN},52.5} \, n_0^{\frac{1+p}{4}} \, \nu_{\mathrm{GHz}}^{\frac{1-p}{2}} \\ \times (1+z)^{\frac{1-p}{2}} \, d_{27}^{-2} \, \mu\mathrm{Jy} \end{aligned} \tag{4.2}$$

Here, ϵ_e and ϵ_B are the fraction of the post-shock energy transferred to the relativistic electrons and amplified magnetic field, respectively (in the above equation, they are scaled to convenient values, $\epsilon_{\mathrm{B},-2} = \epsilon_{\mathrm{B}}/0.01$ and $\epsilon_{e,-1} = \epsilon_{e}/0.1$). The power-law index of the non-thermal electron energy distribution accelerated by the SN blast wave is p,

and $\bar{\epsilon}_{e,-1} \equiv 4\epsilon_{e,-1}(p-2)/(p-1)$. The volume number density of the external medium is n_0 in units of cm^{-3}. $E_{\text{SN},52.5}$ is the energy of the SN normalized to $10^{52.5}$ erg, and $\beta_{\text{SN},-1}$ is the ratio of the mass-averaged speed of the SN ejecta and the speed of light (v/c) normalized to 0.1. The observing frequency in GHz is ν_{GHz}, d_{27} is the luminosity distance normalized to 10^{27} cm, and z is the redshift. The above equations assume we are observing within $\max(\nu_a, \nu_m) < \nu < \nu_c$, with ν_a, ν_m, and ν_c being the self-absorption frequency, peak frequency, and cooling frequency, respectively. We note that the numerical pre-factor of equation 4.2 has a p dependence and $p = 2.5$ has been assumed. We do not include the pre-factor's p-dependence in Equations 2, 4, or 5 for simplicity. The effect of changing p on this pre-factor can be easily incorporated, and we refer interested readers to the work of [123] for more information. Throughout the analysis in this paper, We assume $p = 2.5$, but leave p in our equations for readers to see where this dependence occurs.

We assume the ejecta are homologously expanding with a range of velocities, meaning that the velocity of the ejecta is linearly proportional to the radius (i.e., the fastest moving ejecta are outermost, while the inner ejecta expand slowest). The ejecta expanding with $\beta = v/c$ have associated energy E, this energy is distributed as $E \propto (\beta\Gamma)^{-\alpha}$ for $\beta \geq \beta_{\text{SN}}$, and the integrated energy distribution is normalized to E_{SN}. Here, we take $\alpha = 5$, consistent with the theory for outer SN ejecta [124, 125].

The radio light curve of the SN both before and after t_{dec} can be expressed as $F_\nu = F_p(t/t_{\text{dec}})^{-s}$, where s depends on the energy distribution of mass in the SN blast wave. Then s becomes

$$
s = \begin{cases}
\frac{15p-21-6\alpha}{10+2\alpha}, & t < t_{\text{dec}}; \text{non-relativistic phase} \\
\frac{3(1+p)-6\alpha}{10+2\alpha}, & t < t_{\text{dec}}; \text{deep Newtonian phase} \\
\frac{3(1+p)}{10}, & t > t_{\text{dec}}
\end{cases}
\tag{4.3}
$$

These expressions for s and the corresponding fluxes are given in [117]. The deep Newtonian phase sets in when the speed of the blast wave decreases to $\beta_{\text{DN}} = 0.2\bar{\epsilon}_{e,-1}^{-1/2}$, a few years after explosion [123].
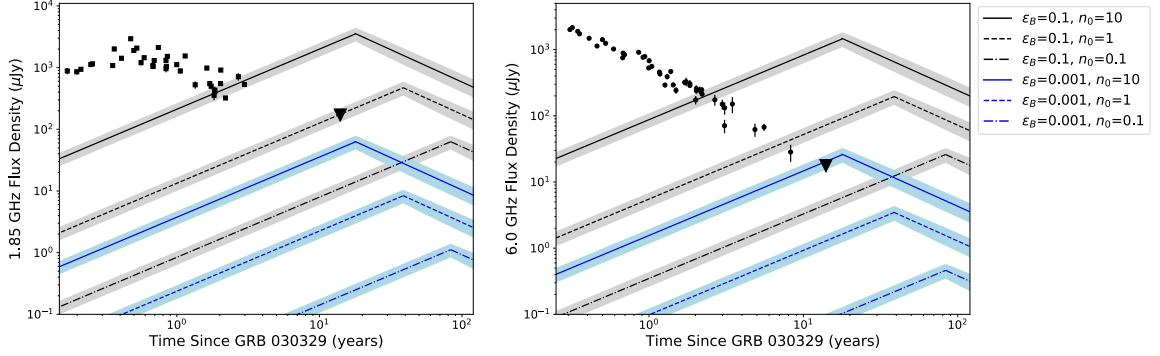
Fig. 4.1. Radio light curves of GRB 030329/SN 2003dh at 1.85 GHz (left) and 6 GHz (right), including the published GRB afterglow and our late-time upper limits (black triangles). Model radio light curves of the radio SNR rebrightening are superimposed as blue and grey bands; each panel shows six models with varying ϵ_B and n_0. For ϵ_B, we adopt values of 0.1 (grey lines) and 10^{-3} (blue lines). For the ambient density, we adopt values of $n_0 = 0.1$ cm^{-3} (dot-dashed lines), $n_0 = 1$ cm^{-3} (dashed lines), and $n_0 = 10$ cm^{-3} (solid lines). For these models, we use the SN energy and velocity of SN 2003dh given in Table 1 (the bands surrounding each model line represent the uncertainties in the SN energy), and assume $\epsilon_e = 0.1$, $p = 2.5$ and $\alpha = 5$. GRB 030329 afterglow data (filled circles and squares) are from [126–131].

During the deep Newtonian phase, when $t_{\mathrm{DN}} < t < t_{\mathrm{dec}}$, the flux density in μJy increases with time as:

$$
\begin{aligned}
F_\nu \approx 440\, \bar{\epsilon}_{e,-1}\, \epsilon_{\mathrm{B},-2}^{\frac{1+p}{4}}\, \beta_{\mathrm{SN},-1}^{\frac{\alpha(11+p)}{10+2\alpha}}\, E_{\mathrm{SN},52.5}^{\frac{11+p}{10+2\alpha}}\, n_0^{\frac{3+5\alpha+p(3+\alpha)}{20+4\alpha}} \\
\times\, \nu_{\mathrm{GHz}}^{\frac{1-p}{2}}\, (1+z)^{\frac{8-5\alpha-p(\alpha+2)}{10+2\alpha}}\, d_{27}^{-2}\left(\frac{t}{29\,\mathrm{yr}}\right)^{\frac{6\alpha-3(1+p)}{10+2\alpha}}
\end{aligned}
\tag{4.4}
$$

If t is greater than $t_{\mathrm{dec,SN}}$, the flux density decreases with time as:

$$
\begin{aligned}
F_\nu \approx 440\, \bar{\epsilon}_{e,-1}\, \epsilon_{\mathrm{B},-2}^{\frac{1+p}{4}}\, E_{\mathrm{SN},52.5}^{\frac{11+p}{10}}\, n_0^{\frac{3(1+p)}{20}}\, \nu_{\mathrm{GHz}}^{\frac{1-p}{2}} (1+z)^{\frac{4-p}{5}} \\
\times\, d_{27}^{-2}\left(\frac{t}{29\,\mathrm{yr}}\right)^{\frac{-3(1+p)}{10}}
\end{aligned}
\tag{4.5}
$$

In this paper, we create model light curves by melding together equations 4.4 and 4.5 at their intersection point, which is approximately the Sedov-Taylor time. The combination of these equations is what we refer to as our model radio light curves and are shown in Figures 1, 2, and 3. Each figure assumes the appropriate explosion parameters for the observed GRB/SN (Table 1). The range of model parameter values (ϵ_B and n_0) are chosen specifically to allow the figures to center and focus on the observational upper-limits for each GRB/SN. We explore a larger parameter space in Figure 4.4. Given our observation times in this paper, we typically expect to be in the deep Newtonian phase ($t_{\mathrm{DN}} < t < t_{\mathrm{dec}}$), hence equation 4.4 would be the relevant equation for the flux density evolution.

We can use this theoretical framework to constrain parameters like ϵ_e, ϵ_B, E_{SN}, and n_0 from a measurement of F_ν. Rearranging equation 4.4 and taking $\alpha = 5$, we find

$$
\begin{aligned}
\bar{\epsilon}_{e,-1}\, \epsilon_{\mathrm{B},-2}^{\frac{1+p}{4}}\, n_0^{\frac{7+2p}{10}} \lesssim \left(\frac{F_\nu}{440\,\mu\mathrm{Jy}}\right)\left(\frac{t}{29\,\mathrm{yr}}\right)^{\frac{3(p-9)}{20}} \beta_{\mathrm{SN},-1}^{-\frac{(55+5p)}{20}} \\
\times\, E_{\mathrm{SN},52.5}^{-\frac{(11+p)}{20}}\, \nu_{\mathrm{GHz}}^{\frac{p-1}{2}}\, (1+z)^{\frac{17+7p}{20}}\, d_{27}^2
\end{aligned}
\tag{4.6}
$$

Figure 4.4 demonstrates the degeneracies between ϵ_B, E_{SN}, and n_0, given observational constraints on GRB 980425/SN 1998bw. We discuss Figures 1–4 in more detail in §5.

Table 4.1.
Basic Data on Target GRB/SNe: [a] [133]; [b] [134]; [c] [135]; [d] [136] errors are taken as 20%; [e] [137]; [f] [138]; [g] [?, 105]; *Value confirmed via private communication with Mazzali.

GRB	SN	z	υ [10^3 km/s]	E_{SN} [10^{51} erg]
030329	2003dh	0.1685^a	29 ± 5.8^d	40 ± 10^e
060218	2006aj	0.0335^b	19 ± 3.8^d	2 ± 0.5^f
980425	1998bw	0.0083^c	24 ± 4.8^d	$50 \pm 5^{g*}$

4.3 Sample

In an effort to detect the predicted radio emission from the GRB/SN remnant, we considered the sample of long GRBs with associated SNe. We calculated which of these were most likely to show a detectable radio re-brightening using the methods outlined in §3.1 of [116]. We took sources that had a time since explosion of over 10 years and were nearby ($z < 0.1$). This narrowed the pool down to two events: GRB 980425/SN 1998bw and GRB 060218/SN 2006aj. We also included GRB 030329/SN 2003dh, which is also >10 years old but further away ($z = 0.17$), as it is a very well-monitored event with the longest radio afterglow ever detected [130,132]. For all other GRB/SNe, the radio SNR is predicted to be faint due to the explosion being either too distant or too recent [116]. Our target sample can be found in Table 1, along with redshifts, SN ejecta velocities at ~ 10 days after explosion [105], and SN energies.

GRB 030329/SN 2003dh is at a low redshift, $z = 0.1685$ [133], for a GRB with typical luminosity (compared to the low-luminosity GRBs that are often detected at such low redshifts). It is one of the most well-studied GRB afterglows with radio coverage between 0.64 and 95 GHz from only a half day out to almost a decade after the initial gamma-ray detection [126–131]. We show the radio observations of the afterglow in Figure 4.1. Original data were obtained at 1.4 and 4.9 GHz; we scaled

Table 4.2.
Log of radio observations

Source	RA	Dec	Telescope	UT Date	Band & Central	Bandwidth	Time on
	(h:m:s)	(° :′:″)		Observed	Frequency	(GHz)	Source
GRB 030329/	10:44:50.02	+21:31:18.10	VLA	2016 Mar 23	C-band (6 GHz)	4 GHz	30 min
SN 2003dh			(C-config)		L-band (1.5 GHz)	1 GHz	54 min
GRB 060218/	03:21:39.67	+16:52:02.20	VLA	2016 Feb 18	C-band (6 GHz)	4 GHz	30 min
SN 2006aj			(C-config)		L-band (1.5 GHz)	1 GHz	54 min
GRB 980425/	19:35:03.17	−52:50:46.1	LBA	2015 Nov 16	L-band (1.65 GHz)	32 MHz	320 min
SN 1998bw							
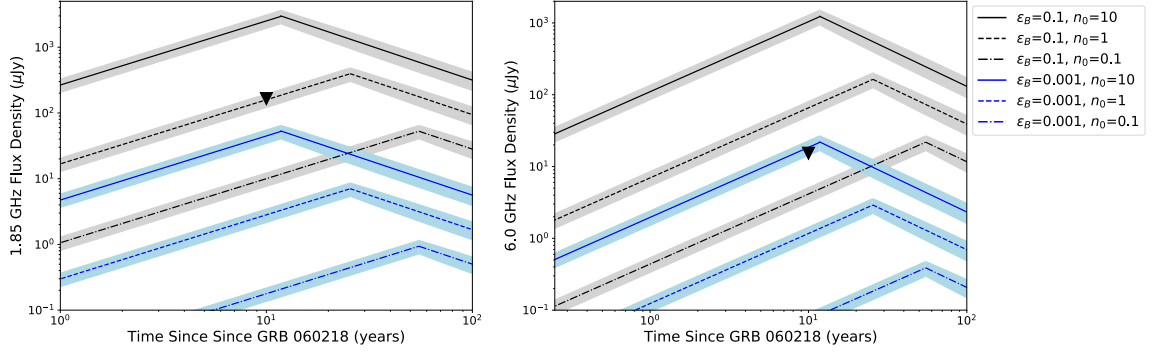
Fig. 4.2. Radio upper limits (black triangles) for GRB 060218/SN 2006aj at 1.85 GHz (left) and 6 GHz (right), overplotted on model radio light curves. The light curve models, assumptions, and symbols are the same as for Figure 1, except we use the SN energy and velocity of SN 2006aj from Table 1. Observations of the GRB 060218 afterglow are not shown, as the GRB flux decreased rapidly and would not be visible over the timescales featured in this plot.

them respectively to our observing frequencies of 1.85 and 6 GHz using the observed radio spectral index, $F_\nu \propto \nu^{-0.54}$ [130]. VLBI observations complement the radio light curve data and provide measurements of the source size and evolution [139–141]. There has also been detailed optical study of the associated SN 2003dh [142], which had a high kinetic energy of 4×10^{52} erg [137].

GRB 060218/SN 2006aj is located at a redshift of $z = 0.0335$ [134]. Despite being closer than GRB 030329, it had a lower intrinsic luminosity [143]. The GRB radio afterglow has been detected, but was faint and had sparse sampling over time [144, 145]. Therefore the GRB blast wave parameters are not well constrained. However, SN 2006aj was well-studied at optical wavelengths (e.g., [146]), yielding a measurement of the SN kinetic energy substantially lower than SN 2003dh (2×10^{51} erg; [138]).

GRB 980425/SN 1998bw The third GRB with associated SN in our sample is GRB 980425/SN 1998bw, at a redshift of 0.0083 [135]. This was the first GRB

found to have an associated SN [103], and a radio counterpart was well-detected and monitored at radio wavelengths [147], although we do not show it in Figure 3 because it had faded by 1 year after explosion [148]. Modeling of the GRB data is consistent with a viewing angle misaligned with the GRB jet axis [149,150]. Optical observations and modeling of SN 1998bw imply a kinetic energy comparable to SN 2003dh, 5×10^{52} erg [77].

4.4   Observations

In order to detect the radio re-brightening of GRB/SNe, we observed the three objects described in Section 4.3 in 2016. Both GRB 030329/SN 2003dh and GRB 060218/SN 2006aj were observed using the NSF's Karl G. Jansky Very Large Array (VLA). GRB 980425/SN 1998bw is a southern source not visible to the VLA, and the host galaxy has bright radio emission, so we observed it with the Australian Long Baseline Array (LBA; Table 2).

Below is a summary of the observations conducted at each telescope. Each GRB/SN was observed in L band (1 – 2 GHz) and both GRB 030329/SN 2003dh and GRB 060218/SN 2006aj were observed in C band (4 – 8 GHz). These particular bands were chosen as a trade-off between sensitivity, resolution, and brightness. Higher frequencies (e.g., C band) are more sensitive than lower frequencies at the VLA, and provide higher resolution on the GRB/SN while resolving out the host galaxy flux. However, the GRB/SNe should be emitting optically-thin synchrotron, and should therefore be brighter at lower frequencies (e.g., L band). To improve our chances of detection, we therefore observe in both L and C bands with the VLA, as the image resolution is limited. Observations with the LBA are much higher resolution but are limited in sensitivity, so in this case we focus on L band observations.

Table 4.3.
Summary of Measurements from Radio Observations: [a]3σ limit on
the spectral luminosity assuming redshifts listed in Table 1.

Source	Frequency	Image r.m.s.	3σ Upper Limit	Time since SN	Luminosity[a]
	(GHz)	(μJy/beam)	(μJy)	(yr)	(10^{27} erg s^{-1} Hz^{-1})
GRB 030329/	6	5.0	17.6	13.0	< 13.8
SN 2003dh	1.85	55	170	13.0	< 133
	1.22	80	245	13.0	< 192
GRB 060218/	6	5.1	15.3	10.0	< 0.4
SN 2006aj	1.85	55	165	10.0	< 4.1
	1.22	91	281	10.0	< 6.9
GRB 980425/	1.65	90	270	17.6	< 0.42
SN 1998bw					

4.4.1   VLA Observations

During the VLA's 2016 C-configuration, we observed GRB 030329/SN 2003dh and GRB 060218/SN 2006aj with the VLA (Program ID VLA/16A-309). Both GRB/SNe were observed for 54 minutes in L band (1 – 2 GHz) and 30 minutes in C band (4 – 8 GHz). The L-band observations had 16 spectral windows with a width of 64 MHz each. The C-band observations had 32 spectral windows, each 128 MHz wide. All spectral windows were sampled with 64 channels, and all observations were carried out in full polarization mode.

For GRB 030329/SN 2003dh, we used 3C286 as the flux calibrator and J1103+2203 as the phase calibrator. For GRB 060218/SN 2006aj, we used 3C147 as the flux calibrator and J0318+1628 as the phase calibrator. The data were edited and reduced using standard routines in both AIPS and CASA [151, 152]. Images were created in AIPS, using a Briggs Robust value of 0. We split the data from each receiver band into two or more frequency chunks and imaged them separately, to assuage imaging artifacts borne of the large fractional bandwidths. As all images yield non-detections, in each receiver band we smoothed the higher-frequency image to the resolution of the lower-frequency image, and then averaged the images together using appropriate noise-based weights in AIPS' `comb`.

GRB 060218/SN 2006aj has a very bright source less than a degree away ($\sim$8 Jy at 1.4 GHz; [153]), so our images of this GRB/SN suffered from strong artifacts and dynamic range issues. We intensively self-calibrated images to reach the noise thresholds listed in Table 4.3; note that the L-band data were much more severely affected by this source than the C-band data.

GRB 030329/SN 2003dh is surrounded by many sources, but none comparable in flux to the bright source in the GRB 060218/SN 2006aj images. Again, we self-calibrated our images to reach the noise thresholds listed in Table 4.3, and the L-band data were more severely affected by imaging artifacts than the C-band data.

A summary of the observations can be seen in Table 4.2, and the results are listed in Table 3. Our observations were conducted 10 and 13 years after the initial explosions of GRB 060218/SN 2006aj and GRB 030329/SN 2003dh, respectively. Neither GRB/SNe were detected in either L or C band, so our observations provide 3σ upper-limits on the flux densities (Table 3). These upper-limits are plotted on top of light curve models in Figures 4.1 and 4.2.

4.4.2 LBA Observations

GRB 980425/SN 1998bw was observed with the LBA using an array comprising the Australia Telescope Compact Array (ATCA; phased array of five 22-meter dishes), Ceduna, Hobart and Parkes, on 16 November 2015 (Program ID V541A). The observing setup used 2×16 MHz subbands in dual polarization, Nyquist sampled with 2 bits (256 Mbps data rate), and centred on a sky frequency of 1.65 GHz. A summary of the observations can be seen in Table 4.2, and the results are listed in Table 3.

The observation had a duration of 12 hours, and GRB 980425/SN 1998bw was phase referenced to J1934−5053 which has 290 mJy of unresolved flux at a separation of 2° from the target. Fringe finders 3C273, 1921−293 and 0208−512 were regularly observed to provide delay calibration; and a compact source, 1519−273, was used to bootstrap the intra-array flux calibration. The calibrator J1923−5329, located 3° from J1934-5053, was observed in a few scans in a phase referencing style similar to that used for GRB 980425/SN 1998bw, to confirm that phase transfer over a few degrees was successful.

All four Stokes parameters were correlated and, after calibration overheads, an on-source time of approximately 5 hours and 20 minutes on GRB 980425/SN 1998bw was achieved. Due to a partial disk failure at ATCA, about 35% of the data from that station, randomly distributed throughout the experiment, were lost prior to correlation. The data were correlated on the LBA DiFX correlator [154] and calibrated
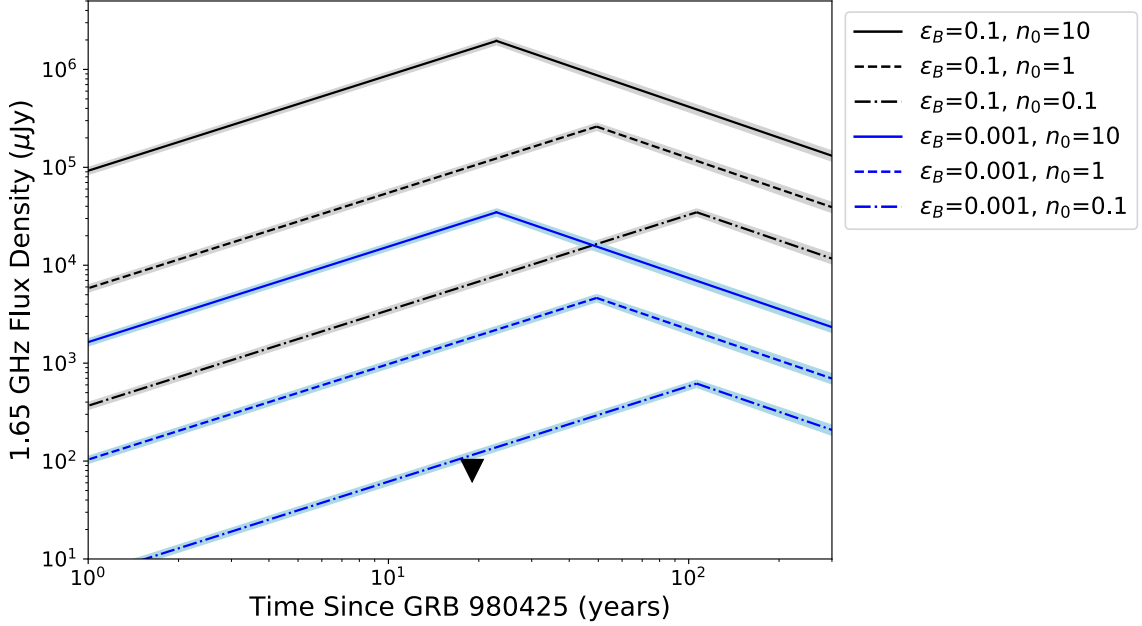
Fig. 4.3. Model radio light curves of GRB 980425/SN 1998bw at 1.85 GHz, with our observational limit over-plotted (black triangle). The light curve models, assumptions, and symbols are the same as for Figure 1, except we use the SN energy and velocity of SN 1998bw from Table 1. Observations of the GRB 980425 afterglow are not shown, as the GRB flux decreased rapidly and was not observed over the timescales featured in this plot.

in NRAO's AIPS package in the standard way for LBA phase referencing using a pipeline implemented in the ParselTongue interface [155].

The resultant naturally-weighted image noise was 90 μJy/beam. GRB 980425/SN 1998bw was not detected, giving a 3-σ upper limit of 0.27 mJy, 17.6 years after the initial explosion. Analysis of the quality of phase transfer from the check source, J1934−5053, indicate that phase calibration was good and thus the non-detection can be safely ascribed to weakness of the source rather than instrumental issues. This upper limit is the lowest limit published for GRB 980425/SN 1998bw [156], and shown on top of light curve models in Figure 4.3.
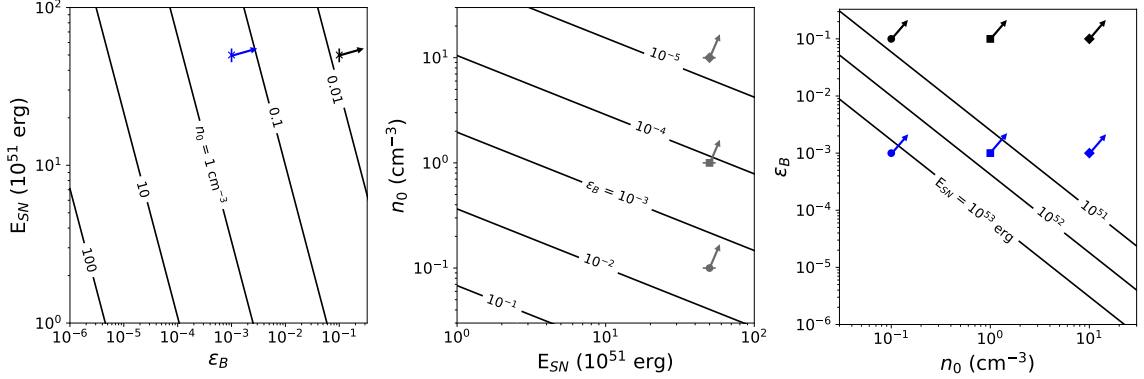
Fig. 4.4. Given our radio upper limit on GRB 980425/SN 1998bw, 17.6 years after explosion, we can constrain the possible parameter space of ϵ_B, n_0, and E_{SN} using Equation 4.6. The three panels illustrate how these three parameters depend on each other, assuming $p = 2.5$, $\alpha = 5$, $\epsilon_e = 0.1$, and $v = 24,000$ km s^{-1}. The points on the plot refer to the fiducial values we assume in our previous figures. Color of the markers represents values of ϵ_B, where black symbols correspond to $\epsilon_B = 0.1$, blue symbols to $\epsilon_B = 0.001$, and gray symbols assume nothing about ϵ_B. The shape of markers corresponds to the values of n_0, where circles are 0.1 cm^{-3}, squares are 1 cm^{-3}, diamonds are 10 cm^{-3}; and crosses are assuming nothing about the density. The arrows attached to each marker point to the regions of the parameter space allowed by our radio upper limits. For example, the square marker in the second panel assumes $n_0 = 1$ cm^{-3} and $E_{SN} = 10^{52.5}$ erg (the energy for SN 1998bw in Table 1); our radio upper limit therefore implies $\epsilon_B \lesssim 10^{-4}$ for those values of n_0 and E_{SN}.

4.5   Analysis

Here, we interpret our radio upper limits in the context of the radio rebrightening during the transition to the Sedov-Taylor phase. We note that non-detections of these GRB/SN sources also imply non-detections of GRB counter jets (the light emitted from a GRB jet that is expelled in a direction away from an observer, which means that the light will reach an observer at a later date than the jet expelled in the direction of the observer). We also conclude that the GRB radio afterglow is no longer

detected at GHz frequencies for any of the three GRB/SN—even for GRB 030329, where the afterglow was traced for almost a decade (Figure 4.1). Our observation of GRB 030329/SN 2003dh was made almost five years after the last of these observations, and our non-detection presented here demonstrates that any future radio detection of GRB 030329/SN 2003dh at GHz frequencies will likely originate from the SN ejecta rather than the GRB afterglow.

4.5.1   Interpreting Radio Upper Limits

Figures 4.1, 4.2 and 4.3 show model light curves (described in §4.2) for each of the target GRB/SNe and our observational limits on flux density. In each of these figures we vary ϵ_B and n_0, while keeping the other model parameters fixed. For ϵ_B we adopt values of 0.1 and 10^{-3}—the former being equal to the assumed value for ϵ_e (i.e., equipartition) and the latter in the range of values that has been derived from GRB afterglow modeling [102]. For GRB afterglows, it has been shown that ϵ_e is fairly narrowly distributed around 0.1 e.g., [157], and $\epsilon_e = 0.1$ is also commonly used for SNe Ib/c [158]. We note that for the slower shocks in "normal" SNRs (with velocities around a few thousand km s^{-1}), ϵ_e and ϵ_B can be one to two orders of magnitude lower than assumed here e.g., [119]. The ejecta of the GRB/SNe have high kinetic energies and should therefore maintain large velocities (around an order of magnitude faster than the velocities seen in typical SNRs), even as they transition to the Sedov-Taylor phase [117]. Therefore, we take $\epsilon_e = 0.1$, but upper limits can be interpreted with other values of ϵ_e using Equation 6. For lower ϵ_e or ϵ_B, we place less stringent constraints on the ambient density or SN energy with our radio upper limits (Equation 4.6, Figure 4).

For n_0 we adopt values of 0.1, 1 and 10 cm^{-3}, spanning a range of most common values found in GRB afterglow modeling [102]. We can use our radio upper limits to constrain the density of the ambient medium surrounding a GRB/SN. Figures 4.1, 4.2 and 4.3 demonstrate how variations in n_0 affect the radio luminosity. We see that

the density of the surrounding medium plays a large role in not only the Sedov-Taylor time but also the light curve peak flux.

The predicted radio light curves also depend on the energy and ejecta velocity of the SN. With higher velocities, we expect that the radio luminosity would peak at earlier times and higher luminosities (Equations 1 and 2). For larger ejecta masses, the radio luminosity would peak at later times and higher luminosities. While ejecta velocities are well constrained by observations, measurements of ejecta mass and E_{SN} are model-dependent and have substantial uncertainty, with possible values for SN 2003dh ranging by an order of magnitude (Table 4.2). We take the SN energies listed in Table 4.3 as fiducial parameters, but can quantify how our upper limits depend on E_{SN} (Figure 4.4). Note that we assume $p = 2.5$ and $\alpha = 5$, which are both typical for SN modeling [158].

Clearly, the light curves depend on multiple uncertain parameters, e.g., ϵ_e, ϵ_B, n_0, and E_{SN}. If we assume values for three of these parameters, we can then place clear constraints on the fourth. In Figure 4.4, we use our 1.65 GHz upper limit for GRB 980425/SN 1998bw to constrain the three more uncertain input parameters (ϵ_B, n_0, and E_{SN}) and illustrate the degeneracies between them, while fixing the other parameters ($p = 2.5$, $\alpha = 5$, and $\epsilon_e = 0.1$). The three different panels demonstrate how a third parameter depends on the other two. For example, if a viewer of the the left panel of Figure 4 selected a value for E_{SN} and ϵ_B, they could read off the value of the corresponding density contour to place an upper limit on n_0. The blue point in this panel marks fiducial values of $\epsilon_B = 0.001$ and $E_{SN} = 10^{52.5}$ erg, and lands between the $n_0 = 1$ cm^{-3} and $n_0 = 0.1$ cm^{-3} contours, implying that $n_0 \lesssim 0.3$ cm^{-3} under these assumptions.

Although we do not include similar plots for GRB 030329/SN 2003dh and GRB 060218/SN 2006aj, the same ideas can be followed and we can calculate the range of expected densities for these sources. For these calculations, we turn to the C-band (6.0 GHz) observations, as they are more constraining than the L-band. We keep the same assumed parameter range for ϵ_B (0.1 and 0.001) and E_{SN} is allowed a range

that spans the uncertainty on the measurements from Table 4.3. For both GRB 030329/SN 2003dh and GRB 060218/SN 2006aj we find $n_0 \lesssim 0.3 - 9$ cm^{-3}.

4.5.2 Implications for GRB/SN Environments

Our radio upper limits probe the density of the circumstellar material (CSM) or interstellar medium (ISM) at the location of the SN forward shock at the time of observation. By estimating the radii of the ejecta and using our upper limits to constrain n_0, we can comment on the environments of GRB/SNe.

We estimate the radius of the SN shock as $R_s = v t_{\mathrm{obs}}$, where v is the SN ejecta velocity (Table 1) and t_{obs} is the time elapsed between explosion and observations (10.0–17.6 yr; Table 3). We find radii of $R_s \approx 0.2$ pc for GRB 060218/SN 2006aj and $R_s \approx 0.4$ pc for GRB 980425/SN 1998bw and GRB 030329/SN 2003dh. These radii are in fact lower limits, with the true blast-wave velocity a factor ~ 3 larger, as the SN has not yet reached the Sedov-Taylor stage, implying that the velocity of the fastest SN ejecta are faster than β_{SN}.

In order to place constraints on the density of the sources that we have observed, we turn to what environments are found around similar sources. Several authors have shown that there is a wide range of densities surrounding long GRBs, spanning many orders of magnitude [102, 159]. [76] suggest that GRB radio samples are biased to a narrow range of CSM densities (1–10 cm^{-3}), as the radio emission will be weak at low densities and self-absorbed at high densities. In a fraction of cases, the radio light curves of long GRBs can be well-fit by expansion into a uniform medium, and this is what we assume here (Section 4.2). However, a uniform-density CSM is almost certainly over-simplistic, as the environments of GRB/SNe should be strongly affected by the evolution and mass loss from the progenitor star e.g., [160, 161].

A simple model for the progenitor's evolution in the years leading up to explosion might be a fast wind (~ 1000 km s^{-1}) sustained for $\sim 10^5$ years, as expected for a Wolf-Rayet star [162]. Such a progenitor should blow a bubble filled with a $\rho \propto r^{-2}$ wind,

implying low densities at radii $\sim$0.1–10 pc [163]. More realistic stellar progenitors yield substantially more complex circumstellar environments. Take for example the 29 $M_\odot$ star whose late stages of evolution are modeled in Figure 3 of [160]. The star is surrounded by a Wolf-Rayet wind-blown bubble, but the bubble is both smaller and denser than one might naively expect because it is expanding into a dense wind from the red supergiant phase that preceded the Wolf-Rayet phase. In this particular simulated CSM, the Wolf-Rayet bubble has a diameter of $\sim$0.3 pc and density $\sim$10 cm^{-3}, and is surrounded by a dense shell of material of density $\sim 10^2 - 10^4$ cm^{-3}. These examples highlight how difficult it is to predict the CSM around a GRB/SN. Even a question as simple as whether the ejecta are expanding into a medium that is enhanced in density over the ISM or evacuated of ISM is difficult to answer and depends on the detailed mass loss of the progenitor star.

Adding to the complexity of the CSM, the SN blast waves studied here are expanding into a medium that has already been shaped by the lower-mass, higher-velocity GRB ejecta. For example, the afterglow of GRB 030329 is best modeled by interaction with a uniform density medium, with n_0 values ranging about an order of magnitude around 1 cm^{-3} out to a radius $\gtrsim 1$ pc e.g., [130, 132]. The SN ejecta in GRB 030329/SN 2003dh has a radius $\lesssim 0.8$ pc at the time of our observations, 13 years after explosion. Therefore, our observations probe the SN blast wave while it is interacting with the GRB-evacuated cavity. Figure 4.1 shows that for equipartition with $\epsilon_e = \epsilon_B = 0.1$ the density should be below 1 cm^{-3}, consistent with only some of the density values found in broadband modeling of the GRB emission. For $\epsilon_e = 0.1$ and $\epsilon_B = 10^{-3}$ the density is less well constrained, $n_0 < 10$ cm^{-3}, which is consistent with all the density values derived from modeling GRB 030329.

The radio afterglow of GRB 060218 can be fit with a stellar wind density profile or a uniform density medium of $n_0 \approx 10^2$ cm^{-3} [144, 164, 165]. Our upper limit shown in Figure 4.2 provides constraints on the density similar to those for GRB 030329: $n_0 < 1$ cm^{-3} for $\epsilon_e = \epsilon_B = 0.1$, and $n_0 < 10$ cm^{-3} for $\epsilon_e = 0.1$ and $\epsilon_B = 10^{-3}$. Those limits on n_0 are still below the value derived from modeling the GRB 060218

afterglow with a uniform density medium. This may indicate that the density of the CSM drops with radius, implying a stellar wind density profile, which means that our upper limit may be breaking the degeneracy between possible density profiles for modeling this GRB afterglow. We emphasize that this depends on the ϵ_e and ϵ_B values, which can both be lower than the ones we show in Figure 4.2.

Finally, the radio emission from SN 1998bw is best modeled by interaction with a stellar wind rather than a uniform CSM [166, 167]. Predictions for the SNR emission associated with a GRB/SN expanding into a wind CSM are outside the scope of this paper. However, Figure 4.3 shows strong constraints on the density: even for $\epsilon_e = 0.1$ and $\epsilon_B = 10^{-3}$, the upper limit on n_0 is 0.1 cm^{-3} at $R_s = 0.4$ pc; see the right panel of Figure 4.4 for the correlation between ϵ_B and n_0. This would be consistent with the density expected for a stellar wind with mass loss rate of $\dot{M} = 6 \times 10^{-7}$ M$_\odot$ yr^{-1} for an expansion velocity $v_w = 1000$ km s^{-1} [166]. This mass loss rate is quite low for typical Wolf-Rayet stars and mass loss rates derived from GRB modeling, although not unprecedented for the latter [168].

4.6 Conclusions

In this paper, we presented observations of three long GRBs with associated SNe in an effort to detect rebrightening radio emission from the SN ejecta entering the Sedov-Taylor phase. We observed GRB 030329/SN 2003dh and GRB 060218/SN 2006aj with the VLA, and GRB 980425/SN 1998bw with the LBA. Our observations resulted in non-detections, with $L_\nu \lesssim [0.4-10^2] \times 10^{27}$ erg s^{-1} Hz^{-1}. By choosing fiducial values for parameters describing the SN energetics and shock microphysics, we place upper limits on the density surrounding the GRB/SNe at radii $\sim$0.2–0.8 pc from the explosion site.

We find that the density limits for GRB 030329/SN 2003dh are similar to the density values derived from afterglow modeling, while the limits for GRB 060218/SN 2006aj and GRB 980425/SN 1998bw are quite low. For GRB 060218/SN 2006aj, the limits on n_0 may break the degeneracy between possible density profiles for modeling the

GRB afterglow, i.e. they prefer a stellar wind profile over a homogeneous CSM, unless ϵ_e and ϵ_B are significantly below 0.1 and 10^{-3}, respectively. In the case of GRB 980425/SN 1998bw, the limits on the density imply a low but not unprecedented mass loss rate of the progenitor's stellar wind.

While our observations resulted in non-detections, our upper limits are ruling out significant fractions of parameter space for some of the physical parameters of GRB/SNe. A future detection of the SNR emission from decades-old GRB/SNe will enable a better understanding of the environments of long GRBs and illuminate the transition from SN to SNR.

5. OFF-AXIS SHORT GRBS FROM STRUCTURED JETS AS COUNTERPARTS TO GW EVENTS

Kathirgamaraju A., Barniol Duran R., Giannios D., 2018, *Monthly Notices of the Royal Astronomical Society*, 473, L121.

Binary neutron star mergers are considered to be the most favorable sources that produce electromagnetic (EM) signals associated with gravitational waves (GWs). These mergers are the likely progenitors of short duration gamma-ray bursts (GRBs). The brief gamma-ray emission (the "prompt" GRB emission) is produced by ultra-relativistic jets, as a result, this emission is strongly beamed over a small solid angle along the jet. It is estimated to be a decade or more before a short GRB jet within the LIGO volume points along our line of sight. For this reason, the study of the prompt signal as an EM counterpart to GW events has been sparse. We argue that for a realistic jet model, one whose luminosity and Lorentz factor vary smoothly with angle, the prompt signal can be detected for a significantly broader range of viewing angles. This can lead to an "off-axis" short GRB as an EM counterpart. Our estimates and simulations show that it is feasible to detect these signals with the aid of the temporal coincidence from a LIGO trigger, even if the observer is substantially misaligned with respect to the jet.

5.1 Introduction

The monumental discovery of gravitational waves by the LIGO collaboration enables us to observe our Universe at a new wavelength ([169, 170]). In particular, gravitational waves allow us to study the merger of compact objects and their properties, offering exquisite tests of general relativity ([171]). The next related major

quest in astronomy is the discovery of an electromagnetic signal produced during such a merger that accompanies the gravitational waves. We will refer to this specific electromagnetic signal as an electromagnetic "counterpart."

By far the most promising source of gravitational waves (GWs) and accompanying electromagnetic (EM) signals are double neutron star (NS-NS) mergers (or neutron star-black hole mergers), hereafter referred to as simply "mergers" (e.g., [172]). Such mergers make for promising detectable GW sources by LIGO within a few hundreds of Mpc ([173]). There are several lines of indirect evidence that suggests these mergers are the most likely progenitors of short GRBs ([174–176]). However, a simultaneous GW and GRB detection would provide a most conclusive evidence that short GRBs are indeed produced during binary mergers.

The "prompt" γ-ray emission from short GRBs is believed to be strongly beamed along an ultra-relativistic jet with half opening angle θ_j and Lorentz factor $\Gamma_{core} \gtrsim 30$ (e.g., [175]). If $\Gamma_{core}\theta_j > 1$, it will be extremely difficult to detect the prompt emission from a short GRB jet that is misaligned by an angle $\theta > \theta_j$ with respect to Earth. In fact, the observed rate of short GRBs indicates that it will be a decade or more before the luminous core of a GRB is detected within the LIGO detectability volume of neutron star mergers (e.g., [177]). This has tended to steer investigations of EM counterparts away from the prompt emission (see however [178–180]), and more towards the less prompt signals that follow days to months after the merger/GW detection; such as "macronova" or "kilonova", off-axis afterglows and radio flares (e.g., [181–187]). Given the poor localization of LIGO ([188]), the faintness of these signals, and their long delay, such detections and their association to the merger will be challenging (e.g., [183]).

Here we investigate a different, prompt signal from the merger; that of the prompt emission from the moderately relativistic $\Gamma \sim$ a few part of the jet, the "sheath", that beams its emission towards the observer (who is located at a substantial angle with respect to the jet's core). In this letter, we argue that by exploiting the timing from a LIGO trigger, one can reliably detect the prompt emission even if the jet is

significantly misaligned with respect to Earth. This is because, in any realistic jet model, there is expected to be a slower, under-luminous sheath surrounding the bright jet core (e.g., [189, 190]). To quantify this claim, we perform large-scale relativistic magnetohydrodynamical (MHD) simulations, which follow the jet from the launching region, through the confining ambient gas and the break out distance where its slower sheath forms. We also provide a calculation to estimate the observed luminosity for an observer located at an arbitrary angle with respect to the jet axis. We find that this endeavor is quite promising.

5.2 Our Model: a structured jet

Just prior to the merger of a binary neutron star system, gravitational and hydrodynamical interactions expel some neutron star material, forming the "dynamical ejecta" (e.g., [191, 192]). The neutron star merger may be followed by the launching of an ultra-relativistic jet. As investigated by previous hydro simulations, the jet is initially collimated by the dynamical ejecta until it breaks out from the surrounding gas ([193–195]). At a larger distance, it dissipates its energy, resulting in a short GRB which lasts for $\lesssim 2$ s and peaks at $\sim$ MeV energies ([175, 176]). In the majority of previous models, this jet consists of a core having uniform luminosity (L_{core}) and Lorentz factor (Γ_{core}) that discontinuously disappears for angles $\theta > \theta_{\mathrm{j}}$. However, these models are not physical and greatly underestimate the prompt emission that may be received by observers who are not aligned within the core of the jet (i.e., off-axis observers).

Recent numerical (e.g., [196, 197]) and theoretical (e.g., [198]) studies show that once a magnetized jet breaks out of the collimating medium, it is expected to develop some "lateral structure". This means that the jet's luminosity and Lorentz factor depend on the polar angle θ (see Fig. 5.1). We find that this extended lateral part, though slower and less luminous, can contribute a significant amount of prompt emission for angles larger than θ_{j}. As a result, it is possible to detect the prompt
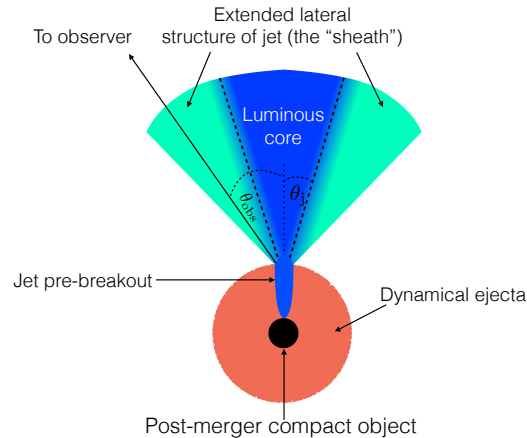
Fig. 5.1. A schematic of a short GRB jet. Mergers produce GWs detectable by LIGO and are the likely progenitors of short GRBs. The prompt emission from the jet's luminous core (routinely observed as a short GRB) is strongly beamed and can only be detected by observers located within θ_j from the jet axis. However, the jet is expected to have a lateral structure that moves slower and is fainter than the luminous core. Given the proximity of a LIGO-triggered short GRB, *Fermi* and *Swift* can potentially detect the prompt emission from this lateral structure even if the jet is misaligned with respect to our line of sight (see Section 5.2.1).

emission from a structured jet for observing angles ($\theta_{\rm obs}$) much larger than θ_j. We call this prompt emission detected by observers with $\theta_{\rm obs} > \theta_j$ an "off-axis" short GRB, this is not off-axis as defined in the traditional sense because our jet does not abruptly vanish at θ_j. Below we provide an estimate for the prospects and feasibility of detecting this "off-axis" prompt emission and mention some of its advantages over other EM counterparts.

5.2.1 Feasibility of detecting the prompt emission from a structured jet

There are currently more than thirty short GRBs with measured redshift ([199]), and their average redshift is ∼0.5 ([176]). Let us now pick a typical short GRB with known redshift, assume it takes place within the LIGO detectability volume, and

estimate its off-axis prompt emission. Had short GRB101219A (see table .1) taken place at a distance of ~ 200 Mpc, it would have resulted in an extremely bright source with a count rate of $\sim 10^6$ photons/s at the *Fermi*/GBM detector. This is a factor of $f \sim 10^4$ above the count rate required for a robust detection of a source coincident with a LIGO trigger by *Fermi* ([200]). With such a large on-axis count rate, even a steeply declining luminosity for the lateral structure of the jet will provide a significant amount of off-axis emission that can be detectable by, e.g., *Fermi*. Assuming, for the sake of an estimate, a jet with a core of luminosity L_{core} and half opening angle θ_{j}, we can take the luminosity for angles $\theta > \theta_{\mathrm{j}}$ (i.e for the lateral structure of the jet) to drop sharply as $L_{\mathrm{obs}}(\theta) = L_{\mathrm{core}}(\theta/\theta_j)^{-6}$ ([201]). Such a jet can still be detected by an observer up to an angle $\theta_{\mathrm{obs}} \sim f^{1/6}\theta_{\mathrm{j}} \sim 5\theta_{\mathrm{j}}$. This makes it $(\theta_{\mathrm{obs}}/\theta_{\mathrm{j}})^2 \sim 20$ times more likely to observe the sheath of the jet in comparison to its core emission. Instead of detecting about 1 EM counterpart per decade from the prompt core emission, the sheath potentially results in $\sim$a few events per year for an instrument with *Fermi's* field of view, increasing the chances to detect such events tremendously. Therefore, the prompt emission from a short GRB could be detected even if the jet is significantly misaligned.

It is quite likely that the off-axis γ-ray emission, by itself, is not sufficiently bright enough to result in a detector trigger. Nevertheless, using the timing of a LIGO trigger can make even a faint γ-ray signal a statistically significant detection. A faint γ-ray signal must come within several seconds after a LIGO trigger to make such a detection possible ([200]). Here, we estimate the temporal difference of these signals. The GW signal, as detected by LIGO, is expected to peak approximately when the merger takes place. The merger will probably initially give birth to a fast-rotating, massive proto-neutron star and can take $\sim$ hundred milliseconds to collapse to a black hole (e.g., [202]). It is likely that the jet forms a few dynamical times later or, all in all, $\sim 0.1 - 1$ sec after the GW signal peak, then the jet has to breakout of the collimating medium which can take a few hundreds of msec ([193]), and expand to a radius r_{jet}, where it radiates. The emission from the jet will, therefore, be further

delayed by $r_{\rm jet}/\Gamma^2 c$, where and Γ is the Lorentz factor of the patch of the jet directed towards the observer. The fast rise and variability of short GRBs indicates the jet core is characterized by $r_{\rm jet}/\Gamma^2_{\rm core} c \sim 10$ msec. In Section 10.6, we argue that the sheath emission is also likely characterized by a delay of $r_{\rm jet}/\Gamma^2 c \sim$ a few seconds, i.e., making a very prompt signal.

The misaligned or "off-axis" prompt emission of short GRBs has largely been ignored. The community has rather focused its efforts on studying off-axis afterglows from short GRBs, the "macronova/kilonova" and radio flare produced by the dynamical ejecta, and the emission from other components (e.g., the cocoon emission; [203, 204]). These signals are expected to peak $\sim$ days to $\sim$ years after the merger and are fainter compared to the prompt emission (e.g., [183, 205]). Coupled with the fact that current GW detectors have very poor localization, associating these signals to a GW source will be difficult. This is where the "off-axis" prompt signal has a considerable advantage, since we expect to detect the prompt emission a few seconds after the GWs, we can capitalize on its temporal coincidence to make the detection. This will also make follow-up searches for the off-axis afterglow and macronova/kilonova easier. Hence, it is very likely that the first detected EM counterpart of a LIGO trigger involving a NS-NS merger will be the fainter, "off-axis" prompt emission from a short GRB jet.

5.3 Numerical simulations

We have recently run relativistic MHD simulations of AGN jets ([207]; hereafter BTG17) using the HARM code ([208]), with recent improvements ([209, 210]). The initial conditions and numerical scheme of these simulations are adapted to the physical setup relevant to this work. We initiate the jets via the rotation of the central magnetized compact object. The jets are, therefore, launched magnetically dominated. By adjusting the density of the gas in the injection radius, the jet is launched with magnetization $\mu = 2p_{\rm mag,0}/\rho_0 c^2 \simeq 25$, where $p_{\rm mag,0}$ is the magnetic pressure

Table 5.1.

Observed parameters of GRB 101219A. From left to right, the columns indicate: GRB identifier, burst duration, fluence in the 15-150 keV band, photon-number index β as a function of frequency $\mathrm{dN}/\mathrm{d}\nu \propto \nu^{-\beta}$, and the burst's redshift. In Section 5.2.1, we use this particular GRB to show that a typical short GRB placed at 200 Mpc (LIGO volume) will be very bright. Consequently, the "off-axis" prompt emission could be detectable even for substantially misaligned observers. This increases the likelihood to detect these objects, using a LIGO trigger, even in the absence of a GRB trigger (data from [199, 206]).

GRB	T_{90}	Fluence	β	z
101219A	0.6 s	4.6×10^{-7} erg cm^{-2}	0.6	0.72

and ρ_0 is the density at the base of the jet. The initial magnetization μ determines maximum Lorentz factor of the jet. We do not take into account neutrino heating which may affect the structure of the jet (e.g., [211, 212])

We considered a scenario in which a low-density funnel is carved along the z-axis at the start of the simulation and we have confined the jet to propagate along high-density walls (similar to "model B" simulations in BTG17). Our simulations, performed in both 2D and 3D, follow jets from the compact object to a scale $\sim 10^3 \times$ larger. These large scale simulations allow us to follow the jet acceleration through conversion of its magnetic energy into kinetic energy. In the context of short GRB jets, as the jet breaks out from the confining medium, it essentially travels through vacuum (or at least very low ambient gas). This is quite advantageous since BTG17 have shown that these type of jets are almost identical in 2D and 3D runs and that they are fairly axisymmetric (see also [210]). For this reason, we focus our efforts on axisymmetric 2D simulations, which are considerably less computationally expensive and can be better resolved numerically.

We mimicked the boundary of the dynamical ejecta by setting the ambient gas density of our previous simulations (see BTG17 model B-2D-vhr for details on jet and ambient gas parameters and numerical resolution) to be essentially zero beyond ~ 100 times the size of the compact object as displayed in Fig. 5.2, which shows both density and velocity (Lorentz factor) contours. After the jet breaks out from the dynamical ejecta, a rarefaction wave crosses the jet and it spreads sideways and accelerates further ([196,197]). For this work, we simulate "steady state" jets that will maintain the conditions at the central engine constant. This means that the rotation of the black hole and the magnetic field strength is kept constant, so that the jet has a constant power throughout the duration of the simulation. Future simulations will explore short-lived jets.

The distance where the radiation from the jet takes place is uncertain; the prompt emission may originate at the transparency radius of the jets or further out, at optically thin conditions (see next Section). The distance at which the jet produces the

γ-ray radiation lies beyond our simulated region. However, we argue that the dynamical range of our current simulations is sufficient for the objectives of our estimates. This is due to the fact that after the phase of lateral expansion and the crossing of the rarefaction wave, the jet becomes approximately conical and its properties "freeze out" as a function of angle (see Fig. 5.4). Therefore, the lateral structure of the jet, which is the key aspect of our study, is set at this distance. It is no longer necessary to follow the jet beyond this point since its properties can be safely extrapolated at larger distances ([196]). Our current simulations with a dynamical range of $\sim 10^3$ already point towards this jet feature after breakout. Future simulations in 2D with even larger dynamical range will be able to test this effect in detail.

5.4   Results and Discussion

We have extracted the jet luminosity $L(\theta)$ and Lorentz factor $\Gamma(\theta)$ from our simulation in Fig. 5.2 at different radii from the central object, see Fig. 5.4. The luminosity $L(\theta)$ is the total (magnetic, kinetic and thermal) luminosity per solid angle of the jet $L(\theta) = dL/d\Omega$. We note that close to the jet axis (z-axis) the luminosity is very low and the velocity is quite small. The jet is characterized by a fast and luminous core of opening angle of $\theta_j \sim 10^o$. The typical cosmological GRB is observed through its core emission. However, for larger angles, the jet Lorentz factor and luminosity drop steeply but remain substantial. These features have been seen in MHD jets before (see, e.g., [213] and references therein), but the exact profiles of $L(\theta)$ and $\Gamma(\theta)$ should depend on their profiles right before breakout, which in turn depend on the properties of the dynamical ejecta (see Section 5.3). Future simulations will explore more realistic dynamical ejecta models (e.g., [191, 193]). Recent hydrodynamical simulations also find an energetic component at large angles (e.g., [204]), and this component is ascribed to the "inner" cocoon (shocked jet material). However in our simulations, the effect of the cocoon on the jet structure is minimized because
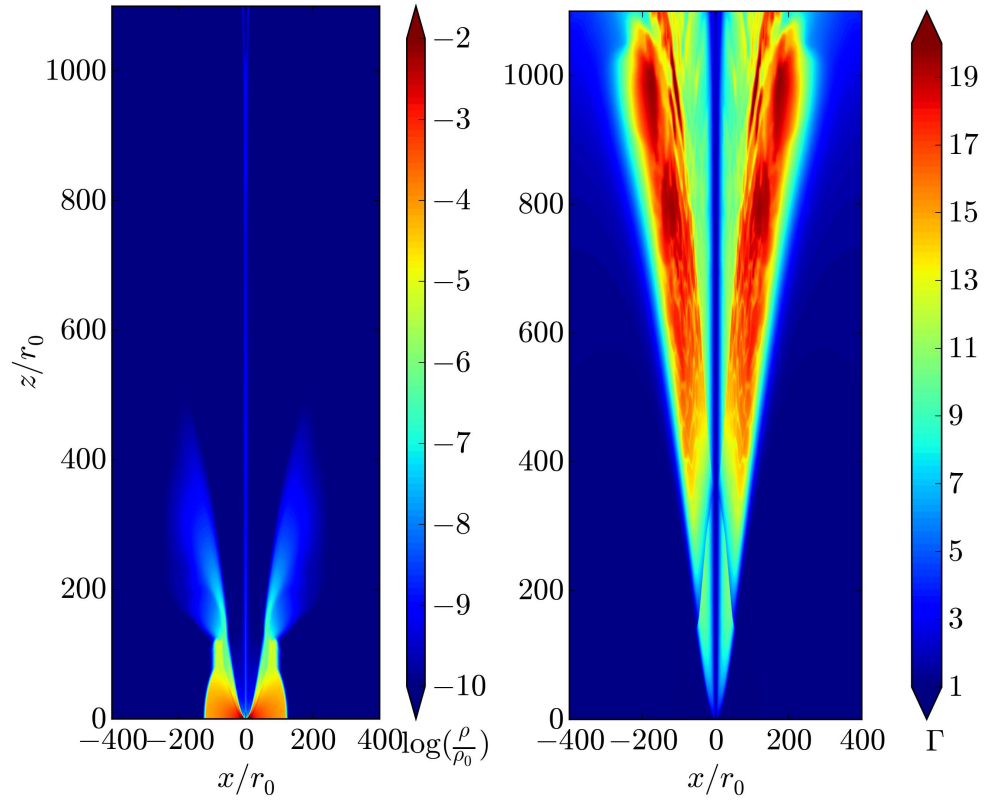
Fig. 5.2. Numerical simulation of a jet that is collimated by and breaks out from the dynamical ejecta. We show 2D cuts of density (left panel) and Lorentz factor (right panel), where r_0 stands for a few times the radius of the central compact object. The jet accelerates as it breaks out from the dynamical ejecta and spread sideways. At large distance the jet turns conical and its lateral structure is fixed.
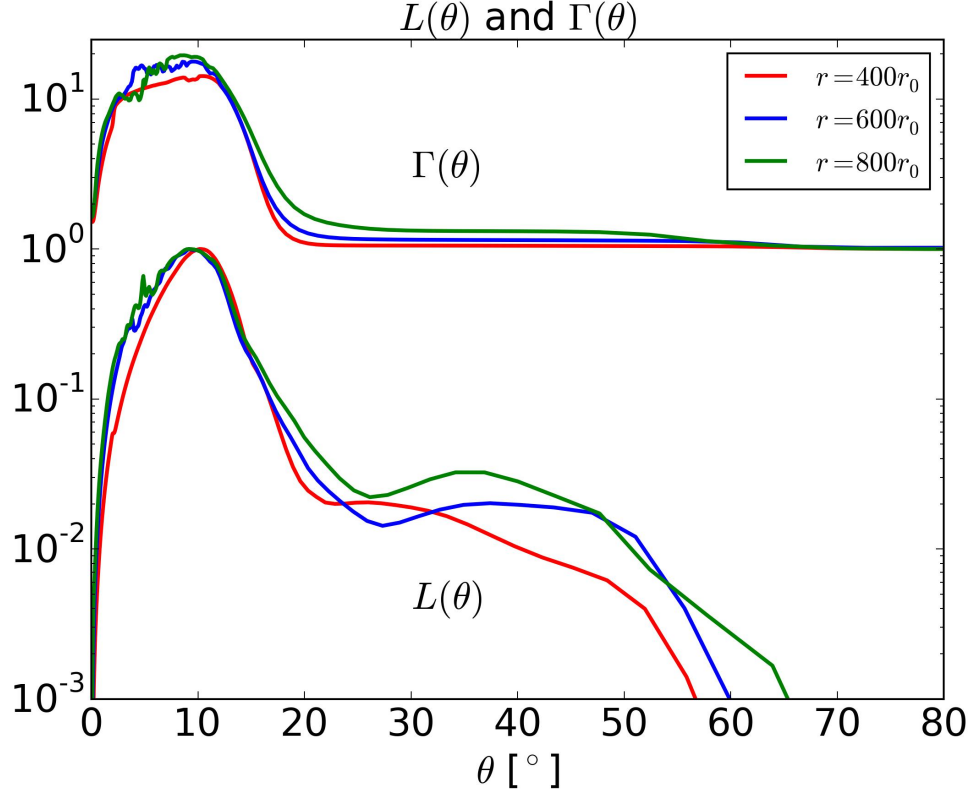
Fig. 5.3. Jet luminosity, $L(\theta)$ (arbitrary units), and jet Lorentz factor, $\Gamma(\theta)$, for different radii r from the compact object for our numerical simulation in Fig. 5.2, r_0 stands for a few times the radius of the central compact object. The luminosity and Lorentz factor profiles are very similar for increasing radii, hence we can assume that the jet structure "freezes out" beyond a certain radius. This allows us to safely extrapolate the jet structure to even larger radii.

we initiate our setup with an evacuated funnel, and the extended component (the "sheath") we obtain consists of rarefied magnetized jet.

As seen in Fig. 5.4, far beyond the breakout radius, there is evidence that quantities "freeze out", i.e., the jet shows a similar profile as a function of angle for increasing radii. We will make use of this fact and show how the observed luminosity can be extracted from our MHD simulations.

5.4.1 Calculating observed luminosity

We now briefly describe how to calculate the observed luminosity as a function of $\theta_{\rm obs}$ for a given $L(\theta)$ and $\Gamma(\theta)$. All quantities in the local co-moving frame will be denoted with a prime and we employ spherical coordinates. Consider an infinitesimal patch of the jet located at a polar angle θ from the jet axis and azimuthal angle of φ (where we take the observer to be located at $\theta_{\rm obs}$ and $\varphi = 0$, see Fig. 5.4.1). The portion of the jet within this patch moves with $\Gamma(\theta)$ at an angle α with respect to the line of sight of the observer, where α is given by $\cos\alpha = \cos\theta_{\rm obs}\cos\theta + \sin\theta_{\rm obs}\sin\theta\cos\varphi$.

Suppose this patch subtends a solid angle $d\Omega_{\rm p}$ on the jet-surface, the luminosity through this patch will be $L_{\rm p} = L(\theta)d\Omega_{\rm p}$. Using a Lorentz transformation, the luminosity within this patch in the co-moving frame can be expressed as $L'_{\rm p} = L_{\rm p}/\Gamma^2(\theta)$. We assume a fixed fraction (η) of this luminosity is converted into radiation. For simplicity, we further assume that the radiation is released instantaneously, is isotropic in the jet co-moving frame and is emitted at a fixed distance $r_{\rm jet}$, which is justifiable since the jet structure "freezes out" at the distances we are considering, therefore the total luminosity from a gradual dissipation would give similar results. The radiated luminosity per unit solid angle in the co-moving frame is therefore $\eta L'_{\rm p}/4\pi$. This luminosity per solid angle has to be boosted to the lab frame, taking into account the inclination α. Therefore, each patch of the jet contributes

$$dL_{\rm obs} = \Gamma(\theta)\delta^3\frac{\eta L'_{\rm p}}{4\pi} = \frac{\eta L(\theta)d\Omega_{\rm p}}{4\pi\Gamma^4(\theta)[1-\beta(\theta)\cos\alpha]^3}. \tag{5.1}$$

Finally, we add the contribution from all patches of the jet which amounts to an integral over the solid angle of the jet, hence,

$$L_{\rm obs}(\theta_{\rm obs}) = \int_0^{2\pi}\int_0^{\theta_{\rm e}} dL_{\rm obs}, \tag{5.2}$$

where $\theta_{\rm e}$ signifies the poloidal extent of the jet. This calculation shows that by extracting $L(\theta)$ and $\Gamma(\theta)$ from our simulations we can estimate the prompt emission seen by an observer at any angle. The observed luminosity of the core can be scaled to the observed average luminosity of on-axis short GRBs, which in turn can give

us a count rate at a detector (e.g., *Fermi* or *Swift*). Fig. 5.4.1 shows the observed luminosity $L_{\text{obs}}(\theta_{\text{obs}})$ (normalized to the peak luminosity) for our simulation in Fig. 5.2, using $L(\theta)$ and $\Gamma(\theta)$ shown in Fig. 5.4, taking $\theta_{\text{e}} \sim 23°$, which marks the extent of the jet with substantial magnetization ($\sigma \gtrsim 10^{-2}$). The observed luminosity decreases quickly as the angle from the jet axis increases; however, at large angles a significant contribution exists. In this example, the jet luminosity at $\sim 40°$ is a factor of ~ 300 fainter than that of the jet core. Nevertheless, it is clear from the estimates presented in Section 2.1 that such a misaligned jet can be still detected, provided that it takes place within the Advanced LIGO detectability volume.

If we had considered the uniform core model for the jet with $\Gamma_{\text{core}} \approx 20$, the ratio of the observed luminosity at $\theta_{\text{obs}} \approx 40°$ to the on-axis ($\theta \lesssim 10°$) luminosity would be $L(\theta_{\text{obs}})/L_{\text{core}} \simeq (\Gamma_{\text{core}}\theta_{\text{obs}})^{-6} \sim 10^{-7}$, which would be negligible. Hence, the "off-axis" prompt emission from a structured jet is significantly larger than that from the uniform jet model, which greatly increases the prospects of detecting it.

The *steady jet* assumption considered above is valid as long as the GRB duration (defined for an on-axis observer) is $T_{\text{GRB}} > r_{\text{jet}}/\Gamma^2 c$, where r_{jet} is the radius at which the jet dissipation occurs, and the γ-rays for an on-axis observer are produced. If this condition is not satisfied then (i) the onset of the emission is delayed by $\sim r_{\text{jet}}/\Gamma^2 c$ and (ii) the luminosity drops by a factor of $\sim \Gamma^2 c T_{\text{GRB}}/r_{\text{jet}}$ with respect to the steady jet calculation performed above. This evidently depends on r_{jet} and $\Gamma(\theta)$, and therefore on a particular jet dissipation model. For an estimate, we will consider the *photospheric* model (e.g., [214, 215]) for the prompt GRB emission. This model predicts that the emission comes from the Thomson photosphere of the jet: $r_{\text{jet}} = r_{\text{ph}} = L\sigma_T/4\pi\Gamma^2\mu m_p c^3$. The corresponding delay of the prompt signal will be $\sim r_{\text{jet}}/2\Gamma^2 c \simeq L\sigma_T/8\pi\Gamma^4\mu m_p c^4 \sim 5 L_{48}\Gamma_{0.5}^{-4}\mu_{1.5}^{-1}$ sec, where we use the notation $A = 10^x A_x$ and *cgs* units. Here we see, that depending on the exact parameters, the signal from the sheath moving with $\Gamma \sim 3$ and of luminosity $L \sim 10^{48}$ erg·sec^{-1} could be delayed by a few to few tens of seconds with respect to the GW signal.
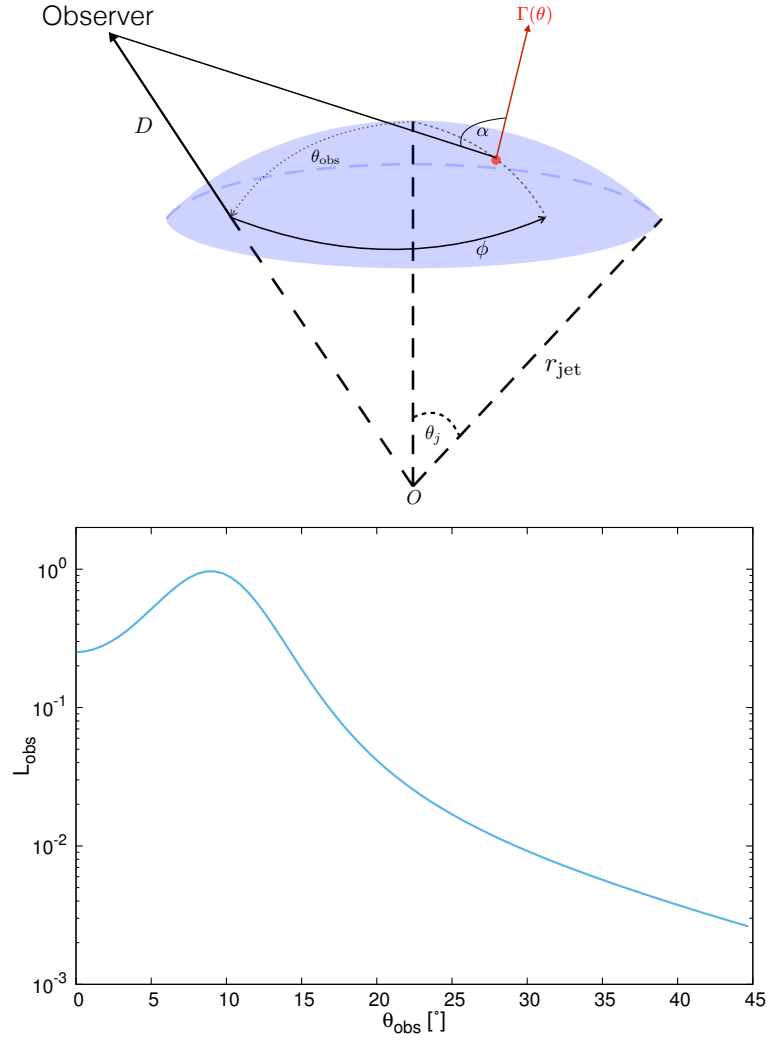
Fig. 5.4. *Top panel:* Geometry of the conical jet, we use spherical coordinates with the origin at O. The observer is located at $(D, \theta_{\mathrm{obs}}, 0)$. We consider a patch of this jet (red dot) at $(r_{\mathrm{jet}}, \theta, \varphi)$ moving with Lorentz factor $\Gamma(\theta)$ with a corresponding angle α between its velocity and line of sight of the observer. *Bottom panel:* Observed luminosity (normalized to peak) as a function of observer angle, $L_{\mathrm{obs}}(\theta_{\mathrm{obs}})$, for our jet simulation output presented in Fig. 5.4. The calculation was performed at $r = 800 r_0$, r_0 is a few times the size of the compact object. In this example, the jet luminosity at $\sim 40^{\mathrm{o}}$ is a factor of 300 fainter than that of the jet core. Nevertheless, such a misaligned jet can be detected by a γ-ray instrument if it takes place within the Advanced LIGO detectability volume.

5.5   Conclusions

In this work, we investigate a different electromagnetic counterpart of gravitational wave events, which is the "off-axis" prompt emission form the associated short GRB. We argue that in a realistically structured jet, the prompt emission can still be detected for substantially misaligned observers and we have performed simulations to support this claim. Even though this prompt signal is much fainter compared to an on-axis short GRB, we stress that the temporal coincidence with a LIGO trigger will be crucial in order to make it a significant detection. The localization of the "off-axis" prompt emission γ-rays will greatly facilitate the source localization, host galaxy identification and detection of longer wavelength signals expected days to years after the burst.

6. THE BINARY NEUTRON STAR EVENT LIGO/VIRGO GW170817 A HUNDRED AND SIXTY DAYS AFTER MERGER: SYNCHROTRON EMISSION ACROSS THE ELECTROMAGNETIC SPECTRUM

Margutti R., Alexander, K. D., Xie, X., Sironi, L., Metzger, B. D., Kathirgamaraju, A. et al., 2018, *The Astrophysical Journal*, 856, L18.
As coauthor, I helped interpret observations using the theory from our previous works and by comparing light curves from different jet models. I also aided in the write up of the text.

We report deep Chandra, HST and VLA observations of the binary neutron star event GW170817 at $t < 160$ d after merger. These observations show that GW170817 has been steadily brightening with time and might have now reached its peak, and constrain the emission process as non-thermal synchrotron emission where the cooling frequency ν_c is above the X-ray band and the synchrotron frequency ν_m is below the radio band. The very simple power-law spectrum extending for eight orders of magnitude in frequency enables the most precise measurement of the index p of the distribution of non-thermal relativistic electrons $N(\gamma) \propto \gamma^{-p}$ accelerated by a shock launched by a NS-NS merger to date. We find $p = 2.17 \pm 0.01$, which indicates that radiation from ejecta with $\Gamma \sim 3 - 10$ dominates the observed emission. While constraining the nature of the emission process, these observations do *not* constrain the nature of the relativistic ejecta. We employ simulations of explosive outflows launched in NS ejecta clouds to show that the spectral and temporal evolution of the non-thermal emission from GW170817 is consistent with both emission from radially stratified quasi-spherical ejecta traveling at mildly relativistic speeds, *and* emission from off-axis collimated ejecta characterized by a narrow cone of ultra-relativistic ma-

terial with slower wings extending to larger angles. In the latter scenario, GW170817 harbored a normal SGRB directed away from our line of sight. Observations at $t \leq 200$ days are unlikely to settle the debate as in both scenarios the observed emission is effectively dominated by radiation from mildly relativistic material.

6.1 Introduction

The joint discovery of gravitational waves [216] and photons from the first binary neutron star (BNS) merger event GW170817 established that gravitational-wave detected BNS mergers can be accompanied by detectable emission across the electromagnetic spectrum, including γ-rays [217, 218]. During the first ~ 15 days the spectrum consisted of a combination of thermal emission powered by the radioactive decay of heavy elements freshly synthesized in the merger ejecta (i.e. the kilonova emission, KN; [219–231]) and non-thermal synchrotron emission dominating in the X-rays and radio bands [232–236]. The thermal component later subsided. During ~ 160 days of intense monitoring, the non-thermal emission brightened with time [237–241] and might have now reached its peak as we show below (see also [241, 242]). The most pressing question regards the intrinsic nature of GW170817.

A first possibility is that GW170817 is an intrinsically sub-luminous event with total gamma-ray energy released $E_{\gamma,iso} \sim 6 \times 10^{46}$ erg. As a comparison, classical cosmological Short Gamma-Ray Bursts (SGRBs) typically have $E_{\gamma,iso} \sim 10^{50} - 10^{52}$ erg [243, 244]. In this scenario, GW170817 did not produce a successful collimated relativistic outflow (i.e. no observer in the Universe observed a classical SGRB in association with GW170817), the emission from GW170817 is quasi-spherical and powered by energy deposited by the interaction of the unsuccessful jet with the BNS ejecta ([245]). The simplest incarnation of this model (i.e. the uniform fireball) fails to reproduce current observations, but a more complex version with highly stratified ejecta with energy $E(> \Gamma\beta) \propto (\Gamma\beta)^{-5}$ (where $\Gamma\beta$ in this context is the specific momentum

Table 6.1.

X-ray Spectral Parameters and inferred flux ranges ($1\,\sigma$ c.l.). Upper limits are provided at the $3\,\sigma$ c.l. [a] 0.5-8 keV count-rate upper limit of 1.2×10^{-4} cps from [235], with updated flux calibration performed with an absorbed power-law model with $\Gamma = 1.4$ as inferred from our joint fit of the CXO observations with IDs 19294 and 20728. [b] This work.
[c] From [235].
[d] From a joint spectral fit of CXO observations, IDs 19294 and 20728. This work.
[e] Flux from [233] re-scaled to the $\Gamma = 1.4$ spectrum. This work.

Obs ID	Time since merger	Γ	Flux (0.3-10 keV)	Unabsorbed Flux (0.3-10 keV)
	(days)		$(10^{-15}\mathrm{erg\,s^{-1}cm^{-2}})$	$(10^{-15}\mathrm{erg\,s^{-1}cm^{-2}})$
18955	2.34	1.4	$< 1.8^a$	$< 1.9^a$
19294	9.21	$0.95^{+0.95}_{-0.19}$	$(4.2 - 9.3)^b$	$(4.4 - 9.6)^b$
		$1.4^{+0.9}_{-0.1}$	$(2.7 - 6.8)^d$	$(2.9 - 7.3)^d$
20728	15.39	$1.6^{+1.5}_{-0.1}$	$(3.0 - 5.6)^c$	$(3.1 - 5.8)^c$
		$1.4^{+0.9}_{-0.1}$	$(3.7 - 7.3)^d$	$(4.0 - 7.8)^d$
18988	15.94	1.4	$(3.8 - 7.5)^e$	$(4.1 - 8.0)^e$
20860/1	109.39	$1.62^{+0.16}_{-0.16}$	$(20. - 25.)^b$	$(22. - 28.)^b$
20936/7/8/9-20945	158.50	$1.61^{+0.17}_{-0.17}$	$(22. - 27.)^b$	$(24. - 29.)^b$

of the outflow) successfully accounts for the observed properties of GW170817. This model was favored by [224, 234, 237, 246, 247].

Here we present deep radio, optical and X-ray observations of GW170817 $\sim$ $110 - 160$ d after merger (Sec. 6.2) and offer an alternative interpretation. We employ hydrodynamical simulations of the jet interaction with the BNS ejecta to show that a core of ultra-relativistic material can successfully break through the closest environment and power a classical SGRB in association with GW170817, in agreement with the recent results by [248, 249]. We further demonstrate in Sec. 6.3 that the very simple power-law spectrum extending for eight orders of magnitude in frequency allows a precise measure of the properties of electrons accelerated at the shock front. In particular it enables inferences on the slope of the non-thermal tail of acceler-

ated particles from which we derive robust constraints on the shock velocity which are independent from the morphology of the outflow (collimated vs. spherical). We demonstrate that all these properties are consistent with a SGRB-like outflow originally directed away from our line of sight (Sec. 6.3). In this scenario GW170817 is not intrinsically subluminous and its unusual observed properties result from a different viewing angle than classical SGRBs, which are viewed along the jet axis. We conclude in Sec. 6.4.

We assume that all electrons are shock accelerated to a power-law energy distribution $N(\gamma) \propto \gamma^{-p}$, i.e. $\xi_N = 1$, which is the standard assumption in GRB studies. If only a fraction of electrons $\xi_N < 1$ is accelerated into the non-thermal tail, the inferred density should be re-scaled as n/ξ_N. We adopt the convention $F_\nu \propto \nu^{-\beta}$ and $\Gamma = \beta + 1$, where β is the spectral index and Γ is the photon index. We assume a distance to NGC 4993 of $39.5\,\mathrm{Mpc}$ ($z = 0.00973$) as listed in the NASA Extragalactic Database. $1\,\sigma$ c.l. uncertainties are listed unless otherwise stated. In this manuscript we employ the notation $Q_x \equiv Q/10^x$.

6.2 Observations and data analysis

6.2.1 Chandra X-ray Observations

We observed GW170817 with the *Chandra* X-ray Observatory (CXO) on 2017 August 19.71UT, $\delta t \approx 2.3\,\mathrm{d}$ after the GW trigger (observation ID 18955; PI: Fong; Program 18400052), leading to a deep X-ray non-detection with $L_x < 3.2 \times 10^{38}\,\mathrm{erg\,s^{-1}}$ ([235]) that sets GW170817 apart from all previous SGRBs seen on-axis ([250]). Further CXO observations obtained at $\delta t \approx 9\,\mathrm{d}$ ([236], observation ID 19294; PI: Troja; Program 18500489) and $\delta t \approx 15\,\mathrm{d}$ ([233, 235, 236], observation IDs 18988, 20728; PIs: Haggard, Troja; Programs 18400410,18508587) since merger revealed X-ray emission at the location of GW170817 with rising temporal behavior.

We independently re-analyzed the CXO observations acquired $\delta t \approx 9\,\mathrm{d}$ post-merger (ID 19294) and originally presented in [236]. *Chandra* ACIS-S data have

Table 6.2.
VLA observations of GW170817.

Time since merger (days)	Mean Freq (GHz)	Freq Range (GHz)	On-source Time (hr)	Flux Density (μJy)
80.10	6.0	$3.976 - 7.896$	1.5	37.4 ± 4.2
112.04	5.0	$3.796 - 5.896$	1.5	69.7 ± 7.5
112.04	7.0	$5.976 - 7.896$	1.5	57.7 ± 4.7
115.05	2.6	$2.088 - 2.984$	0.57	82.3 ± 20.7
115.05	3.4	$2.888 - 3.784$	0.57	95.8 ± 11.0
115.05	9.0	$7.976 - 9.896$	0.69	56.4 ± 10.4
115.05	11.0	$9.976 - 11.896$	0.69	52.5 ± 10.1
115.05	13.0	$11.976 - 13.896$	1.59	42.3 ± 5.7
115.05	15.0	$13.976 - 15.896$	1.59	45.2 ± 7.0
115.05	17.0	$15.976 - 17.896$	1.59	44.0 ± 7.9
162.89	2.6	$2.088 - 3.016$	0.58	104.5 ± 22.3
162.89	3.4	$3.016 - 3.912$	0.58	91.2 ± 17.4
162.89	5.0	$4.000 - 6.000$	0.70	80.8 ± 12.5
162.89	7.0	$6.000 - 8.000$	0.70	61.1 ± 7.3
162.89	9.0	$8.000 - 10.000$	0.70	55 ± 9.9
162.89	11.0	$10.000 - 12.000$	0.70	$34.4 \pm 10.$
162.89	13.0	$12.000 - 14.000$	1.84	41.7 ± 6.3
162.89	15.0	$14.000 - 16.000$	1.84	38.9 ± 7.2
162.89	17.0	$16.000 - 18.000$	1.84	43.5 ± 7.7

been reduced with the `CIAO` software package (v4.9) and relative calibration files, applying standard ACIS data filtering as in [235]. Using `wavdetect` we find that an X-ray source is clearly detected with significance of $5.8\,\sigma$ at the location of the optical counterpart of GW170817. The inferred count-rate in the 0.5-8 keV energy range is $(2.9 \pm 0.8) \times 10^{-4}\,\mathrm{c\,s^{-1}}$ (exposure time of 49.4 ks), consistent with the results from [236]. We employ Cash statistics to fit the spectrum. We adopt an absorbed power-law spectral model with index Γ and Galactic neutral hydrogen column density $\mathrm{NH_{mw}} = 0.0784 \times 10^{22}\,\mathrm{cm^{-2}}$ [251] and use MCMC sampling to constrain the spectral parameters. We find $\Gamma = 0.95^{+0.95}_{-0.19}$. We find no statistical evidence for intrinsic neutral hydrogen absorption and place a limit $\mathrm{NH_{int}} < 7 \times 10^{22}\,\mathrm{cm^{-2}}$ ($3\,\sigma$ c.l.). For these parameters the 0.3-10 keV flux is $(4.2 - 9.3) \times 10^{-15}\,\mathrm{erg\,s^{-1}cm^{-2}}$ ($1\,\sigma$ c.l.), corresponding to an unabsorbed flux of $(4.4 - 9.6) \times 10^{-15}\,\mathrm{erg\,s^{-1}cm^{-2}}$.

Comparison with the X-ray spectrum of GW170817 at $\delta t \approx 15\,\mathrm{d}$ (ID 20728) that we presented in [235] indicates a possibly harder emission at early times ($\Gamma = 0.95^{+0.95}_{-0.19}$ at $\delta t \approx 9\,\mathrm{d}$ vs. $\Gamma = 1.6^{+1.5}_{-0.1}$ at $\delta t \approx 15\,\mathrm{d}$). While we find this possibility intriguing, the limited number statistics of the two spectra does not allow us to draw conclusions as the two Γ values are statistically consistent. A joint spectral fit of the two epochs indicates $\Gamma = 1.4^{+0.9}_{-0.1}$ ($1\,\sigma$ c.l.) with a 3σ upper limit $\mathrm{NH_{int}} < 2.7 \times 10^{22}\,\mathrm{cm^{-2}}$. The corresponding flux ranges are reported in Table 6.1. Our results from the joint fit are broadly consistent with the findings from [236].

Deep X-ray observations of GW170817 have been obtained as soon as the source re-emerged from Sun constraint (PI Wilkes, observation IDs 20860, 20861; Program 18408601; [239, 240, 252, 253]). The CXO started observing GW170817 on 2017 December 3.07UT (107.5 d since merger, ID 20860) for 74.1 ks. An X-ray source is clearly detected at the location of GW170817 with significance of $33.4\,\sigma$ and net count-rate $(1.47 \pm 0.14) \times 10^{-3}\,\mathrm{c\,s^{-1}}$ (0.5-8 keV). The CXO observed the field for an additional 24.7 ks starting on 2017 December 6.45UT (110.9 d since merger, ID 20861). The X-ray source is still detected with a significance of $\sim 15.0\,\sigma$ and net count-rate of $(1.41 \pm 0.24) \times 10^{-3}$ (0.5-8 keV). The joint spectrum can be fit with an

absorbed power-law spectral model with photon index $\Gamma = 1.62 \pm 0.16$ (1 sigma c.l.), consistent with the results from [238]. We find no evidence for intrinsic neutral hydrogen absorption and constrain $\mathrm{NH_{int}} < 0.7 \times 10^{22}\,\mathrm{cm^{-2}}$ ($3\,\sigma$ c.l.). These properties are consistent with the X-ray spectral properties of GW170817 at $t \leq 15$ days. The 0.3-10 keV inferred flux range is $(2.0 - 2.5) \times 10^{-14}\,\mathrm{erg\,s^{-1}cm^{-2}}$, (unabsorbed flux of $(2.2 - 2.8) \times 10^{-14}\,\mathrm{erg\,s^{-1}cm^{-2}}$). This result indicates substantial brightening of the X-ray source during the last ~ 95 d with no measurable spectral evolution (Fig. 6.1).

Further CXO observations have been obtained between 2018 January 17 and 28, 153.4-163.8 d since merger (PI Wilkes, observation IDs 20936, 20937, 20938, 20939, 20945; Program 19408607, total exposure time of 104.8 ks). GW170817 is detected with high confidence in each observation. The total source count-rate is 157.1 ± 12.7 (0.5-8 keV), corresponding to $(1.50 \pm 0.12) \times 10^{-3}\,\mathrm{c\,s^{-1}}$. We do not find evidence for statistically significant spectral evolution during the entire observation. We also do not find evidence for statistically significant temporal variability of the source during the observation. The joint spectrum can be fit with an absorbed power-law spectral model with photon index $\Gamma = 1.61 \pm 0.17$ and $\mathrm{NH_{int}} < 1.0 \times 10^{22}\,\mathrm{cm^{-2}}$ ($3\,\sigma$ c.l.). These results are broadly consistent with the preliminary analysis by [241] and [254]. The corresponding 0.3-10 keV observed flux range is $(2.2 - 2.7) \times 10^{-14}\,\mathrm{erg\,s^{-1}cm^{-2}}$, while the unabsorbed flux is $(2.4 - 2.9) \times 10^{-14}\,\mathrm{erg\,s^{-1}cm^{-2}}$. This result indicates that the source did not experience significant temporal and spectral evolution between ~ 100 d and ~ 150 d since merger. Our findings do not support the claim of declining emission from GW170817 by [242], but suggest that the non-thermal emission from GW170817 is now close to its peak.

6.2.2 HST Observations

We obtained 1 orbit of *Hubble Space Telescope* (*HST*) observations of GW170817 on 1 January 2018 (137 d since merger) using the Advanced Camera for Surveys (ACS) with the F606W filter (PID: 15329; PI: Berger). We produced a drizzled

image corrected for optical distortion using the `astrodrizzle` task in the `drizzlepac` software package provided by STScI. We detect a faint source at the location of the optical counterpart of GW170817, confirmed by relative astrometry with our ACS/F625W image from 27 August 2017 [222]. To measure the flux of the source we first subtract a model of the galaxy surface brightness profile determined using GALFIT v3.0.5 [255]. Using aperture photometry and the ACS/F606W zeropoint provided by the *HST* team, we find an observed AB magnitude of 26.90 ± 0.25 mag. Correcting for Galactic extinction with $E(B - V) = 0.105$ mag [256], the extinction corrected AB magnitude is 26.60 ± 0.25 mag. As a comparison, at 110 d since merger, [257] find $m = 26.44 \pm 0.14$ mag.

6.2.3 VLA Observations

Our radio observations of GW170817 from $0.5 - 39$ d since merger have been reported in [232]. We continued observing GW170817 with the Karl J. Jansky Very Large Array (VLA) under program 17A-231 (PI: Alexander), obtaining observations on 5 November 2017 ($\delta t \sim 80$ d since merger) at a mean frequency of 6 GHz (C band), using a bandwidth of 4 GHz. These new observations were taken in the VLA's B configuration. We analyzed and imaged the VLA data using standard CASA routines [258], using 3C286 as the flux calibrator and J1258−2219 as the phase calibrator. We fit the flux density and position of the emission using the imtool program within the pwkit package [259]. We clearly detect the source with a flux density of $37 \pm 4\ \mu$Jy. The in-band spectral index is poorly constrained, but is clearly optically thin (Table 6.2.1).

We obtained further multi-frequency VLA observations under the same program on 7 December 2017 (C band) and under program 17B-425 (PI: Alexander) on 10 December 2010 (S, X, and Ku bands, spanning the frequency range 2–18 GHz). New observations spanning 2-18 GHz (S, C, X, and Ku bands) were obtained under program 17B-425 on 27 January 2018. We reduced the data using the same procedure

outlined above and cross-checked our results against the automated CASA-based VLA pipeline. The flux densities obtained with each method are fully consistent to within the error bars at all frequencies; we choose to report the pipeline flux densities here because the images have slightly lower rms noise. GW170817 is clearly detected at all radio frequencies and has continued to brighten, enabling us to split the data into narrower frequency bandwidths for imaging. At S band, we divided the data into two 1 GHz subbands, although the effective bandwidth of each after flagging is closer to 750 MHz due to RFI. At higher frequencies, we split the data into 2-GHz bandwidth. We report the measured flux densities in Table 6.2.1. As before, uncertainties were calculated using the imtool package and represent the uncertainty on a point source fit. The December measurements clearly indicate an optically thin spectrum with spectral index $\beta_R = 0.47 \pm 0.08$. This value is consistent with the X-ray spectral index $\beta_X = 0.62 \pm 0.16$ ($\Gamma = \beta + 1$) obtained a few days before (Sec. 6.2.1). The latest VLA observations in January are also optically thin with $\beta_R = 0.55 \pm 0.10$, in good agreement with the CXO spectral index $\beta_X = 0.621 \pm 0.17$ around the same time.

6.2.4   Joint X-Ray and Radio analysis

A joint spectral fit of radio data obtained at $\delta t \sim 111 - 114$ d and X-ray data obtained around $\delta t \approx 109$ d with a simple power-law model $F_\nu \propto \nu^{-\beta_{XR}}$ constrains $\beta_{XR} = 0.588 \pm 0.005$. This value is consistent with the spectral indexes β_X and β_R derived from individual fits within the X-ray and radio bands (Sec. 6.2.1,6.2.3), and shows that at $t \approx 110$ d the broad-band X-ray to radio emission from GW170817 originates from the same non-thermal spectral component.

To refine our measurement of the X-ray to radio spectral slope β_{XR} at ~ 110 d we account for the (mild) temporal evolution of the afterglow flux adopting the iterative procedure that follows. We initially assume a fiducial spectral index value $\beta_i = 0.60$, which is used to construct a "master" radio light-curve of GW170817 at a

given frequency using the entire set of radio observations available at all frequencies. Radio data have been compiled from [232], [234], [260] and [237]. We fit the master radio light-curve with a power-law model $F_\nu \propto t^\alpha$. The best-fitting α is then used to renormalize the flux densities measured at $\delta t = 111 - 114$ d to a common epoch of 109 d since merger (to match the time of CXO observations). Finally, we estimate β_f from a joint fit of the broad-band radio-to-X-ray spectrum at 109 d. This procedure is repeated until convergence (i.e. $\beta_f = \beta_f$ within error bars). We find $\beta_{XR} = 0.585 \pm 0.005$ and $\alpha = 0.73 \pm 0.04$ (Fig. 6.1). As a comparison, from the analysis of radio data alone at $t < 93$ d [237] infer $\beta_R = 0.61 \pm 0.05$, consistent with our results. Our measurement of the spectral slope benefits from the significantly larger baseline of eight orders of magnitude in frequency, and is consequently more precise. We plot in Fig. 6.1 the HST measurement obtained by [257] at 110 d. This comparison shows a remarkable agreement with our bestfitting SED and demonstrates that at 110 d since merger the optical emission from GW170817 is of non-thermal origin and originates from the afterglow.

The X-ray and radio light-curves suggest that GW170817 might be now approaching its peak of non-thermal emission. From a fit of the radio-to-X-ray SED at ~ 160 d we find $\beta_{XR} = 0.584 \pm 0.006$, consistent with the value at 110 d.

We compile in Fig. 6.1 the radio-to-X-ray SEDs of GW170817 at 15 d and 9 d (orange and blue symbols). At these epochs the thermal emission from the radioactive decay of freshly synthesized heavy elements (i.e. the kilonova) dominates the UV-optical-NIR bands. Fig. 6.1 shows that a re-scaled version of the $\beta_{XR} = 0.585$ spectrum that best-fits the 110 d epoch adequately reproduces the X-ray and radio emission from GW170817 at all times. Interestingly, the extrapolation of the X-ray flux density at 9 d with a $\propto \nu^{-0.6}$ spectrum matches the 6 GHz measurement reported by [234] as a potential — but possibly spurious — detection, suggesting that the 6 GHz measurement is in fact a real detection (and the earliest radio detection of GW170817).

Based on these results we conclude that the non-thermal emission from GW experienced negligible spectral evolution across the electromagnetic spectrum in the last ~ 150 d, and that the radio and X-ray radiation from GW170817 continue to represent the same non-thermal emission component. This component of emission is now approaching its peak.

6.3 Interpretation and discussion

6.3.1 A synchrotron spectrum from particles accelerated by shocks with $\Gamma \approx 3 - 10$

The simple power-law spectrum extending over eight orders of magnitude in frequency indicates that radio and X-ray radiation are part of the same non-thermal emission component, which we identify as synchrotron emission. At all times of our monitoring the synchrotron cooling frequency ν_c is above the X-ray band, ν_m is below the radio band and the observed radio and X-ray emission is on the $F_\nu \propto \nu^{-(p-1)/2}$ spectral segment, where p is the index of the non-thermal electrons accelerated into a power-law distribution $N_e(\gamma) \propto \gamma^{-p}$ at the shock front. From our best-fitting β_{XR}, we infer $p = 2.17 \pm 0.01$.

The precise measurement of the power-law slope p (ultimately enabled by the very simple spectral shape) allows us to test with unprecedented accuracy the predictions of the Fermi process for particle acceleration in relativistic shocks. The power-law index in trans-relativistic shocks will lie in between the value $p = 2$ expected at non-relativistic shock speeds [261–263] and $p \simeq 2.22$ at ultra-relativistic velocities [264–267]. From [266], we estimate that the measured $p = 2.17 \pm 0.01$ implies a shock Lorentz factor of $\Gamma \sim 5$ at 110 d (the $3\,\sigma$ c.l. is $\Gamma \sim 3 - 10$). The straightforward implication is then that we are seeing electron acceleration in trans-relativistic shocks in action.[1]

---

[1]We remark, though, that a power-law electron spectrum with slope p might not necessarily result in the canonical radiation spectrum $F_\nu \propto \nu^{-(p-1)/2}$, if one of the following conditions are met: (i) the radiative signature has an appreciable contribution from electrons that cool in the precursor,
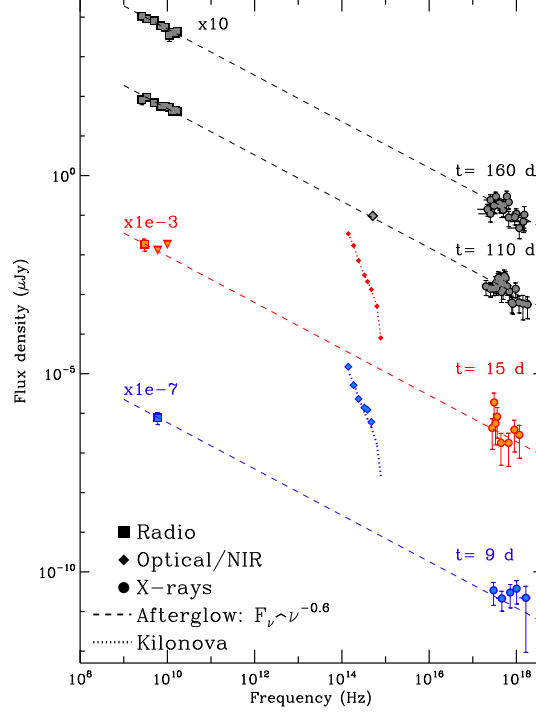
Fig. 6.1. Evolution of the broad-band radio-to-X-ray SED of GW170817 from 9 d until 160 d since merger. The radio and X-ray data are dominated by non-thermal synchrotron emission from the GW170817 afterglow at all times and consistently track each other on a $F_\nu \propto \nu^{-0.6}$ spectral power-law segment. At early times $t \leq 15$ d the optical-NIR is dominated by radioactively powered emission from the KN. By day 110 the KN component has faded away and the detected optical-NIR emission is dominated by the $F_\nu \propto \nu^{-0.6}$ afterglow radiation. Filled circles: CXO data. Filled squares: VLA. Note that while [234] consider their 6 GHz measurement at ~ 10 days only as a potential detection, here we show that it does naturally lie on the $\propto \nu^{-0.6}$ extrapolation of the X-ray data, which suggests that this is in fact a real detection (and the earliest radio detection of GW170817). Filled diamonds at 15 and 9 d: optical-NIR data from [231]. For day 9 we show the actual data from [222, 224, 228, 229], while for day 15 we show the extrapolated values from the best fitting model from [231]. Black dashed line: $F_\nu \propto \nu^{-\beta_{XR}}$ afterglow component with $\beta_{XR} = 0.6$ that best fits the observations at 110 d and 160 d. Dashed red and blue lines: same afterglow model renormalized to match the observed flux level at 15 d and 9d. Dotted line: best fitting KN component. The SED at 15 d and 9 d have been rescaled for displaying purposes. The HST observations from [257] obtained at 110 d (filled diamonds) are shown here for comparison but have not been used in our fits.

As the non-thermal spectrum of GW170817 showed negligible evolution (Fig. 6.1), a similar line of reasoning applies to the previous epochs at $t \leq 15$ d, from which we conclude that the *observed* non-thermal radiation from GW170817 at $t < 115$ d is always dominated by emission from material with relatively small $\Gamma \sim 3 - 10$.

These findings are consistent with the picture favored by [237] (see also [224, 234, 247, 278]) of emission from a quasi-isotropic mildly relativistic fireball with stratified ejecta and no surviving ultra-relativistic jet (i.e. their "choked jet cocoon" scenario), but do not represent a unique prediction from this model as we detail below (see also [247] for an independent study that reached a similar conclusion). A value $\Gamma \sim 3 - 10$ is significantly smaller than the initial $\Gamma \sim$ a few 100 inferred for the luminous SGRBs, which are powered by ultra-relativistic jets seen on axis (which have consistently larger inferred values of p [243]). However, one expects that even a blast wave with large energy $E_{k,iso} \sim 10^{52}$ erg propagating in a low density medium with $n \sim 10^{-4} - 10^{-5}$ cm^{-3} will have decelerated to $\Gamma \sim 4 - 5$ by ~ 110 d since merger, i.e., the shock is mildly relativistic, in excellent agreement with the estimate above based on the physics of particle acceleration at shocks. Current observations are thus also consistent with a scenario where the BNS merger successfully launched an outflow with a collimated ultra-relativistic core (initially pointing away from our line of sight) and less collimated mildly-relativistic wings that dominate the early emission (i.e. the "successful structured jet" model of Sec. 6.3.3; [?, 31, 236, 241, 242, 249, 279, 280]). In this latter scenario the emission that we *observe* is also always dominated by radiation from ejecta with relatively small Γ at all times.

We conclude that the observed optically-thin non-thermal spectrum clearly identifies the nature of the emission as synchrotron radiation from a population of electrons accelerated at trans-relativistic shocks with $\Gamma \sim 3 - 10$. This property, however, is

---

i.e., upstream of the shock front, which has the effect of hardening the observed spectrum [268, 269]; or (*ii*) the magnetic field self-generated by the shock is not uniform in the post-shock region, but decays away from the shock [267, 270–274]. In this case, the observed synchrotron spectrum encodes important information on the decay profile of the turbulent post-shock fields [275–277].

common to both successful structured-jet scenarios and choked-jet scenarios and does *not* identify the nature of the relativistic ejecta.

6.3.2 Off-Axis Relativistic Top-Hat Jets

The late onset of the X-ray and radio emission of GW170817 rules out relativistic jets with properties similar to those of SGRBs seen on-axis ([224, 232–238, 282, 283]). Relativistic jets originally pointing away from our line of sight can instead produce rising X-ray and radio emission as they decelerate into the ambient medium (see e.g. [284]).

We first consider top-hat relativistic jets, i.e. jets characterized by a uniform angular distribution of the Lorentz factor within the jet $\Gamma(\theta)$. This is the simplest jet model and likely an over simplification of real jets in BNS mergers (e.g. [246, 285–288]). The simple top-hat jet model is expected to capture the overall behavior of the observed synchrotron emission from relativistic electrons at the shock fronts only after the core of the jet enters into our line of sight, leading to a peak of emission. Before peak, top-hat jets will underpredict the observed emission when compared to structured jets with similar core (Sec. 6.3.3), i.e. jets with with non-zero $\Gamma(\theta)$ in higher-latitude ejecta at $\theta > \theta_j$.

Figure 6.2 shows an update of our modeling of GW170817 with top-hat jets following the same procedure as in [232, 235, 289] with BOXFIT [290]. We show two representative models for two jet opening angles. Within the top-hat scenario, the most successful models share a preference for low densities $n \sim 10^{-4} \, \text{cm}^3$ and large energies $E_{\text{k,iso}} \sim 10^{52} \, \text{erg}$, with off-axis angles $\theta_{obs} \sim 15° - 25°$. As these plots demonstrate, top-hat jets viewed off-axis fail to reproduce the larger X-ray and radio luminosities of GW170817 at early times $t \lesssim 25$ days and do not naturally account for the mild but steady rise of the non-thermal emission from GW170817. This is expected if the jet in GW170817 has similar core properties as the uniform jets that we are considering here but with $\Gamma(\theta > \theta_j) > 0$ (i.e. a structured jet) and the core of the jet has yet
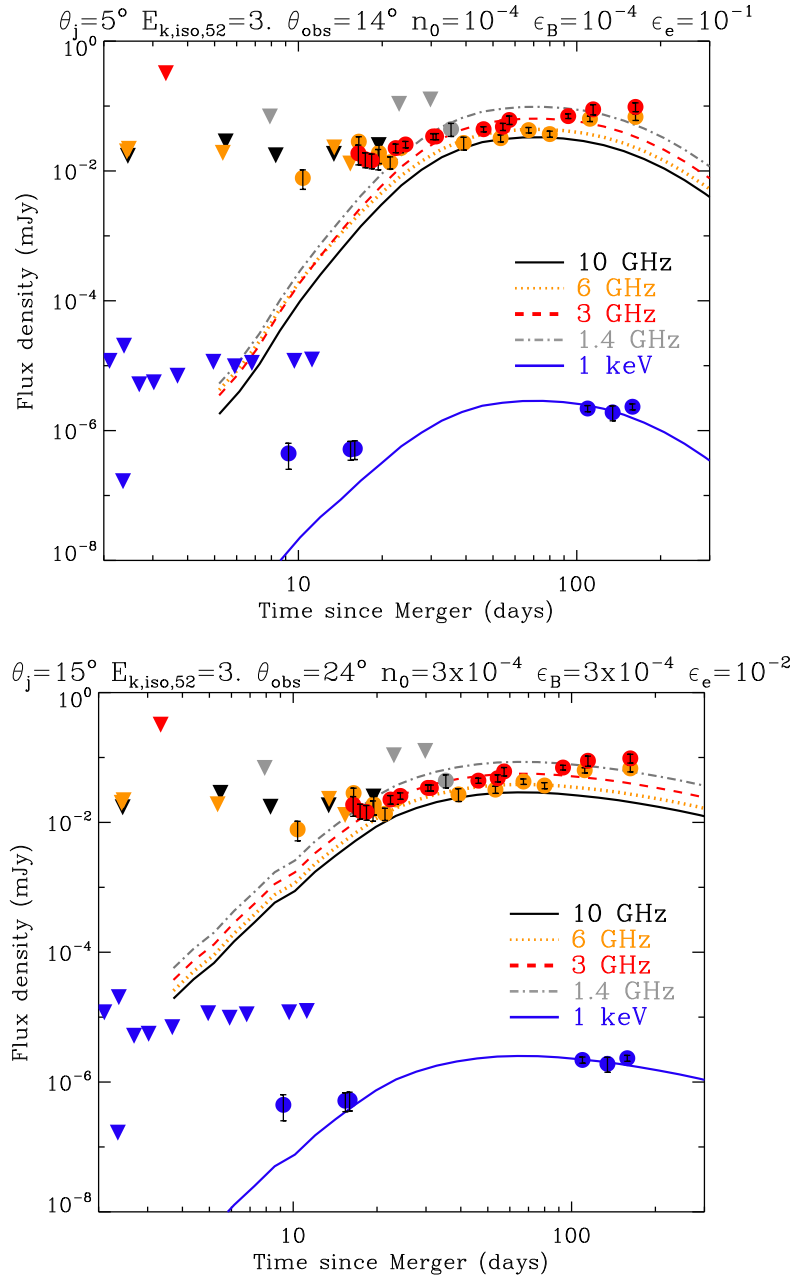
Fig. 6.2. Best-fitting top-hat off-axis jet models with $\theta_j = 5°$ (upper panel) and $\theta_j = 15°$ (lower panel) for $p = 2.1$. These models fail to reproduce observations at early times and do not naturally account for the still-rising light-curve, which is a potential signature of structure $\Gamma(\theta)$ in the jet, with an ultra-relativistic core still out of our line of sight. This is explored and quantified in Sec. 6.3.3.
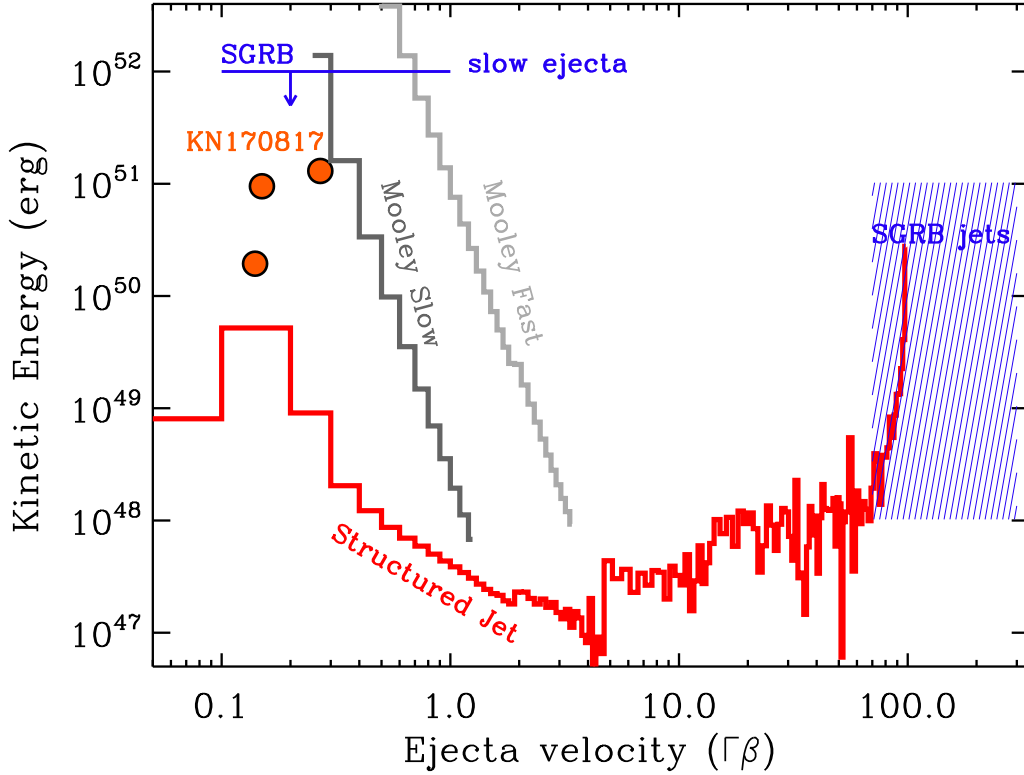
Fig. 6.3. Kinetic energy structure of the ejecta of GW170817 for quasi-spherical outflows from [237] (grey lines) and for the structured jet that we present here (red line). Orange filled dots: kinetic energy of the red, purple and blue kilonova component associated to GW170817 as derived by [231]. Blue lines: SGRBs. For the SGRB slow ejecta we report a representative limit derived from the analysis of very late-time radio observations from [281], while the shaded area mark the beaming-corrected E_k of the jet component in SGRBs as derived by [243] for $\epsilon_B = 0.1$ (note that smaller values of ϵ_B would lead to E_k that would extend to larger values, see e.g. [243], their Fig. 7). This plot highlights the difference between quasi-spherical outflows (which lack an ultra-relativistic component and require a large amount of energy to be coupled to slowly moving ejecta $\Gamma < 2$) and structured ultra-relativistic outflows (which have properties consistent with SGRBs and can be energetically less demanding). The peak time of the non-thermal light-curve of GW170817 will constrain the minimum $\Gamma\beta$ of the ejecta in quasi-spherical models.

to enter into our line of sight (Sec. 6.3.3). The X-rays suggest that GW170817 is reaching its peak of emission, which, in this scenario, would imply that the emission from the core of the jet is now close to entering our line of sight.

In summary, the failure of the simple top-hat jets motivates the exploration of more realistic structured jets models in Sec. 6.3.3 and should not be interpreted as evidence to discard the notion that GW170817 harbored a fully relativistic outflow directed away from our line of sight.

6.3.3   Successful Off-Axis Relativistic Structured Jets

Deviation from the simple top-hat jet picture is naturally expected as the relativistic jet has to propagate through the BNS merger immediate environment (e.g. [246, 248, 280, 285–288, 291]), polluted with $\sim 0.01\,\mathrm{M}_\odot$ of neutron-rich material that was ejected during the merger (the same material produces the radioactively powered KN, e.g. [219]). Here we consider the scenario where the fully relativistic collimated outflow successfully survived the interaction with the BNS merger ejecta and we refer to this model as successful off-axis relativistic structured jet. In this model the outflow has $\Gamma \equiv \Gamma(\theta)$ and $E_{\mathrm{k,iso}} \equiv E_{\mathrm{k,iso}}(\theta)$.

This scenario is clearly different from choked-jets, pure-cocoon models and spherical models (favored by [224,234,237,245,247,278]) where no collimated ultra-relativistic outflow (even when there) survived the interaction with the BNS ejecta. This is clear from Fig. 6.3, where we show the E_k structure of the two types of outflows. The two classes of models have important implications for the nature of GW170817. As the emission from the slower jet wings is subdominant at all times when seen on-axis, GW170817 would be consistent with being a canonical SGRB seen from the side, if indeed powered by a successful off-axis structured relativistic jet. GW170817 would be instead a subluminous event and intrinsically different from the population of known SGRBs in the choked-jets and pure-cocoon models. From Fig. 6.3 it is also clear that quasi-spherical outflows require significantly larger amounts of energy

coupled to slow material with $\Gamma \sim 1$ ($\gtrsim 10^{51}$ erg for the "fast model" from [237]). The quasi-spherical outflows in these models are powered by energy deposited by failed jets. However, observed successful jets in SGRBs have $\leq 3 \times 10^{50}$ erg (shaded region in Fig. 6.3). The two notions can be reconciled only if the most energetic jets never manage to break out, which we find contrived.

Structured off-axis jets have been specifically discussed in the context of GW170817 by [?, 224, 234, 236, 237, 241, 242, 245, 247, 249, 257, 280, 288, 289]. These jets typically have large $E_{\mathrm{k,iso}}(\theta)$ and $\Gamma(\theta)$ close to the axis of the jet, that decrease for larger angles, resulting in a jet with a narrow, ultra-relativistic core and a wider, mildly relativistic sheath. For off-axis observers, the afterglow is initially dominated by the less colli-mated emission from the mildly relativistic wings[2] (which would be also responsible for the detected γ-ray emission). As time progresses, the jet decelerates, beaming ef-fects become less pronounced and the observer will gradually see the more-luminous, initially ultra-relativistic jet core.

We use the moving-mesh relativistic hydrodynamics JET code [292] to simulate the dynamics of explosive outflows launched in neutron star ejecta clouds using an engine model [286] and density structure similar to [224, 245]. We then compute syn-chrotron light curves from the simulation data using standard synchrotron radiation models ([293]). We show in Fig. 6.4 the results for two representative sets of jet-environment parameters that successfully account for current observations across the spectrum (a full description of the jet simulations is presented in [294]). Specifically, the jet has a narrow ultra-relativistic core of $\theta_c \sim 9°$ with $\Gamma \sim 100$ surrounded by a mildly relativistic sheath with $\Gamma \sim 10$ at $10° \lesssim \theta \lesssim 60°$ (see inset of Fig. 6.4) and propagates in a low-density environments with $n = 10^{-5} - 10^{-4}\,\mathrm{cm^{-3}}$. At $t \sim 100$ s, the energy in the ultra-relativistic core is $\sim 4.4 \times 10^{50}$ erg while the sheath carries $\sim 1.4 \times 10^{50}\,$erg (see [294] for details). The observer is located at $\theta_{obs} \sim 17 - 20°$ from the jet axis. We adopt $\epsilon_e = 0.02$ ($\epsilon_e = 0.1$), $\epsilon_B = 0.001$ ($\epsilon_B = 0.0005$) with

---

[2]This component of emission is missing in top-hat jets, which, as a consequence, show a characteristic $\propto t^2$ rise and underpredict the early time observations as shown in Fig. 6.2.
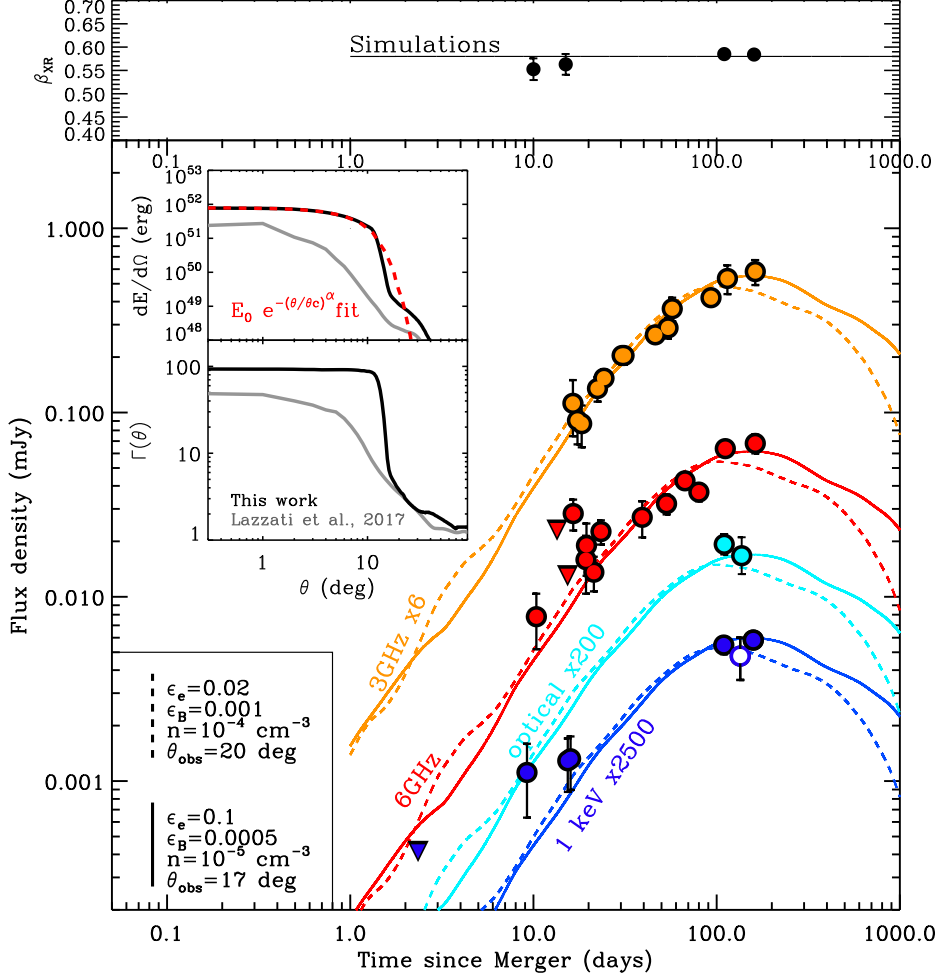
Fig. 6.4. Results from our simulation of a successful off-axis relativistic jet with structure $\Gamma(\theta)$ and $E_{\mathrm{iso}}(\theta)$ displayed in the insets, propagating into a low-density environment with $n \sim 10^{-5} - 10^{-4}\,\mathrm{cm}^{-3}$ and viewed $\sim 20°$ off-axis. We use $p = 2.16$ and the microphysical parameters reported in the figure. These two representative models can adequately reproduce the current set of observations and predict an optically thin synchrotron spectrum at all times, in agreement with our observations (upper panel). The open blue circle is the XMM X-ray measurement from [242]. *Insets*: $E_{\mathrm{iso}}(\theta)$ and average $\Gamma(\theta)$ from our simulations (black solid lines) at $t = 100$ s, compared to the jet structure from [249] (grey lines). The jet in our simulation has quasi-gaussian structure, with $E_{\mathrm{iso}} \propto e^{-(\theta/\theta_c)^\alpha}$ and $\alpha \sim 1.9$, $\theta_c \sim 9°$ (red dashed line). Future observations will be able to constrain the jet-environment parameters.
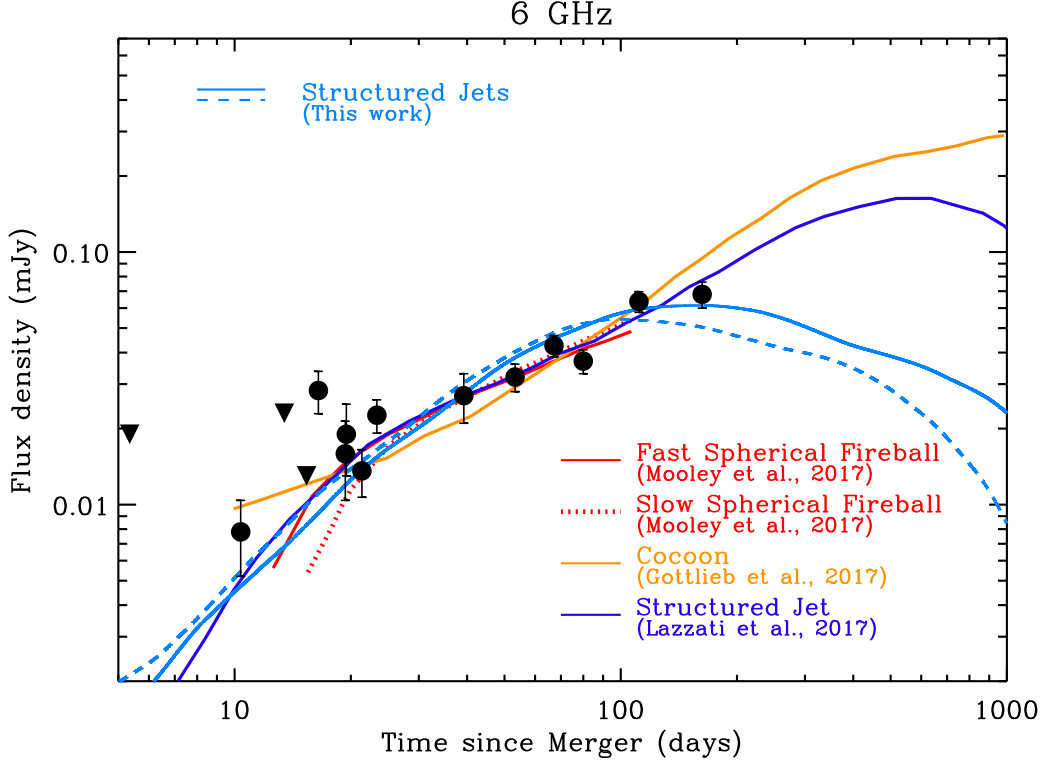
Fig. 6.5. Comparison of models that fit current observations of GW170817 at radio frequencies (6 GHz). Red and orange lines: quasi-spherical stratified ejecta models from [237] and cocoon model from [245] where no ultra-relativistic jetted component survived the interaction with the BNS ejecta (i.e. no observer in the Universe observed a regular SGRB associated with GW170817). Blue lines: structured jet models from [249] (dark blue-line, their best-fitting model) and this work (light-blue lines) where an off-axis ultra-relativistic collimated component is present and contributes to the emission at some point (i.e. GW170817 is consistent with being an ordinary SGRB viewed off-axis). The parameters of our models are the same as in Fig. 6.4. At $t \leq 100$ days all the models displayed predict an extremely similar flux evolution (and spectrum), with no hope for current data to distinguish between the two scenarios. The model by [245] and the structured jet model by [249] predict a continued rise of the radio emission until very late times, and are disfavored by the latest observations at ~ 160 d, which suggest instead a flattening of the radio light-curve. All off-axis jet models have a similar $\theta_{obs} \sim 20°$ and the different late-time evolution is a consequence of the different jet-environment parameters.
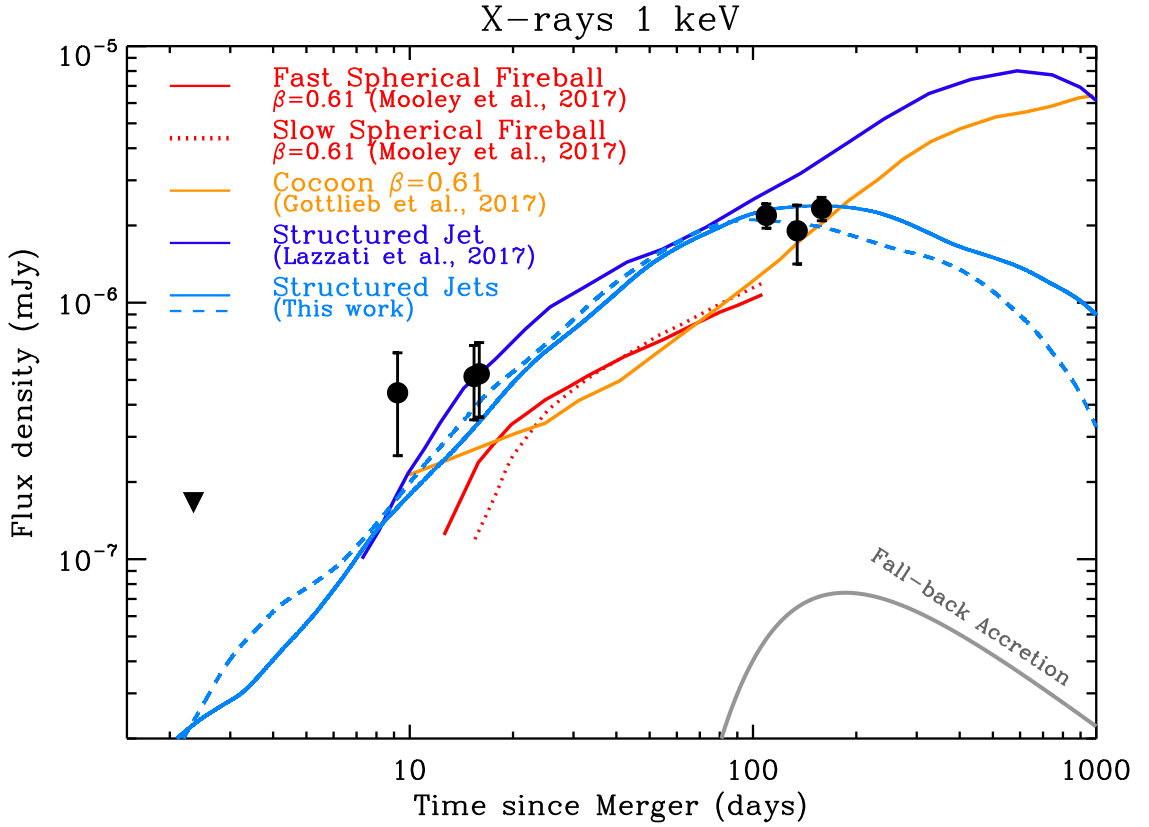
Fig. 6.6. Comparison of successful models at 1 keV. Same color coding as Fig. 6.5. For the spherical models by [237] and [245] we adopt the best fitting spectral index $\beta = 0.61$ from [237] to convert their best fitting radio models into X-rays. These models underpredict the observed X-ray flux. This is a clear indication of a flatter spectral index as we find in Sec. 6.2.3. Using $\beta_{XR} \sim 0.58$ would bring the models to consistency with the observations. The model by [245] and the structured jet model by [249] predict a continued rise of the X-ray emission until very late times, and are disfavored by the latest observations at ~ 150 d, which suggest instead a flattening of the X-ray light-curve. Thick gray line: expected flux from fall-back accretion onto the remnant black hole $F_{\text{fb}}^{obs} = F_{\text{fb}} e^{-\tau_X}$ for the fiducial parameters of Sec. 6.3.4.

$p = 2.16$, within the range of our inferred values (Sec. 6.3.1) for the $n = 10^{-4}\,\mathrm{cm}^{-3}$ ($n = 10^{-5}\,\mathrm{cm}^{-3}$) simulation.

Our model predicts an *observed* broad-band optically thin synchrotron spectrum that extends from the radio to the X-ray band on a $F_\nu \propto \nu^{-(p-1)/2}$ spectral segment, from the time of our first observations at $t \sim 10$ d until now (at the low densities $n \sim 10^{-5} - 10^{-4}\,\mathrm{cm}^{-3}$ favored by our modeling ν_c is not expected to cross the X-ray band at $t < 10^4$ d, see Fig. 6.4, upper panel). These findings are consistent with the independent results by [249] and [257], and demonstrate that the persistent optically-thin non-thermal spectrum $F_\nu \propto \nu^{-0.585}$ that characterizes GW170817 is not a unique prediction of choked-jets and/or pure-cocoon models. Instead it is a natural expectation from fully-relativistic structured outflows with properties similar to those of SGRBs but viewed from the side. Together with the very similar flux temporal evolution (see Fig. 6.5-6.6), this makes these two classes of models virtually impossible to distinguish based on current observations.

We compare the results from our simulations to those presented by [249] in Fig. 6.5-6.6. The major difference is the flux evolution at $t \geq 200$ d, with the [249] models steadily rising until $t \sim 600$ d after merger. As the microphysics parameters ($\epsilon_B = 0.002$, $\epsilon_e = 0.02$, $p = 2.13$) and observing angle ($\theta_{obs} = 21°$) are very similar to the values of one of our simulations, the different behavior can be ascribed to the combination of possibly different assumptions in the code and a narrower ultra-relativistic core, as shown in the inset of Fig. 6.4 (which effectively places the observer more off-axis) more slowly decelerating into a lower density environment ($n \sim 10^{-5}\,\mathrm{cm}^{-3}$ vs. $n \sim 10^{-4}\,\mathrm{cm}^{-3}$). In general, outflows with a fully-relativistic core with isotropic energy $\sim 10^{52}$ erg, propagating into environments with $n \leq 10^{-5}\,\mathrm{cm}^{-3}$ and viewed $\sim 20°$ off-axis will reach a peak at $t_p \geq 600$ days ($t_p \sim 2.1\, E_{k,iso,52}^{1/3}\, n^{-1/3}\, ((\theta_{obs} - \theta_j)/10°)^{8/3}$ days, e.g. [295]).

[224, 234, 237, 245, 247] disfavor the structured off-axis model based on circumstantial evidence related to the energetics of the relativistic core needed to power GW170817 compared to SGRBs. We emphasize that these authors do not rule out

structured off-axis jets in GW170817 but consider this possibility unlikely based on the large $E_{k,iso} \geq 10^{52}$ erg required. We show in Fig. 6.3 the comparison of the kinetic energies in the different components of the outflow of GW170817 from our simulation with the values inferred for SGRBs from [243]. We conclude from this plot that the E_k in the ultra-relativistic ejecta of GW170817 is not unprecedented among SGRBs (shaded blue area, see also [243], their Fig. 7) and that GW170817 is consistent with having harbored a normal SGRB directed away from our line of sight. The shaded blue area cover the range of E_k for an assumed $\epsilon_B = 0.1$. E_k would extend to larger values for smaller $\epsilon_B = 0.01$ (e.g. [243], their Fig. 7), thus reinforcing our argument. In our model the ultra-relativistic component dominates the energetics of the outflow.

Some observational tests to distinguish between the successful structured jet scenario that we support here and the choked-jet/stratified ejecta scenarios have been proposed, including VLBI imaging and the acquisition of a larger sample of GW events with electromagnetic counterparts [234, 237, 249]. Here we note that if a collimated outflow of fully relativistic material survived the interaction with the BNS ejecta, the observed light-curve will experience two temporal breaks in the future, which are apparent from Fig. 6.4 (see also Fig. 6.6-6.5): a peak when radiation from the jet core enters the line of sight at t_p (the flattening of the X-ray and radio light-curves is suggesting that GW170817 is approaching its peak of emission), and a jet-break when the far edge of the jet comes into view. In the case of collimated outflows a counter-jet signature is also expected when the jet transitions into the non-relativistic phase at $t_{NR} \approx 1100 \, (E_{k,iso,53}/n)^{1/3}$ days. For $E_{k,iso} \geq 10^{52}$ erg and $n \leq 10^{-4} \, \mathrm{cm}^{-3}$ which are relevant here, $t_{NR} \geq 30$ yrs and the appearance of the counter-jet will create a bump in the light-curve at a flux level below the sensitivity of current observing facilities.

6.3.4   X-rays from the central compact remnant

Another source of potential X-ray emission is that originating directly from the central compact remnant, as discussed in detail in [296]. We first consider an accreting

black hole. The $\approx 2.5 M_\odot$ black hole created following the merger will still be accreting fall-back debris from the merger event (e.g. [297, 298]). The accretion luminosity at the present epoch t can be estimated as

$$L_{\mathrm{X,fb}} = 0.1 \dot{M}_{\mathrm{fb}} c^2 \approx 3 \times 10^{38} \, \mathrm{erg\,s^{-1}} \left(\frac{\dot{M}_{\mathrm{fb}}(t = 1\mathrm{s})}{10^{-3} M_\odot \, s^{-1}} \right) \left(\frac{t}{120\,\mathrm{d}} \right)^{-5/3}, \qquad (6.1)$$

where we have assumed that the fall-back accretion rate follows a $\propto t^{-5/3}$ decay with a value at 1 second post merger normalized to $10^{-3} M_\odot \, s^{-1}$ (a characteristic value, which is however uncertain by at least an order of magnitude). The $L_{\mathrm{X,fb}}$ estimated above is thus close to the Eddington luminosity $L_{\mathrm{Edd}} \approx 3 \times 10^{38}$ erg s^{-1} of the black hole remnant.

The X-ray emission from the central engine is only visible if not absorbed by the kilonova ejecta along the line of sight. Given the estimated ejecta mass of $\gtrsim 10^{-2} M_\odot$ and mean velocity $v_{\mathrm{ej}} \sim 0.1 - 0.2$ c (e.g. [231] for an updated modeling), the optical depth through the ejecta of radius $R \sim v_{\mathrm{ej}} t$ and density $\rho \sim M_{\mathrm{ej}}/(4\pi R^3/3)$ is approximately given by

$$
\begin{aligned}
\tau_{\mathrm{X}} & \simeq \rho R \kappa_{\mathrm{X}} \\
& \approx 1.2 \left(\frac{\kappa_{\mathrm{X}}}{10^3 \, \mathrm{cm^2 g^{-1}}} \right) \left(\frac{M_{\mathrm{ej}}}{10^{-2} M_\odot} \right) \left(\frac{v_{\mathrm{ej}}}{0.2\,\mathrm{c}} \right)^{-2} \left(\frac{t}{120\mathrm{d}} \right)^{-2}
\end{aligned}
\qquad (6.2)
$$

where $\kappa_{\mathrm{X}} \sim 10^3 \, \mathrm{cm^2\,g^{-1}}$ is the expected bound-free opacity of neutral or singly-ionized heavy r-process nuclei at X-ray energies $\sim$ a few keV (e.g. [219]). Thus, depending on the precise ejecta column along our line of sight, we could have $\tau_{\mathrm{X}} \lesssim 1$ at the present epoch. Even in the case of negligible opacity to X-ray radiation at the present epoch, $L_{\mathrm{X,fb}}$ is $\ll$ than the observed X-ray luminosity $\sim 5 \times 10^{39} \, \mathrm{erg\,s^{-1}}$. The constant radio to X-ray flux ratio over 110 d provides an independent line of evidence against $L_{\mathrm{X,fb}}$ dominating the X-ray energy release at late times. Figure 6.6 shows that $L_{\mathrm{X,fb}}$ never dominates the X-ray emission from GW170817.

We now consider the spin-down luminosity from a magnetar remnant as potential source of X-ray radiation at late times. A long-lived magnetar remnant is already disfavored by the KN emission (e.g. [222–227, 229, 231]), particularly the inferred
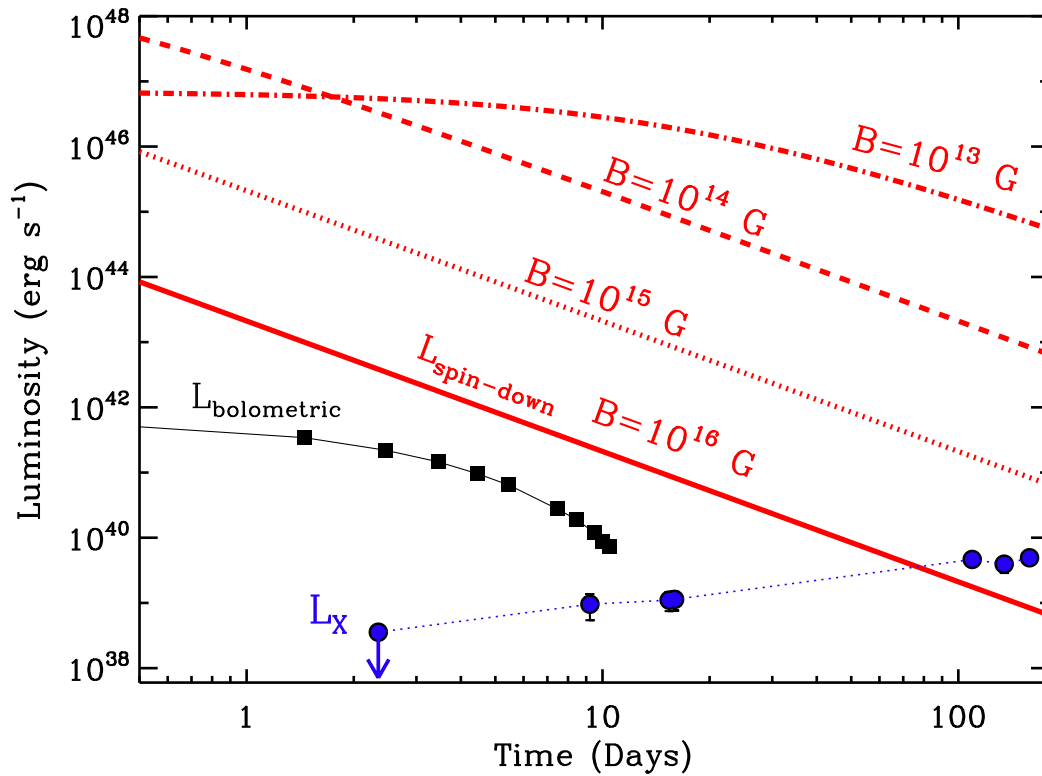
Fig. 6.7. Red lines: spin-down luminosity for a supramassive NS remnant with magnetic field $B = 10^{13}-10^{16}$ G. Black squares: GW170817 bolometric luminosity from [222]. Blue filled circles: X-ray luminosity. The spin-down luminosity is always larger than the bolometric energy release from GW170817 at early times, which argues against a long-lived magnetar remnant.

presence of lanthanide-rich material created from very neutron-rich ejecta (neutrinos from a long-lived neutron star remnant would transform outflowing neutrons back into protons; see [299]). Here we provide an independent argument against the long-lived magnetar scenario. Fig. 6.7 shows the spin-down luminosity L_{sd} for a supramassive NS remnant (Eq. 32-33 from [219]).

At ~ 10 d L_{sd} greatly exceeds the detected X-ray luminosity for any reasonable magnetic field strength $B \leq 10^{17}$ G. However, this argument alone cannot be used to rule out magnetar remnants because at this time $\tau_{\mathrm{X}} \gg 1$, thus significantly suppressing the X-ray luminosity that can escape the system and reach the observer, as we showed in [235] (see also Eq. 2 above). [300] reached the opposite conclusion, as they did not take into account the effects of bound-free opacity from the KN ejecta into their calculations (which, however, is significant). However, as we show in Fig. 6.7, the same magnetar engines would produce luminous optical emission at early times [301] in excess to the observed bolometric luminosity from GW170817 and for this reason are ruled out. Finally, one can rule out the formation of a long-lived magnetar in GW170817 by the large rotational energy $\gtrsim 10^{52}$ erg it would have injected into its environment, either into the GRB jet or the kilonova ejecta. As a comparison, in classical SGRBs, long-lived magnetars with rotational energy in the range $\gtrsim 10^{51} - 10^{54}$ erg are also ruled out [281, 302].

We conclude that a central engine origin of the detected X-ray emission is disfavored at all times.

6.4   Summary and Conclusions

Deep Chandra, HST and VLA observations of the BNS event GW170817 ~ 100 d after merger show a steadily rising emission with $F \propto t^{0.7} \nu^{-0.585}$ across the electromagnetic spectrum, before flattening at ~ 160 d without showing any sign of spectral evolution. These findings rule out simple models of top-hat jets viewed off-axis (which predict $F \propto t^2$ before peak) and uniform spherical outflows (which predict $F \propto t^3$).

We use the very simple power-law spectrum extending from the X-rays to the radio band to estimate that the emission is powered by mildly relativistic material with $\Gamma \sim 3 - 10$. This estimate is solely based on the theory of particle acceleration at shocks (and does not depend on other details of GW170817).

Models of GW170817 where no ultra-relativistic collimated component survives and the outflow is powered by mildly relativistic stratified ejecta (like those favored by [237]) successfully reproduce these observations.[3] Here we offer an alternative interpretation. We employ simulations of the explosive outflows launched in NS ejecta clouds to show that a powerful relativistic core of material can survive the interaction with the BNS ejecta, producing a successful relativistic structured jet (Sec. 6.3.3). In this case, the *observed* emission is also effectively powered by mildly relativistic ejecta if the ultra-relativistic core is directed away from our line of sight. In this paper we showed one particular model (part of a family of successful models) that fits current observations. A detailed description of the jet simulations using the moving mesh relativistic hydrodynamics code JET [292] and light curves is presented in [294].

A key distinction between the two sets of models is that in the former scenario GW170817 would be intrinsically different from classical SGRBs and the first of a new class of transients. In the latter scenario GW170817 can be instead reconciled with an ordinary SGRB viewed from the side (in SGRBs we are not sensitive to the presence of lateral structure in the jet as the emission is always dominated by the brighter relativistic core). Distinguishing between these models is of paramount importance, as it has direct implications on the intrinsic nature of GW170817 and the potential existence of a new class of quasi-spherical transients powered by NS mergers. However, we show here that at the present time the two sets of models predict very similar flux temporal evolution and spectrum. Observations at $t \geq 300$ days, able to track the evolution of ν_c (which evolves much faster $\propto t^{-2}$ in spherical models,

---

[3]We note that to reproduce the flattening of the emission within these models it is necessary to introduce a cut into the velocity distribution of the ejecta at some minimum $\Gamma\beta$ value.
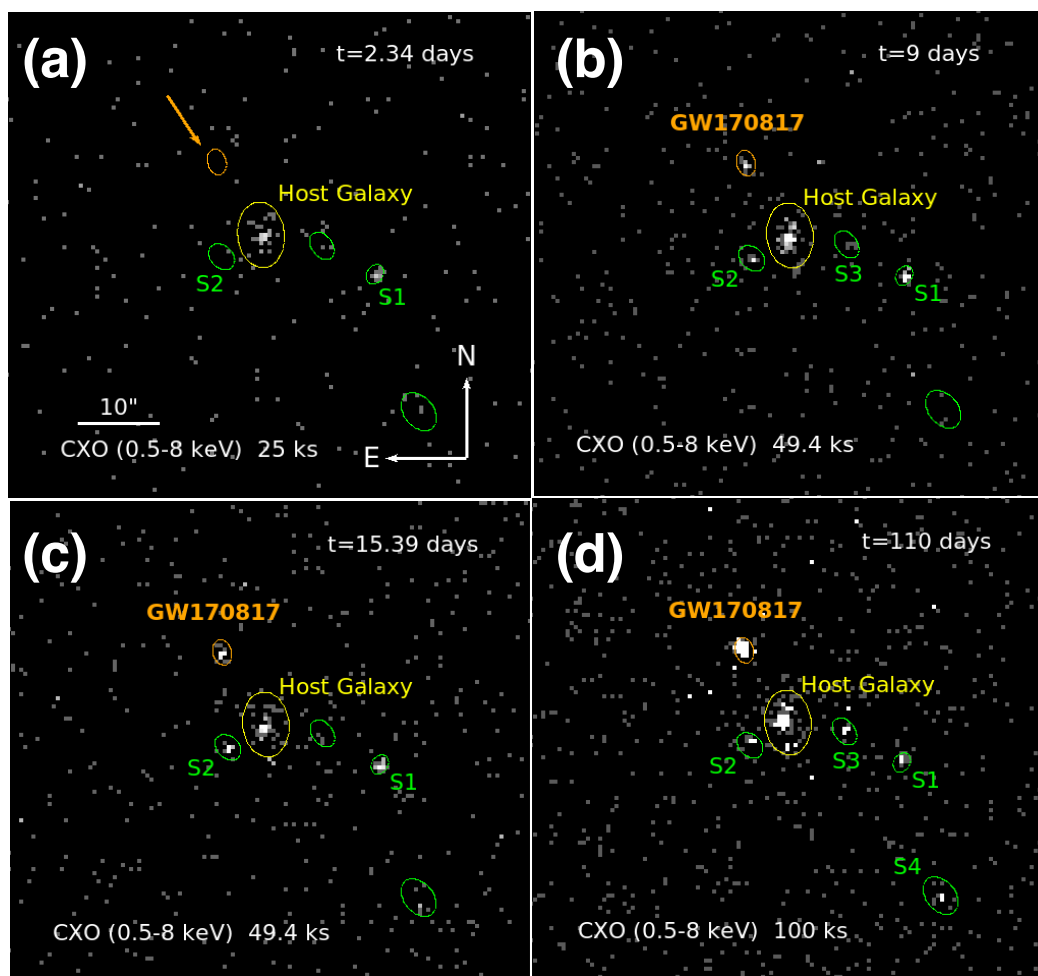
Fig. 6.8. Evolution of the X-ray emission from GW170817 as seen by the CXO.

e.g. [237]) and to constrain the presence of temporal breaks in the flux evolution are the most promising to discriminate between the two scenarios.

We conclude that current observations do *not* distinguish the nature of the relativistic ejecta and cannot be used to rule out the presence of an off-axis originally ultra-relativistic core of collimated ejecta in the outflow of GW170817. The existence of a new class of BNS merger transients is not required by current observations and GW170817 is consistent with being a classical SGRB viewed off-axis.

7. EM COUNTERPARTS OF STRUCTURED JETS FROM 3D GRMHD SIMULATIONS

GW170817/GRB170817A has offered unprecedented insight into binary neutron star post-merger systems. Its Prompt and afterglow emission imply the presence of a tightly collimated relativistic jet with a smooth transverse structure. However, it remains unclear whether and how the central engine can produce such structured jets. Here, we utilize 3D GRMHD simulations starting with a black hole surrounded by a magnetized torus with properties typically expected of a post-merger system. We follow the jet, as it is self-consistently launched, from the scale of the compact object out to more than 3 orders of magnitude in distance. We find that this naturally results in a structured jet, which is collimated by the disk wind into a half-opening angle of roughly 10°, its emission can explain features of both the prompt and afterglow emission of GRB170817A for a 30° observing angle. Our work is the first to compute the afterglow, in the context of a binary merger, from a relativistic magnetized jet self-consistently generated by an accreting black hole, with the jet's transverse structure determined by the accretion physics and not prescribed at any point.

7.1   Introduction

The conjoint detection of the first binary neutron star (NS) merger, GW170817, in both gravitational and electromagnetic waves heralds a new era in multi-messenger astronomy [303, 304]. One of the electromagnetic (EM) counterparts associated with this event was a burst of gamma rays detected about 1.7 seconds after the merger and

lasted for ~ 0.6 seconds (GRB 170817A) (e.g., [305, 306]). This detection provides the most conclusive evidence yet that binary NS mergers are indeed a progenitor of short gamma-ray bursts (GRBs) as hypothesized a few decades ago [174, 307–309]. However, this short GRB and its associated afterglow emission exhibit some peculiar characteristics that are unlike any other burst. For example, it was a faint short GRB despite being, by far, the closest detected to date, and its afterglow showed a shallow rise for several months as opposed to typical afterglows that show a decline from the beginning (e.g., [236, 310, 311]).

In standard GRB theory, the EM emission is produced by a highly relativistic jet launched by a compact object, either a NS or a black hole (BH). In the case of short GRBs, this jet is believed to be produced by the remnant of a binary NS or NS-BH merger (for a review see e.g., [172, 175, 312]). The brief flash of high energy X-rays and gamma rays typically lasting less than 2 seconds (the 'prompt' emission associated with the sGRB) is attributed to an internal mechanism within the jet that is not yet well understood. As the jet propagates through the external, interstellar medium (ISM), it drives a shock that sweeps up and accelerates external particles which in turn radiate predominantly via synchrotron emission (the GRB 'afterglow') that can last up to several months. The most widely used jet model when calculating the emission from a GRB jet is a 'top-hat' jet, where the jet is a conical outflow and the properties of the jet within this cone (e.g., Lorentz factor and energy) are assumed to be constant. Beyond this cone, the jetted outflow ceases abruptly. In the past, the top-hat jet has been able to reproduce the observed characteristics of GRBs, but it fails to explain both the prompt and afterglow emission of GW170817 (e.g., [313]). The key difference is that due to the gravitational wave trigger and impressive follow-up effort of GW170817, it might be the only known GRB viewed at an angle larger than the jet's core (i.e. "off-axis"), for which the prompt and afterglow emission has been detected. The emission received by off-axis observers can vary greatly depending on how the jet's power and Lorentz factor vary as a function of polar angle. Previous studies have suggested that a more realistic model is that

of a structured jet, where the Lorentz factor and energy flux vary smoothly within the jet as a function of polar angle (e.g., [29, 189, 285, 314]). Recent works have used structured jet models to investigate the characteristics and feasibility of detecting the prompt and afterglow emission from such jets as possible EM counterparts to GW events [?, 187, 323]. Now, a year after the detection of GW170817, the structured jet model has been able to successfully reproduce the observed afterglow and can explain some of the peculiar characteristics related to the prompt emission of the short GRB, leading to the interpretation that GRB 170817A may have been a regular short GRB but viewed off-axis (e.g., [242, 294, 315–321]). The detection of superluminal motion in the outflow also provides strong observational evidence for the structured jet model [322].

How the jet distributes its power as a function of the polar angle and distance from the central engine remains an open question. Most numerical studies initiate jet simulations in post merger systems by injecting the jet at a length-scale of a few orders of magnitude larger than that of the central engine. In particular, top-hat jets are injected into an ambient gas to follow its hydrodynamic interactions as it breaks away from the confining medium. Sufficiently far from the break out scale, the jet turns conical and its structure can be determined. A more realistic investigation into jet structures must begin at the central engine, taking into account the initial conditions of the compact object and its surroundings. It must include a consistent jet launching mechanism from the compact object and follow the jet as it collimates and accelerates out to large distances. In this work, we use 3D general relativistic magnetohydrodynamic (GRMHD) simulations to study the jet structure with many of the factors above taken into account. We start with a black hole torus system with properties typically expected from a binary NS post-merger system, and follow the MHD-driven jet, launched self consistently via the accretion and rotation of the compact object, as it is initially collimated by the surrounding disk winds, up to a point where these interactions with the disk winds become insignificant, after which the structure of the jet is extracted. Building upon our previous work [323], we

calculate the emission profiles (prompt and afterglow) produced by the structured jet from these improved simulations.

In Section 7.2 we describe the simulation setup. In Section 10.4 we present the simulation results, which include the jet structure, its emission profile and comparison with the latest observations of GRB 170817A. We discuss these results and conclude in Section 7.4.

7.2 Numerical setup

A detailed description of the simulation setup can be found in [324] (their model B3d[1]) and will be summarized here. Simulations are carried out using HARMPI[2], an enhanced version of the serial open-source code HARM [325, 326] with modifications that consider additional physical processes such as neutrino cooling and nuclear recombination. The initial setup consists of 3 solar mass ($M_\odot$) BH with spin 0.8, surrounded by a torus of ~ 0.03 $M_\odot$ embedded with a poloidal magnetic field prescribed by the vector potential $A_\phi \propto r^5 \rho^2$ and having a maximum field strength of 4×10^{14} G, where r is the radius in spherical coordinates and ρ is density. Although the initial magnetic field may likely be dominated by toroidal components, numerical studies of NS mergers do find the development of a strong poloidal field, of similar magnitude as used here, in the post-merger system ([202]). The top panel of Fig. 7.2 shows a contour plot of the density and magnetic field of the initial setup. Regions outside the BH and torus are set to the floor density, which initially drops off with radius as $\propto r^{-2}$, therefore density contributions from the post-merger and dynamical ejecta are not considered in this setup (e.g., [191, 327]). Following the onset of accretion, a jet is launched $\sim 10^{-2}$ ms after the start of the simulation and $\sim 90\%$ of the jet (in energy) is ejected within the first ~ 1.5 seconds, which is consistent with the duration of the prompt phase of GRB170817A . The bottom panel of Fig. 7.2 shows

---

[1]These simulations were run before GW170817 was detected, thus it does not use the properties inferred from observations of this event.

[2]Available at https://github.com/atchekho/harmpi

a contour plot of the density and magnetic field at ~ 50 ms. The polar, under-dense region consists of the jet which is surrounded by the denser disk winds that initially collimate the jet. By the time the jet reaches a length-scale of ~ 1000 r_g ($r_g = GM/c^2$ is the gravitational radius of a BH with mass M), it propagates out of the confining winds and becomes conical, travelling radially outwards. The simulation is able to accurately track the jet starting from its launching region near the compact object, up to a distance of a few ~ 1000 r_g.

7.3 Results

7.3.1 Jet structure from simulations

In order to calculate the observed emission from the jet we first need to extract its structure from the simulations. The required quantities are the Lorentz factor and energy per solid angle of the jet as a function of the polar angle θ, the energy here includes the electromagnetic, thermal and kinetic energy (without rest mass). Current 3D GRMHD simulations are unable to follow the jet to the scales where the prompt emission and afterglow emission take place (beyond $\sim 10^6$ r_g). We are therefore only able to extract the quantities up to the distance where the simulations are still accurate (~ 2000 r_g), and this structure is plotted in Fig. 7.2. The dashed line in Fig. 7.2 shows the normalized energy per solid angle $(dE/d\Omega)$ of the jet versus polar angle θ, obtained by summing the energy flux over time at a fixed radius of ~ 2000 r_g and averaging over azimuthal angle ϕ. The jet is dominated by electromagnetic and kinetic energy with a small thermal component. This distribution roughly follows a power law decline $\propto \theta^{-3.5}$ between $\sim 5 - 15°$, the total energy of one jet is $\sim 10^{51}$ erg. The next quantity we require is the Lorentz factor distribution of the jet, however the jet may not have undergone complete acceleration at the distances mentioned above. Therefore we find the ratio of the total energy flux to mass flux (μ), which determines the maximum achievable Lorentz factor in MHD jets, and use μ as an estimate for the terminal Lorentz factor of the jet. We calculate the energy-flux–weighted μ averaged
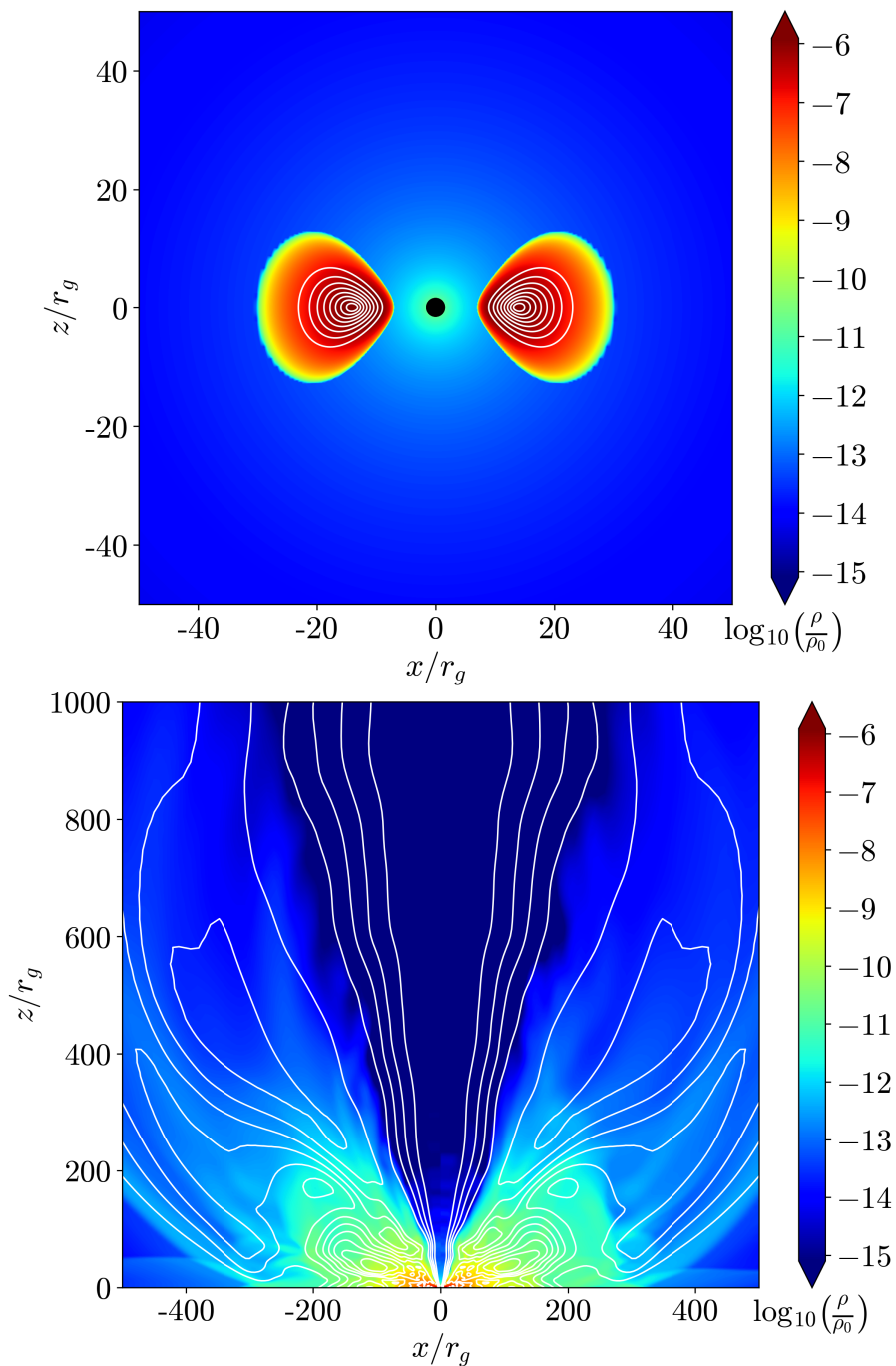
Fig. 7.1. 2D plots (vertical slice) of density and magnetic field line contours of the initial setup (top) and at ~ 0.05 seconds (bottom), axes are in units of r_g (the gravitational radius) and $\rho_0 \approx 7 \times 10^{16}$ g cm^{-3}. The compact object is at the origin, and the bottom panel shows only one of the two jets. The jet is initially collimated by the disk winds and eventually breaks out at $z \sim 1000$ r_g, after which it propagates conically.
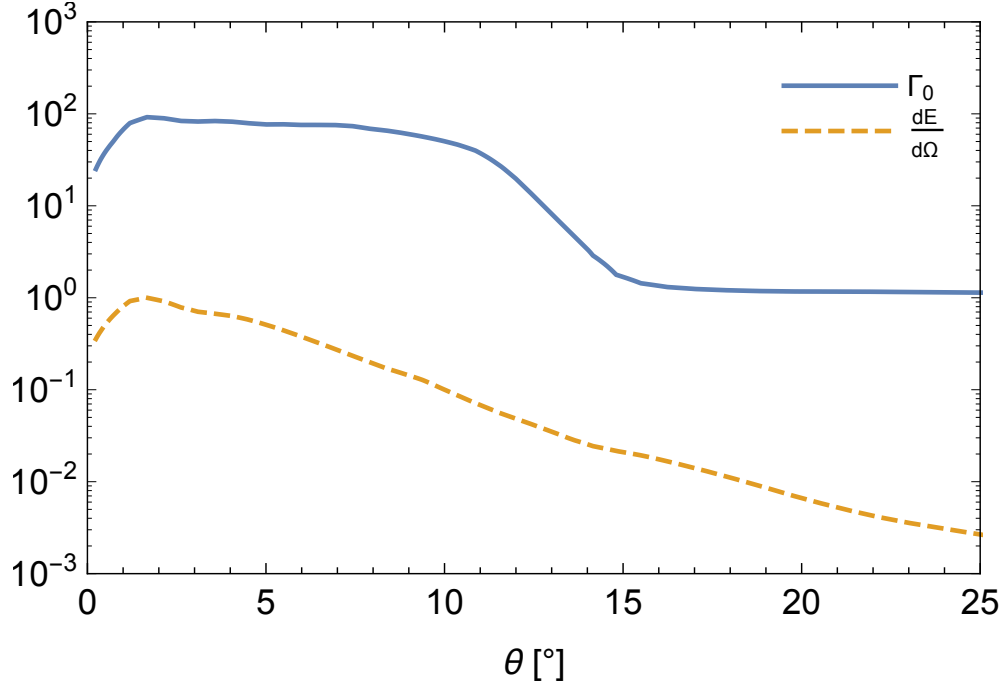
Fig. 7.2. Jet structure self-consistently obtained from our post-merger remnant disk simulations showing the Lorentz factor of the jet Γ_0 (solid line, calculated as energy-flux-weighted ratio of energy flux to mass flux averaged over time, see Sec.7.3.1) and normalized jet energy per solid angle (dashed line). Both quantities have been averaged over azimuthal angle ϕ at a fixed radius of $\sim 2000 \ r_{\mathrm{g}}$.

over time and ϕ at a fixed radius of $\sim 2000 \ r_{\mathrm{g}}$, as a reliable estimate for the terminal Lorentz factor (Γ_0) of the jet as follows

$$\Gamma_0 = \frac{\int \mu \, \mathrm{T}_t^r \, d\phi \, dt}{\int \mathrm{T}_t^r \, d\phi \, dt}, \tag{7.1}$$

where T_t^r is the component of the electromagnetic stress-energy tensor containing the radial energy flux (electromagnetic, thermal and kinetic energy with the rest mass energy subtracted). The solid line in Fig. 7.2 shows the jet Lorentz factor as a function of θ: it remains roughly constant at the value of ~ 100 up to $\sim 10°$ and then declines rapidly as a power law $\propto \theta^{-11}$ to ~ 1 at $15°$. In the next subsections, we will use the jet structure in Fig. 7.2 to calculate the observed emission in both the prompt and afterglow phases.

7.3.2 Prompt emission profile

Using the jet structure in section 7.3.1 we can calculate a luminosity profile for the prompt emission: the total prompt luminosity an observer can expect to receive versus observing angle. Following the calculations done in [323], we estimate the prompt emission luminosity as a function of the observing angle, θ_{obs}, which is the angle between the jet axis and the line of sight towards the observer. We assume a fixed fraction of the energy is radiated instantaneously and isotropically in the co-moving frame of the jet, and transform it to the observer frame (addressing dissipation mechanisms for the prompt emission is beyond the scope of this work). Fig. 7.3 compares the prompt emission profile of observed luminosity L_{obs} (normalized to the peak luminosity L_{peak}) versus observing angle θ_{obs} for our simulated structured jet and a top-hat jet. We adopt a structured jet profile from the simulation, using the energy and Lorentz factor distributions in Fig. 7.2, and only take into account material with Lorentz factor $\gtrsim 3$ (corresponding to $\theta \lesssim 13°$) as implied by observations and constrained by the fact that slower components might initially be too optically thick to contribute to the prompt phase of GRB 170817A [311, 328]. The top-hat jet has half opening angle $13°$ and a constant initial Lorentz factor of 100 which roughly correspond to the extent and maximum Lorentz factor of our structured jet, respectively. The total energy of the top-hat jet is set to be equal to that of the structured jet, thus enabling a fairer comparison. If the count rate of a typical sGRB is scaled to within the LIGO detectability distance (~ 200 Mpc at design sensitivity; [173]), it would be an extremely bright source of $\sim 10^6$ counts/s (e.g., [199]), and since these typical short GRBs are viewed on axis, we can translate the normalized L_{obs} profile in Fig. 7.3 to a count rate by scaling the peak of this profile to 10^6. The required count rate for a robust detection of short GRB that is coincident with a LIGO trigger is estimated to be $\sim 10^3$ counts/s [200], which correspond to $L_{\mathrm{obs}}/L_{\mathrm{peak}} \sim 10^{-3}$. This limit is indicated by the horizontal dashed line in Fig. 7.3,
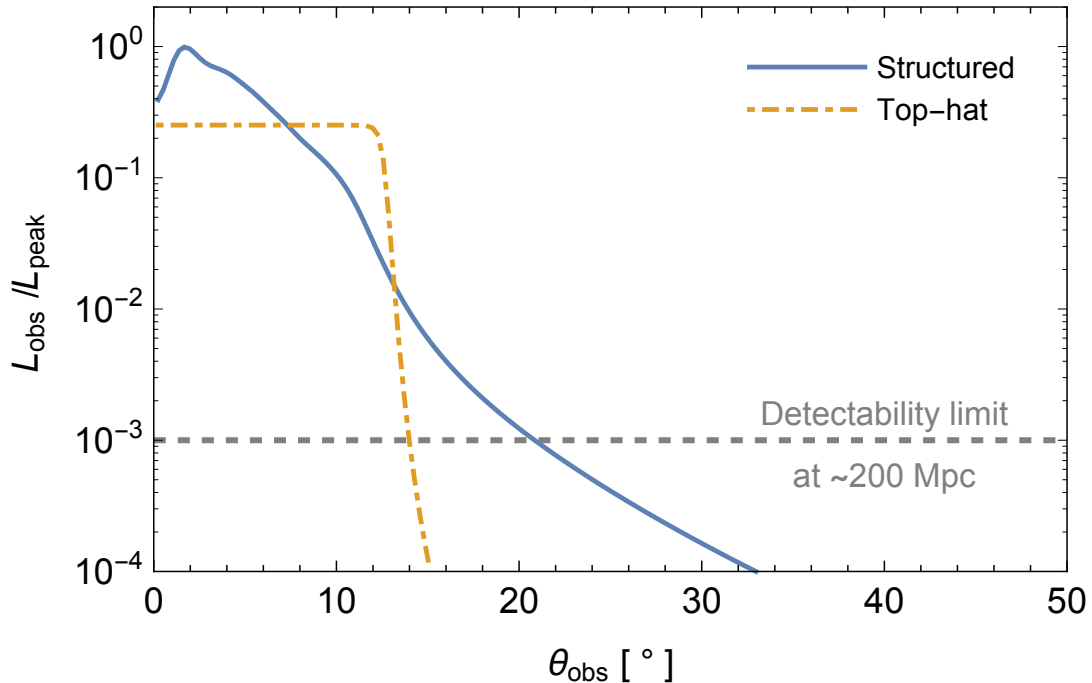
Fig. 7.3. Normalized observed luminosity versus observing angle (θ_{obs}) for the prompt emission of structured (solid line) and top-hat (dashed line) jets. Structure of the jet is obtained from simulations (Fig. 7.2). The top-hat jet has half opening angle 13° (the same angular extent taken for our structured jet – see Sec. 7.3.2) and initial Lorentz factor 100 (equal to the Lorentz factor of the core of our structured jet). Horizontal dashed line indicates an estimate for a robust detection limit of a sGRB with an accompanying GW trigger by LIGO taking place at $\sim$ 200 Mpc. The emission from the structured jet is detectable up to an observing angle of $\sim 20°$ whereas the emission from top-hat jet falls much more steeply and is detectable up to $\sim 14°$. For closer events like GW170817, this detectability limit can be ~ 10 times less (at $L_{obs}/L_{peak} \sim 10^{-4}$), allowing detection up to a viewing angle of $\sim 30°$ in the case of a structured jet.

and it gives us a robust detectability limit for a short GRB with an associated GW trigger from LIGO.

7.3.3 Afterglow emission

The afterglow is calculated using the standard synchrotron emission techniques from forward shocks in an external medium of uniform density (e.g., [17]). Jet spreading is taken into account following [329], who utilize simulations to derive analytic expressions for the dynamics of a spreading jet. Although these expression were derived for a top-hat jet, they are still applicable to the core of our structured jet ($\lesssim 5°$), where the energy and Lorentz factor do not change by more than a factor ~ 2. In order to calculate the afterglow we first need the initial structure of the blast wave, which is obtained from the Lorentz factor and energy profile of our simulated jet in Fig. 7.2. The synchrotron emission is obtained semi-analytically by dividing up the blast wave into 10^4 patches (100 uniform segments along the θ and ϕ directions), calculating the synchrotron emission associated with the forward shock of each patch, and then summing the emission from all patches to obtain the total afterglow emission. We assume each patch coasts at its initial Lorentz factor (Γ_0, shown in Fig. 7.2) until the energy in the swept up, shocked medium is comparable to the initial energy of the patch, after which each patch decelerates as $\Gamma\beta \propto E^{1/2}R^{-3/2}$, where E, R are the kinetic energy and spherical radius of the blast wave respectively and $\beta = \beta(\theta)$, $\Gamma = \Gamma(\theta)$ are the 3-velocity and Lorentz factor of the blast wave respectively during the deceleration phase. The dependence of $\Gamma\beta$ on R will steepen when the jet begins to spread and its observable implications will be discussed in Sec. 7.4. We assume the synchrotron emission from each patch is radiated isotropically in the rest frame of the emitting region, and then transform this to the observer frame. The total afterglow emission is obtained by summing over all patches, covering the entire solid angle of the jet, and taking into account differences in the photon arrival time, $T_{\rm obs} = \int \frac{dR}{\beta c}(1 - \beta \cos\alpha)$, where $T_{\rm obs}$ is the time in the observer frame, α is the angle between velocity vector of a patch of the jet and its line of sight towards the observer, β is the velocity of the patch of the jet and c is the speed of light.

Figure 7.4 shows afterglow light curves from our simulated structured jet and observed data points of GRB170817A afterglow for comparison. We neglect the counter-jet because its afterglow will be too faint to be detected. The parameters used to calculate the light curves in Fig. 7.4 are $E_{\mathrm{j}} = 5 \times 10^{50}$ erg, $n \approx 0.05$ cm^{-3}, $\epsilon_{\mathrm{e}} \approx 0.01$, $\epsilon_{\mathrm{B}} = 10^{-4}$, $p = 2.17$, $\theta_{\mathrm{obs}} = 30°$, where E_{j} is the true energy of the jet (without rest mass energy), $\epsilon_{\mathrm{e}}, \epsilon_{\mathrm{B}}$ are the fractions of the total energy in the shocked electrons and magnetic fields respectively, n is the number density of the uniform external medium and p is the power law slope of the distribution of shocked electrons. In reality, the value of E_{j} depends on the radiative efficiency of the prompt emission. From observations, this efficiency varies between a few percent to more than 90% ([199]), therefore we will assume a median value of 50% efficiency, which means $E_{\mathrm{j}} \approx 5 \times 10^{50}$ erg (half the value of the jet energy obtained from our simulations). The shallow rise in the afterglow (between $\sim 20 - 200$ days) occurs as the entirety of the jet becomes visible to off-axis observers. In our modelling, the slope of this rise (in a uniformly dense external medium) depends only upon the jet structure and observing angle. Since the jet structure is fixed from our simulations, we vary the observing angle and find that $\theta_{\mathrm{obs}} \approx 30°$ produces a rise that matches the observations. The value of p is inferred from observations ([319]) and rest of the parameters are adjusted to match the peak time and flux. These parameters are largely consistent with other works which model the afterglow (e.g., [318,321]). Admittedly, the prompt radiative efficiency (and therefore E_{j}) can vary by a factor ~ 2, which would require a change in the external density and microphysical parameters by a similar factor. However, these changes will not affect the slope of the rise in the afterglow. We find that the observed frequency lies between the minimum and the cooling frequencies, in agreement with observations ([319]).
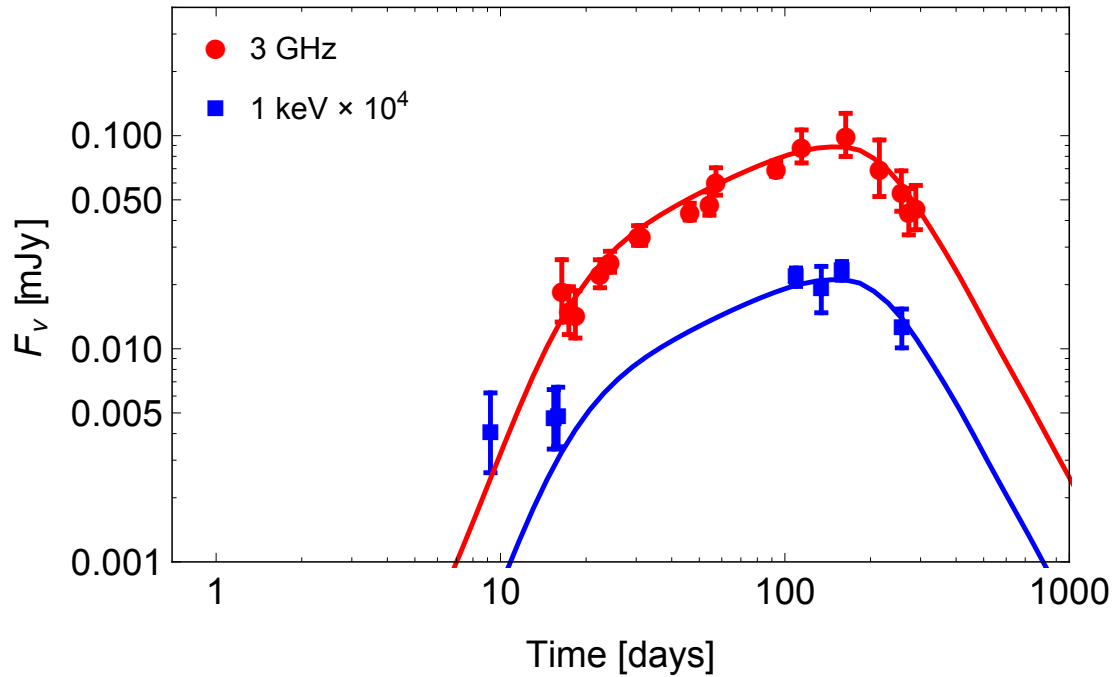
Fig. 7.4. Afterglow light curves for our simulated structured jet (from Fig. 7.2) and observed data for comparison in radio (3 GHz, red points) and X-ray (1 keV, blue squares) (from [315, 319]). Relevant parameters used are $E_j \approx 5 \times 10^{50}$ erg, $n \approx 0.05$ cm^{-3}, $\epsilon_e \approx 0.01$, $\epsilon_B = 10^{-4}$, $p = 2.17$, $\theta_{obs} = 30°$.

7.4   Discussion and Conclusions

Determining how the power and Lorentz factor of a jet are distributed as a function of angle is a multi-scale endeavor. The simulations and analysis carried out in this work start at the central engine, where a jet is self consistently launched, and follows the jet out to larger distances as it collimates, accelerates and interacts with surrounding disk winds. The result is a more realistic description of the transverse jet structure that naturally produces an emission profile consistent with both the prompt and afterglow EM counterparts of GW170817. One aspect not considered here is interactions with the post-merger and dynamical ejecta that can take place at larger scales: in some extreme cases, this may even choke the jet and prevent it from breaking out (e.g., [330]). However, it is likely that jet interactions with the ejecta will result in more energetic outflows at wider angles (e.g., [193, 195, 212, 331, 332]), that can potentially brighten the emission for off-axis observers at earlier times. This could be a reason why the first X-ray point at ~ 10 days in Fig. 7.4 is brighter than the afterglow model of our structured jet.

As seen in Fig. 7.2, the transverse jet structure in Lorentz factor remains approximately constant over most of the jet core before sharply declining at larger angles. In contrast, the energy per solid angle shows a much shallower decline for the majority of the jet's transverse extent. However, $\sim 90\%$ of the jet's energy is concentrated within a polar angle of $10°$, indicating a narrow, energetic jet core in agreement with afterglow fits and the observations (e.g., [321, 322]). The prompt and afterglow emission calculated using this structure obtained from our simulations match the observed data of GRB170817A well. The prompt emission profile in Fig. 7.3 shows that for an event within the LIGO detectability volume, the count rate due to the prompt emission at an observing angle of $\sim 25°$ is the order of $\sim 10^2 - 10^3$ counts/s (Sec. 7.3.2). These values match the data obtained and inferred from GRB170817A (e.g., [304, 333]). In comparison, producing a similar result for the prompt emission with a top-hat jet would require $\theta_j \gtrsim 20°$ (which is also the case for the afterglow; [318]), this is not sup-

ported by observations of GRB170817A. As mentioned previously (e.g., [190, 323]), the prompt emission profile for a structured jet has a much shallower drop off for larger observing angles compared to the emission profile of a uniform top-hat jet. Tied with a coincident LIGO trigger, this enables the detection of the prompt emission for substantially misaligned observers, making this signal a more feasible EM counterpart than previously thought. Indeed, Fig. 7.3 indicates the prompt emission would be detectable, with the aid of a coincident LIGO trigger, up to an observing angle of $\sim 20°$ off-axis for a source at the edge of the LIGO detectability volume ($\sim$ 200 Mpc), and up to $\sim 30°$ for events like GW170817 that are much closer. Let us assume the prompt emission of all short GRBs, from GW events detected by LIGO, are detectable up to a viewing angle of $20°$. Then by integrating the detection probability of GW events ([334]) from an inclination angle of $0°$ to $20°$, we find that a fraction of ~ 0.2 GW events (out of all that produce short GRBs) will have a detectable prompt emission. However this fraction could change appreciably for different jet structures (e.g., [335]).

The afterglow light curves from our structured jet reproduce the observed rise, peak and decline of GRB170817A. The core of the jet begins to spread after it decelerates, which will steepen the decline in the afterglow light curve after the peak (for off-axis observers). The slope of the decline in our afterglow is ≈ -2.4, in agreement with afterglow models where jet spreading is taken into account (e.g., [321]). From the afterglow modelling of our structured jet, we find that the temporal dependence of the observed rise strongly constrains the viewing angle to be close to $30°$, since larger (smaller) viewing angles will produce a steeper (shallower) rise in the afterglow.

8. OBSERVABLE FEATURES OF GW170817 KILONOVA AFTERGLOW

The neutron star merger, GW170817, was followed by an optical-infrared transient (a kilonova) which indicated that a substantial ejection of mass at trans-relativistic velocities occurred during the merger. Modeling of the kilonova is able to constrain the kinetic energy of the ejecta and its characteristic velocity but, not the high-velocity distribution of the ejecta. Yet, this distribution contains crucial information on the merger dynamics. In this work, we assume a power-law distribution of the form $E(> \beta\Gamma) \propto (\beta\Gamma)^{-\alpha}$ for the energy of the kilonova ejecta and calculate the non-thermal signatures produced by the interaction of the ejecta with the ambient gas. We find that ejecta with minimum velocity $\beta_0 \simeq 0.3$ and energy $E \sim 10^{51}$ erg, as inferred from kilonova modeling, has a detectable radio, and possibly X-ray, afterglow for a broad range of parameter space. This afterglow component is expected to dominate the observed emission on a timescale of a few years post merger and peak around a decade later. Its light curve can be used to determine properties of the kilonova ejecta and in particular the ejecta velocity distribution α, the minimum velocity β_0 and its total kinetic energy E. We also predict that an afterglow rebrightening, that is associated with the kilonova component, will be accompanied by a shift of the centroid of the radio source towards the initial position of the explosion.

8.1 Introduction

The gravitational wave source GW170817 marks the first merger of neutron stars ever detected ([336]). A variety of electromagnetic (EM) counterparts were detected following the GW170817 trigger ([337]). These counterparts are powered by ejecta and outflows produced from the merger which range from relativistic to non-relativistic velocities. The relativistic outflows are associated with collimated jets, that produce the EM transient known as a gamma-ray burst (GRB). The trans-relativistic and non-relativistic ejecta consists of material that has become unbound during the merger and outflows released by the remnant material following the merger (e.g., disc winds), which powers the transient known as a kilonova (KN; [181, 182, 338, 339]).

Both a GRB and KN were detected in GW170817, which, for the first time, directly pointed their origin to NS mergers (e.g., [305, 306, 340–345]). The KN consisted of thermal optical/infrared emission which peaked a few days after the detection of GW170817 and is in general agreement with expectations from KN models ([182, 346–348]). The KN is believed to be produced by the radioactive decay of the heaviest elements synthesized in this ejecta. Modeling the multi-wavelength light curves of the KN, one can infer a characteristic ejecta velocity of $\sim 0.1c - 0.3c$ and kinetic energy of $E \sim 10^{51}$ erg (e.g., [349–351]). However, it is not clear how this energy is distributed within the ejecta, which could contain important information on the merger dynamics (e.g., [352]).

The outflows from a NS merger drive an external shock as they propagate through the surrounding medium, this shock accelerates the particles in the external medium causing them to radiate primarily by synchrotron emission. This non-thermal emission associated with the shock is called the afterglow, we will refer to the afterglow associated with the jet as the "GRB afterglow" and the afterglow associated with the KN ejecta as the "KN afterglow" in this manuscript.

The GRB including its long term X-ray to radio afterglow that has been detected from GW170817 so far can be explained as originating from a structured jet with a narrow core (with an opening angle of $\sim 2° - 6°$) which is misaligned by $\sim 20° - 30°$ with respect to our line of site (e.g., [31, 187, 241, 242, 294, 315, 318, 319, 323, 353–355]). Observation of the rather steep decline of this afterglow after its peak indicates the entire jet has come into view. The jet's true energy can, therefore, be constrained by the afterglow modeling and is inferred to be $\sim 10^{50}$ erg (e.g., [356]), not unlike that of other short-duration GRBs [199].

In addition to the GRB afterglow, the KN will have its own afterglow. However, the KN ejecta is slower compared to the jet (but has comparable, if not more, energy), which will lead to the KN afterglow peaking at much later times compared to the GRB afterglow ([352, 357–360]). The KN afterglow contains important information on how the energy is distributed within the KN ejecta and its light curve will be sensitive to any velocity stratification within this ejecta. The KN afterglow is the focus of this paper, we will investigate how the KN afterglow differs for a fairly general energy distribution and develop an analytic framework which can be utilized to constrain properties of the KN ejecta using detections (or even non-detections) of the KN afterglow, with an application to GW170817 as an example.

The structure of the paper is the following. Sec. 8.2 describes our modeling of the KN ejecta, its interaction with the ambient gas, as well as the resulting synchrotron emission from these interactions. In Sec. 8.3, we apply the KN afterglow model to GW170817, making specific predictions on when this afterglow component could be observed and which ejecta properties can be probed by observations. Sec. 8.4 summarizes our conclusions.

8.2 The KN blast wave and its afterglow

During the neutron star merger, a modest fraction of a solar mass is expected to be ejected. The total mass ejected and the angular and velocity distribution of

the ejecta depend on the total mass of the progenitor system, the mass ratio of the neutron stars, and the nuclear equation of state (see, e.g., [361] for a review). In Sec. 2.1, we present a quite general parametrization of the ejecta velocity distribution and proceed to calculate the velocity profile of the shock driven by the ejecta into the ambient gas. Sec. 2.2 focuses on the synchrotron emission from electrons accelerated at this shock.

8.2.1   Properties of the kilonova ejecta and Dynamics of the blast wave

About half a day after the GW170827 trigger, an optical counterpart, AT2017gfo, was discovered ([362–365]). The observed emission started out blue in color, before rapidly evolving over the following days. Broad spectra at day $\sim$2.5 post trigger indicate the presence of distinct optical and near infrared emission components. Subsequently, the blue component fainted rapidly and the overall spectrum softened, peaking in the near-infrared. The widely accepted interpretation for this emission is the KN model ([337, 349, 350, 366–370]). The red KN is likely to be associated with slower ejecta ($\beta \sim 0.1$), while the blue KN can be powered by faster ($\beta \sim 0.3$) ejecta. The former component may have become unbound due to tidal interactions and is predominantly distributed along the equatorial plane while the latter is possibly associated with remnant disk outflows and shock ejected material primarily distributed away from the equatorial plane ([184, 191, 324, 346, 371–375]; see, however, [376, 377] for a different interpretation).

Independent of the details and assumptions involved in the light-curve modeling, the post-merger ejecta appear to be fairly massive with total mass $\gtrsim 0.05 M_\odot$ and velocity $\sim 0.1 - 0.3$ c, corresponding to a kinetic energy in excess of $\sim 10^{51}$ erg. These ejecta masses are broadly consistent with the estimated r-process production rate required to explain the heavy element abundances of the Universe, providing the first direct evidence that binary neutron star mergers can be a dominant site of r-process enrichment ([348, 378–383]).

The modeling of the KN emission is mostly sensitive to the low-end of the velocity distribution of the ejecta[1], with which the bulk of the ejecta is moving. Modeling of this thermal transient does not give much information about any high-velocity tail of the ejecta. However, simulations studying NS mergers find that ejecta powering the KN are likely to be broadly distributed in energy as a function of $\beta\Gamma$, where Γ is the Lorentz factor of the ejecta (e.g., [324, 352, 360]). Motivated by these findings, we assume a power law distribution of the form $E(> \beta\Gamma) \propto (\beta\Gamma)^{-\alpha}$ for the energy of the KN blast wave, where α typically varies between 3 to 5. The distribution is normalized to the total energy (E) at some minimum velocity (β_0). Guided by observations of GW170817, we can assume $E(> \beta_0\Gamma_0) = E = 10^{51}$ erg and $\beta_0 = 0.3\,(0.1)$ for the fast (slow) component.

The stratified ejecta expands driving a shock into the ambient gas. We assume a uniform external medium and approximate the total energy of the blast wave as $E \propto (\beta\Gamma)^2 R^3$, with R the radius of the blast wave. This expression encapsulates the dynamical evolution of the blast wave during the relativistic ([5]) and non-relativistic ([16]) phases. Given the assumed power law distribution for the ejecta's kinetic energy E, the blast velocity initially evolves with radius as $\beta\Gamma \propto R^{-\frac{3}{\alpha+2}}$, where the blast wave is continuously refreshed by slower, more energetic ejecta governed by the power law index α. This continues until the total energy in the shocked external medium is comparable to that of the ejecta, after which point the total energy of the blast wave remains constant (assuming an adiabatic evolution) and the blast velocity evolves as $\beta\Gamma \propto R^{-\frac{3}{2}}$. The radius at which this transition occurs will be called the "deceleration" radius and is given by $R_{\rm dec} = (3E_{\rm iso}/4\pi\Gamma_0(\Gamma_0 - 1)nm_{\rm p}c^2)^{\frac{1}{3}}$, where m_p is the proton mass, c is the speed of light and $E_{\rm iso}$ is the isotropic equivalent energy of the blast wave. The $R_{\rm dec}$ corresponds to the deceleration radius of the slowest material (which also carries the majority of the energy).

---

[1]However, lanthanide-rich materials moving at slower velocities could also be missed in the optical, near infrared as the emission in those bands starts being dominated by the GRB afterglow.

The isotropic equivalent energy E_{iso} of each component is related to the true energy (E) by $E = f_\Omega E_{\text{iso}} = \frac{1}{2}E_{\text{iso}} \int \sin\theta \text{d}\theta$, with f_Ω the solid angle fraction of the blast wave. Employing spherical coordinates, we assume the ejecta is distributed uniformly in the azimuthal direction from $\phi = 0$ to 2π, and divide the polar extent of the blast wave into two main components. Since the slower, "red" component is likely to be distributed on the equatorial plane, we assume $\theta = 60° - 120°$ for its polar extent. The fast component (associated with the "blue" KN) is assumed to be distributed within $\theta = 15° - 60°$ for one hemisphere and $\theta = 120° - 165°$ for the other hemisphere. Changing the angular extent and viewing angle will not considerably affect our results since bulk of the KN ejecta is not relativistic, making beaming effects modest (see last paragraph of Sec. 8.2.2 for further details).

8.2.2   Modeling the KN afterglow

The KN blast wave drives a shock through the external medium, energizing the swept up particles and causing them to radiate via synchrotron emission. This emission is termed the afterglow. We assume that the electrons are accelerated into a power-law distribution above a minimum Lorentz factor $\gamma > \gamma_{\text{m}}$. The analytic expressions for the radiated flux used or derived below are applicable only if the observing frequency is between the minimum (ν_{m}) and cooling (ν_{c}) frequencies. The plotted light curves, however (which are calculated semi-analytically), include the effects of synchrotron and Compton cooling of the electrons, which can lower the overall emission at higher frequencies (e.g., in X-rays), where the spectrum is in the fast cooling regime ($\nu > \nu_{\text{c}}$). The semi-analytic calculations takes into account mission during the "deep-Newtonian" phase as well. This phase occurs when the minimum Lorentz factor of the electrons $\gamma_{\text{m}} \sim 1$, the transition to this phase will be accompanied by a late time flattening of the light curves ([123]).

The KN afterglow emission peaks at the deceleration radius, and the peak flux density can be expressed as (e.g., [357])

$$F_{\nu,\mathrm{pk}} \approx (115\,\mu\mathrm{Jy})\,\epsilon_{\mathrm{e},-1}^{p-1}\,\epsilon_{\mathrm{B},-3}^{\frac{p+1}{4}}\,n_{-2}^{\frac{p+1}{4}}\,\beta_0^{\frac{5p-7}{2}}\,E_{51}\,\nu_{9.5}^{\frac{1-p}{2}}\,d_{26}^{-2}, \tag{8.1}$$

where the prefactor is determined for $p = 2.2$, but does not change by more than a factor 3 when p is varied from 2.1–2.5. Here ϵ_{e} and ϵ_{B} are the fractions of the total energy in the shocked electrons and magnetic fields of the shocked fluid respectively, n is the number density of the uniform external medium, p is the power law slope of the distribution of shocked electrons, E is the true energy (integrated over velocity) of the KN blast wave, ν is the observing frequency and d is the distance to the source. All quantities are in cgs units and we use the notation $Q_x = Q/10^x$.

The time of peak can be obtained by relating the observer time to the radius of the blast wave (R), and substituting $R = R_{\mathrm{dec}}$ to obtain $t_{\mathrm{dec}} \approx \int_0^{R_{\mathrm{dec}}} \frac{dr}{\beta(r)c}(1-\beta(r))$. Here we assume the observer is within line of sight of the KN blast wave. The minimum velocity (β_0) is expected to be, at most, mildly relativistic, in this we can assume $\beta_0 \lesssim 0.5$, and obtain an analytic approximation for the observed peak time as

$$t_{\mathrm{dec}} = t_{\mathrm{pk}} \approx (3.3\mathrm{yr})\left(\frac{E_{\mathrm{iso},51}}{n_{-2}}\right)^{\frac{1}{3}}\beta_0^{-\frac{2}{3}}\left(\frac{2+\alpha}{\beta_0(5+\alpha)}-1\right). \tag{8.2}$$

As mentioned in Sec. 2.1, α typically varies between $3-5$ and will be closely examined in this work. For comparison, we will also consider an extreme case $\alpha \to \infty$, which corresponds to a single velocity component for the blast wave. For the cases where α is between 3 and 5, one finds that the peak times vary by less than a factor ~ 1.5, hence for these cases, we can fix the value of α (here we will use $\alpha = 4$). Then the peak time can be well approximated by a much simpler form

$$t_{\mathrm{pk}}(3 \lesssim \alpha \lesssim 5) \approx (8.5\mathrm{yr})\left(\frac{E_{\mathrm{iso},51}}{n_{-2}}\right)^{\frac{1}{3}}\beta_{0,-0.5}^{-\frac{13}{6}}. \tag{8.3}$$

When $\alpha \to \infty$ (corresponding to a single velocity component) the peak time can be approximated as

$$t_{\mathrm{pk}}(\alpha \to \infty) \approx (22.5\mathrm{yr})\left(\frac{E_{\mathrm{iso},51}}{n_{-2}}\right)^{\frac{1}{3}}\beta_{0,-0.5}^{-\frac{5}{3}}. \tag{8.4}$$

Before the peak (especially at early times of ~ 1 yr), the blast wave can be mildly relativistic. For these situations the slope of the light curve can be expressed as ([384, 385])

$$s = \frac{3\alpha - 6(p-1)}{8 + \alpha},$$

(8.5)

where for $\alpha \to \infty$, we obtain the expected t^3 rise for associated with a spherical, single velocity component blast wave. Hence, the KN afterglow light curve (before peak) can be expressed as a function of time as

$$F_{\nu,\mathrm{KN}}(t) = F_{\nu,\mathrm{pk}} \left(\frac{t}{t_{\mathrm{p}}} \right)^s.$$

(8.6)

We now have three observables which can be used to constrain the properties of the KN, the peak flux ($F_{\nu,\mathrm{pk}}$), peak time (t_{pk}) and slope (s).

Fig. 8.1 shows afterglow light curves for the fast (associated with the "blue" KN) and slow (associated with the "red" KN) components having $\beta_0 = 0.3$ and 0.1 respectively, in a uniform external density $n = 0.1$ cm^{-3}, for an observing angle $\theta_{\mathrm{obs}} = 30°$ (except for the dot-dashed line). The KN afterglow light curves are produced semi-analytically following the same method as in ([31]). Where analytic expressions for the synchrotron emission in a forward shock (e.g., [17, 386]) are used to find the radiated flux in the co-moving frame of the shock, transforming this flux to the observer frame and summing the flux over the entire blast wave while taking into account differences in photon arrival time. These calculations also take into account cooling of the electrons due to synchrotron and self-synchrotron Compton energy losses (e.g., [69]), and emission during the deep-Newtonian phase ([25]), with modifications to include an energy distribution in the blast wave as described in Sec. 8.2.1. Synchrotron self-absorption is not considered in these calculations, which is justifiable since we have verified that the turn-over frequency always lies below the observed bands. This is because the emitting region at ~ 1 yr after the burst is very extended and thus remains optically thin down to very low frequencies.

The afterglow of the slow component (thin lines in Fig. 8.1) peaks much later (~ 100 yrs) compared to the fast component (~ 10 yrs). Therefore, focusing on the
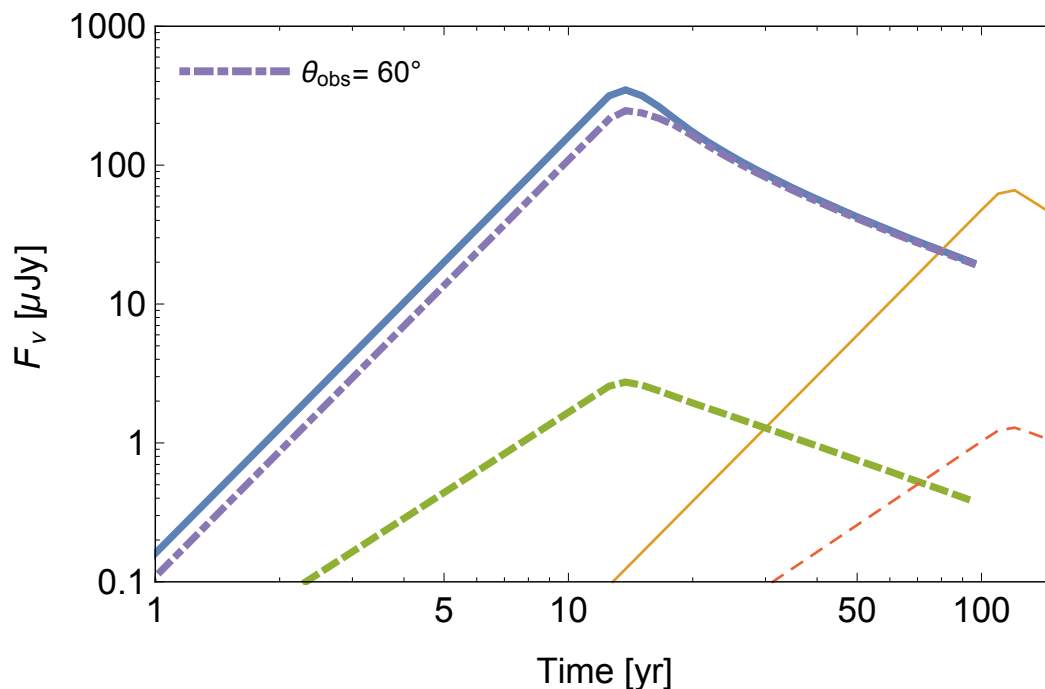
Fig. 8.1. KN afterglow light curves for the fast ($\beta_0 = 0.3$, thick lines) and slow ($\beta_0 = 0.1$, thin lines) components in radio (3GHz, solid lines) and X-ray (1 keV, dashed lines) wavelengths. The magnitude of the X-ray flux density has been multiplied by 10^4. The parameters used are $\alpha \to \infty$, $E = 10^{51}\,\mathrm{erg}$, $\epsilon_\mathrm{e} = 0.1$, $\epsilon_\mathrm{B} = 10^{-3}$, $\theta_\mathrm{obs} = 30°$ (except for the dot-dashed line), $n = 0.1\,\mathrm{cm}^{-3}$. The density is on the higher end compared to typical afterglow models of GW170817 to give a best case scenario for the detectability of the KN afterglow. It is evident that even for this best case, the rise and peak of the slow component occurs much later and is fainter compared to that of the fast component. Therefore, in this work we will only focus on the afterglow of the fast component, which is relevant for the current timescale of GW170817. Dot-dashed line shows radio afterglow of fast component for $\theta_\mathrm{obs} = 60°$ and is almost identical to the $\theta_\mathrm{obs} = 30°$ light curve, demonstrating that viewing angle effects are not significant for the KN afterglow.

current timescales of ~ 1 yr since GW170817, we will restrict our discussion to the afterglow of the fast component throughout this manuscript. The dot-dashed line in Fig. 8.1 shows the radio light curve of the fast component for $\theta_{\mathrm{obs}} = 60°$, with all other parameters kept the same as before. This light curve is almost identical to the $\theta_{\mathrm{obs}} = 30°$ light curve, which demonstrates that the exact angular geometry and its affect on beaming are of minor importance here (as mentioned in Sec 8.2.1).

8.3 Application to GW170817

In this section we apply our KN afterglow model to GW170817 as an example case, with focus on how properties of the ejecta can be constrained using detections (or even a non-detection) of the KN afterglow emission. In Sec 8.3.1, we present general expressions with the prediction of the afterglow flattening/rebrigheting associated with the emergence of the KN afterglow, and summarize what we can learn from this emergence. Sec. 8.3.2 focuses on the much smaller parameter space of the model for which one can fit the observed GRB afterglow with a structured jet model. In this case, our predictions for the expected emission from KN component become much more definite.

8.3.1 Constraining the KN of GW170817

In order to produce example light curves for the KN afterglow, we have to assume some values for the microphysical parameters (ϵ_{e}, ϵ_{B}, particle index (p)), and the external density (n). As a guide for our choice, we use typical parameters inferred from the fitting and observations of GRB170817A afterglow (associated with the jet), as well as typical parameters inferred for other afterglows of short GRBs, which are, $\epsilon_e = 0.1$, $\epsilon_{\mathrm{B}} = 10^{-3}$, $n = 10^{-2} \, \mathrm{cm}^{-3}$, $p = 2.2$ [69, 70, 199, 319, 387–392].

Fig. 8.2 shows KN afterglow of the fast component in radio (3 GHz) and X-ray (1 keV) for different values of α with the "typical" parameters mentioned above. In the same plot we show observed data points for the afterglow of GRB170817A

(data obtained from [315, 319, 393, 394]) along with the theoretical prediction of the afterglow from the structured jet model presented in [31]. The KN afterglow light curves are produced semi-analytically following the same method as detailed in Sec. 8.2.

Equation 8.6 accurately reproduces the radio afterglow shown in the top panel of Fig. 8.2, the slope before peak matches the value obtained from equation 8.5 and the peak times of ~ 15 yr for $\alpha = 3 - 5$ and ~ 30 yr for $\alpha \to \infty$ is consistent with equations 8.3 and 8.4 respectively. However, this equation does not apply to the X-ray afterglow (bottom panel) since at 1 keV, the spectrum is above the cooling frequency for the timescales shown and parameters chosen. The slope of the light curve during the fast cooling phase (the fast cooling analog of equation 8.5) can be derived following a similar method presented in [384, 385] to obtain

$$s_{\nu > \nu_{\rm c}} = \frac{2(\alpha + 2) - 6p}{8 + \alpha}, \tag{8.7}$$

which is in good agreement with the X-ray light curves presented in the bottom panel of Fig. 8.2.

It might be more difficult to detect the KN afterglow in the X-ray band if it is in the fast cooling regime, therefore, we will focus our analysis on the radio emission for the remainder of this work. An X-ray detection of the KN afterglow, for more favorable parameters than our reference case, is however possible.

Fig. 8.2 and equation 8.5 show that observations of the rise in the afterglow can be used to constrain α well before the peak (provided p is known, e.g., from multi-frequency observations). The peak time and flux can be used to constrain quantities such as β_0 and E. However, as we show below, even a non-detection of the KN afterglow can be used to constrain properties of the KN outflow.

We have observed the peak in the afterglow of GRB170817A at ~ 150 days, and the decline post-peak follows a power law in time with slope ~ -2.4 ([315, 394]). Therefore, the decline of the GRB afterglow can be modelled as

$$F_{\rm d}\left(t\right) \approx \left(100\,\mu{\rm Jy}\right) \left(\frac{t}{0.44\,{\rm yr}}\right)^{-2.4}. \tag{8.8}$$
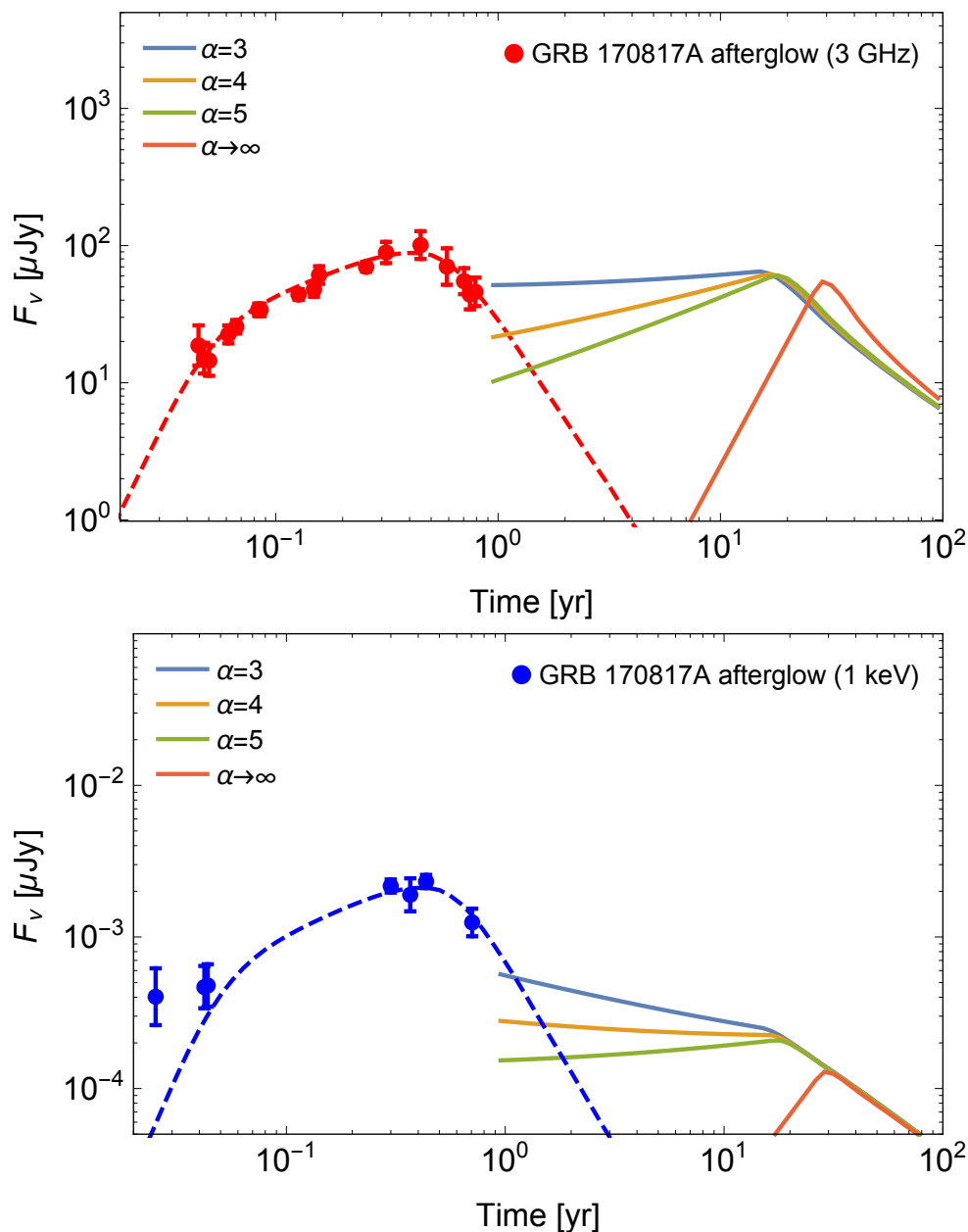
Fig. 8.2. A predicted rebrightening in the GW170817 afterglow. Observed data of GRB170817A afterglow (points) along with the afterglow model from [31] (dashed lines) in radio (top panel) and X-ray (bottom panel). Solid lines show KN afterglow light curves for varying α (see insert labels), which peak at later times resulting in a flattening/rebrightening in the overall afterglow. The X-ray afterglow of the KN is above the cooling frequency for the times considered here. Therefore, detection in the radio is more favourable. Data points obtained from [315, 319, 393, 394].
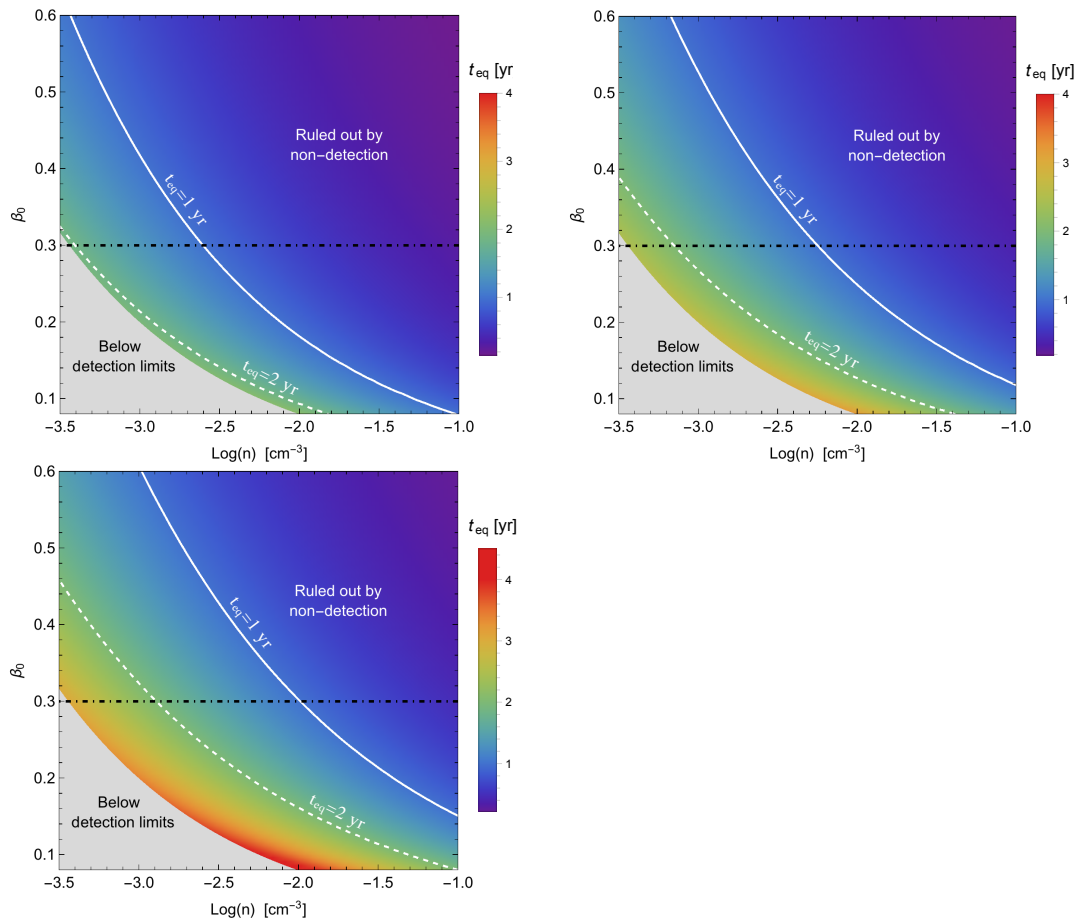
Fig. 8.3. Contour plot of the time of emergence of the KN afterglow $t_{\rm eq}$ (equation 8.10) for minimum speed of the KN blast wave (β_0) vs. external density (n) fixing $\alpha = 3$ (top left), $\alpha = 4$ (top right) and $\alpha = 5$ (bottom left). The solid and dashed lines show the $t_{\rm eq} = 1$ yr and $t_{\rm eq} = 2$ yr contours respectively. The peak of the KN afterglow in the gray, shaded region lies below the detectability limit ($F_{\nu,\rm p} \approx 5\,\mu{\rm Jy}$) in radio and therefore is not detectable. Horizontal, dot-dashed line marks $\beta_0 = 0.3$ which is the typical velocity of the fast component inferred from observations of the blue KN. The emergence of the KN afterglow has not been detected yet implying $t_{\rm eq} \gtrsim 1$ yr, which corresponds to regions below the $t_{\rm eq} = 1$ contour in the above figures.
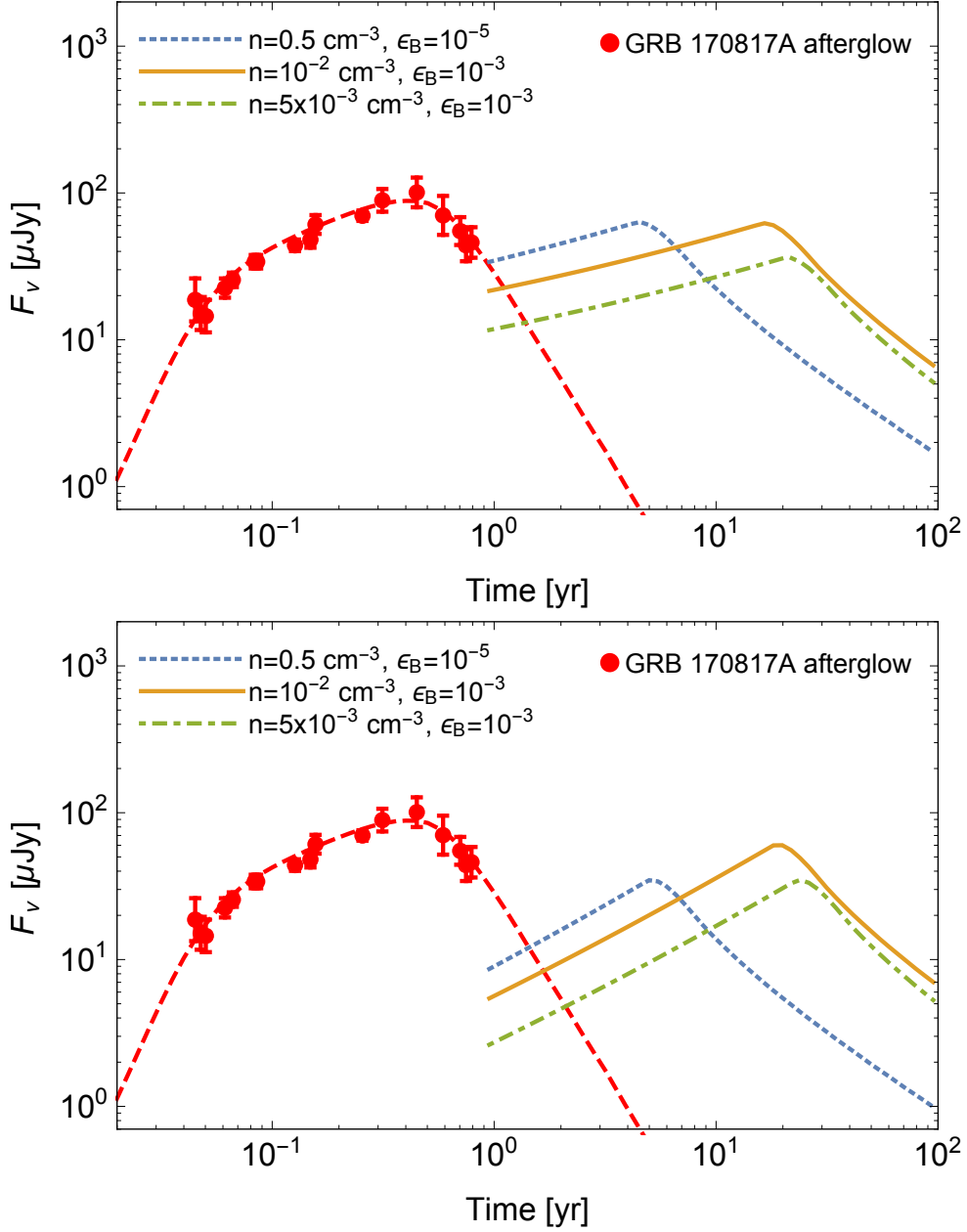
Fig. 8.4. Radio (3 GHz) data of GRB170817A afterglow (points) along with structured jet afterglow model from [31] (dashed line) and KN afterglow light curves with fixed $\alpha = 4$ (top panel) and $\alpha = 6$ (bottom panel) for a range of n and ϵ_B that are typically inferred from fitting the GRB170817A afterglow. The solid line ($n = 10^{-2}$ cm^{-3}, $\epsilon_B = 10^{-3}$) uses the same parameters as in our calculations in Sec 8.3.1 . It is evident that varying the parameters within this range does not significantly alter the light curves. An afterglow rebrightening may be expected within ~ 2 years after the merger.

By equating 8.6 and 8.8, we can find the time at which the flux from the afterglow and KN will be equal (t_{eq}). After this time, it will be possible to detect the KN afterglow. The general expression for t_{eq} is

$$t_{eq} = \left(\frac{(100\mu\mathrm{Jy})(0.44\mathrm{yr})^{2.4}\, t_p^s}{F_{\nu,p}} \right)^{\frac{1}{s+2.4}} = \left(\frac{14\, t_p^s}{F_{\nu,p}} \right)^{\frac{1}{s+2.4}}. \tag{8.9}$$

For $3 \lesssim \alpha \lesssim 5$, we can substitute expression 8.3 for t_p and obtain

$$t_{eq} \approx \left(\frac{0.2\,(8.3)^{\frac{3\alpha-6(p-1)}{\alpha+8}} \nu_{9.5}^{\frac{p-1}{2}} \beta_{0,-0.5}^{-\frac{6(\alpha-5)+(5\alpha+14)p}{2(\alpha+8)}}}{f_\Omega\, E_{iso,51}^{\frac{2(p+3)}{\alpha+8}} \epsilon_{B,-3}^{\frac{p+1}{4}} \epsilon_{e,-1}^{p-1} n_{-2}^{-\frac{\alpha(p+5)+16}{4(\alpha+8)}}} \right)^{\frac{5(\alpha+8)}{126-30p+27\alpha}}, \tag{8.10}$$

where we have substituted $d = 40$ Mpc for the distance to the source. If we substitute $\alpha = 4$ and $p = 2.2$ for example, t_{eq} becomes

$$t_{eq} \approx (2\,\mathrm{yr})\, n_{-2}^{-0.33}\, \beta_{0,-0.5}\, E_{iso,51}^{-0.31}\, \nu_{9.5}^{0.21}\, \epsilon_{e,-1}^{-0.43}\, \epsilon_{B,-3}^{-0.29}\, f_\Omega^{-0.36}. \tag{8.11}$$

Fig. 8.3 shows a contour plot of t_{eq} for β_0 vs n where each panel corresponds to a different value of α. The rest of the parameters used are $\epsilon_e = 0.1$, $\epsilon_B = 10^{-3}$, $E_{iso} = 10^{51}$ erg, $p = 2.2$ and $\nu = 3$ GHz.

The rebrightening time t_{eq} can also be calculated for $\alpha \to \infty$ case using equation 8.4. We do not focus on this case here since the afterglow at t_{eq} will most likely be too faint to detect (see Fig. 8.2). However, the peak of the KN afterglow may still be bright enough to be detected. Interestingly, therefore, if the KN ejecta are characterized by a very steep velocity profile, its afterglow emission could fall below detectability limits in the near future, only to re-emerge several years, or even a decade, later.

We have not yet observed the emergence of the KN afterglow in GW170817, indicating that t_{eq} must be greater than the current observing time ($t_{eq} \gtrsim 1$ yr). Using this condition on t_{eq}, we can place some constraints on the dynamical and microphysical quantities related to the KN afterglow (such as β_0 and α) even without a detection. For example, if we substitute $\epsilon_e = 0.1$, $E_{iso} = 10^{51}$ erg, $p = 2.2$, $\alpha = 4$ and $\nu = 3$ GHz, the condition $t_{eq} \gtrsim 1$ yr yields

$$\beta_0 \lesssim 0.25\, n_{-2}^{-0.33}\, \epsilon_{B,-3}^{0.28}. \tag{8.12}$$

This equality ($t_\mathrm{eq} = 1$ yr) is shown by the solid, white lines in Fig 8.3 (with $\epsilon_\mathrm{B} = 10^{-3}$). For regions above the $t_\mathrm{eq} = 1$ yr contour, t_eq is less than 1 yr, which means these regions are excluded since no rebrightening/flattening has been observed in the afterglow of GW170817. For comparison, Fig. 8.3 also shows the $t_\mathrm{eq} = 2$ yr contour. In order for the KN afterglow to be detectable, at the very least, its peak flux must be greater than sensitivity limits of detectors. For radio observations, we will use a sensitivity limit $5\,\mu$Jy so that the detectability condition is $F_{\nu,\mathrm{p}} \gtrsim 5\,\mu$Jy, with $F_{\nu,\mathrm{p}}$ given in equation 8.1 . Substituting the same parameters used to obtain 8.12, this detectability condition yields

$$\beta_0 \gtrsim 0.08\, n_{-2}^{-0.4}\, \epsilon_{\mathrm{B},-3}^{-0.4}. \tag{8.13}$$

Regions which do not satisfy this condition are shaded gray in Fig. 8.3 (using $\epsilon_\mathrm{B} = 10^{-3}$) and the KN afterglow will not be detectable for parameters in this region. The horizontal dot-dashed line marks where $\beta_0 = 0.3$, which is the characteristic velocity inferred from observations of the blue KN (see Sec. 8.2). The range of densities for the x-axis of Fig. 8.3 was chosen guided by afterglow modelings of GW170817 ([318, 320, 356, 395]). From these conditions, we can begin to constrain properties of the KN. For example, from Fig. 8.3, we see that for $\alpha = 3$ (top panel), if $\beta_0 = 0.3$, the external density must be $\lesssim 0.005$ cm^{-3}, otherwise the KN afterglow would have been detected by now.

8.3.2 Combined Constraints from the jet afterglow

Using the analytic expressions given in Sec. 8.2 the analysis carried out in Sec. 8.3 can be done for different values of microphysical parameters (ϵ_e and ϵ_B) and external density (n), provided that the observed frequency lies between ν_m and ν_c for the choice of parameters. In this example (Fig. 8.2), values that provided a good fit for the afterglow observations of GRB170817A were used. The typical values of density and ϵ_B found from fitting the GRB afterglow of GW170817 range from $\sim 10^{-3} - 10^{-1}$ cm^{-3} and $\sim 10^{-5} - 10^{-3}$ respectively (e.g., [320, 356, 395]), where higher densities

require lower values of ϵ_B to fit the afterglow (see e.g., Fig. 3 of [395]). This inverse proportionality becomes evident if one uses the expression for the peak flux of a GRB afterglow (e.g., [37]) and expresses n in terms of ϵ_B (keeping other parameters fixed) to find $n \propto \epsilon_B^{-1}$ (this is also the case for the peak of the KN afterglow; equation 8.1).

Fig. 8.4 shows the radio afterglow light curves of the KN for these range of densities and ϵ_B to demonstrate how the light curves would vary for different choices of these parameters which provide reasonable fits for the GRB afterglow. Fig. 8.4 shows that within this range (that spans 2 orders of magnitude), the flux density of the afterglow does not change by more than a factor ~ 2 when compared to our example case of $n = 10^{-2}$ cm^{-3} and $\epsilon_B = 10^{-3}$ (see Fig. 8.4). Which means our conclusions will remain the same for this broad range of parameter space obtained when fitting the GRB afterglow. An afterglow rebrightening, due to the emergence of the KN component, may be expected within ~ 2 years after the merger.

8.4 Discussion/Conclusions

GW170817 was followed by an optical-IR transient, AT2017gfo, which revealed that the merger was accompanied by a substantial ejection of mass $M_{\rm ej} \sim 0.05 M_\odot$ at trans-relativistic velocities $\beta_0 \sim 0.1 - 0.3$. The KN modeling is able to constrain the kinetic energy of the ejecta and its characteristic velocity but is less sensitive to the high-velocity distribution of the ejecta. Yet, this distribution contains crucial information on the merger dynamics. In this work, we assume a power-law distribution of the form $E(> \beta\Gamma) \propto (\beta\Gamma)^{-\alpha}$ for the energy of the KN ejecta and calculate the resulting afterglow powered by the KN ejecta. We find that:

1. A fast KN component with minimum velocity $\beta_0 \simeq 0.3$ and energy $E \sim 10^{51}$ erg, which is likely responsible for the observed blue KN emission, can produce a detectable radio, and possibly X-ray, afterglow for a broad range of the parameter space.
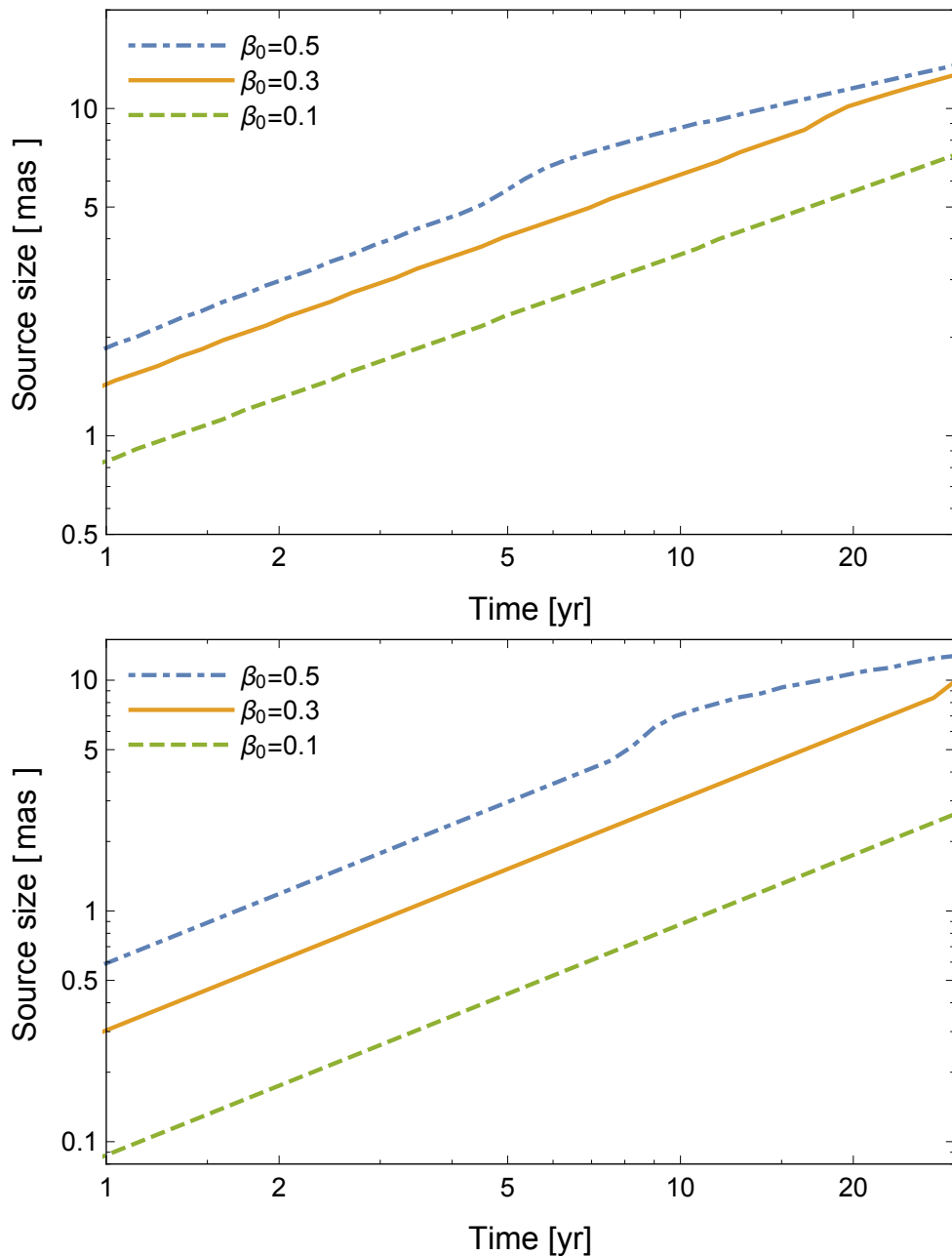
Fig. 8.5. Angular size of the source (associated with KN afterglow) vs. time for the case where $\alpha = 4$ (top panel) and $\alpha \to \infty$ (bottom panel) fixing $n = 10^{-2}$ cm^{-3} and $E = 10^{51}$ erg. Three different values of β_0 are shown in each case. Given a typical size of the source of ~ 10 mas at around ~ 1 decade post trigger and corresponding flux density $\sim 50 - 100$ μJy, resolving the source may be possible if the KN rebrightening is observed.

2. For $3 \lesssim \alpha \lesssim 6$, the KN afterglow is expected to emerge, by dominating the afterglow emission, on a timescale of a few years and peak around a decade later.

3. For steep values of $\alpha \to \infty$, the afterglow emission can drop below detectability levels before the KN afterglow emerges on a decade time scale.

4. The time of emergence $t_{\rm eq}$ (equation 8.9), the rise slope of the light curve s (equation 8.5) and the peak time $t_{\rm p}$ (equation 8.2) can be used to determine properties of the KN ejecta, in particular, the ejecta velocity distribution α, the minimum velocity β_0 and its kinetic energy E.

Studies have found that the velocity distribution of the KN ejecta (the value of α) is affected by the NS equation of state (e.g., softer equations of state tend to produce faster ejecta velocities; [327, 352]) and the nature of the post-merger remnant (e.g., winds from a hypermassive NS can drive the ejecta to higher velocities; [**?**]). The analytic expressions in this paper show how the KN afterglow can be used to constrain the value of α, thereby providing an indirect method of probing the equation of state and post-merger remnant. The GRB afterglow of GW170817 has been characterized by a superluminal apparent speed in the radio ([353]). This finding is consistent with the misaligned jet interpretation used to describe the non-thermal emission observed so far from this event (see also [396] for an investigation into the radio map of GW170817). On the other hand, the KN blast is expected to quasi isotropic with its radio image centered around the merger location. We, therefore, predict that any afterglow rebrightening –marking the emergence of the KN component– will be accompanied by a shift of the centroid of the radio towards the initial position of the explosion. Ultimately, the KN afterglow may be sufficiently bright and extended for the source to be resolved, Fig. 8.5 shows the size of the source vs. time with $n = 10^{-2}$ cm^{-3} and $E = 10^{51}$ erg. The size is obtained by calculating the extent of the blast wave which contributes to half of the afterglow emission and projecting this extent perpendicular to the line of sight. For $\beta_0 \simeq 0.3$, the typical size of the source is ~ 10 mas at around twenty years post merger.

As of the time of writing of this work, the afterglow emission from GW170817 is declining quite steeply ([394]), which is expected from a structured jet model that is moderately misaligned with respect to our line of sight (e.g., [31, 317, 356, 397–399]). We find here that the ejecta responsible for the KN may cause the afterglow light curve to rebrighten in the near future and be detectable for decades to come.

9. TIDAL DISRUPTION EVENTS AND ACCRETION DISCS

A tidal disruption event (TDE) occurs when the tidal forces from a blackhole rip apart a nearby orbiting star. In our most recent paper [323], we investigated TDEs around supermassive blackholes (SMBHs) that are surrounded by a pre-existing accretion disc (see chapter 10). These discs are believed to be present in Active Galactic Nuclei (AGNs). In this chapter, we briefly introduce the basics of TDE theory.

9.1 The tidal radius

When the tidal forces from a black hole exceeds the self-gravity of a star, the star becomes tidally disrupted, the distance (from the SMBH) at which this happens is called the tidal radius (r_t) [400]. To determine r_t, we have to equate this tidal force to the force of self-gravity. Take a star whose center of mass (CoM) is located at a distance R from the SMBH. Consider an element of this star of mass m located a distance x from the center of the star, with $|x| \leq R_*$ (see fig. 9.1). The force of gravity exerted by the star on this element (assuming a uniform stellar density) is $GM_* mx/R_*^3$, where M_* and R_* are the mass and radius of the star respectively. The tidal force (F_t) exerted by the SMBH on this element is the difference between the gravitational forces the SMBH exerts on the CoM of the star and this stellar element,

$$F_t = \frac{GM_{bh}m}{(R-x)^2} - \frac{GM_{bh}m}{R^2} \approx \frac{GM_{bh}mx}{R^3},$$

(9.1)

where M_{bh} is the mass of the SMBH. We have used the fact that $x \ll R$ and expanded the above expression to the first order in x/R.
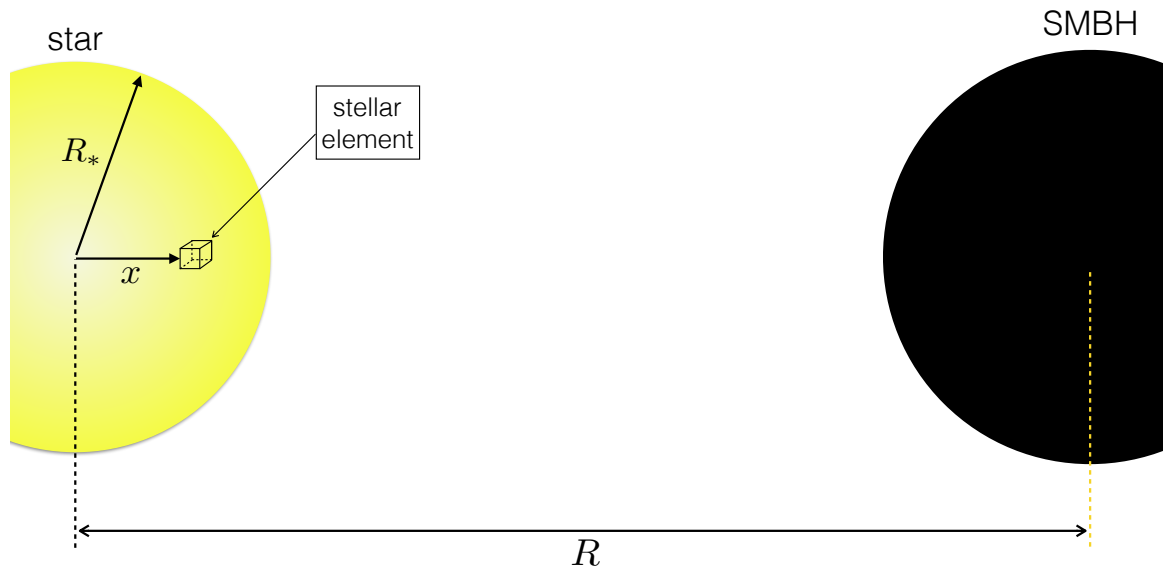
Fig. 9.1. Diagram illustrating the quantities used in the calculations of chapter 9. A star of radius R_* orbits a supermassive blackhole (SMBH) a distance R away. We consider the forces acting on a stellar element a distance x from the center of the star.

By equating the tidal force to the force of gravity exerted by the star on this element, we obtain the tidal radius [401]

$$r_{\mathrm{t}} = R_* \left(\frac{M_{\mathrm{bh}}}{M_*} \right)^{\frac{1}{3}}.$$

(9.2)

9.2 Dynamics of a disrupted star

The pericenter passage of a disrupted star must be very small (at most r_t) which means the orbit is highly eccentric. We therefore assume the star initially approaches the SMBH on a parabolic orbit, hence the energy of the star before disruption

$$E = \frac{1}{2}M_* v_*^2 - \frac{GM_* M_{\text{bh}}}{R} \approx 0. \tag{9.3}$$

Throughout our work, we assume the pericenter distance is equal to r_t. So when the star reaches the pericenter, it is disrupted and roughly half of the stellar material forms a bound stream that orbits, and eventually falls back to the SMBH while the other half remains unbound [401, 402]. The total force felt by a stellar element at disruption is the sum of the gravitational force exerted by the SMBH and the star

$$F = \frac{GM_{\text{bh}}m}{(r_t - x)^2} - \frac{GM_* mx}{R_*^3} \approx \frac{GM_{\text{bh}}m}{r_t^2} + \frac{GM_{\text{bh}}mx}{r_t^3}, \tag{9.4}$$

where we have expanded in terms of x/r_t, and retained terms up to first order since $x \ll r_t$ (see previous section and fig. 9.1 for definition of x and a stellar element). The total specific energy of this element at disruption is therefore

$$\epsilon = \frac{1}{2}v_*^2 - \frac{GM_{\text{bh}}}{r_t} - \frac{GM_{\text{bh}}x}{r_t^2} \approx -\frac{GM_{\text{bh}}x}{r_t^2}, \tag{9.5}$$

where we have used (9.3) to obtain the last equality and the negative sign indicates material within $0 < x \leq R_*$ is bound to the SMBH.

Using Kepler's law and the energy of an elliptic orbit, we can relate the time period of the bound disrupted material (T) to its specific energy, ϵ,

$$T = 2\pi GM_{\text{bh}}(2\epsilon)^{-\frac{3}{2}}. \tag{9.6}$$

With this, we can, for example, obtain the time it takes for the most bound material to fall back to the SMBH (t_{fall}). The energy of the most bound material can be found by substituting $x = R_*$ in equation (9.5). Plugging this quantity in (9.6), we find

$$t_{\text{fall}} = \frac{\pi R_*^{\frac{3}{2}}}{\sqrt{2GM_{\text{bh}}}} \left(\frac{M_{\text{bh}}}{M_*} \right). \tag{9.7}$$

This quantity will be useful in the next chapter as it provides an estimate on the trigger time of a TDE flare since disruption.

Throughout this work, we assume $a \gg r_{\text{t}}$ (a is the semi-major axis of the bound orbits) to simplify many expressions, here we justify it. From Kepler's law, we have $a^3 = GM_{\text{bh}}T^2/4\pi^2$. the minimum value for a will correspond to when $t = t_{\text{fall}}$, giving

$$a_{\text{min}} = \left(\frac{GM_{\text{bh}}t_{\text{fall}}^2}{4\pi^2} \right)^{\frac{1}{3}} \approx r_{\text{t}} \left(\frac{M_{\text{bh}}}{M_*} \right)^{\frac{1}{3}}. \tag{9.8}$$

The minimum mass for a SMBH in our applications is $10^5 M_\odot$ and $M_* \sim M_\odot$ where $M_\odot$ is a solar mass. Therefore $a/r_{\text{t}} \gtrsim 100$ which means $a \gg r_{\text{t}}$.

Following the disruption, the bound stream orbits and eventually falls onto the SMBH. The fall back rate, $\dot{M}$, of this bound material is given by $\dot{M} = (dM/d\epsilon)(d\epsilon/dt)$. We assume that $dM/d\epsilon$ is constant (valid at late times) and from equation (9.6) we have $d\epsilon/dt \propto t^{-5/3}$, therefore $\dot{M} \propto t^{-5/3}$ [403]. The assumption $dM/d\epsilon$ is constant is not valid at early times because the structure of the star can affect the energy distribution at early times [404, 405].

10. EFFECTS OF TDES IN THE PRESENCE OF A PRE-EXISTING ACCRETION DISC

Numerous tidal disruption event (TDE) candidates originating from galactic centres have been detected (e.g., by *Swift* and ASASSN). Some of their host galaxies show typical characteristics of a weak active galactic nucleus (AGN), indicative of a pre-existing accretion disc around the supermassive blackhole (SMBH). In this work, we develop an analytic model to study how a pre-existing accretion disc affects a TDE. We assume the density of the disc $\rho \propto R^{-\lambda}$, R being the radial distance from the SMBH and λ varying between $0.5 - 1.5$. Interactions between the pre-existing accretion disc and the stream of the tidally disrupted star can stall the stream far from the SMBH, causing a sudden drop in the rate of fallback of gas into the SMBH. These interactions could explain the steep cut-off observed in the light curve of some TDE candidates (e.g., *Swift* J1644 and J2058). With our model, it is possible to use the time of this cut-off to constrain some properties pertaining to the pre-existing accretion disc, such as λ and the disc viscosity parameter α. We demonstrate this by applying our theory to the TDE candidates *Swift* J1644, J2058 and ASASSN-14li. Our analysis favours a disc profile with $\lambda \sim 1$ for viscosity parameters $\alpha \sim 0.01 - 0.1$.

10.1 Introduction

Stars orbiting too close to a supermassive blackhole (SMBH) get pulled apart by strong tidal forces, resulting in a tidal disruption event (TDE). In order for this

to occur, the pericentre passage of the star must be within the tidal radius $r_{\mathrm{t}} = R_*(M_{\mathrm{bh}}/M_*)^{\frac{1}{3}}$ where R_* and M_* are the radius and mass of the star, respectively, and M_{bh} is the mass of the SMBH [401]. Following a TDE, about half of the stellar material forms a bound debris stream (BDS) that eventually returns to the vicinity of the SMBH and can lead to tidal disruption flares (e.g., [405–408]).

Many tidal disruption flare candidates have been detected at multiple wavelengths (a detailed list of these candidates is given in The Open TDE Catalog[1]). There is also evidence that some TDEs launch powerful relativistic jets (e.g., [409–412]). Simulations show that magnetic fields from the disrupted material alone may be insufficient to produce a jet in these events (such as in *Swift* J1644). A possible solution to this problem is found if the magnetic field of a pre-existing accretion disc is included in these systems [413, 414].

In recent years, the All-Sky Automated Survey for Supernovae (ASASSN) has detected multiple TDE candidates at galactic centres [415]. In particular, ASASSN-14li [416, 417], shows evidence that its host galaxy harbours a weak active galatic nuleus (AGN) [418, 419]. AGNs are powered by an accretion disc which funnels gas into a SMBH.

Optical observations from a majority of TDE host galaxies yield line emission ratios similar to that of AGNs [420]. This supports the claim that TDE rates are enhanced in AGNs (e.g., [421]). Furthermore, many TDE host galaxies show properties similar to post-merger galaxies [422, 423], and galaxy mergers are believed to be correlated with AGN activity (e.g., [424]). These results stress the importance of understanding how TDEs behave in the presence of a pre-existing accretion disc.

Previous work by [425] investigated the effect of TDEs in the presence of a very low-density, static corona. They found that the interaction between the BDS and the corona lead to Kelvin-Helmholtz instabilities, which may, in some cases, dissolve the TDE stellar stream. Their results were relevant for the disruption of giant stars. In this work, we study how a rotationally supported pre-existing accretion disc can affect

---

[1]https://tde.space

the dynamics of the BDS. Our study identifies observable effects even in the case of the disruption of main sequence stars. In general, the accretion disc can alter the fallback of the BDS onto the SMBH, thereby modifying the duration of the flare and their observed light curves. We find our results to be very sensitive to the accretion disc model. This enables us to use TDEs to probe the structure of accretion discs at galactic centres.

In Section 4.2 we describe the model used for the pre-existing accretion disc and the BDS. In Section 4.3 we calculate the dynamics of the BDS as it travels through the accretion disc and study how this might affect TDE observations. In Section 4.4 we present our results and apply our theory to TDE candidates around accreting SMBHs in 4.5. We discuss our results and conclude in Section 4.6.

10.2   Modelling the pre-existing accretion disc and the bound debris stream

In this work we consider a SMBH surrounded by a pre-existing accretion disc. The disc extends out to a scale comparable to the Bondi radius, typically a fraction of a parsec. Before the TDE, as the star gets closer to the black hole, it travels unimpededly towards it. The stellar density is much larger than the density of the accretion disc, so the stellar trajectory is not affected by the presence of the accretion disc. As the star is disrupted, the bound stellar material, now in the form of a BDS, expands as it traverses through the accretion disc. We assume a geometrically thick disc, as expected in low-luminosity AGN systems. We take the height of the disc (H) to be on the order of $R/2$, R being the radial distance from the SMBH. Using the solid angle subtended by the disc, we estimate roughly half of all possible stellar orbits will lie within the plane of the disc in our model. For simplicity, in what follows, we assume a coplanar disc-BDS configuration.

10.2.1 The pre-existing accretion disc around the SMBH

We parametrize the density of the pre-existing accretion disc around the black hole by assuming it accretes at some fraction of the Eddington accretion rate. The Eddington luminosity of a black hole of mass $M_{\rm bh}$ is $L_{\rm edd} \approx 10^{44} M_6$ erg/s, where $M_6 = M_{\rm bh}/10^6 M_\odot$. The mass accretion rate that corresponds to this luminosity depends on the efficiency η, and is given by

$$\dot{M}_{\rm edd} = \frac{L_{\rm edd}}{\eta c^2} = \frac{4\pi G M_{\rm bh} m_{\rm p}}{\eta \sigma_{\rm T} c}, \tag{10.1}$$

where $\sigma_{\rm T}$ is the Thomson cross-section for an electron, $m_{\rm p}$ is the mass of a proton, c is the speed of light and G is the gravitational constant. We can normalize a given mass accretion rate to the black hole, $\dot{M}$, to this quantity by defining $\dot{m} = \dot{M}/\dot{M}_{\rm edd}$. Therefore, if a pre-existing accretion disc is present, its mass accretion rate is given by

$$\dot{M} = \frac{4\pi G M_{\rm bh} m_{\rm p}}{\eta \sigma_{\rm T} c} \dot{m} = (10^{23}\,{\rm g/s})\,\dot{m} M_6 \eta^{-1}. \tag{10.2}$$

The mass accretion rate from a thick disc can be obtained by extending the thin disc model [426], to a scale height of the disc $H \sim R/2$, where R is the radial distance from the black hole, and it is given by

$$\dot{M} = \frac{\pi}{2} R^2 \alpha v_{\rm k} \rho, \tag{10.3}$$

where α is the viscosity parameter, $v_{\rm k}$ is the Keplerian speed and ρ is the density of the disc at a distance R. The Keplerian speed at a distance R from the black hole is $v_{\rm k} = c\sqrt{R_{\rm g}/R}$, where $R_{\rm g} = GM_{\rm bh}/c^2 \approx 1.5 \times 10^{11} M_6$ cm.

The number density of particles in the disc is $n = \rho/m_{\rm p}$. At a distance $R_0 = 10R_{\rm g}$, the number density n_0 can be obtained using equations (10.2) and (10.3), and is given by

$$n_0 = \frac{8c^2}{10^{\frac{3}{2}} \sigma_{\rm T} G} \left(\frac{\dot{m}}{\alpha\eta}\right) M_{\rm bh}^{-1} \approx (1.7 \times 10^{12}\,{\rm cm}^{-3})\,\dot{m} M_6^{-1} \alpha^{-1} \eta^{-1}. \tag{10.4}$$

From now on, we will use $\mu = \frac{\alpha\eta}{\dot{m}}$ to parametrize the disc density close to the SMBH. We will explore typical values of $\eta, \alpha \lesssim 0.1$ and $\dot{m} \lesssim 0.01$ for which μ may be of order

unity . We assume that far from the SMBH ($R \gtrsim R_0$), the density of the accretion disk drops as $\propto R^{-\lambda}$. Therefore, the density at distance R is

$$n = n_0 \left(\frac{R}{R_0} \right)^{-\lambda}. \qquad (10.5)$$

Throughout this work, we consider λ to be within $0.5 - 1.5$, which are the limits set by the CDAF [427, 428] and ADAF [429] models for accretion discs, respectively. We will show how TDE observations might allow us to constrain the important parameter λ, that sets the density profile of the disc.

10.2.2 Geometry and dynamics of the bound debris stream

We assume the star approaches the SMBH on a highly elliptical orbit with a pericentre distance $r_\mathrm{p} \sim r_\mathrm{t}$, in order to avoid the complications that arise from deeply penetrating orbits. After the star is disrupted by the SMBH, the stellar debris forms an elongated, cylindrical stream [430] of diameter h. Initially, the temperature of the stream evolves adiabatically as $T \propto \rho^{(\gamma-1)}$, where $\gamma = 5/3$ and ρ is the density of the stream [431]. The stream initially evolves under self-gravity, to find its scaling, we equate the gas pressure of the stream to its self-gravitational energy density. The pressure of an adiabatic gas is $P \propto \rho^\gamma$, if we choose a stream element of mass $\sim \rho h^3$, its self-gravitational energy density will be $G(\rho h^3)\rho/h \propto \rho^2 h^2$. Hence $\rho^\gamma \propto (\rho h)^2$, owing to the cylindrical geometry of the stream, $\rho \propto h^{-2}R^{-1}$, see equation (10.9). Therefore the streams diameter scales as $h \propto R^{1/4}$ [402, 432]. When the stream has cooled to a temperature $T_\mathrm{rec} \approx 10^4 \mathrm{K}$ it undergoes recombination, during which the temperature of the stream (for a solar-type star) remains roughly constant [431]. When the stream starts recombining it no longer self-gravitates, instead it expands laterally at its internal sound speed $c_\mathrm{s} \approx \sqrt{\gamma k_\mathrm{b} T_\mathrm{rec}/m_\mathrm{p}} \approx 1.6 \times 10^6$ cm/s [430]. After recombination, the stream continues to evolve adiabatically. Following this evolution, the diameter h of the BDS is given in equation (10) of [430] as

$$h = 2R_* \left(\frac{\min[R, r_\mathrm{rec}]}{r_\mathrm{p}} \right)^{\frac{1}{4}} + \max[c_\mathrm{s}(t - t_\mathrm{rec}), 0], \qquad (10.6)$$

where $r_{\rm rec}$ and $t_{\rm rec}$ are the radius and time at which recombination occurs and $r_{\rm p}$ is the pericentre distance of the star. Throughout this work, we will assume $r_{\rm p} = r_{\rm t}$. We can relate the apocentre distance of each stream element to the time of its apocentre passage using Kepler's third law

$$r_{\rm apo} = 2a - r_{\rm t} \approx 2a = 2\left(\frac{GM_{\rm bh}\,t_{\rm apo}^2}{\pi^2}\right)^{\frac{1}{3}}, \tag{10.7}$$

where a is the semi-major axis and we have used the fact that $r_{\rm t} \ll a$. Unless otherwise specified, we take $t = t_{\rm apo}$ and $r = r_{\rm apo}$ from now on. According to equation (10.6), for times $t \gg t_{\rm rec}$, $h \approx c_{\rm s}t$ is a good approximation [430].

A useful timescale is the fallback time of the most bound material ($t_{\rm fall}$). The specific orbital energy of the most bound material is $\sim GM_{\rm bh}R_*/r_{\rm t}^2$ (e.g., [433]). Using Kepler's law in terms of orbital energy, we find

$$t_{\rm fall} = \frac{\pi R_*^{\frac{3}{2}}}{M_*}\left(\frac{M_{\rm bh}}{2G}\right)^{\frac{1}{2}} \approx (3.6 \times 10^6 s)\frac{r_*^{\frac{3}{2}} M_6^{\frac{1}{2}}}{m_*}, \tag{10.8}$$

where $m_* = M_*/M_\odot$ and $r_* = R_*/R_\odot$.

We approximate the length of the stream to be $l \approx 2a \approx r$. Assuming a uniform stream, we can calculate its number density as

$$n_{\rm s} = \frac{M_*}{2\pi(h/2)^2 r m_{\rm p}}. \tag{10.9}$$

The factor of 2 in the denominator appears because roughly half of the star remains bound to the SMBH. Another quantity we will use later is the apocentre velocity of the stream element. It is given by the vis-viva equation

$$v_{\rm apo} = \sqrt{GM_{\rm bh}\left(\frac{2}{r} - \frac{1}{a}\right)}. \tag{10.10}$$

We use the exact expression for r given in equation (10.7) and Taylor-expand it in powers of $r_{\rm t}/a$. Keeping only the first order term (since $r_{\rm t} \ll a$) we find

$$v_{\rm apo} \approx \frac{1}{a}\sqrt{GM_{\rm bh}\frac{r_{\rm t}}{2}}. \tag{10.11}$$

10.3 Interactions between the pre-existing disc and the BDS

All interactions between the disc and the BDS are considered at the apocentre passage of each stream element. Each stream element travels the slowest at its apocentre passage, therefore the time of interactions with the disc is maximized at this point. Also the density ratio of the stream to that of the disc is lower at this point. This means that the disc can have a more significant impact on the BDS at or after apocentre passage.

We can approximate the relative velocity between the BDS and the disc at apocentre to be the Keplerian velocity (the assumed velocity of the accretion disc), since

$$\frac{v_{\mathrm{apo}}}{v_{\mathrm{k}}(r)} \approx \sqrt{\frac{r_{\mathrm{t}}}{a}} \ll 1. \tag{10.12}$$

Therefore, at apocentre, we can assume the BDS is stationary and the disc material "rams" the stream with speed $\sim v_{\mathrm{k}}$. Since this paper focuses on interactions at apocentre passage, our results are insensitive to whether the disc is prograde or retrograde to the BDS as the interactions at apocentre will be described similarly in both cases.

Interactions between the disc and BDS can manifest in the form of a shock which propagates through the BDS. These shocks can directly affect the trajectory of the BDS and prevent it from reaching the black hole (Section 10.3.1). The velocity difference between the disc and the shocked BDS can lead to the development of KH instabilities (Section 10.3.2). If this instability grows sufficiently fast within the BDS, it can completely disrupt it and also prevent the BDS from reaching the black hole. In some cases, the interactions may not be strong enough to form a shock or to trigger the instabilities. For these cases, we estimate the momentum imparted by the disc onto the BDS and assess whether the BDS trajectory is perturbed enough to prevent it from reaching the black hole (Section 10.3.3).

10.3.1 Interaction via shocks

The interaction between the disc and BDS produces a shock that travels laterally through the stream. The speed of the shock front, in the frame of the shocked fluid, can be approximated by equating the ram pressure of the disc with the ram pressure of the shock. This yields

$$v_{\text{sh}} \approx \frac{1}{3} \left(\frac{n}{n_{\text{s}}} \right)^{\frac{1}{2}} v_{\text{k}} = \frac{10^{\frac{1}{4}} c}{15} \left(\frac{\pi m_{\text{p}}}{\mu \sigma_{\text{T}} M_*} \right)^{\frac{1}{2}} h \left(\frac{10 G M_{\text{bh}}}{c^2 r} \right)^{\frac{\lambda}{2}}. \tag{10.13}$$

The time taken for the shock to cross the debris stream at apocentre is

$$t_{\text{cross}} = \frac{h}{4 v_{\text{sh}}} = \frac{3 \times 5^{\frac{3}{4}}}{2^{\frac{9}{4}} c} \left(\frac{\mu \sigma_{\text{T}} M_*}{\pi m_{\text{p}}} \right)^{\frac{1}{2}} \left(\frac{c^3 t_{\text{apo}}}{\pi \, 5^{\frac{3}{2}} G M_{\text{bh}}} \right)^{\frac{\lambda}{3}}, \tag{10.14}$$

which, given the geometry of the problem, turns out to be independent of h. The factor of 4 appears in the denominator due to the reference frame considered: $4 v_{\text{sh}}$ corresponds to the speed at which the shock propagates into the stream, in the stream rest frame. These calculations are only valid for a strong shock (i.e. when the Mach number, $v_{\text{sh}}/c_{\text{sound}} \gg 1$).

The time when $t_{\text{cross}} \approx t_{\text{apo}}$ yields the time when the shock completely crosses the BDS at apocentre ("shock-crossing time"), which is given by

$$t_{\text{shock}} = \left[\frac{3 \times 5^{\frac{3}{4}}}{2^{\frac{9}{4}} c} \left(\frac{\mu \sigma_{\text{T}} M_*}{\pi m_{\text{p}}} \right)^{\frac{1}{2}} \left(\frac{\pi \, 5^{\frac{3}{2}} G M_{\text{bh}}}{c^3} \right)^{-\frac{\lambda}{3}} \right]^{\frac{3}{3-\lambda}}. \tag{10.15}$$

Considering the range of values for the parameter $\lambda = 0.5 - 1.5$, the shock-crossing time for the fiducial parameters is

$$t_{\text{shock}} \approx \begin{cases} (6 \times 10^6 \text{s}) \, \mu^{\frac{3}{5}} m_*^{\frac{3}{5}} M_6^{-\frac{1}{5}} & \lambda = 0.5 & (10.16\text{a}) \\[2mm] (10^8 \text{s}) \, \mu^{\frac{3}{4}} m_*^{\frac{3}{4}} M_6^{-\frac{1}{2}} & \lambda = 1 & (10.16\text{b}) \\[2mm] (7 \times 10^9 \text{s}) \, \mu m_* M_6^{-1} & \lambda = 1.5. & (10.16\text{c}) \end{cases}$$

Since the density of the disc $\rho \propto R^{-\lambda}$, larger values of λ imply a steeper drop in density. This results in weaker interactions which lead to a lower shock velocity and a longer time for the shock to cross the BDS. However, for flat disc profiles ($\lambda \sim 0.5$) and $\mu \sim 1$, the shock crosses within a few months after the TDE.

The shock alters the velocity of the BDS, but if the shock is too weak, it may not sufficiently modify the trajectory of the BDS so as to prevent the stream from falling back to the SMBH. In these cases, we find that the KH instability that grows in the disc-BDS interface is able to stall the BDS. We show below that as along as a shock exists, KH instabilities develop along the interface of the disc and BDS. These instabilities will disrupt the entire stream on a timescale similar to the shock-crossing time (at $t_{\rm shock}$), preventing the BDS from falling back to the black hole.

10.3.2 Kelvin-Helmholtz instability

As the shock crosses the BDS, the shocked fluid becomes prone to KH instability (since it is in pressure balance with the disc material). This instability will disrupt the stream when it grows to a wavelength of size $\sim h$ [425]. The time taken for this growth is given by (e.g. [434])

$$t_{\rm KH} \approx \frac{h}{v_{\rm k}} \left(1 + \frac{n_{\rm s}}{n}\right)^{\frac{1}{2}} = \frac{h}{3v_{\rm sh}} \left(1 + \frac{n}{n_{\rm s}}\right)^{\frac{1}{2}}, \tag{10.17}$$

where we have used equation (10.13) to obtain the last equality. In deriving the above equation, we ignore self-gravity of the stream since $t_{\rm rec} < t_{\rm fall}$ in all cases considered throughout this paper (see Section 10.2.2). For the parameters considered in this work, the disc is less dense than the stream (i.e. $n/n_{\rm s} \ll 1$), allowing us to approximate $t_{\rm KH} \approx h/3v_{\rm sh} \approx t_{\rm cross}$. This approximation is valid even if the shock is weak. Therefore, as long as a shock exists, the KH instability will disrupt the BDS when the shock completely crosses the stream at $t_{\rm shock}$. So the fallback of material onto the SMBH gets cut-off at $t_{\rm shock}$ provided there is a shock. A shock exists when

$$\frac{T_{\rm sh}}{T_{\rm s}}(t_{\rm shock}) \geq 1, \tag{10.18}$$

where $T_{\rm sh}$ is the temperature of the shocked fluid and $T_{\rm s}$ is the temperature of the pre-shocked BDS, and we have evaluated the ratio at $t_{\rm shock}$. For a more detailed calculation on the shock conditions see Appendix .2.

10.3.3   Momentum imparted by the disc

In some situations, the interaction between the disc and BDS is not strong enough to produce a shock (e.g., if the disc density is too low or if the temperature of the BDS is too high). For these cases condition (10.18) is not satisfied, so a shock does not propagate through the BDS. When there is no shock, the momentum imparted by the disc onto the BDS might be sufficient to affect its trajectory. Consider a stream element at apocentre, its initial momentum will be $v_{\mathrm{apo}}(t)dm$, where t corresponds to the apocentre time of this element and $dm = \frac{M_*}{2r}dr$ (we take a slice of the stream in the radial direction). Let ρ be the density of the disc. The disc "sees" a cross-section $h(t)dr$ of the stream. The amount of momentum transferred from the disc onto the stream element after some time τ since disruption will be $\sim \rho v_{\mathrm{k}}^2 h \tau dr$. From momentum conservation, we obtain

$$v_{\mathrm{s}}(\tau)dm = v_{\mathrm{apo}}(t)dm - \rho v_{\mathrm{k}}^2 h \tau dr, \tag{10.19}$$

where v_{s} is the final speed of the stream element. In order to stall the stream, that is, to prevent it from reaching the black hole, we will assume the momentum imparted by the disc should reduce the BDS velocity by at least a factor of ~ 2 (i.e. $v_{\mathrm{s}}(\tau) = 0.5 v_{\mathrm{apo}}$). Expressing the above equation in terms of time, we find that the time for this velocity change to occur is

$$\tau = \frac{5^{\frac{3}{2}} \pi^{\frac{2}{3}} G^{\frac{1}{6}} \sigma_{\mathrm{T}} \mu}{16 \, c_{\mathrm{s}} \, c^2 m_{\mathrm{p}}} \, M_*^{\frac{5}{6}} R_*^{\frac{1}{2}} M_{\mathrm{bh}}^{\frac{1}{3}} \left(\frac{c^3}{5^{\frac{3}{2}} \pi G M_{\mathrm{bh}}} \right)^{\frac{2\lambda}{3}} t^{\frac{2\lambda-5}{3}}, \tag{10.20}$$

where we used $h = c_{\mathrm{s}} t$, which is valid since $t_{\mathrm{rec}} < t_{\mathrm{fall}}$.

The maximum time each stream element has to interact with the disc is of the order of its apocentre time t. Equating $\tau \approx t$ yields the "stalling time" of the stream (due to impulse from the disc), given by

$$\tau_{\mathrm{stall}} = \left(\frac{5^{\frac{3}{2}} \pi^{\frac{2}{3}} G^{\frac{1}{6}} \sigma_{\mathrm{T}} \mu}{16 \, c_{\mathrm{s}} \, c^2 m_{\mathrm{p}}} \, M_*^{\frac{5}{6}} R_*^{\frac{1}{2}} M_{\mathrm{bh}}^{\frac{1}{3}} \left(\frac{c^3}{5^{\frac{3}{2}} \pi G M_{\mathrm{bh}}} \right)^{\frac{2\lambda}{3}} \right)^{\frac{3}{8-2\lambda}}. \tag{10.21}$$

Considering the range of values for the parameter $\lambda = 0.5 - 1.5$, the stalling time of the stream for the fiducial parameters is

$$
\tau_{\text{stall}} \approx \begin{cases} (2 \times 10^7\text{s})\, \mu^{\frac{3}{7}}\, r_*^{\frac{3}{14}} m_*^{\frac{5}{14}} & \lambda = 0.5 & (10.22\text{a}) \\[2mm] (10^8\text{s})\, \mu^{\frac{1}{2}}\, r_*^{\frac{1}{4}} m_*^{\frac{5}{12}} M_6^{-\frac{1}{6}} & \text{If } \lambda = 1 & (10.22\text{b}) \\[2mm] (2 \times 10^9\text{s})\, \mu^{\frac{3}{5}}\, r_*^{\frac{3}{10}} m_*^{\frac{1}{2}} M_6^{-\frac{2}{5}} & \lambda = 1.5. & (10.22\text{c}) \end{cases}
$$

As in the case of the shock-crossing time, the stalling time increases with λ since the density of the disc falls of more steeply as λ increases.

10.3.4 The cut-off time

From the above calculations, we can estimate a timescale at which the fallback of the BDS onto the SMBH ceases. We will call this the "cut-off time" (t_{cutoff}) and define it as

$$
t_{\text{cutoff}} = \begin{cases} t_{\text{shock}} - t_{\text{fall}} & \text{if } \frac{T_{\text{sh}}}{T_{\text{s}}}(t_{\text{shock}}) \geq 1 & (10.23\text{a}) \\[2mm] \tau_{\text{stall}} - t_{\text{fall}} & \text{otherwise.} & (10.23\text{b}) \end{cases}
$$

In order to represent observations more accurately, we assume the TDE is detected at a time similar to the fallback time of the most bound material, hence we subtract t_{fall} in the above equation. We show a plot of $t_{\text{shock}}, \tau_{\text{stall}}$ and t_{fall} versus SMBH mass in Fig. 10.1 (top panel), in the same figure we show the corresponding cut-off time t_{cutoff} (bottom panel). Since these time scales depend on both the disc density and its profile, as an example for this plot we choose $\lambda = 1$, $\dot{m} = \alpha = 0.01$ and $\eta = 0.1$ (other parameters are considered and discussed in section 10.4). We find that for lower mass SMBHs, the cutoff time is due to shock-crossing given by equation (10.23a), but for SMBHs of mass $\gtrsim 5 \times 10^5 M_\odot$, there is no shock in the BDS since condition (10.18) is not satisfied. In this case the stalling mechanism transitions to impulse caused by the disc, equation (10.23b). This transition is seen as a discontinuous jump in the cut-off time.
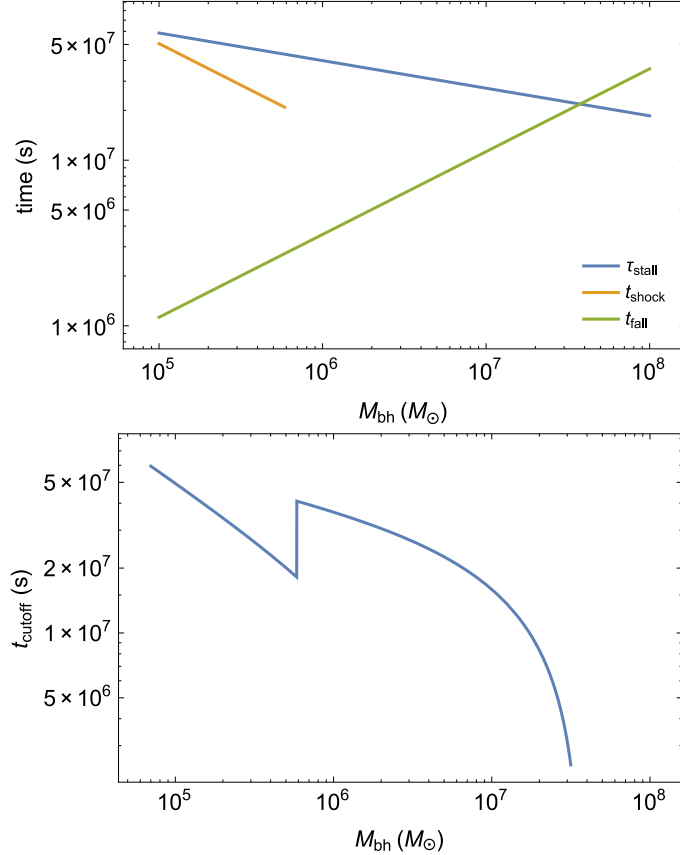
Fig. 10.1. Various timescales (top panel) and the cut-off time (bottom panel) associated with a TDE that interacts with a pre-existing accretion disc. We assume a solar-type star and take $\lambda = 1, \dot{m} = \alpha = 0.01, \eta = 0.1$ (see equations (10.8), (10.15), (10.21) and (4.23) for analytic expressions of timescales). The discontinuous jump in the cut-off time at $5 \times 10^5 M_\odot$ appears because the stalling mechanism of the BDS changes from being due to a shock crossing the BDS to the disc imparting its momentum to the BDS.

10.3.5 Identifying cut-off time from observations

Tidal disruption flares caused by the BDS are interpreted in two ways: 1. they are powered by the accretion of the bound material on to the SMBH, which can manifest in the form of a jet or outflows (e.g., [407, 409, 435]), 2. they are caused by emission from the resulting accretion disc, which forms when the BDS that shocks

itself circularizes (e.g., [406, 432, 436]). In both these scenarios, the flare should drop in luminosity (or cease) when the mass feeding the flare stops. The time at which this happens should coincide with the cut-off time, assuming the viscosity and the radiative cooling timescales of the system powering the flare are shorter than t_{cutoff}. Hence, regardless of which mechanism powering the flare, the cut-off time is a robust observable that can be used in our model to determine the properties of the pre-existing accretion disc.

After the cut-off time we might observe a steep decay in the luminosity of the flare since the stream of mass powering the flare has ceased. If the host galaxy harbours an AGN, the tidal disruption flare luminosity will decay to some constant quiescent value $L_{\text{q}} = \eta \dot{M} c^2$ corresponding to the AGN power. Hence from observations, we can identify the cut-off time when the light curve of the flare becomes significantly steeper. The steeper the decay, the easier it will be to identify t_{cutoff}. We can gauge the steepness of this decay by calculating the ratio of the flare luminosity at the cut-off time (L_{c}) to the quiescent luminosity L_{q} of the AGN (see Fig. 10.2 for an illustration of the cut-off time and associated luminosities). We can estimate L_{c} by assuming the mass of the BDS falls back at a rate $\dot{M}_{\text{fb}} \propto t^{-s}$

$$L_{\text{c}} = f_{\text{b}}\, \eta_{\text{fb}} \dot{M}_{\text{fb}}(t_{\text{cutoff}})c^2 = (s-1) f_{\text{b}}\, \eta_{\text{fb}} \frac{M_* c^2}{2\, t_{\text{fall}}} \left(\frac{t_{\text{cutoff}}}{t_{\text{fall}}} \right)^{-s}, \qquad (10.24)$$

where f_{b} is the beaming factor of the flare ($f_{\text{b}} = 1$ if the flare is not beamed and > 1 if the flare is beamed), η_{fb} is the radiative efficiency from the accretion of the fallback material. From this we can calculate $L_{\text{c}}/L_{\text{q}}$. If this ratio is large, it implies a substantial steepening in luminosity at t_{cutoff}. This in turn would make identifying t_{cutoff} easier.

Theory predicts the temporal index, s, should be $s = 5/3$ [401, 403], in Fig. 10.3 we plot the luminosity ratio $L_{\text{c}}/L_{\text{q}}$ versus $\dot{m}$ using $s = 5/3$ for multiple values of α and λ keeping the SMBH mass fixed at $10^6 M_\odot$. Here we use the analytic expression for t_{cutoff} in L_{c}, see equation (23). We see that in most cases, $L_{\text{c}}/L_{\text{q}} \gg 1$ which means t_{cutoff} should be easily observable (provided L_{c} is above the sensitivity limits of the instrument). In Fig. 10.3 we see the luminosity ratio can be less than unity for larger
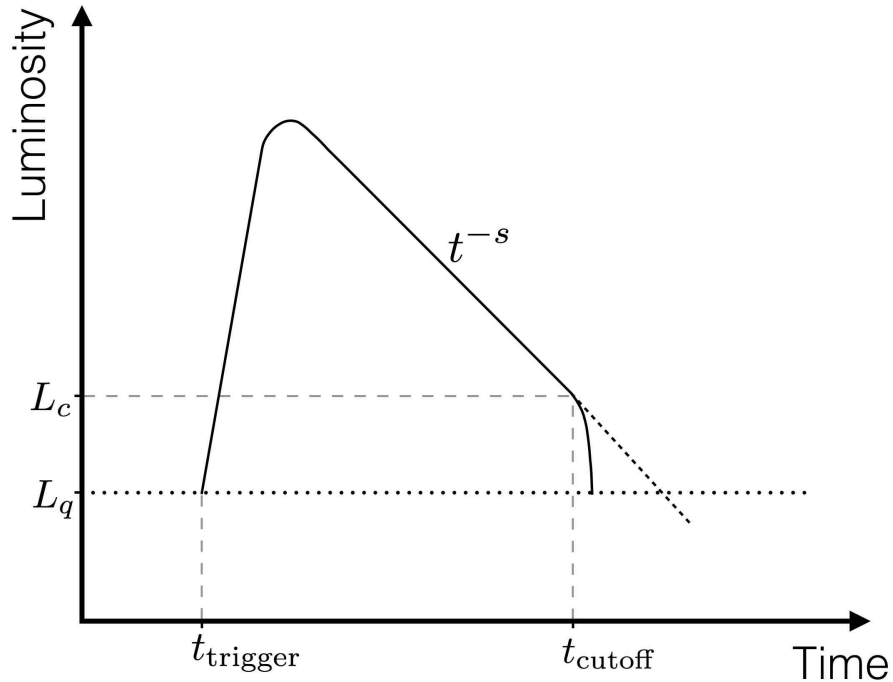
Fig. 10.2. Diagram illustrating the light curve of a tidal disruption flare. At t_c we expect the luminosity to sharply drop from L_c to the quiescent value L_q (horizontal dotted line) due to the interaction of the BDS and a pre-existing accretion disc. The dashed line indicates what the flare would look like if no pre-existing accretion disc is present.

values of $\lambda \approx 1.5$, which means t_{cutoff} cannot be identified in these cases, since the disc density is small and the interaction between the disc and the BDS is weak. We show in the next section that the cut-off time for these large values of λ is on the order of hundreds of years and therefore will be of little observational relevance.

10.4   Results

In Fig. 10.4 we show the cut-off time versus accretion rate ($\dot{m}$) for a SMBH of $10^6 M_\odot$ for multiple density profiles of the disc. We see the cut-off time differs significantly for different values of λ, indicating that this timescale is very sensitive to the density profile of the disc.
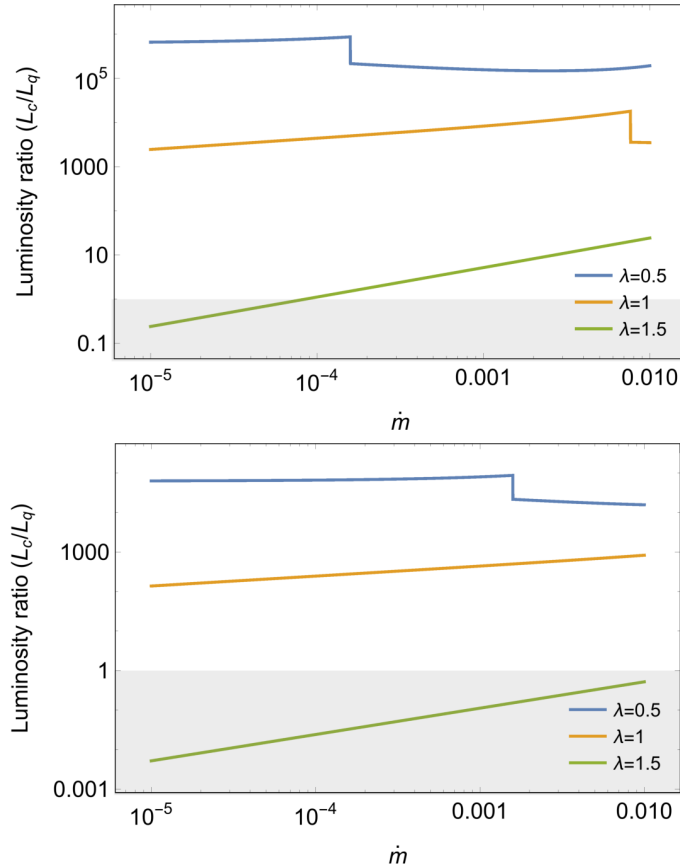
Fig. 10.3. L_c/L_q versus accretion rate $\dot{m}$ (normalized to Eddington) for SMBH mass $10^6 M_\odot$ and multiple values of λ with $\alpha = 0.01$ (top panel) and $\alpha = 0.1$ (bottom panel). We assume a solar-type star and $s = 5/3$, $\eta = 0.1$, $f_b \eta_{fb} = 1$. In most cases this ratio is very large, which suggests a high chance of identifying t_{cutoff}, the shaded area shows the region in which t_{cutoff} cannot be identified.

In order to understand the dependence of the cut-off time on the SMBH mass and also on the value of λ, we plot t_{cutoff} versus $\dot{m}$ for multiple SMBH masses in Fig. 10.5. The different panels show different values of $\lambda = 0.5, 1, 1.5$ (top, middle and bottom panels, respectively). As mentioned in Section 10.3.5, for $\lambda = 1.5$ it will be impossible to identify the cut-off time and Fig. 10.5 shows that t_{cutoff} exceeds a century for these low-density accretion discs. Hence even the absence of a cut-off time can provide us with a lower limit for λ.
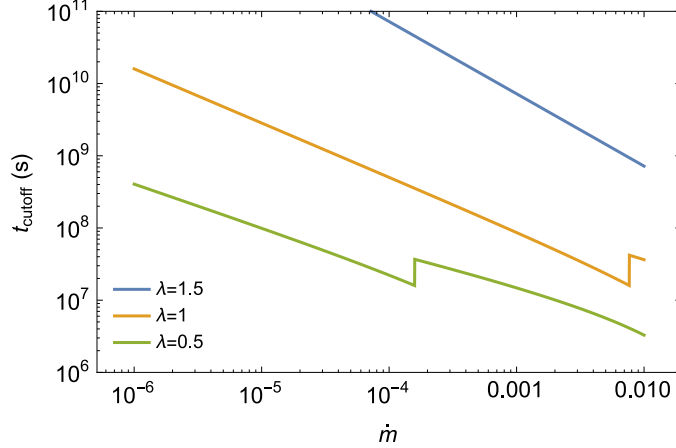
Fig. 10.4. Cut-off time versus accretion rate $\dot{m}$ (normalized to Eddington) for a fixed SMBH mass of $10^6 M_\odot$ and multiple density profiles (λ) of the disc. We assume a solar-type star and take $\alpha = 0.01$ and $\eta = 0.1$ (see Section 10.3 for analytic expressions of $t_{\rm cutoff}$). For disc profiles of $\lambda \lesssim 1$ and reasonably high accretion rates $\dot{m} \gtrsim 10^{-4}$, the cut-off time is ~ 1 year after the TDE, and can therefore be observable.

10.5 Applications to Observations

As mentioned above, in the presence of a pre-existing accretion disc, the tidal disruption flare should drop in luminosity at the cut-off time (provided the flare luminosity is larger than the luminosity of the quiescent AGN at this time). Hence we can attempt to identify $t_{\rm cutoff}$ from TDE observations and use it to constrain the properties of a potential pre-existing accretion disc . We apply this theory to 3 observed TDE candidates, *Swift* J1644, *Swift* J2058 and ASASSN-14li.

10.5.1 *Swift* J1644 and J2058

The *Swift* J1644 TDE candidate was initially thought to be a GRB. However, the long lasting X-ray flare associated with this event led to the current consensus of it being a TDE candidate (e.g., [409, 410]). *Swift* J1644 is likely to be the first example of a jetted TDE [435]. The X-ray emission lasted for ~ 370 days (in the host galaxy
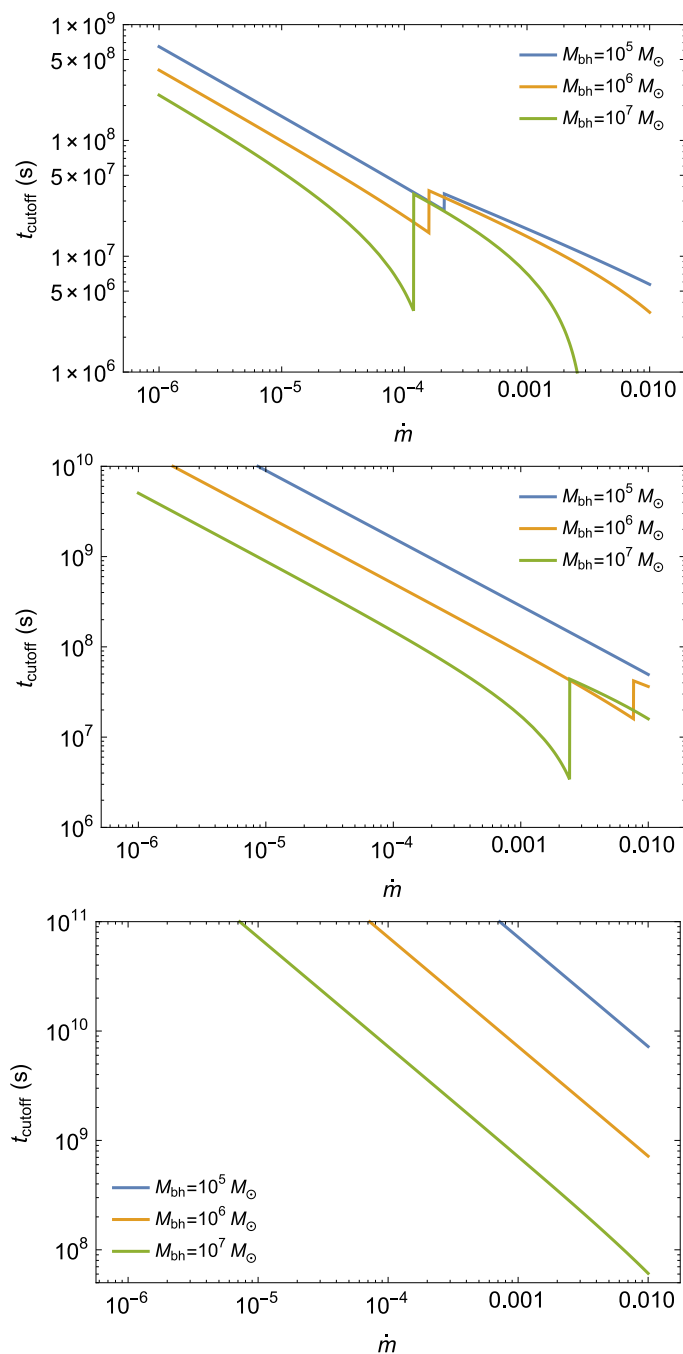
Fig. 10.5. Cut-off time versus accretion rate $\dot{m}$ (normalized to Eddington) for various SMBH masses with $\lambda = 0.5$ (top panel), $\lambda = 1$ (middle panel) and $\lambda = 1.5$ (bottom panel). We assume a solar-type star and take $\alpha = 0.01$, $\eta = 0.1$ (see Section 10.3 for analytic expressions of t_{cutoff}).

frame) after which the luminosity (in X-ray) dropped by 2 orders of magnitude to a constant value of $L_x \sim 5 \times 10^{42}$ erg s^{-1} and has been observed for more than 4 years now [437], this value is also consistent with the upper limits obtained from the pre-outburst measurements of J1644 [438]. Assuming a $\sim 30\%$ of the total power is emitted in X-rays, the bolometric luminosity would be $L \sim 3L_x \approx 10^{43}$ erg s^{-1}. We can interpret this luminosity as the quiescent accretion from the pre-existing disc onto the SMBH and take t_{cutoff} to be the time at which the drop in X-ray luminosity was observed. The mass of the SMBH for this event is constrained within $\sim 10^5 - 10^7 M_\odot$ [413]. Using this we can calculate

$$\dot{m} = \frac{L}{L_{edd}} \approx \frac{10^{43}}{10^{38} M_{bh}}, \tag{10.25}$$

where M_{bh}, α, η and λ are the unknown parameters. Assuming a solar-type star was disrupted and fixing $\eta = 0.1$, we plot t_{cutoff} versus M_{bh} for multiple values of λ and α in Fig. 10.6. The dashed horizontal line shows the observed cut-off time of the flare. If this cut-off occurred due to the interaction of the BDS with the pre-existing accretion disc, we can use our model to infer values of the density profile of this disc λ. From Fig. 10.6 we find λ is constrained between $\sim 1.2 - 1.4$ if $\alpha = 0.01$ and between $0.9 - 1.1$ if $\alpha = 0.1$.

Swift J2058 is another TDE candidate with many similar properties to that of *Swift* J1644 [411]. The flare had a sharp cut-off at ~ 200 d, after which the luminosity (in X-rays) dropped below 8.4×10^{42} erg s^{-1} [412], these authors also found the SMBH mass to be constrained between $10^4 - 10^6 M_\odot$. Using this upper limit on the quiescent luminosity and equation (10.25), we find $\dot{m} \lesssim 0.3/M_6$ (assuming a pre-existing accretion disc is present). We can repeat the procedure done for *Swift* J1644 to find some limits on λ (we cannot constrain λ since a quiescent luminosity was not observed, so the value of $\dot{m}$ is not known). If $\alpha = 0.01$ we do not find any limit on λ. If $\alpha = 0.1$ we find $\lambda \lesssim 1.2$ for $M_{bh} = 10^5 M_\odot$ and $\lambda \lesssim 1$ for $M_{bh} = 10^6 M_\odot$.
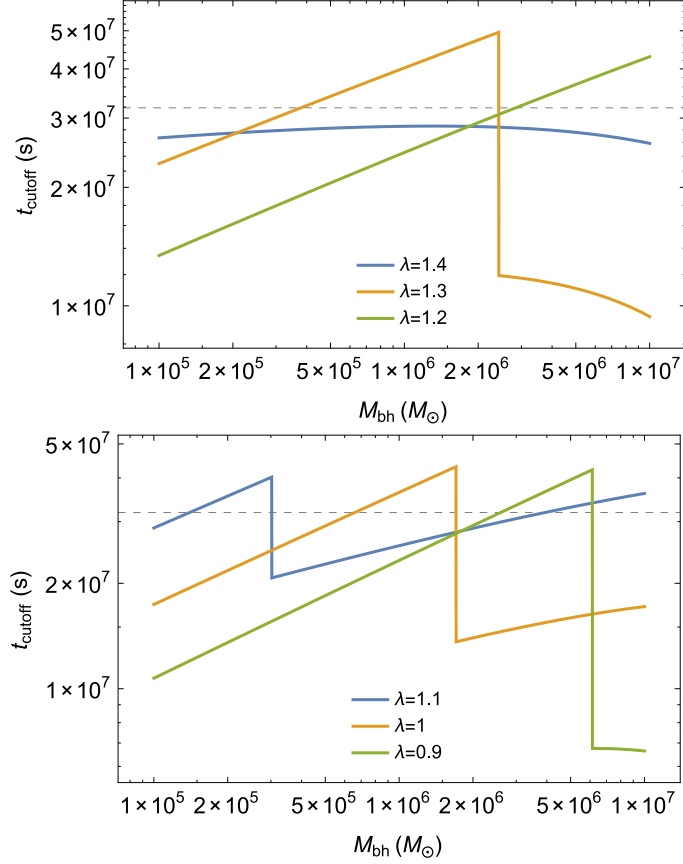
Fig. 10.6. Cut-off time versus SMBH mass for multiple values of λ. We assume a solar-type star, taking $\alpha = 0.01$ (top panel) and $\alpha = 0.1$ (bottom panel), fixing $\eta = 0.1$ using $\dot{m}$ from equation (10.25). The dashed line shows the observed cut-off time of TDE *Swift* J1644 (e.g., [410]). Given that $M_{\rm bh}$ is constrained to be $\sim 10^5 - 10^7 M_\odot$ and other values of λ do now match the observed cut-off time for this TDE, we constrain $\lambda \sim 1.2 - 1.4$ for $\alpha = 0.01$ (top panel) and $\lambda \sim 0.9 - 1.1$ for $\alpha = 0.1$ (bottom panel).

10.5.2 ASASSN-14li

The flare of ASASSN-14li event shows many similar characteristics to those of other TDE candidates, such as broad hydrogen and helium lines and strong blue continuum emission [416]. Recent X-ray observations [417] show this flare continuing for more than 600 days (hence $t_{\mathrm{cutoff}} > 600$ d). The host galaxy of ASASSN-14li shows evidence of being a weak AGN, with an estimated lower limit of $\sim 2 \times 10^{41}$ erg s^{-1} on its quiescent emission [419]. Using equation (10.25) we obtain $\dot{m} \gtrsim 2000/M_{\mathrm{bh}}$ where the SMBH mass is constrained between $10^6 - 10^7 M_\odot$ (e.g, [417]). From these limits of $\dot{m}$ and t_{cutoff} we can possibly rule out some accretion disc profiles using our model, as we describe below.

In Fig. 10.7 we plot t_{cutoff} versus $\dot{m}$ for multiple values of λ, α and M_{bh}. The dashed vertical and horizontal lines represent the lower limits on $\dot{m}$ and t_{cutoff}, respectively. Hence from observational constraints, only solutions in the shaded quadrant of each plot are valid. If $M_{\mathrm{bh}} = 10^6 M_\odot$, we find $\lambda \gtrsim 1$ for $\alpha = 0.01$ and $\lambda \gtrsim 0.7$ for $\alpha = 0.1$. If $M_{\mathrm{bh}} = 10^7 M_\odot$, we find $\lambda \gtrsim 1$ for $\alpha = 0.01$ and we do not obtain any interesting limit on λ if $\alpha = 0.1$.

For the TDEs considered in this section, their light curve cut-offs occur at or after a few hundred days since disruption. Using equation (10.7), we estimate that for a fiducial SMBH mass of $M_{\mathrm{bh}} = 10^6 M_\odot$ the distance at which we probe the pre-existing accretion disc profile is $\gtrsim 10^{-3}$ pc. Therefore, TDE observations are able to probe the gas properties very close to the SMBH, which is an important yet difficult region to probe with other methods.

10.6 Discussion and Conclusions

In this paper we have analytically explored how TDEs are affected by a pre-existing accretion disc. In particular, we find that not all the disrupted stellar material falls into the SMBH. The fallback of stellar material can be stalled due to its interaction with the pre-existing accretion disc. This yields an abrupt cut-off in the
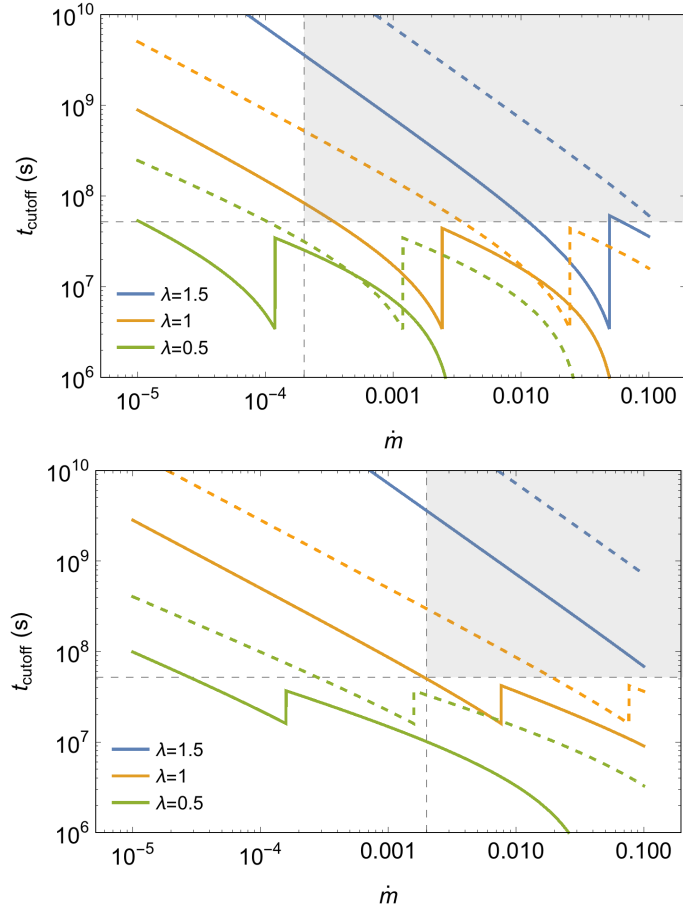
Fig. 10.7. Cut-off time versus accretion rate $\dot{m}$ for multiple values of λ with $M_{\rm bh} = 10^6 M_\odot$ (top panel) and $M_{\rm bh} = 10^7 M_\odot$ (bottom panel). We assume a solar-type star, taking $\alpha = 0.01$ (solid lines) and $\alpha = 0.1$ (dashed lines), fixing $\eta = 0.1$. Dashed vertical and horizontal lines represent the lower limits on $\dot{m}$ and $t_{\rm cutoff}$ respectively and are inferred from observations of ASASSN-14li [417, 419]. These inferred values restrict solutions to the shaded quadrant.

light curve of TDEs and this cut-off time can be used to obtain valuable information on the pre-existing accretion disc density. Our framework allows us to use TDE light curves as powerful tools in diagnosing the otherwise elusive gas properties close to the SMBHs.

We have applied our theoretical framework to TDEs in which an abrupt cut-off has been observed: *Swift* J1644 and J2508. In the first case, the sharp cut-off observed in the X-ray light curve settles to a constant luminosity, indicative of a low-luminosity AGN activity [437]. This strongly implies the presence of a pre-existing accretion disc around the SMBH for this object. These observations allow us to constrain the pre-existing accretion disc density to drop as $\propto R^{-(0.9-1.4)}$ for a disc viscosity parameter of $\alpha \sim 0.01 - 0.1$. In the second case, the sharp cut-off is also observed in the TDE X-ray light curve; however, only an upper limit is available for the emission after the sharp cut-off [412]. This allows us to constrain the pre-existing accretion disc density profile to be roughly $\propto R^{-1}$ or shallower for $\alpha \sim 0.1$. Although these two cases pertain to TDEs accompanied by a jet, our theoretical framework can also be applied to TDEs without a jet. For example, in the case of ASASSN-14li, the host galaxy shows evidence of weak AGN activity [419], which could indicate the presence of a pre-existing accretion disc. Even though this TDE does not display an abrupt cut-off in its light curve, a meaningful constrain can still be obtained with the absence of a cut-off. We find that the pre-existing accretion disc profile in this case must be roughly $\propto R^{-1}$ or steeper for $\alpha \sim 0.01$, since shallower profiles would have already prevented the stellar material from reaching the SMBH, in which case the abrupt cut-off should have already been detected.

Radio observations of TDEs provide an independent method of constraining the gas density close to the SMBH. This is done by modelling the radio emission assuming that it originates in a shock, which is produced as a TDE outflow interacts with the gas surrounding the SMBH. For example, for the case of *Swift* J1644, [439] estimate a density profile of $\lambda \sim 1.5$ at a distance of ~ 0.1 pc from the SMBH (albeit with a steeper profile for $\lesssim 0.1$ pc). A density profile of $\lambda \sim 2.5$ is estimated for ASASSN-14li

on a scale of ~ 0.01 pc [418]. Although our findings above are roughly consistent with these profiles, our method probes the density profile at much smaller scales, of the order of 10^{-3} pc. Densities inferred at larger scales might reflect densities close to (or beyond) the Bondi radius.

We now briefly investigate the detectability of the emission which could arise from the shocked BDS and show that it would be observationally unimportant. To estimate the luminosity of the shocked BDS we need the mass of the shocked material M_{sh}, which can be found by integrating $\dot{M}_{\mathrm{fb}}(t)$ in equation (10.24) from t_{cutoff} to infinity. From the shock jump conditions, the internal energy of this shocked material is $\approx M_{\mathrm{sh}} v_{\mathrm{sh}}^2$ where v_{sh} is of the order of the sound speed ($c_{\mathrm{s}} \approx 1.6 \times 10^6$ cm/s) at the cut-off time. This internal energy provides an upper limit for the emission of the shocked fluid. Hence the observed luminosity should be less than $\approx M_{\mathrm{sh}} v_{\mathrm{sh}}^2 / t_{\mathrm{cutoff}} \sim 10^{35}$ erg/s, which would be quite difficult to detect.

After the BDS is stalled, it is reasonable to expect that the stalled material will accrete on to the SMBH at a much larger time given by the accretion timescale. If the accretion of this stalled material is powerful enough, it could lead to a rise in the quiescent luminosity which would last also on the order of the accretion timescale. From the cut-off time, we can obtain a cut-off distance using equation (10.7) and use it to estimate the accretion timescale ($\sim R/\alpha v_{\mathrm{k}}$). For typical parameters of r_*, m_*, M_6, μ and λ of order unity, the accretion timescale is ~ 10 yrs, and the corresponding accretion rate of the stalled material is $\sim 0.01 \dot{M}_{\mathrm{edd}}$. Therefore, if the quiescent accretion rate of the AGN is lower than this value, the accretion of the stalled material could lead to a flare that would last ~ 10 yrs. These calculations assume the BDS was stalled by shocks (see equation 10.15). On a more speculative note, this could explain the recent observations of a decade long TDE flare presented in [440].

So far, it seems that tidal disruption flares with jetted emission have produced an easily observable cut-off in their light curves. In addition to the two *Swift* candidates mentioned in this paper, *Swift* J1112 is another TDE candidate in which a cut-off may also have been observed [441]. This cut-off has previously been attributed to the

accretion rate transitioning from super- to sub-Eddington values (e.g., [413,442–444]). However, if this cut-off did occur due to the presence of a pre-existing disc, as proposed in this work, it would be more easily detectable in a jetted flare because its emission would be brighter due to beaming effects (see section 10.3.5). If this is the case, it is worth investigating the correlation between observed jetted TDE flares and AGN activity, since numerical studies show that a pre-existing disc may be required to produce a jet during TDEs [413, 414].

In order to develop a complete analytic model, some simplifications have been made. We assume a complete stellar disruption and a penetration parameter of $\beta = r_{\rm t}/r_{\rm p} = 1$. We further assume a spherically symmetric density distribution for the disc in order to mimic a thick pre-existing accretion disc, whereas in reality the disc will have some poloidal density structure. Also, our theoretical analysis is performed only at the apocentre passage of the BDS. In addition, we do not consider magnetic fields in the pre-existing disc nor in the BDS, but numerical studies suggest that including these fields may shorten the cut-off time. Recent simulations by [445] show that the magnetic pressure in the BDS might cause the stream to break self-gravity faster than at the time of recombination. This makes the stream more susceptible to interactions with the disc thereby shortening the light curve cut-off time. Magnetic fields within the disc might amplify the drag force on the BDS and enhance the instabilities across the disc-stream interface, thereby stalling the BDS more efficiently [414]. Hence the exclusion of magnetic fields in our work gives an upper limit on the cut-off times. These issues remain to be investigated through numerical simulations which follow the entire stream, consider magnetic fields in the stream and pre-existing accretion disc and also consider the accretion disc structure. Such simulations will also allow us to determine the slope of the light curve after $t_{\rm cutoff}$, which cannot be predicted by our current model.

We encourage long-term observations of TDE candidates to see if an abrupt cut-off is observed in their light curves, which can be caused by a pre-existing accretion disc. Also, identifying the quiescent luminosity that the TDE light curve settles to

would indicate the level at which a possible low-luminosity AGN radiates. These two pieces of information, along with a constrain on the mass of the SMBH, would allow us to determine the gas density profile well-below the Bondi radius. Even the absence of a TDE light curve cut-off yields important constrains on the gas density profile (as demonstrated in the case of ASASSN-14li). Long-term observations may also be able to detect the late time emission associated with the accretion of the stalled stellar material, as briefly discussed above.

In the future, we can apply our theory to X-ray observations of some TDE host galaxies. As an example, we will consider a *Chandra* observation of the host galaxy of TDE XMMSL1 J0740-85 [446] during cycle 19. Latest observations of this TDE and its host galaxy gives us a lower limit on the cut-off time at ~ 1 year and an upper limit in the quiescent X-ray emission at $\sim 5 \times 10^{40}$ erg/s [446]. These limits already exclude the steepest density profiles of $\lambda \sim 0.5$ for the pre-existing accretion disc (see Fig. 10.8).

The observations during *Chandra* cycle 19 will take place ~ 3 years after the detection of XMMSL1 J0740-85, we present a hypothetical scenario where an upper limit of $t_{\rm cutoff} \lesssim 3$ years is obtained during this cycle. Using this assumption, we show how our theory can be used to infer properties of the pre-existing disc, this is presented in Fig. 10.8. For example, if a quiescent luminosity of 10^{40} erg/s is detected by *Chandra*, the limits $1 \leq t_{\rm cutoff} \leq 3$ years constrains the density profile of the pre-existing disk at $0.6 \lesssim \lambda \lesssim 0.8$ for a viscosity parameter of $\eta = 0.01$.
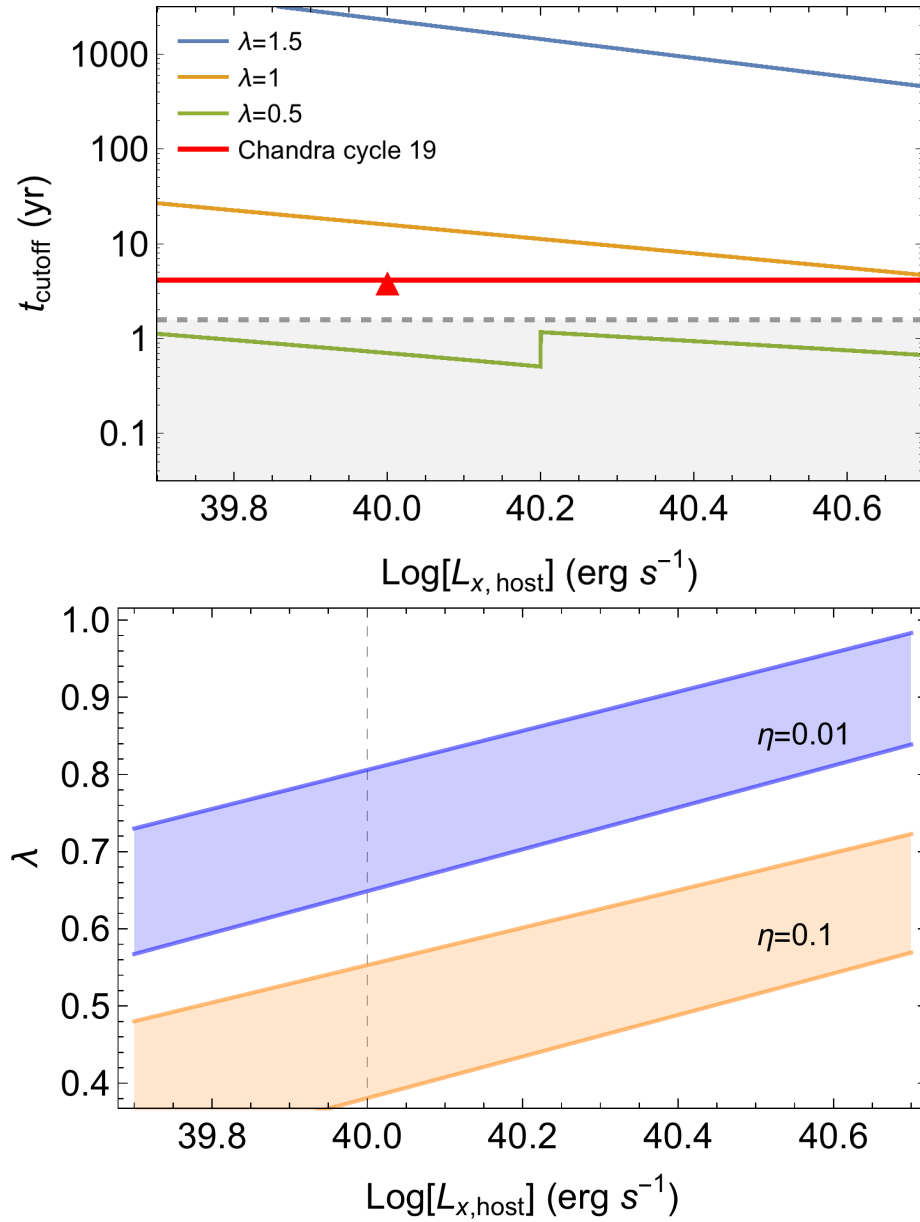
Fig. 10.8. **Top:** Model-predicted t_{cutoff} (eq. 10.23b) as a function of the X-ray luminosity (colored lines) of a LLAGN for different λ values and $\eta = 0.01$ Model predictions falling in the shaded region are already excluded by the lower limit on t_{cutoff} inferred from the X-ray light curve of XMMSL1 J0740-85. A possible X-ray detection of the host galaxy at 10^{40} erg s^{-1} during Cycle 19 (red line) is marked with a red triangle. **Bottom:** Constraints placed on λ as a function of L_X from a probable *Chandra* detection of $t_{\mathrm{cutoff}} \lesssim 3$ yrs for $\eta = 0.01$ and 0.1.

11. CONCLUSIONS AND OUTLOOK

We have investigated a wide range of phenomena that are all produced by the death of stars in uncommon ways, these phenomena are categorized as transients and their detection falls under the field of time domain astronomy. Using analytic, semi-analytic and numerical methods, we have modeled the emission of these transients and have identified their observational implications. Our research has already been utilized by multiple astronomers in order to interpret observations of transients and constraint the properties of their source and its environment. Our work is especially timely due to the rapid growth in time domain astronomy, which has been possible due to the current and upcoming surveys in radio (e.g., SKA, VAST, VLA), optical (e.g., PTF, LSST) and X-ray (e.g., *Fermi, Swift*). Additionally, this field has recently undergone a revolutionary change after the advent of cutting edge gravitational wave detectors (LIGO, VIRGO), which has made it possible to detect transients in both gravitational and electromagnetic waves. This was demonstrated by the first ever detection of a NS merger (GW170817) in both gravitational and electromagnetic waves, which heralded a new era of multi-messenger astronomy. Our work on the transients of NS mergers successfully predicted the first observed electromagnetic counterpart of GW170817. Subsequent observations and further analysis confirmed our explanation behind the origin of the electromagnetic counterpart, and using numerical simulations, we were able to successfully reproduce the observed emission. This work has helped unravel many of the peculiar characteristics of GW170817, and currently, our interpretation is widely used by astronomers to explain the emission observed from this event.

With this robust test and applicability of our model, we are now poised to investigate them further for general cases, with increasing sophistication and rigor. This study will be useful in preparation for the numerous multimessenger transients expected to be detected in the near future.

APPENDICES

Table 1.

Different parameters considered in Figure 1 that match the on-axis optical flux at 1 d for the 5th decile. The rows are arranged in the order of descending flux of the light curves (in Figure 1) at 200 days. For example, the first row corresponds to the parameters of the light curve with the brightest flux at 200 days (at 0° and 20°). The row in italics indicates the set of parameters used for the afterglow light curves in the bottom panel of Figure 3.1 (dashed lines in Figure 1).

ϵ_B	n [cm^{-3}]	E_{iso} [erg]	η [%]
2×10^{-4}	0.1	9×10^{53}	4
3×10^{-3}	0.1	2×10^{53}	20
9×10^{-5}	1	7×10^{53}	5
8×10^{-4}	*1*	*2×10^{53}*	*20*
1×10^{-2}	1	4×10^{52}	100
2×10^{-4}	10	2×10^{53}	20

.1   Optical afterglow light curves for various parameters

In Section 3.2.1 we considered a set of parameters that matches the optical flux at 1 day for each decile. These parameters were used to calculate the off-axis optical light curves and to estimate an approximate critical angle, $\theta_{\text{v,crit}}$ (see section 3.3.1). Here we show that our conclusions on $\theta_{\text{v,crit}}$ remain approximately the same when we consider different sets of parameters that also match the optical flux at 1 day. We allow n, E_{iso} and ϵ_B to vary in a large range (see Figure 1 and Table .1) while fixing $\epsilon_e = 0.1$ and $\theta_j = 0.2$. For the parameters considered in this Appendix, $\theta_{\text{v,crit}}$ remains approximately the same until the 5th decile. For lower deciles, $\theta_{\text{v,crit}}$ is smaller since the on-axis optical afterglow emission is weaker, just as discussed in Section 3.4.
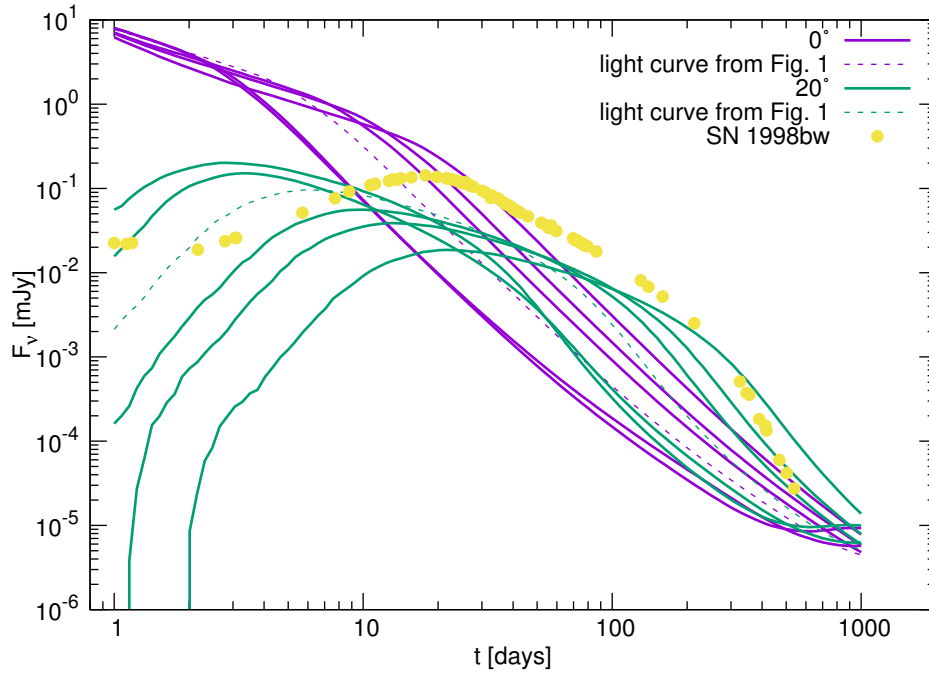
Fig. 1. Optical ($\sim$ 2 eV) GRB afterglow light curves (lines) both on-axis (0°, these have a flux of $\sim$ 5 mJy at 1 day) and off-axis (20°) for multiple parameters (see Table .1) and the SN optical emission (points); for the latter we use observations of SN 1998bw. The GRB afterglow light curves are modeled from afterglow observations in the 5th decile. Dashed lines correspond to the light curves in the bottom panel of Fig. 1 (its parameters are in italics in Table 1). The SN optical emission outshines the off-axis afterglow emission unless the viewing angle is very close to twice the half-opening angle of the GRB jet ($\theta_j = 0.2$). We fix $\epsilon_e = 0.1$, source is placed at a distance $d_L = 300$ Mpc. Afterglow light curves are produced with the Afterglow Library ([30])

.2 Conditions for a shock in the BDS

The temperature evolution of a tidally disrupted debris stream (for a solar-type star) has been studied by [431] Initially, the debris stream evolves adiabatically until recombination starts when $T = T_{\rm rec} \sim 10^4 {\rm K}$, at which point the volume of the stream is $V_{\rm rec}$. During recombination, the temperature of the star remains roughly constant until its volume has expanded to $V' \sim (15)^3 V_{\rm rec}$ [431]. After this point, the stream continues to evolve adiabatically. So the temperature of the stream ($T_{\rm s}$) as a function of volume is given by

$$
T_{\rm s} \approx
\begin{cases}
T_* \left(\dfrac{V_*}{V}\right)^{\frac{2}{3}} & V_* \leq V \leq V_{\rm rec} & (1{\rm a}) \\[2ex]
T_{\rm rec} & V_{\rm rec} \leq V \leq V' & (1{\rm b}) \\[2ex]
T_{\rm rec} \left(\dfrac{V'}{V}\right)^{\frac{2}{3}} & V \geq V' & (1{\rm c})
\end{cases}
$$

where V_* and T_* are the initial volume and temperature of the star, and

$$
V = \pi \left(\frac{h}{2}\right)^2 r \tag{2}
$$

is the volume of the stream. Using equations (10.6) and (10.7) we can obtain how $T_{\rm s}$ evolves with time. For the relevant timescales discussed in the main text, we only need (1c) to describe the temperature of the BDS. We find

$$
T_{\rm s} \approx \frac{(15)^2 \pi^{\frac{4}{9}} 2^{\frac{1}{6}} G^{\frac{7}{9}} m_{\rm p}}{3^{\frac{2}{3}} c_{\rm s}^{\frac{4}{3}} k_{\rm b}} R_* M_* M_{\rm bh}^{-\frac{2}{9}} t^{-\frac{16}{9}}, \tag{3}
$$

where $k_{\rm b}$ is the Boltzmann constant.

The temperature of the shocked debris fluid ($T_{\rm sh}$) can be obtained using the shock jump conditions

$$
T_{\rm sh} \approx \frac{5}{16} \frac{m_{\rm p}}{\gamma k_{\rm b}} v_{\rm sh}^2 + \frac{7}{8} T_{\rm s} \approx 2 \times 10^{-9} v_{\rm sh}^2 + \frac{7}{8} T_{\rm s} \tag{4}
$$

Where $\gamma = 5/3$ and $v_{\rm sh}$ is given in equation (10.13). In order for a shock to exist (at $t_{\rm shock}$), we require the Mach number, $v_{\rm sh}/c_{\rm sound} \geq 1$. From the Rankine-Hugoniot

conditions we find this is equivalent to saying $T_{\mathrm{sh}}/T_{\mathrm{s}} \geq 1$. Evaluating this temperature ratio at t_{shock} we find

$$\frac{T_{\mathrm{sh}}}{T_{\mathrm{s}}}(t_{\mathrm{shock}}) = \frac{c_{\mathrm{s}}^{\frac{10}{3}}}{\gamma R_*}\left(\frac{3^{-5}5^3 c^{-16}}{2^{\frac{219}{2}}\pi^{12}G^7}\left(\frac{\mu\sigma_{\mathrm{T}}}{m_{\mathrm{p}}}\right)^8\frac{M_{\mathrm{bh}}^2}{M_*}\left(\frac{3^7\,2^{\frac{49}{2}}c^{16}M_*^3}{\pi^4\,5^5\,G^3 M_{\mathrm{bh}}^6}\right)^\lambda\right)^{\frac{1}{3(3-\lambda)}} + \frac{7}{8}. \qquad (5)$$

From this equation we can, for instance, find a constraint on the SMBH mass for which a shock exists, and it is given by

$$M_{\mathrm{bh}} \leq \left(\frac{3^{-5}\,5^3\,c_{\mathrm{s}}^{30}c^{-16}\gamma^{-9}}{2^{\frac{165}{2}}\pi^{12}\,G^7 R_*^9\,M_*}\left(\frac{\mu\sigma_{\mathrm{T}}}{m_{\mathrm{p}}}\right)^8\left(\frac{3^7\,2^{\frac{31}{2}}c^{16}\gamma^3 R_*^3 M_*^3}{\pi^4\,5^5\,G^3\,c_{\mathrm{s}}^{10}}\right)^\lambda\right)^{\frac{1}{2(3\lambda-1)}}. \qquad (6)$$

This expression allows us to analytically determine the SMBH mass at which the stalling mechanism of the BDS transitions from shock-crossing to momentum imparted by the disk (this transition is seen as a discontinuous jump in Fig. 10.1 and Fig. 10.6).

REFERENCES

[1] L. D. Landau and E. M. Lifshitz, *Fluid mechanics*, 1959.

[2] G. B. Rybicki and A. P. Lightman, *Radiative processes in astrophysics*, 1979.

[3] T. Piran, "The physics of gamma-ray bursts," *Reviews of Modern Physics*, vol. 76, pp. 1143–1210, Oct. 2004.

[4] P. Kumar and B. Zhang, "The physics of gamma-ray bursts and relativistic jets," *Physics Reports*, vol. 561, pp. 1–109, Feb. 2015.

[5] R. D. Blandford and C. F. McKee, "Fluid dynamics of relativistic blast waves," *Physics of Fluids*, vol. 19, pp. 1130–1138, Aug. 1976.

[6] C. D. Dermer and G. Menon, *High Energy Radiation from Black Holes: Gamma Rays, Cosmic Rays, and Neutrinos*, 2009.

[7] E. Waxman, "Gamma-ray bursts and collisionless shocks," *Plasma Physics and Controlled Fusion*, vol. 48, pp. B137–B151, Dec 2006.

[8] C. Hededal, "Gamma-Ray Bursts, Collisionless Shocks and Synthetic Spectra," Ph.D. dissertation, -, Jun 2005.

[9] B. Paczynski and J. E. Rhoads, "Radio Transients from Gamma-Ray Bursters," *Astrophysical Journal Letters*, vol. 418, p. L5, Nov. 1993.

[10] C. D. Matzner and C. F. McKee, "The Expulsion of Stellar Envelopes in Core-Collapse Supernovae," *Astrophysical Journal*, vol. 510, pp. 379–403, Jan. 1999.

[11] J. C. Tan, C. D. Matzner, and C. F. McKee, "Trans-relativistic blast waves in supernovae as gamma-ray burst progenitors," *Astrophysical Journal*, vol. 551, no. 2, p. 946, 2001.

[12] R. Margutti, A. M. Soderberg, M. H. Wieringa, P. G. Edwards, R. A. Chevalier, B. J. Morsony, R. Barniol Duran, L. Sironi, B. A. Zauderer, D. Milisavljevic, A. Kamble, and E. Pian, "The Signature of the Central Engine in the Weakest Relativistic Explosions: GRB 100316D," *Astrophysical Journal*, vol. 778, p. 18, Nov. 2013.

[13] M. J. Rees, "Appearance of Relativistically Expanding Radio Sources," *Nature*, vol. 211, pp. 468–470, Jul 1966.

[14] R. Sari, "Hydrodynamics of Gamma-Ray Burst Afterglow," *Astrophysical Journal Letters*, vol. 489, pp. L37–L40, Nov. 1997.

[15] G. Taylor, "The Formation of a Blast Wave by a Very Intense Explosion. I. Theoretical Discussion," *Proceedings of the Royal Society of London Series A*, vol. 201, pp. 159–174, Mar. 1950.

[16] L. I. Sedov, *Similarity and Dimensional Methods in Mechanics*, 1959.

[17] R. Sari, T. Piran, and R. Narayan, "Spectra and Light Curves of Gamma-Ray Burst Afterglows," *Astrophysical Journal Letters*, vol. 497, pp. L17–L20, Apr. 1998.

[18] E. Fermi, "On the Origin of the Cosmic Radiation," *Physical Review*, vol. 75, pp. 1169–1174, Apr. 1949.

[19] M. G. Baring, "Diffusive Shock Acceleration : the Fermi Mechanism." in *Very High Energy Phenomena in the Universe; Moriond Workshop*, Y. Giraud-Heraud and J. Tran Thanh van, Eds., 1997, p. 97.

[20] J. Granot and R. Sari, "The Shape of Spectral Breaks in Gamma-Ray Burst Afterglows," *Astrophysical Journal*, vol. 568, pp. 820–829, Apr. 2002.

[21] R. Barniol Duran, E. Nakar, T. Piran, and R. Sari, "The afterglow of a relativistic shock breakout and low-luminosity grbs," *Monthly Notices of the Royal Astronomical Society*, vol. 448, no. 1, pp. 417–428, 2015.

[22] K. Leventis, H. J. van Eerten, Z. Meliani, and R. A. M. J. Wijers, "Practical flux prescriptions for gamma-ray burst afterglows, from early to late times," *Monthly Notices of the Royal Astronomical Society*, vol. 427, pp. 1329–1343, Dec. 2012.

[23] R. D. Blandford and J. P. Ostriker, "Particle acceleration by astrophysical shocks," *Astrophysical Journal Letters*, vol. 221, pp. L29–L32, Apr. 1978.

[24] R. Blandford and D. Eichler, "Particle acceleration at astrophysical shocks: A theory of cosmic ray origin," *Physics Reports*, vol. 154, pp. 1–75, Oct. 1987.

[25] L. Sironi and D. Giannios, "A late-time flattening of light curves in gamma-ray burst afterglows," *Astrophysical Journal*, vol. 778, no. 2, p. 107, 2013.

[26] J. E. Rhoads, "The Dynamics and Light Curves of Beamed Gamma-Ray Burst Afterglows," *Astrophysical Journal*, vol. 525, pp. 737–749, Nov. 1999.

[27] R. Sari, T. Piran, and J. P. Halpern, "Jets in Gamma-Ray Bursts," *Astrophysical Journal Letters*, vol. 519, pp. L17–L20, Jul. 1999.

[28] J. Granot, M. Miller, T. Piran, W. M. Suen, and P. A. Hughes, "Light Curves from an Expanding Relativistic Jet," in *Gamma-ray Bursts in the Afterglow Era*, E. Costa, F. Frontera, and J. Hjorth, Eds., 2001, p. 312.

[29] P. Kumar and J. Granot, "The Evolution of a Structured Relativistic Jet and Gamma-Ray Burst Afterglow Light Curves," *Astrophysical Journal*, vol. 591, pp. 1075–1085, Jul. 2003.

[30] H. J. van Eerten and A. I. MacFadyen, "Observational implications of gamma-ray burst afterglow jet simulations and numerical light curve calculations," *Astrophysical Journal*, vol. 751, no. 2, p. 155, 2012.

[31] A. Kathirgamaraju, A. Tchekhovskoy, D. Giannios, and R. Barniol Duran, "EM counterparts of structured jets from 3D GRMHD simulations," *arXiv e-prints*, p. arXiv:1809.05099, Sep. 2018.

[32] R. Wijers and T. Galama, "Physical parameters of grb 970508 and grb 971214 from their afterglow synchrotron emission," *Astrophysical Journal*, vol. 523, no. 1, p. 177, 1999.

[33] A. Panaitescu and P. Kumar, "Analytic light curves of gamma-ray burst afterglows: homogeneous versus wind external media," *Astrophysical Journal*, vol. 543, no. 1, p. 66, 2000.

[34] J. E. Rhoads, "How to tell a jet from a balloon: A proposed test for beaming in gamma-ray bursts," *Astrophysical Journal Letters*, vol. 487, no. 1, p. L1, 1997.

[35] J. Granot, A. Panaitescu, P. Kumar, and S. E. Woosley, "Off-axis afterglow emission from jetted gamma-ray bursts," *Astrophysical Journal Letters*, vol. 570, no. 2, p. L61, 2002.

[36] T. Totani and A. Panaitescu, "Orphan Afterglows of Collimated Gamma-Ray Bursts: Rate Predictions and Prospects for Detection," *Astrophysical Journal*, vol. 576, pp. 120–134, Sep. 2002.

[37] E. Nakar, T. Piran, and J. Granot, "The Detectability of Orphan Afterglows," *Astrophysical Journal*, vol. 579, pp. 699–705, Nov. 2002.

[38] Y. C. Zou, X. F. Wu, and Z. G. Dai, "Estimation of the detectability of optical orphan afterglows," *Astronomy & Astrophysics*, vol. 461, pp. 115–119, Jan. 2007.

[39] E. M. Rossi, R. Perna, and F. Daigne, "'Orphan' afterglows in the Universal structured jet model for γ-ray bursts," *Monthly Notices of the Royal Astronomical Society*, vol. 390, pp. 675–682, Oct. 2008.

[40] S. B. Cenko, S. R. Kulkarni, A. Horesh, A. Corsi, D. B. Fox, J. Carpenter, D. A. Frail, P. E. Nugent, D. A. Perley, D. Gruber, A. Gal-Yam, P. J. Groot, G. Hallinan, E. O. Ofek, A. Rau, C. L. MacLeod, A. A. Miller, J. S. Bloom, A. V. Filippenko, M. M. Kasliwal, N. M. Law, A. N. Morgan, D. Polishook, D. Poznanski, R. M. Quimby, B. Sesar, K. J. Shen, J. M. Silverman, and A. Sternberg, "Discovery of a Cosmological, Relativistic Outburst via its Rapidly Fading Optical Emission," *Astrophysical Journal*, vol. 769, p. 130, Jun. 2013.

[41] A. Corsi, A. Gal-Yam, S. R. Kulkarni, D. A. Frail, P. A. Mazzali, S. B. Cenko, M. M. Kasliwal, Y. Cao, A. Horesh, N. Palliyaguru, D. A. Perley, R. R. Laher, F. Taddia, G. Leloudas, K. Maguire, P. E. Nugent, J. Sollerman, and M. Sullivan, "Radio observations of a sample of broad-lined type Ic supernovae discovered by PTF/iPTF: A search for relativistic explosions," *ArXiv e-prints*, Dec. 2015.

[42] M. Modjaz, Y. Q. Liu, F. B. Bianco, and O. Graur, "The Spectral SN-GRB Connection: Systematic Spectral Comparisons between Type Ic Supernovae, broad-lined Type Ic Supernovae with and without Gamma-Ray Bursts," *ArXiv e-prints*, Sep. 2015.

[43] S. E. Woosley and J. S. Bloom, "The Supernova Gamma-Ray Burst Connection," *Ann. Rev. Astron. Asrophys.*, vol. 44, pp. 507–556, Sep. 2006.

[44] J. Hjorth and J. S. Bloom, *The Gamma-Ray Burst - Supernova Connection*, Nov. 2012, pp. 169–190.

[45] A. Melandri, E. Pian, V. D?Elia, P. D?Avanzo, M. Della Valle, P. Mazzali, G. Tagliaferri, Z. Cano, A. Levan, P. M∆oller *et al.*, "Diversity of gamma-ray burst energetics vs. supernova homogeneity: Sn 2013cq associated with grb 130427a," *Astronomy & Astrophysics*, vol. 567, p. A29, 2014.

[46] R. A. Chevalier, "Self-similar solutions for the interaction of stellar ejecta with an external medium," *Astrophysical Journal*, vol. 258, pp. 790–797, Jul. 1982.

[47] ——, "The radio and X-ray emission from type II supernovae," *Astrophysical Journal*, vol. 259, pp. 302–310, Aug. 1982.

[48] ——, "Synchrotron Self-Absorption in Radio Supernovae," *Astrophysical Journal*, vol. 499, pp. 810–819, May 1998.

[49] R. Barniol Duran and D. Giannios, "Radio rebrightening of the grb afterglow by the accompanying supernova," *Monthly Notices of the Royal Astronomical Society*, vol. 454, pp. 1711–1718, 2015.

[50] B. Paczynski, "Gamma-Ray Bursts at Low Redshift," *Acta Astronomica*, vol. 51, pp. 1–4, Mar. 2001.

[51] A. Levinson, E. O. Ofek, E. Waxman, and A. Gal-Yam, "Orphan gamma-ray burst radio afterglows: candidates and constraints on beaming," *Astrophysical Journal*, vol. 576, no. 2, p. 923, 2002.

[52] E. Berger, S. Kulkarni, D. Frail, and A. Soderberg, "A radio survey of type ib and ic supernovae: Searching for engine-driven supernovae," *Astrophysical Journal*, vol. 599, no. 1, p. 408, 2003.

[53] A. M. Soderberg, D. Frail, and M. Wieringa, "Constraints on off-axis gamma-ray burst jets in type ibc supernovae from late-time radio observations," *Astrophysical Journal Letters*, vol. 607, no. 1, p. L13, 2004.

[54] A. Gal-Yam, E. O. Ofek, D. Poznanski, A. Levinson, E. Waxman, D. A. Frail, A. M. Soderberg, E. Nakar, W. Li, and A. V. Filippenko, "Radio and Optical Follow-up Observations of a Uniform Radio Transient Search: Implications for Gamma-Ray Bursts and Supernovae," *Astrophysical Journal*, vol. 639, pp. 331–339, Mar. 2006.

[55] A. Soderberg, E. Nakar, E. Berger, and S. Kulkarni, "Late-time radio observations of 68 type ibc supernovae: strong constraints on off-axis gamma-ray bursts," *Astrophysical Journal*, vol. 638, no. 2, p. 930, 2006.

[56] M. F. Bietenholz, F. De Colle, J. Granot, N. Bartel, and A. M. Soderberg, "Radio limits on off-axis GRB afterglows and VLBI observations of SN 2003gk," *Monthly Notices of the Royal Astronomical Society*, vol. 440, pp. 821–832, May 2014.

[57] G. Ghirlanda, D. Burlon, G. Ghisellini, R. Salvaterra, M. G. Bernardini, S. Campana, S. Covino, P. D'Avanzo, V. D'Elia, A. Melandri, T. Murphy, L. Nava, S. D. Vergani, and G. Tagliaferri, "GRB Orphan Afterglows in Present and Future Radio Transient Surveys," *Publications of the Astronomical Society of Australia*, vol. 31, p. e022, May 2014.

[58] B. D. Metzger, P. K. G. Williams, and E. Berger, "Extragalactic Synchrotron Transients in the Era of Wide-field Radio Surveys. I. Detection Rates and Light Curve Characteristics," *Astrophysical Journal*, vol. 806, p. 224, Jun. 2015.

[59] D. Lazzati, B. J. Morsony, C. H. Blackwell, and M. C. Begelman, "Unifying the zoo of jet-driven stellar explosions," *Astrophysical Journal*, vol. 750, no. 1, p. 68, 2012.

[60] E. Ramirez-Ruiz, A. Celotti, and M. J. Rees, "Events in the life of a cocoon surrounding a light, collapsar jet," *Monthly Notices of the Royal Astronomical Society*, vol. 337, no. 4, pp. 1349–1356, 2002.

[61] W. Zhang, S. E. Woosley, and A. Heger, "The Propagation and Eruption of Relativistic Jets from the Stellar Progenitors of Gamma-Ray Bursts," *Astrophysical Journal*, vol. 608, pp. 365–377, Jun. 2004.

[62] W. Zhang and A. MacFadyen, "The dynamics and afterglow radiation of gamma-ray bursts. i. constant density medium," *Astrophysical Journal*, vol. 698, no. 2, p. 1261, 2009.

[63] H. van Eerten and R. Wijers, "Gamma-ray burst afterglow scaling coefficients for general density profiles," *Monthly Notices of the Royal Astronomical Society*, vol. 394, no. 4, pp. 2164–2174, 2009.

[64] H. van Eerten, W. Zhang, and A. MacFadyen, "Off-axis gamma-ray burst afterglow modeling based on a two-dimensional axisymmetric hydrodynamics simulation," *Astrophysical Journal*, vol. 722, no. 1, p. 235, 2010.

[65] H. van Eerten, K. Leventis, Z. Meliani, R. Wijers, and R. Keppens, "Gamma-ray burst afterglows from transrelativistic blast wave simulations," *Monthly Notices of the Royal Astronomical Society*, vol. 403, no. 1, pp. 300–316, 2010.

[66] H. J. van Eerten and A. I. MacFadyen, "Synthetic off-axis light curves for low-energy gamma-ray bursts," *Astrophysical Journal Letters*, vol. 733, no. 2, p. L37, 2011.

[67] J. Granot, E. Ramirez-Ruiz, G. B. Taylor, D. Eichler, Y. E. Lyubarsky, R. A. M. J. Wijers, B. M. Gaensler, J. D. Gelfand, and C. Kouveliotou, "Diagnosing the Outflow from the SGR 1806-20 Giant Flare with Radio Observations," *Astrophysical Journal*, vol. 638, pp. 391–396, Feb. 2006.

[68] D. Kann, S. Klose, B. Zhang, D. Malesani, E. Nakar, A. Pozanenko, A. Wilson, N. Butler, P. Jakobsson, S. Schulze *et al.*, "The afterglows of swift-era gamma-ray bursts. i. comparing pre-swift and swift-era long/soft (type ii) grb optical afterglows," *Astrophysical Journal*, vol. 720, no. 2, p. 1513, 2010.

[69] P. Beniamini, L. Nava, R. B. Duran, and T. Piran, "Energies of GRB blast waves and prompt efficiencies as implied by modelling of X-ray and GeV afterglows," *Monthly Notices of the Royal Astronomical Society*, vol. 454, pp. 1073–1085, Nov. 2015.

[70] R. Santana, R. Barniol Duran, and P. Kumar, "Magnetic Fields in Relativistic Collisionless Shocks," *Astrophysical Journal*, vol. 785, p. 29, Apr. 2014.

[71] P. A. Curran, P. A. Evans, M. de Pasquale, M. J. Page, and A. J. van der Horst, "On the Electron Energy Distribution Index of Swift Gamma-ray Burst Afterglows," *Astrophysical Journal Letters*, vol. 716, pp. L135–L139, Jun. 2010.

[72] R. Barniol Duran, "Constraining the magnetic field in GRB relativistic collisionless shocks using radio data," *Monthly Notices of the Royal Astronomical Society*, vol. 442, pp. 3147–3154, Aug. 2014.

[73] L. Sironi and A. Spitkovsky, "Particle Acceleration in Relativistic Magnetized Collisionless Electron-Ion Shocks," *Astrophysical Journal*, vol. 726, p. 75, Jan. 2011.

[74] G. Ghirlanda, G. Ghisellini, and C. Firmani, "Probing the existence of the E_{peak}-E_{iso} correlation in long gamma ray bursts," *Monthly Notices of the Royal Astronomical Society*, vol. 361, pp. L10–L14, Jul. 2005.

[75] A. Goldstein, V. Connaughton, M. S. Briggs, and E. Burns, "Estimating Long GRB Jet Opening Angles and Rest-frame Energetics," *Astrophysical Journal*, vol. 818, p. 18, Feb. 2016.

[76] P. Chandra and D. A. Frail, "A Radio-selected Sample of Gamma-Ray Burst Afterglows," *Astrophysical Journal*, vol. 746, p. 156, Feb. 2012.

[77] K. Iwamoto, P. A. Mazzali, K. Nomoto, H. Umeda, T. Nakamura, F. Patat, I. J. Danziger, T. R. Young, T. Suzuki, T. Shigeyama, T. Augusteijn, V. Doublier, J.-F. Gonzalez, H. Boehnhardt, J. Brewer, O. R. Hainaut, C. Lidman, B. Leibundgut, E. Cappellaro, M. Turatto, T. J. Galama, P. M. Vreeswijk, C. Kouveliotou, J. van Paradijs, E. Pian, E. Palazzi, and F. Frontera, "A hypernova model for the supernova associated with the γ-ray burst of 25 April 1998," *Nature*, vol. 395, pp. 672–674, Oct. 1998.

[78] A. Clocchiatti, N. B. Suntzeff, R. Covarrubias, and P. Candia, "The Ultimate Light Curve of SN 1998bw/GRB 980425," *Astronomical Journal*, vol. 141, p. 163, May 2011.

[79] R. A. Chevalier and C. Fransson, "Circumstellar Emission from Type Ib and Ic Supernovae," *Astrophysical Journal*, vol. 651, pp. 381–391, Nov. 2006.

[80] J. C. Tan, C. D. Matzner, and C. F. McKee, "Trans-Relativistic Blast Waves in Supernovae as Gamma-Ray Burst Progenitors," *Astrophysical Journal*, vol. 551, pp. 946–972, Apr. 2001.

[81] R. Sari and P. Mészáros, "Impulsive and Varying Injection in Gamma-Ray Burst Afterglows," *Astrophysical Journal Letters*, vol. 535, pp. L33–L37, May 2000.

[82] A. Panaitescu and P. Kumar, "The slow decay of some radio afterglows - a puzzle for the simplest γ-ray burst fireball model," *Monthly Notices of the Royal Astronomical Society*, vol. 350, pp. 213–231, May 2004.

[83] G. Ghirlanda, R. Salvaterra, S. Campana, S. D. Vergani, J. Japelj, M. G. Bernardini, D. Burlon, P. D'Avanzo, A. Melandri, A. Gomboc, F. Nappo, R. Paladini, A. Pescalli, O. S. Salafia, and G. Tagliaferri, "Unveiling the population of orphan γ-ray bursts," *Astronomy & Astrophysics*, vol. 578, p. A71, Jun. 2015.

[84] T. Murphy, S. Chatterjee, D. L. Kaplan, J. Banyer, M. E. Bell, H. E. Bignall, G. C. Bower, R. A. Cameron, D. M. Coward, J. M. Cordes, S. Croft, J. R. Curran, S. G. Djorgovski, S. A. Farrell, D. A. Frail, B. M. Gaensler, D. K. Galloway, B. Gendre, A. J. Green, P. J. Hancock, S. Johnston, A. Kamble, C. J. Law, T. J. W. Lazio, K. K. Lo, J.-P. Macquart, N. Rea, U. Rebbapragada, C. Reynolds, S. D. Ryder, B. Schmidt, R. Soria, I. H. Stairs, S. J. Tingay, U. Torkelsson, K. Wagstaff, M. Walker, R. B. Wayth, and P. K. G. Williams, "VAST: An ASKAP Survey for Variables and Slow Transients," *Publications of the Astronomical Society of Australia*, vol. 30, p. e006, Feb. 2013.

[85] D. Wanderman and T. Piran, "The luminosity function and the rate of Swift's gamma-ray bursts," *Monthly Notices of the Royal Astronomical Society*, vol. 406, pp. 1944–1958, Aug. 2010.

[86] D. Guetta, T. Piran, and E. Waxman, "The Luminosity and Angular Distributions of Long-Duration Gamma-Ray Bursts," *Astrophysical Journal*, vol. 619, pp. 412–419, Jan. 2005.

[87] T. Oosterloo, M. Verheijen, and W. van Cappellen, "The latest on Apertif," in *ISKAF2010 Science Meeting*, 2010, p. 43.

[88] R. S. Booth, W. J. G. de Blok, J. L. Jonas, and B. Fanaroff, "MeerKAT Key Project Science, Specifications, and Proposals," *ArXiv e-prints*, Oct. 2009.

[89] R. A. Perley, C. J. Chandler, B. J. Butler, and J. M. Wrobel, "The Expanded Very Large Array: A New Telescope for New Science," *Astrophysical Journal Letters*, vol. 739, p. L1, Sep. 2011.

[90] C. L. Carilli and S. Rawlings, "Motivation, key science projects, standards and assumptions," *NAR*, vol. 48, pp. 979–984, Dec. 2004.

[91] A. M. Soderberg, S. R. Kulkarni, E. Berger, D. W. Fox, M. Sako, D. A. Frail, A. Gal-Yam, D. S. Moon, S. B. Cenko, S. A. Yost, M. M. Phillips, S. E. Persson, W. L. Freedman, P. Wyatt, R. Jayawardhana, and D. Paulson, "The sub-energetic γ-ray burst GRB 031203 as a cosmic analogue to the nearby GRB 980425," *Nature*, vol. 430, pp. 648–650, Aug. 2004.

[92] D. Giannios, "Superflares from magnetars revealing the GRB central engine," *Monthly Notices of the Royal Astronomical Society*, vol. 403, pp. L51–L53, Mar. 2010.

[93] J. van Paradijs, C. Kouveliotou, and R. A. M. J. Wijers, "Gamma-Ray Burst Afterglows," *Ann. Rev. Astron. Asrophys.*, vol. 38, pp. 379–425, 2000.

[94] D. A. Frail, S. R. Kulkarni, R. Sari, S. G. Djorgovski, J. S. Bloom, T. J. Galama, D. E. Reichart, E. Berger, F. A. Harrison, P. A. Price, S. A. Yost, A. Diercks, R. W. Goodrich, and F. Chaffee, "Beaming in Gamma-Ray Bursts: Evidence for a Standard Energy Reservoir," *Astrophysical Journal Letters*, vol. 562, pp. L55–L58, Nov. 2001.

[95] P. Mészáros, "Theories of Gamma-Ray Bursts," *Ann. Rev. Astron. Asrophys.*, vol. 40, pp. 137–169, 2002.

[96] N. Gehrels, E. Ramirez-Ruiz, and D. B. Fox, "Gamma-Ray Bursts in the Swift Era," *Ann. Rev. Astron. Asrophys.*, vol. 47, pp. 567–617, Sep. 2009.

[97] E. Costa, F. Frontera, J. Heise, M. Feroci, J. in't Zand, F. Fiore, M. N. Cinti, D. Dal Fiume, L. Nicastro, M. Orlandini, E. Palazzi, M. Rapisarda#, G. Zavattini, R. Jager, A. Parmar, A. Owens, S. Molendi, G. Cusumano, M. C. Maccarone, S. Giarrusso, A. Coletta, L. A. Antonelli, P. Giommi, J. M. Muller, L. Piro, and R. C. Butler, "Discovery of an X-ray afterglow associated with the γ-ray burst of 28 February 1997," *Nature*, vol. 387, pp. 783–785, Jun. 1997.

[98] J. van Paradijs, P. J. Groot, T. Galama, C. Kouveliotou, R. G. Strom, J. Telting, R. G. M. Rutten, G. J. Fishman, C. A. Meegan, M. Pettini, N. Tanvir, J. Bloom, H. Pedersen, H. U. Nørdgaard-Nielsen, M. Linden-Vørnle, J. Melnick, G. van der Steene, M. Bremer, R. Naber, J. Heise, J. in't Zand, E. Costa, M. Feroci, L. Piro, F. Frontera, G. Zavattini, L. Nicastro, E. Palazzi, K. Bennett, L. Hanlon, and A. Parmar, "Transient optical emission from the error box of the γ-ray burst of 28 February 1997," *Nature*, vol. 386, pp. 686–689, Apr. 1997.

[99] D. A. Frail, S. R. Kulkarni, L. Nicastro, M. Feroci, and G. B. Taylor, "The radio afterglow from the γ-ray burst of 8 May 1997," *Nature*, vol. 389, pp. 261–263, Sep. 1997.

[100] D. A. Frail, E. Waxman, and S. R. Kulkarni, "A 450 Day Light Curve of the Radio Afterglow of GRB 970508: Fireball Calorimetry," *Astrophysical Journal*, vol. 537, pp. 191–204, Jul. 2000.

[101] R. Sari, T. Piran, and R. Narayan, "Spectra and Light Curves of Gamma-Ray Burst Afterglows," *Astrophysical Journal Letters*, vol. 497, pp. L17–L20, Apr. 1998.

[102] J. Granot and A. J. van der Horst, "Gamma-Ray Burst Jets and their Radio Observations," *PASA*, vol. 31, p. e008, Feb. 2014.

[103] T. J. Galama, P. M. Vreeswijk, J. van Paradijs, C. Kouveliotou, T. Augusteijn, H. Böhnhardt, J. P. Brewer, V. Doublier, J.-F. Gonzalez, B. Leibundgut, C. Lidman, O. R. Hainaut, F. Patat, J. Heise, J. in't Zand, K. Hurley, P. J. Groot, R. G. Strom, P. A. Mazzali, K. Iwamoto, K. Nomoto, H. Umeda, T. Nakamura, T. R. Young, T. Suzuki, T. Shigeyama, T. Koshut, M. Kippen, C. Robinson, P. de Wildt, R. A. M. J. Wijers, N. Tanvir, J. Greiner, E. Pian, E. Palazzi, F. Frontera, N. Masetti, L. Nicastro, M. Feroci, E. Costa, L. Piro, B. A. Peterson, C. Tinney, B. Boyle, R. Cannon, R. Stathakis, E. Sadler, M. C. Begam, and P. Ianna, "An unusual supernova in the error box of the γ-ray burst of 25 April 1998," *Nature*, vol. 395, pp. 670–672, Oct. 1998.

[104] J. Hjorth, J. Sollerman, P. Møller, J. P. U. Fynbo, S. E. Woosley, C. Kouveliotou, N. R. Tanvir, J. Greiner, M. I. Andersen, A. J. Castro-Tirado, J. M. Castro Cerón, A. S. Fruchter, J. Gorosabel, P. Jakobsson, L. Kaper, S. Klose, N. Masetti, H. Pedersen, K. Pedersen, E. Pian, E. Palazzi, J. E. Rhoads, E. Rol, E. P. J. van den Heuvel, P. M. Vreeswijk, D. Watson, and R. A. M. J. Wijers, "A very energetic supernova associated with the γ-ray burst of 29 March 2003," *Nature*, vol. 423, pp. 847–850, Jun. 2003.

[105] P. A. Mazzali, K. S. Kawabata, K. Maeda, R. J. Foley, K. Nomoto, J. Deng, T. Suzuki, M. Iye, N. Kashikawa, Y. Ohyama, A. V. Filippenko, Y. Qiu, and J. Wei, "The Aspherical Properties of the Energetic Type Ic SN 2002ap as Inferred from Its Nebular Spectra," *Astrophysical Journal*, vol. 670, pp. 592–599, Nov. 2007.

[106] J. Hjorth and J. S. Bloom, *The Gamma-Ray Burst - Supernova Connection*, Nov. 2012, pp. 169–190.

[107] T. Matheson, A. V. Filippenko, W. Li, D. C. Leonard, and J. C. Shields, "Optical Spectroscopy of Type IB/C Supernovae," *Astronomical Journal*, vol. 121, pp. 1648–1675, Mar. 2001.

[108] S. E. Woosley and J. S. Bloom, "The Supernova Gamma-Ray Burst Connection," *Ann. Rev. Astron. Asrophys.*, vol. 44, pp. 507–556, Sep. 2006.

[109] M. R. Drout, A. M. Soderberg, A. Gal-Yam, S. B. Cenko, D. B. Fox, D. C. Leonard, D. J. Sand, D.-S. Moon, I. Arcavi, and Y. Green, "The First Systematic Study of Type Ibc Supernova Multi-band Light Curves," *Astrophysical Journal*, vol. 741, p. 97, Nov. 2011.

[110] A. Melandri, E. Pian, V. D'Elia, P. D'Avanzo, M. Della Valle, P. A. Mazzali, G. Tagliaferri, Z. Cano, A. J. Levan, P. Møoller, L. Amati, M. G. Bernardini, D. Bersier, F. Bufano, S. Campana, A. J. Castro-Tirado, S. Covino, G. Ghirlanda, K. Hurley, D. Malesani, N. Masetti, E. Palazzi, S. Piranomonte, A. Rossi, R. Salvaterra, R. L. C. Starling, M. Tanaka, N. R. Tanvir, and S. D. Vergani, "Diversity of gamma-ray burst energetics vs. supernova homogeneity: SN 2013cq associated with GRB 130427A," *Astronomy & Astrophysics*, vol. 567, p. A29, Jul. 2014.

[111] J. Zhang, X. Wang, J. Vinkó, J. C. Wheeler, L. Chang, Y. Yang, L. Wang, Q. Zhai, L. Rui, J. Mo, T. Zhang, Y. Zhang, J. Wang, J. Mao, C. Wang, W. Yi, Y. Xin, W. Li, B. Lun, K. Lu, H. Sai, X. Zheng, X. Zhang, X. Zhou, and J. Bai, "Optical Observations of the Young Type Ic Supernova SN 2014L in M99," *ArXiv e-prints*, Jun. 2018.

[112] S. Taubenberger, S. Benetti, M. Childress, R. Pakmor, S. Hachinger, P. A. Mazzali, V. Stanishev, N. Elias-Rosa, I. Agnoletto, F. Bufano, M. Ergon, A. Harutyunyan, C. Inserra, E. Kankare, M. Kromer, H. Navasardyan, J. Nicolas, A. Pastorello, E. Prosperi, F. Salgado, J. Sollerman, M. Stritzinger, M. Turatto, S. Valenti, and W. Hillebrandt, "High luminosity, slow ejecta and persistent carbon lines: SN 2009dc challenges thermonuclear explosion scenarios," *Monthly Notices of the Royal Astronomical Society*, vol. 412, pp. 2735–2762, Apr. 2011.

[113] L. Tomasella, E. Cappellaro, M. L. Pumo, A. Jerkstrand, S. Benetti, N. Elias-Rosa, M. Fraser, C. Inserra, A. Pastorello, M. Turatto, J. P. Anderson, L. Galbany, C. P. Gutiérrez, E. Kankare, G. Pignata, G. Terreran, S. Valenti, C. Barbarino, F. E. Bauer, M. T. Botticella, T.-W. Chen, A. Gal-Yam, A. Harutyunyan, D. A. Howell, K. Maguire, A. Morales Garoffolo, P. Ochner, S. J. Smartt, S. Schulze, D. R. Young, and L. Zampieri, "SNe 2013K and 2013am: observed and physical properties of two slow, normal Type IIP events," *Monthly Notices of the Royal Astronomical Society*, vol. 475, pp. 1937–1959, Apr. 2018.

[114] A. Panaitescu and P. Kumar, "Properties of Relativistic Jets in Gamma-Ray Burst Afterglows," *Astrophysical Journal*, vol. 571, pp. 779–789, Jun. 2002.

[115] G. Dubner and E. Giacani, "Radio emission from supernova remnants," , vol. 23, p. 3, Sep. 2015.

[116] R. Barniol Duran and D. Giannios, "Radio rebrightening of the GRB afterglow by the accompanying supernova," *Monthly Notices of the Royal Astronomical Society*, vol. 454, pp. 1711–1718, Dec. 2015.

[117] A. Kathirgamaraju, R. Barniol Duran, and D. Giannios, "GRB off-axis afterglows and the emission from the accompanying supernovae," *Monthly Notices of the Royal Astronomical Society*, vol. 461, pp. 1568–1575, Sep. 2016.

[118] E. G. Berezhko and H. J. Völk, "The theory of synchrotron emission from supernova remnants," *Astronomy & Astrophysics*, vol. 427, pp. 525–536, Nov. 2004.

[119] S. K. Sarbadhicary, C. Badenes, L. Chomiuk, D. Caprioli, and D. Huizenga, "Supernova remnants in the Local Group - I. A model for the radio luminosity function and visibility times of supernova remnants," *Monthly Notices of the Royal Astronomical Society*, vol. 464, pp. 2326–2340, Jan. 2017.

[120] C. J. Stockdale, L. A. Maddox, J. J. Cowan, A. Prestwich, R. Kilgard, and S. Immler, "A Radio and X-Ray Study of Historical Supernovae in M83," *Astronomical Journal*, vol. 131, pp. 889–894, Feb. 2006.

[121] J. A. Dittmann, A. M. Soderberg, L. Chomiuk, R. Margutti, W. M. Goss, D. Milisavljevic, and R. A. Chevalier, "A Mid-life Crisis? Sudden Changes in Radio and X-Ray Emission from Supernova 1970G," *Astrophysical Journal*, vol. 788, p. 38, Jun. 2014.

[122] R. Barniol Duran, E. Nakar, T. Piran, and R. Sari, "The afterglow of a relativistic shock breakout and low-luminosity GRBs," *Monthly Notices of the Royal Astronomical Society*, vol. 448, pp. 417–428, Mar. 2015.

[123] L. Sironi and D. Giannios, "A Late-time Flattening of Light Curves in Gamma-Ray Burst Afterglows," *Astrophysical Journal*, vol. 778, p. 107, Dec. 2013.

[124] C. D. Matzner and C. F. McKee, "The Expulsion of Stellar Envelopes in Core-Collapse Supernovae," *Astrophysical Journal*, vol. 510, pp. 379–403, Jan. 1999.

[125] J. C. Tan, C. D. Matzner, and C. F. McKee, "Trans-Relativistic Blast Waves in Supernovae as Gamma-Ray Burst Progenitors," *Astrophysical Journal*, vol. 551, pp. 946–972, Apr. 2001.

[126] E. Berger, S. R. Kulkarni, G. Pooley, D. A. Frail, V. McIntyre, R. M. Wark, R. Sari, A. M. Soderberg, D. W. Fox, S. Yost, and P. A. Price, "A common origin for cosmic explosions inferred from calorimetry of GRB030329," *Nature*, vol. 426, pp. 154–157, Nov. 2003.

[127] D. A. Frail, A. M. Soderberg, S. R. Kulkarni, E. Berger, S. Yost, D. W. Fox, and F. A. Harrison, "Accurate Calorimetry of GRB 030329," *Astrophysical Journal*, vol. 619, pp. 994–998, Feb. 2005.

[128] L. Resmi, C. H. Ishwara-Chandra, A. J. Castro-Tirado, D. Bhattacharya, A. P. Rao, M. Bremer, S. B. Pandey, D. K. Sahu, B. C. Bhatt, R. Sagar, G. C. Anupama, A. Subramaniam, A. Lundgren, J. Gorosabel, S. Guziy, A. de Ugarte Postigo, J. M. Castro Cerón, and T. Wiklind, "Radio, millimeter and optical monitoring of GRB 030329 afterglow: constraining the double jet model," *Astronomy & Astrophysics*, vol. 440, pp. 477–485, Sep. 2005.

[129] A. J. van der Horst, E. Rol, R. A. M. J. Wijers, R. Strom, L. Kaper, and C. Kouveliotou, "The Radio Afterglow of GRB 030329 at Centimeter Wavelengths: Evidence for a Structured Jet or Nonrelativistic Expansion," *Astrophysical Journal*, vol. 634, pp. 1166–1172, Dec. 2005.

[130] A. J. van der Horst, A. Kamble, L. Resmi, R. A. M. J. Wijers, D. Bhattacharya, B. Scheers, E. Rol, R. Strom, C. Kouveliotou, T. Oosterloo, and C. H. Ishwara-Chandra, "Detailed study of the GRB 030329 radio afterglow deep into the non-relativistic phase," *Astronomy & Astrophysics*, vol. 480, pp. 35–43, Mar. 2008.

[131] R. A. Mesler, Y. M. Pihlström, G. B. Taylor, and J. Granot, "VLBI and Archival VLA and WSRT Observations of the GRB 030329 Radio Afterglow," *Astrophysical Journal*, vol. 759, p. 4, Nov. 2012.

[132] R. A. Mesler and Y. M. Pihlström, "Calorimetry of GRB 030329: Simultaneous Model Fitting to the Broadband Radio Afterglow and the Observed Image Expansion Rate," *Astrophysical Journal*, vol. 774, p. 77, Sep. 2013.

[133] J. Greiner, M. Peimbert, C. Esteban, A. Kaufer, A. Jaunsen, J. Smoke, S. Klose, and O. Reimer, "Redshift of GRB 030329." *GRB Coordinates Network*, vol. 2020, 2003.

[134] N. Mirabal, J. P. Halpern, D. An, J. R. Thorstensen, and D. M. Terndrup, "GRB 060218/SN 2006aj: A Gamma-Ray Burst and Prompt Supernova at z = 0.0335," *Astrophysical Journal Letters*, vol. 643, pp. L99–L102, Jun. 2006.

[135] C. Lidman, T. Augusteijn, O. R. Hainaut, H. Boehnhardt, F. Patat, and B. Leibundgut, "GRB 980425," , vol. 6895, May 1998.

[136] P. A. Mazzali, K. Nomoto, K. Maeda, and J. Deng, "Supernovae and Gamma-ray Bursts," in *Revista Mexicana de Astronomia y Astrofisica Conference Series*, ser. Revista Mexicana de Astronomia y Astrofisica, vol. 27, vol. 30, Aug. 2007, pp. 23–28.

[137] P. A. Mazzali, J. Deng, N. Tominaga, K. Maeda, K. Nomoto, T. Matheson, K. S. Kawabata, K. Z. Stanek, and P. M. Garnavich, "The Type Ic Hypernova SN 2003dh/GRB 030329," *Astrophysical Journal Letters*, vol. 599, pp. L95–L98, Dec. 2003.

[138] P. A. Mazzali, J. Deng, K. Nomoto, D. N. Sauer, E. Pian, N. Tominaga, M. Tanaka, K. Maeda, and A. V. Filippenko, "A neutron-star-driven X-ray flash associated with supernova SN 2006aj," *Nature*, vol. 442, pp. 1018–1020, Aug. 2006.

[139] G. B. Taylor, D. A. Frail, E. Berger, and S. R. Kulkarni, "The Angular Size and Proper Motion of the Afterglow of GRB 030329," *Astrophysical Journal Letters*, vol. 609, pp. L1–L4, Jul. 2004.

[140] G. B. Taylor, E. Momjian, Y. Pihlström, T. Ghosh, and C. Salter, "Late-Time Observations of the Afterglow and Environment of GRB 030329," *Astrophysical Journal*, vol. 622, pp. 986–990, Apr. 2005.

[141] Y. M. Pihlström, G. B. Taylor, J. Granot, and S. Doeleman, "Stirring the Embers: High-Sensitivity VLBI Observations of GRB 030329," *Astrophysical Journal*, vol. 664, pp. 411–415, Jul. 2007.

[142] K. Z. Stanek, T. Matheson, P. M. Garnavich, P. Martini, P. Berlind, N. Caldwell, P. Challis, W. R. Brown, R. Schild, K. Krisciunas, M. L. Calkins, J. C. Lee, N. Hathi, R. A. Jansen, R. Windhorst, L. Echevarria, D. J. Eisenstein, B. Pindor, E. W. Olszewski, P. Harding, S. T. Holland, and D. Bersier, "Spectroscopic Discovery of the Supernova 2003dh Associated with GRB 030329," *Astrophysical Journal Letters*, vol. 591, pp. L17–L20, Jul. 2003.

[143] B. E. Cobb, C. D. Bailyn, P. G. van Dokkum, and P. Natarajan, "SN 2006aj and the Nature of Low-Luminosity Gamma-Ray Bursts," *Astrophysical Journal Letters*, vol. 645, pp. L113–L116, Jul. 2006.

[144] A. M. Soderberg, S. R. Kulkarni, E. Nakar, E. Berger, P. B. Cameron, D. B. Fox, D. Frail, A. Gal-Yam, R. Sari, S. B. Cenko, M. Kasliwal, R. A. Chevalier, T. Piran, P. A. Price, B. P. Schmidt, G. Pooley, D.-S. Moon, B. E. Penprase, E. Ofek, A. Rau, N. Gehrels, J. A. Nousek, D. N. Burrows, S. E. Persson, and P. J. McCarthy, "Relativistic ejecta from X-ray flash XRF 060218 and the rate of cosmic explosions," *Nature*, vol. 442, pp. 1014–1017, Aug. 2006.

[145] Y. Kaneko, E. Ramirez-Ruiz, J. Granot, C. Kouveliotou, S. E. Woosley, S. K. Patel, E. Rol, J. J. M. in 't Zand, A. J. van der Horst, R. A. M. J. Wijers, and R. Strom, "Prompt and Afterglow Emission Properties of Gamma-Ray Bursts with Spectroscopically Identified Supernovae," *Astrophysical Journal*, vol. 654, pp. 385–402, Jan. 2007.

[146] J. Sollerman, A. O. Jaunsen, J. P. U. Fynbo, J. Hjorth, P. Jakobsson, M. Stritzinger, C. Féron, P. Laursen, J.-E. Ovaldsen, J. Selj, C. C. Thöne, D. Xu, T. Davis, J. Gorosabel, D. Watson, R. Duro, I. Ilyin, B. L. Jensen, N. Lysfjord, T. Marquart, T. B. Nielsen, J. Näränen, H. E. Schwarz, S. Walch, M. Wold, and G. Östlin, "Supernova 2006aj and the associated X-Ray Flash 060218," *Astronomy & Astrophysics*, vol. 454, pp. 503–509, Aug. 2006.

[147] S. R. Kulkarni, D. A. Frail, M. H. Wieringa, R. D. Ekers, E. M. Sadler, R. M. Wark, J. L. Higdon, E. S. Phinney, and J. S. Bloom, "Radio emission from the unusual supernova 1998bw and its association with the γ-ray burst of 25 April 1998," *Nature*, vol. 395, pp. 663–669, Oct. 1998.

[148] D. A. Frail, S. R. Kulkarni, E. Berger, and M. H. Wieringa, "A Complete Catalog of Radio Afterglows: The First Five Years," *Astronomical Journal*, vol. 125, pp. 2299–2306, May 2003.

[149] K. Ioka and T. Nakamura, "Peak Luminosity-Spectral Lag Relation Caused by the Viewing Angle of the Collimated Gamma-Ray Bursts," *Astrophysical Journal Letters*, vol. 554, pp. L163–L167, Jun. 2001.

[150] R. Yamazaki, D. Yonetoku, and T. Nakamura, "An Off-Axis Jet Model For GRB 980425 and Low-Energy Gamma-Ray Bursts," *Astrophysical Journal Letters*, vol. 594, pp. L79–L82, Sep. 2003.

[151] J. P. McMullin, B. Waters, D. Schiebel, W. Young, and K. Golap, "CASA Architecture and Applications," in *Astronomical Data Analysis Software and Systems XVI*, ser. Astronomical Society of the Pacific Conference Series, R. A. Shaw, F. Hill, and D. J. Bell, Eds., vol. 376, Oct. 2007, p. 127.

[152] E. W. Greisen, "AIPS, the VLA, and the VLBA," in *Information Handling in Astronomy - Historical Vistas*, ser. Astrophysics and Space Science Library, A. Heck, Ed., vol. 285, Mar. 2003, p. 109.

[153] J. J. Condon, W. D. Cotton, E. W. Greisen, Q. F. Yin, R. A. Perley, G. B. Taylor, and J. J. Broderick, "The NRAO VLA Sky Survey," *Astronomical Journal*, vol. 115, pp. 1693–1716, May 1998.

[154] A. T. Deller, W. F. Brisken, C. J. Phillips, J. Morgan, W. Alef, R. Cappallo, E. Middelberg, J. Romney, H. Rottmann, S. J. Tingay, and R. Wayth, "DiFX-2: A More Flexible, Efficient, Robust, and Powerful Software Correlator," *PASP*, vol. 123, p. 275, Mar. 2011.

[155] M. Kettenis, H. J. van Langevelde, C. Reynolds, and B. Cotton, "ParselTongue: AIPS Talking Python," in *Astronomical Data Analysis Software and Systems XV*, ser. Astronomical Society of the Pacific Conference Series, C. Gabriel, C. Arviset, D. Ponz, and S. Enrique, Eds., vol. 351, Jul. 2006, p. 497.

[156] M. J. Michałowski, A. Kamble, J. Hjorth, D. Malesani, R. F. Reinfrank, L. Bonavera, J. M. Castro Cerón, E. Ibar, J. S. Dunlop, J. P. U. Fynbo, M. A. Garrett, P. Jakobsson, D. L. Kaplan, T. Krühler, A. J. Levan, M. Massardi, S. Pal, J. Sollerman, N. R. Tanvir, A. J. van der Horst, D. Watson, and K. Wiersema, "The Optically Unbiased GRB Host (TOUGH) Survey. VI. Radio Observations at z ~ 1 and Consistency with Typical Star-forming Galaxies," *Astrophysical Journal*, vol. 755, p. 85, Aug. 2012.

[157] P. Beniamini and A. J. van der Horst, "Electrons' energy in GRB afterglows implied by radio peaks," *Monthly Notices of the Royal Astronomical Society*, vol. 472, pp. 3161–3168, Dec. 2017.

[158] R. A. Chevalier and C. Fransson, "Circumstellar Emission from Type Ib and Ic Supernovae," *Astrophysical Journal*, vol. 651, pp. 381–391, Nov. 2006.

[159] S. B. Cenko, D. A. Frail, F. A. Harrison, J. B. Haislip, D. E. Reichart, N. R. Butler, B. E. Cobb, A. Cucchiara, E. Berger, J. S. Bloom, P. Chandra, D. B. Fox, D. A. Perley, J. X. Prochaska, A. V. Filippenko, K. Glazebrook, K. M. Ivarsen, M. M. Kasliwal, S. R. Kulkarni, A. P. LaCluyze, S. Lopez, A. N. Morgan, M. Pettini, and V. R. Rana, "Afterglow Observations of Fermi Large Area Telescope Gamma-ray Bursts and the Emerging Class of Hyper-energetic Events," *Astrophysical Journal*, vol. 732, p. 29, May 2011.

[160] E. Ramirez-Ruiz, G. García-Segura, J. D. Salmonson, and B. Pérez-Rendón, "The State of the Circumstellar Medium Surrounding Gamma-Ray Burst Sources and Its Effect on the Afterglow Appearance," *Astrophysical Journal*, vol. 631, pp. 435–445, Sep. 2005.

[161] R. L. C. Starling, A. J. van der Horst, E. Rol, R. A. M. J. Wijers, C. Kouveliotou, K. Wiersema, P. A. Curran, and P. Weltevrede, "Gamma-Ray Burst

Afterglows as Probes of Environment and Blast Wave Physics. II. The Distribution of p and Structure of the Circumburst Medium," *Astrophysical Journal*, vol. 672, pp. 433–442, Jan. 2008.

[162] P. A. Crowther, "Physical Properties of Wolf-Rayet Stars," *Ann. Rev. Astron. Asrophys.*, vol. 45, pp. 177–219, Sep. 2007.

[163] R. Weaver, R. McCray, J. Castor, P. Shapiro, and R. Moore, "Interstellar bubbles. II - Structure and evolution," *Astrophysical Journal*, vol. 218, pp. 377–395, Dec. 1977.

[164] K. Toma, K. Ioka, T. Sakamoto, and T. Nakamura, "Low-Luminosity GRB 060218: A Collapsar Jet from a Neutron Star, Leaving a Magnetar as a Remnant?" *Astrophysical Journal*, vol. 659, pp. 1420–1430, Apr. 2007.

[165] C. M. Irwin and R. A. Chevalier, "Jet or shock breakout? The low-luminosity GRB 060218," *Monthly Notices of the Royal Astronomical Society*, vol. 460, pp. 1680–1704, Aug. 2016.

[166] Z.-Y. Li and R. A. Chevalier, "Radio Supernova SN 1998bw and Its Relation to GRB 980425," *Astrophysical Journal*, vol. 526, pp. 716–726, Dec. 1999.

[167] K. W. Weiler, N. Panagia, and M. J. Montes, "SN 1998bw/GRB 980425 and Radio Supernovae," *Astrophysical Journal*, vol. 562, pp. 670–678, Dec. 2001.

[168] A. J. van der Horst, Z. Paragi, A. G. de Bruyn, J. Granot, C. Kouveliotou, K. Wiersema, R. L. C. Starling, P. A. Curran, R. A. M. J. Wijers, A. Rowlinson, G. A. Anderson, R. P. Fender, J. Yang, and R. G. Strom, "A comprehensive radio view of the extremely bright gamma-ray burst 130427A," *Monthly Notices of the Royal Astronomical Society*, vol. 444, pp. 3151–3163, Nov. 2014.

[169] B. P. Abbott, R. Abbott, T. D. Abbott, M. R. Abernathy, F. Acernese, K. Ackley, C. Adams, T. Adams, P. Addesso, R. X. Adhikari, and et al., "GW151226: Observation of Gravitational Waves from a 22-Solar-Mass Binary Black Hole Coalescence," *Physical Review Letters*, vol. 116, no. 24, p. 241103, Jun. 2016.

[170] ——, "GW151226: Observation of Gravitational Waves from a 22-Solar-Mass Binary Black Hole Coalescence," *Physical Review Letters*, vol. 116, no. 24, p. 241103, Jun. 2016.

[171] ——, "Observation of Gravitational Waves from a Binary Black Hole Merger," *Physical Review Letters*, vol. 116, no. 6, p. 061102, Feb. 2016.

[172] W. H. Lee and E. Ramirez-Ruiz, "The progenitors of short gamma-ray bursts," *New Journal of Physics*, vol. 9, p. 17, Jan. 2007.

[173] D. V. Martynov, E. D. Hall, B. P. Abbott, R. Abbott, T. D. Abbott, C. Adams, R. X. Adhikari, R. A. Anderson, S. B. Anderson, K. Arai, and et al., "Sensitivity of the Advanced LIGO detectors at the beginning of gravitational wave astronomy," *Physical Review D*, vol. 93, no. 11, p. 112004, Jun. 2016.

[174] D. Eichler, M. Livio, T. Piran, and D. N. Schramm, "Nucleosynthesis, neutrino bursts and gamma-rays from coalescing neutron stars," *Nature*, vol. 340, pp. 126–128, Jul. 1989.

[175] E. Nakar, "Short-hard gamma-ray bursts," , vol. 442, pp. 166–236, Apr. 2007.

[176] E. Berger, "Short-Duration Gamma-Ray Bursts," *Ann. Rev. Astron. Asrophys.*, vol. 52, pp. 43–105, Aug. 2014.

[177] D. Wanderman and T. Piran, "The rate, luminosity function and time delay of non-Collapsar short GRBs," *Monthly Notices of the Royal Astronomical Society*, vol. 448, pp. 3026–3037, Apr. 2015.

[178] C. S. Kochanek and T. Piran, "Gravitational Waves and gamma -Ray Bursts," *Astrophysical Journal Letters*, vol. 417, p. L17, Nov. 1993.

[179] B. Patricelli, M. Razzano, G. Cella, F. Fidecaro, E. Pian, M. Branchesi, and A. Stamerra, "Prospects for joint observations of gravitational waves and gamma rays from merging neutron star binaries," , vol. 11, p. 056, Nov. 2016.

[180] D. Lazzati, A. Deich, B. J. Morsony, and J. C. Workman, "Off-axis emission of short γ-ray bursts and the detectability of electromagnetic counterparts of gravitational-wave-detected binary mergers," *Monthly Notices of the Royal Astronomical Society*, vol. 471, pp. 1652–1661, Oct. 2017.

[181] L.-X. Li and B. Paczyński, "Transient Events from Neutron Star Mergers," *Astrophysical Journal Letters*, vol. 507, pp. L59–L62, Nov. 1998.

[182] B. D. Metzger, G. Martínez-Pinedo, S. Darbha, E. Quataert, A. Arcones, D. Kasen, R. Thomas, P. Nugent, I. V. Panov, and N. T. Zinner, "Electromagnetic counterparts of compact object mergers powered by the radioactive decay of r-process nuclei," *Monthly Notices of the Royal Astronomical Society*, vol. 406, pp. 2650–2662, Aug. 2010.

[183] B. D. Metzger and E. Berger, "What is the Most Promising Electromagnetic Counterpart of a Neutron Star Binary Merger?" *Astrophysical Journal*, vol. 746, p. 48, Feb. 2012.

[184] D. Kasen, N. R. Badnell, and J. Barnes, "Opacities and Spectra of the r-process Ejecta from Neutron Star Mergers," *Astrophysical Journal*, vol. 774, p. 25, Sep. 2013.

[185] E. Nakar and T. Piran, "Detectable radio flares following gravitational waves from mergers of binary neutron stars," *Nature*, vol. 478, pp. 82–84, Oct. 2011.

[186] K. Hotokezaka and T. Piran, "Mass ejection from neutron star mergers: different components and expected radio signals," *Monthly Notices of the Royal Astronomical Society*, vol. 450, pp. 1430–1440, Jun. 2015.

[187] G. P. Lamb and S. Kobayashi, "Electromagnetic Counterparts to Structured Jets from Gravitational Wave Detected Mergers," *ArXiv e-prints*, Jun. 2017.

[188] B. P. Abbott, R. Abbott, T. D. Abbott, M. R. Abernathy, F. Acernese, K. Ackley, C. Adams, T. Adams, P. Addesso, R. X. Adhikari, and et al., "Localization and Broadband Follow-up of the Gravitational-wave Transient GW150914," *Astrophysical Journal Letters*, vol. 826, p. L13, Jul. 2016.

[189] E. Rossi, D. Lazzati, and M. J. Rees, "Afterglow light curves, viewing angle and the jet structure of γ-ray bursts," *Monthly Notices of the Royal Astronomical Society*, vol. 332, pp. 945–950, Jun. 2002.

[190] O. S. Salafia, G. Ghisellini, A. Pescalli, G. Ghirlanda, and F. Nappo, "Structure of gamma-ray burst jets: intrinsic versus apparent properties," *Monthly Notices of the Royal Astronomical Society*, vol. 450, pp. 3549–3558, Jul. 2015.

[191] K. Hotokezaka, K. Kiuchi, K. Kyutoku, H. Okawa, Y.-i. Sekiguchi, M. Shibata, and K. Taniguchi, "Mass ejection from the merger of binary neutron stars," *Physical Review D*, vol. 87, no. 2, p. 024001, Jan. 2013.

[192] S. Rosswog, "The dynamic ejecta of compact object mergers and eccentric collisions," *Philosophical Transactions of the Royal Society of London Series A*, vol. 371, pp. 20 120 272–20 120 272, Apr. 2013.

[193] H. Nagakura, K. Hotokezaka, Y. Sekiguchi, M. Shibata, and K. Ioka, "Jet Collimation in the Ejecta of Double Neutron Star Mergers: A New Canonical Picture of Short Gamma-Ray Bursts," *Astrophysical Journal Letters*, vol. 784, p. L28, Apr. 2014.

[194] A. Murguia-Berthier, G. Montes, E. Ramirez-Ruiz, F. De Colle, and W. H. Lee, "Necessary Conditions for Short Gamma-Ray Burst Production in Binary Neutron Star Mergers," *Astrophysical Journal Letters*, vol. 788, p. L8, Jun. 2014.

[195] P. C. Duffell, E. Quataert, and A. I. MacFadyen, "A Narrow Short-duration GRB Jet from a Wide Central Engine," *Astrophysical Journal*, vol. 813, p. 64, Nov. 2015.

[196] A. Tchekhovskoy, R. Narayan, and J. C. McKinney, "Magnetohydrodynamic simulations of gamma-ray burst jets: Beyond the progenitor star," , vol. 15, pp. 749–754, Nov. 2010.

[197] S. S. Komissarov, N. Vlahakis, and A. Königl, "Rarefaction acceleration of ultrarelativistic magnetized jets in gamma-ray burst sources," *Monthly Notices of the Royal Astronomical Society*, vol. 407, pp. 17–28, Sep. 2010.

[198] K. Sapountzis and N. Vlahakis, "Rarefaction wave in relativistic steady magnetohydrodynamic flows," *Physics of Plasmas*, vol. 21, no. 7, p. 072124, Jul. 2014.

[199] W. Fong, E. Berger, R. Margutti, and B. A. Zauderer, "A Decade of Short-duration Gamma-Ray Burst Broadband Afterglows: Energetics, Circumburst Densities, and Jet Opening Angles," *Astrophysical Journal*, vol. 815, p. 102, Dec. 2015.

[200] V. Connaughton, E. Burns, A. Goldstein, L. Blackburn, M. S. Briggs, B.-B. Zhang, J. Camp, N. Christensen, C. M. Hui, P. Jenke, T. Littenberg, J. E. McEnery, J. Racusin, P. Shawhan, L. Singer, J. Veitch, C. A. Wilson-Hodge, P. N. Bhat, E. Bissaldi, W. Cleveland, G. Fitzpatrick, M. M. Giles, M. H. Gibby, A. von Kienlin, R. M. Kippen, S. McBreen, B. Mailyan, C. A. Meegan, W. S. Paciesas, R. D. Preece, O. J. Roberts, L. Sparke, M. Stanbro, K. Toelge, and P. Veres, "Fermi GBM Observations of LIGO Gravitational-wave Event GW150914," *Astrophysical Journal Letters*, vol. 826, p. L6, Jul. 2016.

[201] A. Pescalli, G. Ghirlanda, O. S. Salafia, G. Ghisellini, F. Nappo, and R. Salvaterra, "Luminosity function and jet structure of Gamma-Ray Burst," *Monthly Notices of the Royal Astronomical Society*, vol. 447, pp. 1911–1921, Feb. 2015.

[202] L. Rezzolla, B. Giacomazzo, L. Baiotti, J. Granot, C. Kouveliotou, and M. A. Aloy, "The Missing Link: Merging Neutron Stars Naturally Produce Jet-like Structures and Can Power Short Gamma-ray Bursts," *Astrophysical Journal Letters*, vol. 732, p. L6, May 2011.

[203] E. Nakar and T. Piran, "The Observable Signatures of GRB Cocoons," *Astrophysical Journal*, vol. 834, p. 28, Jan. 2017.

[204] O. Gottlieb, E. Nakar, and T. Piran, "The cocoon emission - an electromagnetic counterpart to gravitational waves from neutron star mergers," *ArXiv e-prints*, May 2017.

[205] B. D. Metzger, "Kilonovae," *Living Reviews in Relativity*, vol. 20, p. 3, May 2017.

[206] R. Chornock and E. Berger, "GRB 101219A: gemini-north host redshift." *GRB Coordinates Network*, vol. 11518, 2011.

[207] R. Barniol Duran, A. Tchekhovskoy, and D. Giannios, "Simulations of AGN jets: magnetic kink instability versus conical shocks," *Monthly Notices of the Royal Astronomical Society*, vol. 469, pp. 4957–4978, Aug. 2017.

[208] C. F. Gammie, J. C. McKinney, and G. Tóth, "HARM: A Numerical Scheme for General Relativistic Magnetohydrodynamics," *Astrophysical Journal*, vol. 589, pp. 444–457, May 2003.

[209] A. Tchekhovskoy, R. Narayan, and J. C. McKinney, "Efficient generation of jets from magnetically arrested accretion on a rapidly spinning black hole," *Monthly Notices of the Royal Astronomical Society*, vol. 418, pp. L79–L83, Nov. 2011.

[210] O. Bromberg and A. Tchekhovskoy, "Relativistic MHD simulations of core-collapse GRB jets: 3D instabilities and magnetic dissipation," *Monthly Notices of the Royal Astronomical Society*, vol. 456, pp. 1739–1760, Feb. 2016.

[211] M. V. Barkov and A. S. Pozanenko, "Model of the extended emission of short gamma-ray bursts," *Monthly Notices of the Royal Astronomical Society*, vol. 417, pp. 2161–2165, Nov. 2011.

[212] A. Murguia-Berthier, E. Ramirez-Ruiz, G. Montes, F. De Colle, L. Rezzolla, S. Rosswog, K. Takami, A. Perego, and W. H. Lee, "The Properties of Short Gamma-Ray Burst Jets Triggered by Neutron Star Mergers," *Astrophysical Journal Letters*, vol. 835, p. L34, Feb. 2017.

[213] A. Tchekhovskoy, J. C. McKinney, and R. Narayan, "Simulations of ultrarelativistic magnetodynamic jets from gamma-ray burst engines," *Monthly Notices of the Royal Astronomical Society*, vol. 388, pp. 551–572, Aug. 2008.

[214] P. Mészáros and M. J. Rees, "Steep Slopes and Preferred Breaks in Gamma-Ray Burst Spectra: The Role of Photospheres and Comptonization," *Astrophysical Journal*, vol. 530, pp. 292–298, Feb. 2000.

[215] D. Giannios, "Prompt emission spectra from the photosphere of a GRB," *Astronomy & Astrophysics*, vol. 457, pp. 763–770, Oct. 2006.

[216] B. P. Abbott, R. Abbott, T. D. Abbott, F. Acernese, K. Ackley, C. Adams, T. Adams, P. Addesso, R. X. Adhikari, V. B. Adya, and et al., "GW170817: Observation of Gravitational Waves from a Binary Neutron Star Inspiral," *Physical Review Letters*, vol. 119, no. 16, p. 161101, Oct. 2017.

[217] A. Goldstein, P. Veres, E. Burns, M. S. Briggs, R. Hamburg, D. Kocevski, C. A. Wilson-Hodge, R. D. Preece, S. Poolakkil, O. J. Roberts, C. M. Hui, V. Connaughton, J. Racusin, A. von Kienlin, T. Dal Canton, N. Christensen, T. Littenberg, K. Siellez, L. Blackburn, J. Broida, E. Bissaldi, W. H. Cleveland, M. H. Gibby, M. M. Giles, R. M. Kippen, S. McBreen, J. McEnery, C. A. Meegan, W. S. Paciesas, and M. Stanbro, "An Ordinary Short Gamma-Ray Burst with Extraordinary Implications: Fermi-GBM Detection of GRB 170817A," *Astrophysical Journal Letters*, vol. 848, p. L14, Oct. 2017.

[218] V. Savchenko, C. Ferrigno, E. Kuulkers, A. Bazzano, E. Bozzo, S. Brandt, J. Chenevez, T. J.-L. Courvoisier, R. Diehl, A. Domingo, L. Hanlon, E. Jourdain, A. von Kienlin, P. Laurent, F. Lebrun, A. Lutovinov, A. Martin-Carrillo, S. Mereghetti, L. Natalucci, J. Rodi, J.-P. Roques, R. Sunyaev, and P. Ubertini, "INTEGRAL Detection of the First Prompt Gamma-Ray Signal Coincident with the Gravitational-wave Event GW170817," *Astrophysical Journal Letters*, vol. 848, p. L15, Oct. 2017.

[219] B. D. Metzger, "Kilonovae," *Living Reviews in Relativity*, vol. 20, p. 3, May 2017.

[220] R. Chornock, E. Berger, D. Kasen, P. S. Cowperthwaite, M. Nicholl, V. A. Villar, K. D. Alexander, P. K. Blanchard, T. Eftekhari, W. Fong, R. Margutti, P. K. G. Williams, J. Annis, D. Brout, D. A. Brown, H.-Y. Chen, M. R. Drout, B. Farr, R. J. Foley, J. A. Frieman, C. L. Fryer, K. Herner, D. E. Holz, R. Kessler, T. Matheson, B. D. Metzger, E. Quataert, A. Rest, M. Sako, D. M. Scolnic, N. Smith, and M. Soares-Santos, "The Electromagnetic Counterpart of the Binary Neutron Star Merger LIGO/Virgo GW170817. IV. Detection of Near-infrared Signatures of r-process Nucleosynthesis with Gemini-South," *Astrophysical Journal Letters*, vol. 848, p. L19, Oct. 2017.

[221] D. A. Coulter, R. J. Foley, C. D. Kilpatrick, M. R. Drout, A. L. Piro, B. J. Shappee, M. R. Siebert, J. D. Simon, N. Ulloa, D. Kasen, B. F. Madore, A. Murguia-Berthier, Y.-C. Pan, J. X. Prochaska, E. Ramirez-Ruiz, A. Rest, and C. Rojas-Bravo, "Swope Supernova Survey 2017a (SSS17a), the Optical Counterpart to a Gravitational Wave Source," *ArXiv e-prints*, Oct. 2017, arXiv:1710.05452.

[222] P. S. Cowperthwaite, E. Berger, V. A. Villar, B. D. Metzger, M. Nicholl, R. Chornock, P. K. Blanchard, W. Fong, R. Margutti, M. Soares-Santos, K. D. Alexander, S. Allam, J. Annis, D. Brout, D. A. Brown, R. E. Butler, H.-Y. Chen, H. T. Diehl, Z. Doctor, M. R. Drout, T. Eftekhari, B. Farr, D. A. Finley, R. J. Foley, J. A. Frieman, C. L. Fryer, J. García-Bellido, M. S. S. Gill, J. Guillochon, K. Herner, D. E. Holz, D. Kasen, R. Kessler, J. Marriner, T. Matheson, E. H. Neilsen, Jr., E. Quataert, A. Palmese, A. Rest, M. Sako, D. M. Scolnic, N. Smith, D. L. Tucker, P. K. G. Williams, E. Balbinot, J. L. Carlin, E. R. Cook, F. Durret, T. S. Li, P. A. A. Lopes, A. C. C. Lourenço, J. L. Marshall, G. E. Medina, J. Muir, R. R. Muñoz, M. Sauseda, D. J. Schlegel, L. F. Secco, A. K. Vivas, W. Wester, A. Zenteno, Y. Zhang, T. M. C. Abbott,

M. Banerji, K. Bechtol, A. Benoit-Lévy, E. Bertin, E. Buckley-Geer, D. L. Burke, D. Capozzi, A. Carnero Rosell, M. Carrasco Kind, F. J. Castander, M. Crocce, C. E. Cunha, C. B. D'Andrea, L. N. da Costa, C. Davis, D. L. DePoy, S. Desai, J. P. Dietrich, A. Drlica-Wagner, T. F. Eifler, A. E. Evrard, E. Fernandez, B. Flaugher, P. Fosalba, E. Gaztanaga, D. W. Gerdes, T. Giannantonio, D. A. Goldstein, D. Gruen, R. A. Gruendl, G. Gutierrez, K. Honscheid, B. Jain, D. J. James, T. Jeltema, M. W. G. Johnson, M. D. Johnson, S. Kent, E. Krause, R. Kron, K. Kuehn, N. Nuropatkin, O. Lahav, M. Lima, H. Lin, M. A. G. Maia, M. March, P. Martini, R. G. McMahon, F. Menanteau, C. J. Miller, R. Miquel, J. J. Mohr, E. Neilsen, R. C. Nichol, R. L. C. Ogando, A. A. Plazas, N. Roe, A. K. Romer, A. Roodman, E. S. Rykoff, E. Sanchez, V. Scarpine, R. Schindler, M. Schubnell, I. Sevilla-Noarbe, M. Smith, R. C. Smith, F. Sobreira, E. Suchyta, M. E. C. Swanson, G. Tarle, D. Thomas, R. C. Thomas, M. A. Troxel, V. Vikram, A. R. Walker, R. H. Wechsler, J. Weller, B. Yanny, and J. Zuntz, "The Electromagnetic Counterpart of the Binary Neutron Star Merger LIGO/Virgo GW170817. II. UV, Optical, and Near-infrared Light Curves and Comparison to Kilonova Models," *Astrophysical Journal Letters*, vol. 848, p. L17, Oct. 2017.

[223] M. R. Drout, A. L. Piro, B. J. Shappee, C. D. Kilpatrick, J. D. Simon, C. Contreras, D. A. Coulter, R. J. Foley, M. R. Siebert, N. Morrell, K. Boutsia, F. Di Mille, T. W.-S. Holoien, D. Kasen, J. A. Kollmeier, B. F. Madore, A. J. Monson, A. Murguia-Berthier, Y.-C. Pan, J. X. Prochaska, E. Ramirez-Ruiz, A. Rest, C. Adams, K. Alatalo, E. Bañados, J. Baughman, T. C. Beers, R. A. Bernstein, T. Bitsakis, A. Campillay, T. T. Hansen, C. R. Higgs, A. P. Ji, G. Maravelias, J. L. Marshall, C. Moni Bidin, J. L. Prieto, K. C. Rasmussen, C. Rojas-Bravo, A. L. Strom, N. Ulloa, J. Vargas-González, Z. Wan, and D. D. Whitten, "Light Curves of the Neutron Star Merger GW170817/SSS17a: Implications for R-Process Nucleosynthesis," *ArXiv e-prints*, Oct. 2017, arXiv:1710.05443.

[224] M. M. Kasliwal, E. Nakar, L. P. Singer, D. L. Kaplan, D. O. Cook, A. Van Sistine, R. M. Lau, C. Fremling, O. Gottlieb, J. E. Jencson, S. M. Adams, U. Feindt, K. Hotokezaka, S. Ghosh, D. A. Perley, P.-C. Yu, T. Piran, J. R. Allison, G. C. Anupama, A. Balasubramanian, K. W. Bannister, J. Bally, J. Barnes, S. Barway, E. Bellm, V. Bhalerao, D. Bhattacharya, N. Blagorodnova, J. S. Bloom, P. R. Brady, C. Cannella, D. Chatterjee, S. B. Cenko, B. E. Cobb, C. Copperwheat, A. Corsi, K. De, D. Dobie, S. W. K. Emery, P. A. Evans, O. D. Fox, D. A. Frail, C. Frohmaier, A. Goobar, G. Hallinan, F. Harrison, G. Helou, T. Hinderer, A. Y. Q. Ho, A. Horesh, W.-H. Ip, R. Itoh, D. Kasen, H. Kim, N. P. M. Kuin, T. Kupfer, C. Lynch, K. Madsen, P. A. Mazzali, A. A. Miller, K. Mooley, T. Murphy, C.-C. Ngeow, D. Nichols, S. Nissanke, P. Nugent, E. O. Ofek, H. Qi, R. M. Quimby, S. Rosswog, F. Rusu, E. M. Sadler, P. Schmidt, J. Sollerman, I. Steele, A. R. Williamson, Y. Xu, L. Yan, Y. Yatsu, C. Zhang, and W. Zhao, "Illuminating Gravitational Waves: A Concordant Picture of Photons from a Neutron Star Merger," *ArXiv e-prints*, Oct. 2017, arXiv:1710.05436.

[225] M. Nicholl, E. Berger, D. Kasen, B. D. Metzger, J. Elias, C. Briceño, K. D. Alexander, P. K. Blanchard, R. Chornock, P. S. Cowperthwaite, T. Eftekhari, W. Fong, R. Margutti, V. A. Villar, P. K. G. Williams, W. Brown, J. Annis, A. Bahramian, D. Brout, D. A. Brown, H.-Y. Chen, J. C. Clemens, E. Dennihy, B. Dunlap, D. E. Holz, E. Marchesini, F. Massaro, N. Moskowitz, I. Pelisoli,

A. Rest, F. Ricci, M. Sako, M. Soares-Santos, and J. Strader, "The Electromagnetic Counterpart of the Binary Neutron Star Merger LIGO/Virgo GW170817. III. Optical and UV Spectra of a Blue Kilonova from Fast Polar Ejecta," *Astrophysical Journal Letters*, vol. 848, p. L18, Oct. 2017.

[226] E. Pian, P. D'Avanzo, S. Benetti, M. Branchesi, E. Brocato, S. Campana, E. Cappellaro, S. Covino, V. D'Elia, J. P. U. Fynbo, F. Getman, G. Ghirlanda, G. Ghisellini, A. Grado, G. Greco, J. Hjorth, C. Kouveliotou, A. Levan, L. Limatola, D. Malesani, P. A. Mazzali, A. Melandri, P. Møller, L. Nicastro, E. Palazzi, S. Piranomonte, A. Rossi, O. S. Salafia, J. Selsing, G. Stratta, M. Tanaka, N. R. Tanvir, L. Tomasella, D. Watson, S. Yang, L. Amati, L. A. Antonelli, S. Ascenzi, M. G. Bernardini, M. Boër, F. Bufano, A. Bulgarelli, M. Capaccioli, P. Casella, A. J. Castro-Tirado, E. Chassande-Mottin, R. Ciolfi, C. M. Copperwheat, M. Dadina, G. De Cesare, A. di Paola, Y. Z. Fan, B. Gendre, G. Giuffrida, A. Giunta, L. K. Hunt, G. L. Israel, Z.-P. Jin, M. M. Kasliwal, S. Klose, M. Lisi, F. Longo, E. Maiorano, M. Mapelli, N. Masetti, L. Nava, B. Patricelli, D. Perley, A. Pescalli, T. Piran, A. Possenti, L. Pulone, M. Razzano, R. Salvaterra, P. Schipani, M. Spera, A. Stamerra, L. Stella, G. Tagliaferri, V. Testa, E. Troja, M. Turatto, S. D. Vergani, and D. Vergani, "Spectroscopic identification of r-process nucleosynthesis in a double neutron-star merger," *Nature*, vol. 551, pp. 67–70, Nov. 2017.

[227] S. J. Smartt, T.-W. Chen, A. Jerkstrand, M. Coughlin, E. Kankare, S. A. Sim, M. Fraser, C. Inserra, K. Maguire, K. C. Chambers, M. E. Huber, T. Krühler, G. Leloudas, M. Magee, L. J. Shingles, K. W. Smith, D. R. Young, J. Tonry, R. Kotak, A. Gal-Yam, J. D. Lyman, D. S. Homan, C. Agliozzo, J. P. Anderson, C. R. Angus, C. Ashall, C. Barbarino, F. E. Bauer, M. Berton, M. T. Botticella, M. Bulla, J. Bulger, G. Cannizzaro, Z. Cano, R. Cartier, A. Cikota, P. Clark, A. De Cia, M. Della Valle, L. Denneau, M. Dennefeld, L. Dessart, G. Dimitriadis, N. Elias-Rosa, R. E. Firth, H. Flewelling, A. Flörs, A. Franckowiak, C. Frohmaier, L. Galbany, S. González-Gaitán, J. Greiner, M. Gromadzki, A. N. Guelbenzu, C. P. Gutiérrez, A. Hamanowicz, L. Hanlon, J. Harmanen, K. E. Heintz, A. Heinze, M.-S. Hernandez, S. T. Hodgkin, I. M. Hook, L. Izzo, P. A. James, P. G. Jonker, W. E. Kerzendorf, S. Klose, Z. Kostrzewa-Rutkowska, M. Kowalski, M. Kromer, H. Kuncarayakti, A. Lawrence, T. B. Lowe, E. A. Magnier, I. Manulis, A. Martin-Carrillo, S. Mattila, O. McBrien, A. Müller, J. Nordin, D. O'Neill, F. Onori, J. T. Palmerio, A. Pastorello, F. Patat, G. Pignata, P. Podsiadlowski, M. L. Pumo, S. J. Prentice, A. Rau, A. Razza, A. Rest, T. Reynolds, R. Roy, A. J. Ruiter, K. A. Rybicki, L. Salmon, P. Schady, A. S. B. Schultz, T. Schweyer, I. R. Seitenzahl, M. Smith, J. Sollerman, B. Stalder, C. W. Stubbs, M. Sullivan, H. Szegedi, F. Taddia, S. Taubenberger, G. Terreran, B. van Soelen, J. Vos, R. J. Wainscoat, N. A. Walton, C. Waters, H. Weiland, M. Willman, P. Wiseman, D. E. Wright, L. Wyrzykowski, and O. Yaron, "A kilonova as the electromagnetic counterpart to a gravitational-wave source," *Nature*, vol. 551, pp. 75–79, Nov. 2017.

[228] M. Soares-Santos, D. E. Holz, J. Annis, R. Chornock, K. Herner, E. Berger, D. Brout, H.-Y. Chen, R. Kessler, M. Sako, S. Allam, D. L. Tucker, R. E. Butler, A. Palmese, Z. Doctor, H. T. Diehl, J. Frieman, B. Yanny, H. Lin, D. Scolnic, P. Cowperthwaite, E. Neilsen, J. Marriner, N. Kuropatkin, W. G. Hartley, F. Paz-Chinchón, K. D. Alexander, E. Balbinot, P. Blanchard, D. A. Brown, J. L. Carlin, C. Conselice, E. R. Cook, A. Drlica-Wagner, M. R. Drout, F. Durret, T. Eftekhari, B. Farr, D. A. Finley, R. J. Foley, W. Fong, C. L.

Fryer, J. García-Bellido, M. S. S. Gill, R. A. Gruendl, C. Hanna, D. Kasen, T. S. Li, P. A. A. Lopes, A. C. C. Lourenço, R. Margutti, J. L. Marshall, T. Matheson, G. E. Medina, B. D. Metzger, R. R. Muñoz, J. Muir, M. Nicholl, E. Quataert, A. Rest, M. Sauseda, D. J. Schlegel, L. F. Secco, F. Sobreira, A. Stebbins, V. A. Villar, K. Vivas, A. R. Walker, W. Wester, P. K. G. Williams, A. Zenteno, Y. Zhang, T. M. C. Abbott, F. B. Abdalla, M. Banerji, K. Bechtol, A. Benoit-Lévy, E. Bertin, D. Brooks, E. Buckley-Geer, D. L. Burke, A. Carnero Rosell, M. Carrasco Kind, J. Carretero, F. J. Castander, M. Crocce, C. E. Cunha, C. B. D'Andrea, L. N. da Costa, C. Davis, S. Desai, J. P. Dietrich, P. Doel, T. F. Eifler, E. Fernandez, B. Flaugher, P. Fosalba, E. Gaztanaga, D. W. Gerdes, T. Giannantonio, D. A. Goldstein, D. Gruen, J. Gschwend, G. Gutierrez, K. Honscheid, B. Jain, D. J. James, T. Jeltema, M. W. G. Johnson, M. D. Johnson, S. Kent, E. Krause, R. Kron, K. Kuehn, S. Kuhlmann, O. Lahav, M. Lima, M. A. G. Maia, M. March, R. G. McMahon, F. Menanteau, R. Miquel, J. J. Mohr, R. C. Nichol, B. Nord, R. L. C. Ogando, D. Petravick, A. A. Plazas, A. K. Romer, A. Roodman, E. S. Rykoff, E. Sanchez, V. Scarpine, M. Schubnell, I. Sevilla-Noarbe, M. Smith, R. C. Smith, E. Suchyta, M. E. C. Swanson, G. Tarle, D. Thomas, R. C. Thomas, M. A. Troxel, V. Vikram, R. H. Wechsler, J. Weller, Dark Energy Survey, and Dark Energy Camera GW-EM Collaboration, "The Electromagnetic Counterpart of the Binary Neutron Star Merger LIGO/Virgo GW170817. I. Discovery of the Optical Counterpart Using the Dark Energy Camera," *Astrophysical Journal Letters*, vol. 848, p. L16, Oct. 2017.

[229] N. R. Tanvir, A. J. Levan, C. González-Fernández, O. Korobkin, I. Mandel, S. Rosswog, J. Hjorth, P. D'Avanzo, A. S. Fruchter, C. L. Fryer, T. Kangas, B. Milvang-Jensen, S. Rosetti, D. Steeghs, R. T. Wollaeger, Z. Cano, C. M. Copperwheat, S. Covino, V. D'Elia, A. de Ugarte Postigo, P. A. Evans, W. P. Even, S. Fairhurst, R. Figuera Jaimes, C. J. Fontes, Y. I. Fujii, J. P. U. Fynbo, B. P. Gompertz, J. Greiner, G. Hodosan, M. J. Irwin, P. Jakobsson, U. G. Jørgensen, D. A. Kann, J. D. Lyman, D. Malesani, R. G. McMahon, A. Melandri, P. T. O'Brien, J. P. Osborne, E. Palazzi, D. A. Perley, E. Pian, S. Piranomonte, M. Rabus, E. Rol, A. Rowlinson, S. Schulze, P. Sutton, C. C. Thöne, K. Ulaczyk, D. Watson, K. Wiersema, and R. A. M. J. Wijers, "The Emergence of a Lanthanide-rich Kilonova Following the Merger of Two Neutron Stars," *Astrophysical Journal Letters*, vol. 848, p. L27, Oct. 2017.

[230] S. Valenti, David, J. Sand, S. Yang, E. Cappellaro, L. Tartaglia, A. Corsi, S. W. Jha, D. E. Reichart, J. Haislip, and V. Kouprianov, "The Discovery of the Electromagnetic Counterpart of GW170817: Kilonova AT 2017gfo/DLT17ck," *Astrophysical Journal Letters*, vol. 848, p. L24, Oct. 2017.

[231] V. A. Villar, J. Guillochon, E. Berger, B. D. Metzger, P. S. Cowperthwaite, M. Nicholl, K. D. Alexander, P. K. Blanchard, R. Chornock, T. Eftekhari, W.-f. Fong, R. Margutti, and P. K. G. Williams, "The Combined Ultraviolet, Optical, and Near-Infrared Light Curves of the Kilonova Associated with the Binary Neutron Star Merger GW170817: Unified Data Set, Analytic Models, and Physical Implications," *ArXiv e-prints*, Oct. 2017, arXiv:1710.11576.

[232] K. D. Alexander, E. Berger, W. Fong, P. K. G. Williams, C. Guidorzi, R. Margutti, B. D. Metzger, J. Annis, P. K. Blanchard, D. Brout, D. A. Brown, H.-Y. Chen, R. Chornock, P. S. Cowperthwaite, M. Drout, T. Eftekhari, J. Frieman, D. E. Holz, M. Nicholl, A. Rest, M. Sako, M. Soares-Santos, and V. A.

Villar, "The Electromagnetic Counterpart of the Binary Neutron Star Merger LIGO/Virgo GW170817. VI. Radio Constraints on a Relativistic Jet and Predictions for Late-time Emission from the Kilonova Ejecta," *Astrophysical Journal Letters*, vol. 848, p. L21, Oct. 2017.

[233] D. Haggard, M. Nynka, J. J. Ruan, V. Kalogera, S. B. Cenko, P. Evans, and J. A. Kennea, "A Deep Chandra X-Ray Study of Neutron Star Coalescence GW170817," *Astrophysical Journal Letters*, vol. 848, p. L25, Oct. 2017.

[234] G. Hallinan, A. Corsi, K. P. Mooley, K. Hotokezaka, E. Nakar, M. M. Kasliwal, D. L. Kaplan, D. A. Frail, S. T. Myers, T. Murphy, K. De, D. Dobie, J. R. Allison, K. W. Bannister, V. Bhalerao, P. Chandra, T. E. Clarke, S. Giacintucci, A. Y. Q. Ho, A. Horesh, N. E. Kassim, S. R. Kulkarni, E. Lenc, F. J. Lockman, C. Lynch, D. Nichols, S. Nissanke, N. Palliyaguru, W. M. Peters, T. Piran, J. Rana, E. M. Sadler, and L. P. Singer, "A Radio Counterpart to a Neutron Star Merger," *ArXiv e-prints*, Oct. 2017, arXiv:1710.05435.

[235] R. Margutti, E. Berger, W. Fong, C. Guidorzi, K. D. Alexander, B. D. Metzger, P. K. Blanchard, P. S. Cowperthwaite, R. Chornock, T. Eftekhari, M. Nicholl, V. A. Villar, P. K. G. Williams, J. Annis, D. A. Brown, H. Chen, Z. Doctor, J. A. Frieman, D. E. Holz, M. Sako, and M. Soares-Santos, "The Electromagnetic Counterpart of the Binary Neutron Star Merger LIGO/Virgo GW170817. V. Rising X-Ray Emission from an Off-axis Jet," *Astrophysical Journal Letters*, vol. 848, p. L20, Oct. 2017.

[236] E. Troja, L. Piro, H. van Eerten, R. T. Wollaeger, M. Im, O. D. Fox, N. R. Butler, S. B. Cenko, T. Sakamoto, C. L. Fryer, R. Ricci, A. Lien, R. E. Ryan, O. Korobkin, S.-K. Lee, J. M. Burgess, W. H. Lee, A. M. Watson, C. Choi, S. Covino, P. D'Avanzo, C. J. Fontes, J. B. González, H. G. Khandrika, J. Kim, S.-L. Kim, C.-U. Lee, H. M. Lee, A. Kutyrev, G. Lim, R. Sánchez-Ramírez, S. Veilleux, M. H. Wieringa, and Y. Yoon, "The X-ray counterpart to the gravitational-wave event GW170817," *Nature*, vol. 551, pp. 71–74, Nov. 2017.

[237] K. P. Mooley, E. Nakar, K. Hotokezaka, G. Hallinan, A. Corsi, D. A. Frail, A. Horesh, T. Murphy, E. Lenc, D. L. Kaplan, K. De, D. Dobie, P. Chandra, A. Deller, O. Gottlieb, M. M. Kasliwal, S. R. Kulkarni, S. T. Myers, S. Nissanke, T. Piran, C. Lynch, V. Bhalerao, S. Bourke, K. W. Bannister, and L. P. Singer, "A mildly relativistic wide-angle outflow in the neutron star merger GW170817," *ArXiv e-prints*, Nov. 2017, arXiv:1711.11573.

[238] J. J. Ruan, M. Nynka, D. Haggard, V. Kalogera, and P. Evans, "Brightening X-ray Emission from GW170817/GRB170817A: Further Evidence for an Outflow," *ArXiv e-prints*, Dec. 2017, arXiv:1712.02809.

[239] Margutti et al., " LIGO/Virgo GW170817: Chandra X-ray brightening of the counterpart 108 days since merger," *Atel*, vol. 11037, 2017.

[240] E. Troja, L. Piro, G. Ryan, H. van Eerten, T. Sakamoto, and S. B. Cenko, "LIGO/Virgo G298048: Late-time detection of the X-ray afterglow with Chandra," *GCN*, vol. 22201, Dec. 2017.

[241] E. Troja, L. Piro, G. Ryan, H. van Eerten, R. Ricci, M. H. Wieringa, S. Lotti, T. Sakamoto, and S. B. Cenko, "The outflow structure of GW170817 from late-time broad-band observations," *Monthly Notices of the Royal Astronomical Society*, vol. 478, pp. L18–L23, Jul. 2018.

[242] P. D'Avanzo, S. Campana, O. S. Salafia, G. Ghirlanda, G. Ghisellini, A. Melandri, M. G. Bernardini, M. Branchesi, E. Chassande-Mottin, S. Covino, V. D'Elia, L. Nava, R. Salvaterra, G. Tagliaferri, and S. D. Vergani, "The evolution of the X-ray afterglow emission of GW 170817/ GRB 170817A in XMM-Newton observations," *Astronomy & Astrophysics*, vol. 613, p. L1, May 2018.

[243] W. Fong, E. Berger, R. Margutti, and B. A. Zauderer, "A Decade of Short-duration Gamma-Ray Burst Broadband Afterglows: Energetics, Circumburst Densities, and Jet Opening Angles," *Astrophysical Journal*, vol. 815, p. 102, Dec. 2015.

[244] E. Berger, "Short-Duration Gamma-Ray Bursts," *Ann. Rev. Astron. Asrophys.*, vol. 52, pp. 43–105, Aug. 2014.

[245] O. Gottlieb, E. Nakar, T. Piran, and K. Hotokezaka, "A cocoon shock breakout as the origin of the γ-ray emission in GW170817," *ArXiv e-prints*, Oct. 2017, arXiv:1710.05896.

[246] O. Gottlieb, E. Nakar, and T. Piran, "The cocoon emission - an electromagnetic counterpart to gravitational waves from neutron star mergers," *Monthly Notices of the Royal Astronomical Society*, vol. 473, pp. 576–584, Jan. 2018.

[247] E. Nakar, O. Gottlieb, T. Piran, M. M. Kasliwal, and G. Hallinan, "From γ to Radio: The Electromagnetic Counterpart of GW170817," *Astrophysical Journal*, vol. 867, p. 18, Nov 2018.

[248] D. Lazzati, A. Deich, B. J. Morsony, and J. C. Workman, "Off-axis emission of short γ-ray bursts and the detectability of electromagnetic counterparts of gravitational-wave-detected binary mergers," *Monthly Notices of the Royal Astronomical Society*, vol. 471, pp. 1652–1661, Oct. 2017.

[249] D. Lazzati, R. Perna, B. J. Morsony, D. López-Cámara, M. Cantiello, and J. C. Workman, "Late time afterglow observations reveal a collimated relativistic jet in the ejecta of the binary neutron star merger GW170817," *ArXiv e-prints*, Dec. 2017, arXiv:1712.03237.

[250] W. Fong, E. Berger, P. K. Blanchard, R. Margutti, P. S. Cowperthwaite, R. Chornock, K. D. Alexander, B. D. Metzger, V. A. Villar, M. Nicholl, T. Eftekhari, P. K. G. Williams, J. Annis, D. Brout, D. A. Brown, H.-Y. Chen, Z. Doctor, H. T. Diehl, D. E. Holz, A. Rest, M. Sako, and M. Soares-Santos, "The Electromagnetic Counterpart of the Binary Neutron Star Merger LIGO/Virgo GW170817. VIII. A Comparison to Cosmological Short-duration Gamma-Ray Bursts," *Astrophysical Journal Letters*, vol. 848, p. L23, Oct. 2017.

[251] P. M. W. Kalberla, W. B. Burton, D. Hartmann, E. M. Arnal, E. Bajaja, R. Morras, and W. G. L. Pöppel, "The Leiden/Argentine/Bonn (LAB) Survey of Galactic HI. Final data release of the combined LDS and IAR surveys with improved stray-radiation corrections," *Astronomy & Astrophysics*, vol. 440, pp. 775–782, Sep. 2005.

[252] R. Margutti, W. Fong, T. Eftekhari, K. Alexander, E. Berger, and R. Chornock, "LIGO/Virgo GW170817: Chandra X-ray brightening of the counterpart 108 days since merger," *The Astronomer's Telegram*, vol. 11037, Dec. 2017.

[253] Haggard et al., " LIGO/Virgo G298048: Brightening X-ray Emission from GW170817/GRB170817A/SSS17a ," *GRB Coordinates Network*, vol. 22206, 2017.

[254] D. Haggard, M. Nynka, J. J. Ruan, V. Kalogera, S. B. Cenko, P. Evans, and J. A. Kennea, "A Deep Chandra X-Ray Study of Neutron Star Coalescence GW170817," *Astrophysical Journal Letters*, vol. 848, p. L25, Oct. 2017.

[255] C. Y. Peng, L. C. Ho, C. D. Impey, and H.-W. Rix, "Detailed Decomposition of Galaxy Images. II. Beyond Axisymmetric Models," *Astronomical Journal*, vol. 139, pp. 2097–2129, Jun 2010.

[256] E. F. Schlafly and D. P. Finkbeiner, "Measuring Reddening with Sloan Digital Sky Survey Stellar Spectra and Recalibrating SFD," *Astrophysical Journal*, vol. 737, p. 103, Aug. 2011.

[257] J. D. Lyman, G. P. Lamb, A. J. Levan, I. Mandel, N. R. Tanvir, S. Kobayashi, B. Gompertz, J. Hjorth, A. S. Fruchter, T. Kangas, D. Steeghs, I. A. Steele, Z. Cano, C. Copperwheat, P. A. Evans, J. P. U. Fynbo, C. Gall, M. Im, L. Izzo, P. Jakobsson, B. Milvang-Jensen, P. O'Brien, J. P. Osborne, E. Palazzi, D. A. Perley, E. Pian, S. Rosswog, A. Rowlinson, S. Schulze, E. R. Stanway, P. Sutton, C. C. Thöne, A. de Ugarte Postigo, D. J. Watson, K. Wiersema, and R. A. M. J. Wijers, "The optical afterglow of the short gamma-ray burst associated with GW170817," *Nature Astronomy*, vol. 2, pp. 751–754, Jul 2018.

[258] J. P. McMullin, B. Waters, D. Schiebel, W. Young, and K. Golap, "CASA Architecture and Applications," in *Astronomical Data Analysis Software and Systems XVI*, ser. Astronomical Society of the Pacific Conference Series, R. A. Shaw, F. Hill, and D. J. Bell, Eds., vol. 376, Oct. 2007, p. 127.

[259] P. K. G. Williams, M. Clavel, E. Newton, and D. Ryzhkov, "pwkit: Astronomical utilities in Python," Astrophysics Source Code Library, Apr. 2017, ascl:1704.001.

[260] S. Kim, S. Schulze, L. Resmi, J. González-López, A. B. Higgins, C. H. Ishwara-Chandra, F. E. Bauer, I. de Gregorio-Monsalvo, M. De Pasquale, A. de Ugarte Postigo, D. A. Kann, S. Martín, S. R. Oates, R. L. C. Starling, N. R. Tanvir, J. Buchner, S. Campana, Z. Cano, S. Covino, A. S. Fruchter, J. P. U. Fynbo, D. H. Hartmann, J. Hjorth, P. Jakobsson, A. J. Levan, D. Malesani, M. J. Michałowski, B. Milvang-Jensen, K. Misra, P. T. OBrien, R. Sánchez-Ramírez, C. C. Thöne, D. J. Watson, and K. Wiersema, "ALMA and GMRT Constraints on the Off-axis Gamma-Ray Burst 170817A from the Binary Neutron Star Merger GW170817," *Astrophysical Journal Letters*, vol. 850, p. L21, Dec. 2017.

[261] A. R. Bell, "The acceleration of cosmic rays in shock fronts. I," *Monthly Notices of the Royal Astronomical Society*, vol. 182, pp. 147–156, Jan. 1978.

[262] R. D. Blandford and J. P. Ostriker, "Particle acceleration by astrophysical shocks," *Astrophysical Journal Letters*, vol. 221, pp. L29–L32, Apr. 1978.

[263] R. Blandford and D. Eichler, "Particle Acceleration at Astrophysical Shocks - a Theory of Cosmic-Ray Origin," , vol. 154, pp. 1–+, Oct. 1987.

[264] J. G. Kirk, A. W. Guthmann, Y. A. Gallant, and A. Achterberg, "Particle Acceleration at Ultrarelativistic Shocks: An Eigenfunction Method," *Astrophysical Journal*, vol. 542, pp. 235–242, Oct. 2000.

[265] A. Achterberg, Y. A. Gallant, J. G. Kirk, and A. W. Guthmann, "Particle acceleration by ultrarelativistic shocks: theory and simulations," *Monthly Notices of the Royal Astronomical Society*, vol. 328, pp. 393–408, Dec. 2001.

[266] U. Keshet and E. Waxman, "Energy Spectrum of Particles Accelerated in Relativistic Collisionless Shocks," *Physical Review Letters*, vol. 94, no. 11, pp. 111 102–+, Mar. 2005.

[267] L. Sironi, A. Spitkovsky, and J. Arons, "The Maximum Energy of Accelerated Particles in Relativistic Collisionless Shocks," *Astrophysical Journal*, vol. 771, p. 54, Jul. 2013.

[268] L. Sironi and A. Spitkovsky, "Synthetic Spectra from Particle-In-Cell Simulations of Relativistic Collisionless Shocks," *Astrophysical Journal Letters*, vol. 707, pp. L92–L96, Dec. 2009.

[269] R. Zakine and M. Lemoine, "The elusive synchrotron precursor of collisionless shocks," *Astronomy & Astrophysics*, vol. 601, p. A64, May 2017.

[270] A. Spitkovsky, "On the Structure of Relativistic Collisionless Shocks in Electron-Ion Plasmas," *Astrophysical Journal Letters*, vol. 673, pp. L39–L42, Jan. 2008.

[271] P. Chang, A. Spitkovsky, and J. Arons, "Long-Term Evolution of Magnetic Turbulence in Relativistic Collisionless Shocks: Electron-Positron Plasmas," *Astrophysical Journal*, vol. 674, pp. 378–387, Feb. 2008.

[272] U. Keshet, B. Katz, A. Spitkovsky, and E. Waxman, "Magnetic Field Evolution in Relativistic Unmagnetized Collisionless Shocks," *Astrophysical Journal Letters*, vol. 693, pp. L127–L130, Mar. 2009.

[273] S. F. Martins, R. A. Fonseca, L. O. Silva, and W. B. Mori, "Ion Dynamics and Acceleration in Relativistic Shocks," *Astrophysical Journal Letters*, vol. 695, pp. L189–L193, Apr. 2009.

[274] T. Haugbølle, "Three-dimensional Modeling of Relativistic Collisionless Ion-electron Shocks," *Astrophysical Journal Letters*, vol. 739, p. L42, Oct. 2011.

[275] E. Rossi and M. J. Rees, "Gamma-ray burst afterglow emission with a decaying magnetic field," *Monthly Notices of the Royal Astronomical Society*, vol. 339, pp. 881–886, Mar. 2003.

[276] M. Lemoine, "Synchrotron signature of a relativistic blast wave with decaying microturbulence," *Monthly Notices of the Royal Astronomical Society*, vol. 428, pp. 845–866, Jan. 2013.

[277] M. Lemoine, Z. Li, and X.-Y. Wang, "On the magnetization of gamma-ray burst blast waves," *Monthly Notices of the Royal Astronomical Society*, vol. 435, pp. 3009–3016, Nov. 2013.

[278] O. S. Salafia, G. Ghisellini, G. Ghirlanda, and M. Colpi, "GRB170817A: a giant flare from a jet-less double neutron-star merger?" *ArXiv e-prints*, Nov. 2017, arXiv:1711.03112.

[279] Z.-P. Jin, X. Li, H. Wang, Y.-Z. Wang, H.-N. He, Q. Yuan, F.-W. Zhang, Y.-C. Zou, Y.-Z. Fan, and D.-M. Wei, "Short GRBs with small opening angles: implications on local neutron star merger rate and GRB/GW association," *ArXiv e-prints*, Aug. 2017, arXiv:1708.07008.

[280] A. Murguia-Berthier, E. Ramirez-Ruiz, C. D. Kilpatrick, R. J. Foley, D. Kasen, W. H. Lee, A. L. Piro, D. A. Coulter, M. R. Drout, B. F. Madore, B. J. Shappee, Y.-C. Pan, J. X. Prochaska, A. Rest, C. Rojas-Bravo, M. R. Siebert, and J. D. Simon, "A Neutron Star Binary Merger Model for GW170817/GRB 170817A/SSS17a," *Astrophysical Journal Letters*, vol. 848, p. L34, Oct. 2017.

[281] W. Fong, B. D. Metzger, E. Berger, and F. Özel, "Radio Constraints on Long-lived Magnetar Remnants in Short Gamma-Ray Bursts," *Astrophysical Journal*, vol. 831, p. 141, Nov. 2016.

[282] J. Granot, R. Gill, D. Guetta, and F. De Colle, "Off-Axis Emission of Short GRB Jets from Double Neutron Star Mergers and GRB 170817A," *ArXiv e-prints*, Oct. 2017, arXiv:1710.06421.

[283] N. Fraija, F. De Colle, P. Veres, S. Dichiara, R. Barniol Duran, and A. Galvan-Gamez, "The short GRB 170817A: Modelling the off-axis emission and implications on the ejecta magnetization," *ArXiv e-prints*, Oct. 2017, arXiv:1710.08514.

[284] J. Granot, A. Panaitescu, P. Kumar, and S. E. Woosley, "Off-Axis Afterglow Emission from Jetted Gamma-Ray Bursts," *Astrophysical Journal Letters*, vol. 570, pp. L61–L64, May 2002.

[285] M. A. Aloy, H.-T. Janka, and E. Müller, "Relativistic outflows from remnants of compact object mergers and their viability for short gamma-ray bursts," *Astronomy & Astrophysics*, vol. 436, pp. 273–311, Jun. 2005.

[286] P. C. Duffell, E. Quataert, and A. I. MacFadyen, "A Narrow Short-duration GRB Jet from a Wide Central Engine," *Astrophysical Journal*, vol. 813, p. 64, Nov. 2015.

[287] D. Lazzati, D. López-Cámara, M. Cantiello, B. J. Morsony, R. Perna, and J. C. Workman, "Off-axis Prompt X-Ray Transients from the Cocoon of Short Gamma-Ray Bursts," *Astrophysical Journal Letters*, vol. 848, p. L6, Oct. 2017.

[288] A. Kathirgamaraju, R. Barniol Duran, and D. Giannios, "Off-axis short GRBs from structured jets as counterparts to GW events," *Monthly Notices of the Royal Astronomical Society*, vol. 473, pp. L121–L125, Jan. 2018.

[289] C. Guidorzi, R. Margutti, D. Brout, D. Scolnic, W. Fong, K. D. Alexander, P. S. Cowperthwaite, J. Annis, E. Berger, P. K. Blanchard, R. Chornock, D. L. Coppejans, T. Eftekhari, J. A. Frieman, D. Huterer, M. Nicholl, M. Soares-Santos, G. Terreran, V. A. Villar, and P. K. G. Williams, "Improved constraints on H0 from a combined analysis of gravitational-wave and electromagnetic emission from GW170817," *Astrophysical Journal Letters*, vol. 851, p. L36, Dec. 2017.

[290] H. J. van Eerten and A. I. MacFadyen, "Gamma-Ray Burst Afterglow Scaling Relations for the Full Blast Wave Evolution," *Astrophysical Journal Letters*, vol. 747, p. L30, Mar. 2012.

[291] A. Murguia-Berthier, G. Montes, E. Ramirez-Ruiz, F. De Colle, and W. H. Lee, "Necessary Conditions for Short Gamma-Ray Burst Production in Binary Neutron Star Mergers," *Astrophysical Journal Letters*, vol. 788, p. L8, Jun. 2014.

[292] P. C. Duffell and A. I. MacFadyen, "Rayleigh-Taylor Instability in a Relativistic Fireball on a Moving Computational Grid," *Astrophysical Journal*, vol. 775, p. 87, Oct 2013.

[293] R. Sari, T. Piran, and R. Narayan, "Spectra and Light Curves of Gamma-Ray Burst Afterglows," *Astrophysical Journal Letters*, vol. 497, p. L17, Apr. 1998.

[294] X. Xie, J. Zrake, and A. MacFadyen, "Numerical Simulations of the Jet Dynamics and Synchrotron Radiation of Binary Neutron Star Merger Event GW170817/GRB 170817A," *Astrophysical Journal*, vol. 863, p. 58, Aug. 2018.

[295] J. Granot and R. Sari, "The Shape of Spectral Breaks in Gamma-Ray Burst Afterglows," *Astrophysical Journal*, vol. 568, pp. 820–829, Apr. 2002.

[296] K. Murase, M. W. Toomey, K. Fang, F. Oikonomou, S. S. Kimura, K. Hotokezaka, K. Kashiyama, K. Ioka, and P. Mészáros, "Double Neutron Star Mergers and Short Gamma-ray Bursts: Long-lasting High-energy Signatures and Remnant Dichotomy," *Astrophysical Journal*, vol. 854, p. 60, Feb 2018.

[297] S. Rosswog, "Fallback accretion in the aftermath of a compact binary merger," *Monthly Notices of the Royal Astronomical Society*, vol. 376, pp. L48–L51, Mar. 2007.

[298] B. D. Metzger, A. Arcones, E. Quataert, and G. Martínez-Pinedo, "The effects of r-process heating on fallback accretion in compact object mergers," *Monthly Notices of the Royal Astronomical Society*, vol. 402, pp. 2771–2777, Mar. 2010.

[299] B. D. Metzger and R. Fernández, "Red or blue? A potential kilonova imprint of the delay until black hole formation following a neutron star merger," *Monthly Notices of the Royal Astronomical Society*, vol. 441, pp. 3444–3453, Jul. 2014.

[300] D. Pooley, P. Kumar, and J. C. Wheeler, "GW170817 Most Likely Made a Black Hole," *ArXiv e-prints*, Dec. 2017, arXiv:1712.03240.

[301] B. D. Metzger and A. L. Piro, "Optical and X-ray emission from stable millisecond magnetars formed from the merger of binary neutron stars," *Monthly Notices of the Royal Astronomical Society*, vol. 439, pp. 3916–3930, Apr. 2014.

[302] B. Margalit and B. D. Metzger, "Constraining the Maximum Mass of Neutron Stars from Multi-messenger Observations of GW170817," *Astrophysical Journal Letters*, vol. 850, p. L19, Dec. 2017.

[303] B. P. Abbott, R. Abbott, T. D. Abbott, F. Acernese, K. Ackley, C. Adams, T. Adams, P. Addesso, R. X. Adhikari, V. B. Adya, and et al., "Multi-messenger Observations of a Binary Neutron Star Merger," *Astrophysical Journal Letters*, vol. 848, p. L12, Oct. 2017.

[304] ——, "Gravitational Waves and Gamma-Rays from a Binary Neutron Star Merger: GW170817 and GRB 170817A," *Astrophysical Journal Letters*, vol. 848, p. L13, Oct. 2017.

[305] A. Goldstein, P. Veres, E. Burns, and et al., "An Ordinary Short Gamma-Ray Burst with Extraordinary Implications: Fermi-GBM Detection of GRB 170817A," *Astrophysical Journal Letters*, vol. 848, p. L14, Oct. 2017.

[306] A. S. Pozanenko, M. V. Barkov, P. Y. Minaev, A. A. Volnova, E. D. Mazaeva, A. S. Moskvitin, M. A. Krugov, V. A. Samodurov, V. M. Loznikov, and M. Lyutikov, "GRB 170817A Associated with GW170817: Multi-frequency Observations and Modeling of Prompt Gamma-Ray Emission," *Astrophysical Journal Letters*, vol. 852, p. L30, Jan. 2018.

[307] S. I. Blinnikov, I. D. Novikov, T. V. Perevodchikova, and A. G. Polnarev, "Exploding Neutron Stars in Close Binaries," *Soviet Astronomy Letters*, vol. 10, pp. 177–179, Apr. 1984.

[308] B. Paczynski, "Gamma-ray bursters at cosmological distances," *Astrophysical Journal Letters*, vol. 308, pp. L43–L46, Sep. 1986.

[309] R. Narayan, B. Paczynski, and T. Piran, "Gamma-ray bursts as the death throes of massive binary stars," *Astrophysical Journal Letters*, vol. 395, pp. L83–L86, Aug. 1992.

[310] W. Fong, E. Berger, P. K. Blanchard, R. Margutti, P. S. Cowperthwaite, R. Chornock, K. D. Alexander, B. D. Metzger, V. A. Villar, M. Nicholl, T. Eftekhari, P. K. G. Williams, J. Annis, D. Brout, D. A. Brown, H.-Y. Chen, Z. Doctor, H. T. Diehl, D. E. Holz, A. Rest, M. Sako, and M. Soares-Santos, "The Electromagnetic Counterpart of the Binary Neutron Star Merger LIGO/Virgo GW170817. VIII. A Comparison to Cosmological Short-duration Gamma-Ray Bursts," *Astrophysical Journal Letters*, vol. 848, p. L23, Oct. 2017.

[311] R. Margutti, E. Berger, W. Fong, C. Guidorzi, K. D. Alexander, B. D. Metzger, P. K. Blanchard, P. S. Cowperthwaite, R. Chornock, T. Eftekhari, M. Nicholl, V. A. Villar, P. K. G. Williams, J. Annis, D. A. Brown, H. Chen, Z. Doctor, J. A. Frieman, D. E. Holz, M. Sako, and M. Soares-Santos, "The Electromagnetic Counterpart of the Binary Neutron Star Merger LIGO/Virgo GW170817. V. Rising X-Ray Emission from an Off-axis Jet," *Astrophysical Journal*, vol. 848, p. L20, Oct. 2017.

[312] B. D. Metzger and E. Berger, "What is the Most Promising Electromagnetic Counterpart of a Neutron Star Binary Merger?" *Astrophysical Journal*, vol. 746, p. 48, Feb. 2012.

[313] J. Granot, D. Guetta, and R. Gill, "Lessons from the Short GRB 170817A: The First Gravitational-wave Detection of a Binary Neutron Star Merger," *Astrophysical Journal*, vol. 850, p. L24, Dec. 2017.

[314] H. T. Janka, M. A. Aloy, P. A. Mazzali, and E. Pian, "Off-Axis Properties of Short Gamma-Ray Bursts," *Astrophysical Journal*, vol. 645, pp. 1305–1314, Jul. 2006.

[315] K. D. Alexander, R. Margutti, P. K. Blanchard, W. Fong, E. Berger, A. Hajela, T. Eftekhari, R. Chornock, P. S. Cowperthwaite, D. Giannios, C. Guidorzi, A. Kathirgamaraju, A. MacFadyen, B. D. Metzger, M. Nicholl, L. Sironi, V. A. Villar, P. K. G. Williams, X. Xie, and J. Zrake, "A Decline in the X-Ray through Radio Emission from GW170817 Continues to Support an Off-axis Structured Jet," *Astrophysical Journal*, vol. 863, p. L18, Aug. 2018.

[316] D. Dobie, D. L. Kaplan, T. Murphy, E. Lenc, K. P. Mooley, C. Lynch, A. Corsi, D. Frail, M. Kasliwal, and G. Hallinan, "A Turnover in the Radio Light Curve of GW170817," *Astrophysical Journal Letters*, vol. 858, p. L15, May 2018.

[317] G. P. Lamb and S. Kobayashi, "GRB 170817A as a jet counterpart to gravitational wave trigger GW 170817," *Monthly Notices of the Royal Astronomical Society*, p. 1056, May 2018.

[318] D. Lazzati and et al., "Late Time Afterglow Observations Reveal a Collimated Relativistic Jet in the Ejecta of the Binary Neutron Star Merger GW170817," , vol. 120, p. 241103, Jun. 2018.

[319] R. Margutti, K. D. Alexander, X. Xie, L. Sironi, B. D. Metzger, A. Kathirgamaraju, W. Fong, P. K. Blanchard, E. Berger, A. MacFadyen, D. Giannios, C. Guidorzi, A. Hajela, R. Chornock, P. S. Cowperthwaite, T. Eftekhari, M. Nicholl, V. A. Villar, P. K. G. Williams, and J. Zrake, "The Binary Neutron Star Event LIGO/Virgo GW170817 160 Days after Merger: Synchrotron Emission across the Electromagnetic Spectrum," *Astrophysical Journal*, vol. 856, p. L18, Mar. 2018.

[320] L. Resmi, S. Schulze, C. H. Ishwara-Chandra, K. Misra, J. Buchner, M. De Pasquale, R. Sánchez- Ramírez, S. Klose, S. Kim, N. R. Tanvir, and P. T. O'Brien, "Low-frequency View of GW170817/GRB 170817A with the Giant Metrewave Radio Telescope," *Astrophysical Journal*, vol. 867, p. 57, Nov. 2018.

[321] E. Troja, E. T. H. van Eerten, G. Ryan, R. Ricci, J. M. Burgess, M. Wieringa, L. Piro, S. B. Cenko, and T. Sakamoto, "A year in the life of GW170817: the rise and fall of a structured jet from a binary neutron star merger," *ArXiv e-prints*, Aug. 2018.

[322] K. P. Mooley, A. T. Deller, O. Gottlieb, E. Nakar, G. Hallinan, S. Bourke, D. A. Frail, A. Horesh, A. Corsi, and K. Hotokezaka, "Superluminal motion of a relativistic jet in the neutron star merger GW170817," *ArXiv e-prints*, Jun. 2018.

[323] A. Kathirgamaraju, R. Barniol Duran, and D. Giannios, "TDE fallback cut-off due to a pre-existing accretion disc," *Monthly Notices of the Royal Astronomical Society in press*, Apr. 2017.

[324] R. Fernández, A. Tchekhovskoy, E. Quataert, F. Foucart, and D. Kasen, "Long-term GRMHD Simulations of Neutron Star Merger Accretion Disks: Implications for Electromagnetic Counterparts," *ArXiv e-prints*, p. arXiv:1808.00461, Aug. 2018.

[325] C. F. Gammie, J. C. McKinney, and G. Tóth, "HARM: A Numerical Scheme for General Relativistic Magnetohydrodynamics," *ApJ*, vol. 589, pp. 444–457, May 2003.

[326] S. C. Noble, C. F. Gammie, J. C. McKinney, and L. Del Zanna, "Primitive Variable Solvers for Conservative General Relativistic Magnetohydrodynamics," *ApJ*, vol. 641, pp. 626–637, Apr. 2006.

[327] Y. Sekiguchi, K. Kiuchi, K. Kyutoku, M. Shibata, and K. Taniguchi, "Dynamical mass ejection from the merger of asymmetric binary neutron stars: Radiation-hydrodynamics study in general relativity," *Physical Review D*, vol. 93, p. 124046, Jun. 2016.

[328] J. Burgess and et al., "Viewing short Gamma-ray Bursts from a different angle," *ArXiv e-prints*, p. arXiv:1710.05823, Oct. 2017.

[329] P. C. Duffell and T. Laskar, "On the Deceleration and Spreading of Relativistic Jets. I. Jet Dynamics," *Astrophysical Journal*, vol. 865, p. 94, Oct. 2018.

[330] O. Gottlieb, E. Nakar, and T. Piran, "The cocoon emission - an electromagnetic counterpart to gravitational waves from neutron star mergers," *Monthly Notices of the Royal Astronomical Society*, vol. 473, pp. 576–584, Jan. 2018.

[331] O. Bromberg, A. Tchekhovskoy, O. Gottlieb, E. Nakar, and T. Piran, "The γ-rays that accompanied GW170817 and the observational signature of a magnetic jet breaking out of NS merger ejecta," *Monthly Notices of the Royal Astronomical Society*, vol. 475, pp. 2971–2977, Apr. 2018.

[332] P. C. Duffell, E. Quataert, D. Kasen, and H. Klion, "Jet Dynamics in Compact Object Mergers: GW170817 Likely had a Successful Jet," *ArXiv e-prints*, p. arXiv:1806.10616, Jun. 2018.

[333] D. Finstad, S. De, D. A. Brown, E. Berger, and C. M. Biwer, "Measuring the Viewing Angle of GW170817 with Electromagnetic and Gravitational Waves," *Astrophysical Journal*, vol. 860, p. L2, Jun. 2018.

[334] B. F. Schutz, "Networks of gravitational wave detectors and three figures of merit," *Classical and Quantum Gravity*, vol. 28, p. 125023, Jun. 2011.

[335] P. Beniamini, M. Petropoulou, R. Barniol Duran, and D. Giannios, "A lesson from GW170817: most neutron star mergers result in tightly collimated successful GRB jets," *ArXiv e-prints*, p. arXiv:1808.04831, Aug. 2018.

[336] B. P. Abbott, R. Abbott, T. D. Abbott, F. Acernese, K. Ackley, C. Adams, T. Adams, P. Addesso, R. X. Adhikari, V. B. Adya, and et al., "GW170817: Observation of Gravitational Waves from a Binary Neutron Star Inspiral," *Physical Review Letters*, vol. 119, no. 16, p. 161101, Oct. 2017.

[337] ——, "Multi-messenger Observations of a Binary Neutron Star Merger," *Astrophysical Journal Letters*, vol. 848, p. L12, Oct. 2017.

[338] S. R. Kulkarni, "Modeling Supernova-like Explosions Associated with Gamma-ray Bursts with Short Durations," *arXiv e-prints*, pp. astro–ph/0 510 256, Oct. 2005.

[339] S. Rosswog, "Mergers of Neutron Star-Black Hole Binaries with Small Mass Ratios: Nucleosynthesis, Gamma-Ray Bursts, and Electromagnetic Transients," *Astrophysical Journal*, vol. 634, pp. 1202–1213, Dec. 2005.

[340] B. P. Abbott, R. Abbott, T. D. Abbott, F. Acernese, K. Ackley, C. Adams, T. Adams, P. Addesso, R. X. Adhikari, V. B. Adya, and et al., "Gravitational Waves and Gamma-Rays from a Binary Neutron Star Merger: GW170817 and GRB 170817A," *Astrophysical Journal Letters*, vol. 848, p. L13, Oct. 2017.

[341] M. Soares-Santos, D. E. Holz, J. Annis, R. Chornock, K. Herner, E. Berger, D. Brout, H. Y. Chen, , and et al., "The Electromagnetic Counterpart of the Binary Neutron Star Merger LIGO/Virgo GW170817. I. Discovery of the Optical Counterpart Using the Dark Energy Camera," *Astrophysical Journal*, vol. 848, p. L16, Oct. 2017.

[342] D. A. Coulter, R. J. Foley, C. D. Kilpatrick, M. R. Drout, A. L. Piro, B. J. Shappee, M. R. Siebert, J. D. Simon, N. Ulloa, D. Kasen, B. F. Madore, A. Murguia-Berthier, Y. C. Pan, J. X. Prochaska, E. Ramirez-Ruiz, A. Rest, and C. Rojas-Bravo, "Swope Supernova Survey 2017a (SSS17a), the optical counterpart to a gravitational wave source," *Science*, vol. 358, pp. 1556–1558, Dec. 2017.

[343] L. Hu, X. Wu, I. Andreoni, M. C. B. Ashley, J. Cooke, X. Cui, F. Du, Z. Dai, B. Gu, Y. Hu, H. Lu, X. Li, Z. Li, E. Liang, L. Liu, B. Ma, Z. Shang, T. Sun, N. B. Suntzeff, C. Tao, S. A. Udden, L. Wang, X. Wang, H. Wen, D. Xiao, J. Su, J. Yang, S. Yang, X. Yuan, H. Zhou, H. Zhang, J. Zhou, and Z. Zhu, "Optical observations of LIGO source GW 170817 by the Antarctic Survey Telescopes at Dome A, Antarctica," *Science Bulletin*, vol. 62, pp. 1433–1438, Oct. 2017.

[344] V. Savchenko, C. Ferrigno, E. Kuulkers, and et al., "INTEGRAL Detection of the First Prompt Gamma-Ray Signal Coincident with the Gravitational-wave Event GW170817," *Astrophysical Journal Letters*, vol. 848, p. L15, Oct. 2017.

[345] Y. Utsumi, M. Tanaka, N. Tominaga, M. Yoshida, S. Barway, T. Nagayama, T. Zenko, K. Aoki, T. Fujiyoshi, H. Furusawa, K. S. Kawabata, S. Koshida, C.-H. Lee, T. Morokuma, K. Motohara, F. Nakata, R. Ohsawa, K. Ohta, H. Okita, A. Tajitsu, I. Tanaka, T. Terai, N. Yasuda, F. Abe, Y. Asakura, I. A. Bond, S. Miyazaki, T. Sumi, P. J. Tristram, S. Honda, R. Itoh, Y. Itoh, M. Kawabata, K. Morihana, H. Nagashima, T. Nakaoka, T. Ohshima, J. Takahashi, M. Takayama, W. Aoki, S. Baar, M. Doi, F. Finet, N. Kanda, N. Kawai, J. H. Kim, D. Kuroda, W. Liu, K. Matsubayashi, K. L. Murata, H. Nagai, T. Saito, Y. Saito, S. Sako, Y. Sekiguchi, Y. Tamura, M. Tanaka, M. Uemura, and M. S. Yamaguchi, "J-GEM observations of an electromagnetic counterpart to the neutron star merger GW170817," *Publications of the Astronomical Society of Japan*, vol. 69, p. 101, Dec. 2017.

[346] J. Barnes and D. Kasen, "Effect of a High Opacity on the Light Curves of Radioactively Powered Transients from Compact Object Mergers," *Astrophysical Journal*, vol. 775, p. 18, Sep. 2013.

[347] M. Tanaka and K. Hotokezaka, "Radiative Transfer Simulations of Neutron Star Merger Ejecta," *Astrophysical Journal*, vol. 775, p. 113, Oct. 2013.

[348] K. Hotokezaka, P. Beniamini, and T. Piran, "Neutron star mergers as sites of r-process nucleosynthesis and short gamma-ray bursts," *International Journal of Modern Physics D*, vol. 27, p. 1842005, 2018.

[349] P. S. Cowperthwaite, E. Berger, V. A. Villar, B. D. Metzger, M. Nicholl, R. Chornock, P. K. Blanchard, W. Fong, R. Margutti, M. Soares-Santos, K. D. Alexander, S. Allam, J. Annis, D. Brout, D. A. Brown, R. E. Butler, H. Y. Chen, H. T. Diehl, Z. Doctor, M. R. Drout, T. Eftekhari, B. Farr, D. A. Finley, R. J. Foley, J. A. Frieman, C. L. Fryer, J. García-Bellido, M. S. S. Gill, J. Guillochon, K. Herner, D. E. Holz, D. Kasen, R. Kessler, J. Marriner, T. Matheson, J. Neilsen, E. H., E. Quataert, A. Palmese, A. Rest, M. Sako, D. M. Scolnic, N. Smith, D. L. Tucker, P. K. G. Williams, E. Balbinot, J. L. Carlin, E. R. Cook, F. Durret, T. S. Li, P. A. A. Lopes, A. C. C. Lourenço, J. L. Marshall, G. E. Medina, J. Muir, R. R. Muñoz, M. Sauseda, D. J. Schlegel, L. F. Secco, A. K. Vivas, W. Wester, A. Zenteno, Y. Zhang, T. M. C. Abbott, M. Banerji, K. Bechtol, A. Benoit-Lévy, E. Bertin, E. Buckley-Geer, D. L. Burke, D. Capozzi, A. Carnero Rosell, M. Carrasco Kind, F. J. Castander, M. Crocce, C. E. Cunha, C. B. D'Andrea, L. N. da Costa, C. Davis, D. L. DePoy, S. Desai, J. P. Dietrich, A. Drlica-Wagner, T. F. Eifler, A. E. Evrard, E. Fernandez, B. Flaugher, P. Fosalba, E. Gaztanaga, D. W. Gerdes, T. Giannantonio, D. A. Goldstein, D. Gruen, R. A. Gruendl, G. Gutierrez, K. Honscheid, B. Jain, D. J. James, T. Jeltema, M. W. G. Johnson, M. D. Johnson, S. Kent, E. Krause, R. Kron, K. Kuehn, N. Nuropatkin, O. Lahav, M. Lima, H. Lin, M. A. G. Maia, M. March, P. Martini, R. G. McMahon, F. Menanteau, C. J. Miller, R. Miquel, J. J. Mohr, E. Neilsen, R. C. Nichol, R. L. C. Ogando, A. A. Plazas, N. Roe, A. K. Romer, A. Roodman, E. S. Rykoff, E. Sanchez, V. Scarpine, R. Schindler, M. Schubnell, I. Sevilla-Noarbe, M. Smith, R. C. Smith, F. Sobreira, E. Suchyta, M. E. C. Swanson, G. Tarle, D. Thomas, R. C. Thomas, M. A. Troxel, V. Vikram, A. R. Walker, R. H. Wechsler, J. Weller, B. Yanny, and J. Zuntz, "The Electromagnetic Counterpart of the Binary Neutron Star Merger LIGO/Virgo GW170817. II. UV, Optical, and Near-infrared Light Curves and Comparison to Kilonova Models," *Astrophysical Journal*, vol. 848, p. L17, Oct. 2017.

[350] M. Nicholl, E. Berger, D. Kasen, B. D. Metzger, J. Elias, C. Briceño, K. D. Alexander, P. K. Blanchard, R. Chornock, P. S. Cowperthwaite, T. Eftekhari, W. Fong, R. Margutti, V. A. Villar, P. K. G. Williams, W. Brown, J. Annis, A. Bahramian, D. Brout, D. A. Brown, H. Y. Chen, J. C. Clemens, E. Dennihy, B. Dunlap, D. E. Holz, E. Marchesini, F. Massaro, N. Moskowitz, I. Pelisoli, A. Rest, F. Ricci, M. Sako, M. Soares-Santos, and J. Strader, "The Electromagnetic Counterpart of the Binary Neutron Star Merger LIGO/Virgo GW170817. III. Optical and UV Spectra of a Blue Kilonova from Fast Polar Ejecta," *Astrophysical Journal*, vol. 848, p. L18, Oct. 2017.

[351] I. Arcavi, "The First Hours of the GW170817 Kilonova and the Importance of Early Optical and Ultraviolet Observations for Constraining Emission Models," *Astrophysical Journal*, vol. 855, p. L23, Mar. 2018.

[352] D. Radice, A. Perego, K. Hotokezaka, S. A. Fromm, S. Bernuzzi, and L. F. Roberts, "Binary Neutron Star Mergers: Mass Ejection, Electromagnetic Counterparts and Nucleosynthesis," *arXiv e-prints*, p. arXiv:1809.11161, Sep. 2018.

[353] K. P. Mooley, A. T. Deller, O. Gottlieb, E. Nakar, G. Hallinan, S. Bourke, D. A. Frail, A. Horesh, A. Corsi, and K. Hotokezaka, "Superluminal motion of a relativistic jet in the neutron-star merger GW170817," *Nature*, vol. 561, pp. 355–359, Sep. 2018.

[354] G. Ghirlanda, O. S. Salafia, Z. Paragi, M. Giroletti, J. Yang, B. Marcote, J. Blanchard, I. Agudo, T. An, M. G. Bernardini, R. Beswick, M. Branchesi, S. Campana, C. Casadio, E. Chassande-Mottin, M. Colpi, S. Covino, P. D'Avanzo, V. D'Elia, S. Frey, M. Gawronski, G. Ghisellini, L. I. Gurvits, P. G. Jonker, H. J. van Langevelde, A. Melandri, J. Moldon, L. Nava, A. Perego, M. A. Perez-Torres, C. Reynolds, R. Salvaterra, G. Tagliaferri, T. Venturi, S. D. Vergani, and M. Zhang, "Re-solving the jet/cocoon riddle of the first gravitational wave with an electromagnetic counterpart," *arXiv e-prints*, Aug. 2018.

[355] P. Beniamini, M. Petropoulou, R. Barniol Duran, and D. Giannios, "A lesson from GW170817: most neutron star mergers result in tightly collimated successful GRB jets," *Monthly Notices of the Royal Astronomical Society*, vol. 483, pp. 840–851, Feb. 2019.

[356] E. T. H. van Eerten, G. Ryan, R. Ricci, J. M. Burgess, M. Wieringa, L. Piro, S. B. Cenko, and T. Sakamoto, "A year in the life of GW170817: the rise and fall of a structured jet from a binary neutron star merger," *arXiv e-prints*, p. arXiv:1808.06617, Aug. 2018.

[357] E. Nakar and T. Piran, "Detectable radio flares following gravitational waves from mergers of binary neutron stars," *Nature*, vol. 478, pp. 82–84, Oct. 2011.

[358] T. Piran, E. Nakar, and S. Rosswog, "The electromagnetic signals of compact binary mergers," *Monthly Notices of the Royal Astronomical Society*, vol. 430, pp. 2121–2136, Apr. 2013.

[359] K. D. Alexander, E. Berger, W. Fong, P. K. G. Williams, C. Guidorzi, R. Margutti, B. D. Metzger, J. Annis, P. K. Blanchard, D. Brout, D. A. Brown, H. Y. Chen, R. Chornock, P. S. Cowperthwaite, M. Drout, T. Eftekhari, J. Frieman, D. E. Holz, M. Nicholl, A. Rest, M. Sako, M. Soares-Santos, and V. A. Villar, "The Electromagnetic Counterpart of the Binary Neutron Star Merger LIGO/Virgo GW170817. VI. Radio Constraints on a Relativistic Jet and Predictions for Late-time Emission from the Kilonova Ejecta," *Astrophysical Journal*, vol. 848, p. L21, Oct. 2017.

[360] K. Hotokezaka, K. Kiuchi, M. Shibata, E. Nakar, and T. Piran, "Synchrotron Radiation from the Fast Tail of Dynamical Ejecta of Neutron Star Mergers," *Astrophysical Journal*, vol. 867, p. 95, Nov. 2018.

[361] L. Baiotti and L. Rezzolla, "Binary neutron star mergers: a review of Einstein's richest laboratory," *Reports on Progress in Physics*, vol. 80, p. 096901, Sep. 2017.

[362] I. Arcavi, G. Hosseinzadeh, D. A. Howell, C. McCully, D. Poznanski, D. Kasen, J. Barnes, M. Zaltzman, S. Vasylyev, D. Maoz, and S. Valenti, "Optical emission from a kilonova following a gravitational-wave-detected neutron-star merger," *Nature*, vol. 551, pp. 64–66, Nov. 2017.

[363] V. M. Lipunov, E. Gorbovskoy, V. G. Kornilov, N. . Tyurina, P. Balanutsa, A. Kuznetsov, D. Vlasenko, D. Kuvshinov, I. Gorbunov, D. A. H. Buckley, A. V. Krylov, R. Podesta, C. Lopez, F. Podesta, H. Levato, C. Saffe, C. Mallamachi, S. Potter, N. M. Budnev, O. Gress, Y. Ishmuhametova, V. Vladimirov, D. Zimnukhov, V. Yurkov, Y. Sergienko, A. Gabovich, R. Rebolo, M. Serra-Ricart, G. Israelyan, V. Chazov, X. Wang, A. Tlatov, and M. I. Panchenko,

"MASTER Optical Detection of the First LIGO/Virgo Neutron Star Binary Merger GW170817," *Astrophysical Journal*, vol. 850, p. L1, Nov. 2017.

[364] S. J. Smartt, T. W. Chen, A. Jerkstrand, M. Coughlin, E. Kankare, S. A. Sim, M. Fraser, C. Inserra, K. Maguire, K. C. Chambers, M. E. Huber, T. Krühler, G. Leloudas, M. Magee, L. J. Shingles, K. W. Smith, D. R. Young, J. Tonry, R. Kotak, A. Gal-Yam, J. D. Lyman, D. S. Homan, C. Agliozzo, J. P. Anderson, C. R. Angus, C. Ashall, C. Barbarino, F. E. Bauer, M. Berton, M. T. Botticella, M. Bulla, J. Bulger, G. Cannizzaro, Z. Cano, R. Cartier, A. Cikota, P. Clark, A. De Cia, M. Della Valle, L. Denneau, M. Dennefeld, L. Dessart, G. Dimitriadis, N. Elias-Rosa, R. E. Firth, H. Flewelling, A. Flörs, A. Franckowiak, C. Frohmaier, L. Galbany, S. González-Gaitán, J. Greiner, M. Gromadzki, A. N. Guelbenzu, C. P. Gutiérrez, A. Hamanowicz, L. Hanlon, J. Harmanen, K. E. Heintz, A. Heinze, M. S. Hernandez, S. T. Hodgkin, I. M. Hook, L. Izzo, P. A. James, P. G. Jonker, W. E. Kerzendorf, S. Klose, Z. Kostrzewa- Rutkowska, M. Kowalski, M. Kromer, H. Kuncarayakti, A. Lawrence, T. B. Lowe, E. A. Magnier, I. Manulis, A. Martin-Carrillo, S. Mattila, O. McBrien, A. Müller, J. Nordin, D. O'Neill, F. Onori, J. T. Palmerio, A. Pastorello, F. Patat, G. Pignata, P. Podsiadlowski, M. L. Pumo, S. J. Prentice, A. Rau, A. Razza, A. Rest, T. Reynolds, R. Roy, A. J. Ruiter, K. A. Rybicki, L. Salmon, P. Schady, A. S. B. Schultz, T. Schweyer, I. R. Seitenzahl, M. Smith, J. Sollerman, B. Stalder, C. W. Stubbs, M. Sullivan, H. Szegedi, F. Taddia, S. Taubenberger, G. Terreran, B. van Soelen, J. Vos, R. J. Wainscoat, N. A. Walton, C. Waters, H. Weiland, M. Willman, P. Wiseman, D. E. Wright, L. Wyrzykowski, and O. Yaron, "A kilonova as the electromagnetic counterpart to a gravitational-wave source," *Nature*, vol. 551, pp. 75–79, Nov. 2017.

[365] S. Valenti, David, J. Sand, S. Yang, E. Cappellaro, L. Tartaglia, A. Corsi, S. W. Jha, D. E. Reichart, J. Haislip, and V. Kouprianov, "The Discovery of the Electromagnetic Counterpart of GW170817: Kilonova AT 2017gfo/DLT17ck," *Astrophysical Journal*, vol. 848, p. L24, Oct. 2017.

[366] R. Chornock, E. Berger, D. Kasen, P. S. Cowperthwaite, M. Nicholl, V. A. Villar, K. D. Alexander, P. K. Blanchard, T. Eftekhari, W. Fong, R. Margutti, P. K. G. Williams, J. Annis, D. Brout, D. A. Brown, H. Y. Chen, M. R. Drout, B. Farr, R. J. Foley, J. A. Frieman, C. L. Fryer, K. Herner, D. E. Holz, R. Kessler, T. Matheson, B. D. Metzger, E. Quataert, A. Rest, M. Sako, D. M. Scolnic, N. Smith, and M. Soares-Santos, "The Electromagnetic Counterpart of the Binary Neutron Star Merger LIGO/Virgo GW170817. IV. Detection of Near-infrared Signatures of r-process Nucleosynthesis with Gemini-South," *Astrophysical Journal*, vol. 848, p. L19, Oct. 2017.

[367] P. A. Evans, S. B. Cenko, J. A. Kennea, S. W. K. Emery, N. P. M. Kuin, O. Korobkin, R. T. Wollaeger, C. L. Fryer, K. K. Madsen, F. A. Harrison, Y. Xu, E. Nakar, K. Hotokezaka, A. Lien, S. Campana, S. R. Oates, E. Troja, A. A. Breeveld, F. E. Marshall, S. D. Barthelmy, A. P. Beardmore, D. N. Burrows, G. Cusumano, A. D'Aì, P. D'Avanzo, V. D'Elia, M. de Pasquale, W. P. Even, C. J. Fontes, K. Forster, J. Garcia, P. Giommi, B. Grefenstette, C. Gronwall, D. H. Hartmann, M. Heida, A. L. Hungerford, M. M. Kasliwal, H. A. Krimm, A. J. Levan, D. Malesani, A. Melandri, H. Miyasaka, J. A. Nousek, P. T. O'Brien, J. P. Osborne, C. Pagani, K. L. Page, D. M. Palmer, M. Perri, S. Pike, J. L. Racusin, S. Rosswog, M. H. Siegel, T. Sakamoto, B. Sbarufatti,

G. Tagliaferri, N. R. Tanvir, and A. Tohuvavohu, "Swift and NuSTAR observations of GW170817: Detection of a blue kilonova," *Science*, vol. 358, pp. 1565–1570, Dec. 2017.

[368] C. McCully, D. Hiramatsu, D. A. Howell, G. Hosseinzadeh, I. Arcavi, D. Kasen, J. Barnes, M. M. Shara, T. B. Williams, P. Väisänen, S. B. Potter, E. Romero-Colmenero, S. M. Crawford, D. A. H. Buckley, J. Cooke, I. Andreoni, T. A. Pritchard, J. Mao, M. Gromadzki, and J. Burke, "The Rapid Reddening and Featureless Optical Spectra of the Optical Counterpart of GW170817, AT 2017gfo, during the First Four Days," *Astrophysical Journal*, vol. 848, p. L32, Oct. 2017.

[369] M. R. Drout, A. L. Piro, B. J. Shappee, C. D. Kilpatrick, J. D. Simon, C. Contreras, D. A. Coulter, R. J. Foley, M. R. Siebert, N. Morrell, K. Boutsia, F. Di Mille, T. W. S. Holoien, D. Kasen, J. A. Kollmeier, B. F. Madore, A. J. Monson, A. Murguia-Berthier, Y. C. Pan, J. X. Prochaska, E. Ramirez-Ruiz, A. Rest, C. Adams, K. Alatalo, E. Bañados, J. Baughman, T. C. Beers, R. A. Bernstein, T. Bitsakis, A. Campillay, T. T. Hansen, C. R. Higgs, A. P. Ji, G. Maravelias, J. L. Marshall, C. Moni Bidin, J. L. Prieto, K. C. Rasmussen, C. Rojas-Bravo, A. L. Strom, N. Ulloa, J. Vargas-González, Z. Wan, and D. D. Whitten, "Light curves of the neutron star merger GW170817/SSS17a: Implications for r-process nucleosynthesis," *Science*, vol. 358, pp. 1570–1574, Dec. 2017.

[370] N. R. Tanvir, A. J. Levan, C. González-Fernández, O. Korobkin, I. Mandel, S. Rosswog, J. Hjorth, P. D'Avanzo, A. S. Fruchter, C. L. Fryer, T. Kangas, B. Milvang-Jensen, S. Rosetti, D. Steeghs, R. T. Wollaeger, Z. Cano, C. M. Copperwheat, S. Covino, V. D'Elia, A. de Ugarte Postigo, P. A. Evans, W. P. Even, S. Fairhurst, R. Figuera Jaimes, C. J. Fontes, Y. I. Fujii, J. P. U. Fynbo, B. P. Gompertz, J. Greiner, G. Hodosan, M. J. Irwin, P. Jakobsson, U. G. Jørgensen, D. A. Kann, J. D. Lyman, D. Malesani, R. G. McMahon, A. Melandri, P. T. O'Brien, J. P. Osborne, E. Palazzi, D. A. Perley, E. Pian, S. Piranomonte, M. Rabus, E. Rol, A. Rowlinson, S. Schulze, P. Sutton, C. C. Thöne, K. Ulaczyk, D. Watson, K. Wiersema, and R. A. M. J. Wijers, "The Emergence of a Lanthanide-rich Kilonova Following the Merger of Two Neutron Stars," *Astrophysical Journal*, vol. 848, p. L27, Oct. 2017.

[371] D. Kasen, R. Fernández, and B. D. Metzger, "Kilonova light curves from the disc wind outflows of compact object mergers," *Monthly Notices of the Royal Astronomical Society*, vol. 450, pp. 1777–1786, Jun. 2015.

[372] B. D. Metzger and R. Fernández, "Red or blue? A potential kilonova imprint of the delay until black hole formation following a neutron star merger," *Monthly Notices of the Royal Astronomical Society*, vol. 441, pp. 3444–3453, Jul. 2014.

[373] A. Perego, D. Radice, and S. Bernuzzi, "AT 2017gfo: An Anisotropic and Three-component Kilonova Counterpart of GW170817," *Astrophysical Journal*, vol. 850, p. L37, Dec. 2017.

[374] D. Radice, F. Galeazzi, J. Lippuner, L. F. Roberts, C. D. Ott, and L. Rezzolla, "Dynamical mass ejection from binary neutron star mergers," *Monthly Notices of the Royal Astronomical Society*, vol. 460, pp. 3255–3271, Aug. 2016.

[375] D. M. Siegel and B. D. Metzger, "Three-dimensional GRMHD Simulations of Neutrino-cooled Accretion Disks from Neutron Star Mergers," *Astrophysical Journal*, vol. 858, p. 52, May 2018.

[376] E. Waxman, E. O. Ofek, D. Kushnir, and A. Gal-Yam, "Constraints on the ejecta of the GW170817 neutron star merger from its electromagnetic emission," *Monthly Notices of the Royal Astronomical Society*, vol. 481, pp. 3423–3441, Dec. 2018.

[377] Y.-W. Yu, L.-D. Liu, and Z.-G. Dai, "A Long-lived Remnant Neutron Star after GW170817 Inferred from Its Associated Kilonova," *Astrophysical Journal*, vol. 861, p. 114, Jul. 2018.

[378] P. Beniamini, K. Hotokezaka, and T. Piran, "r-process Production Sites as Inferred from Eu Abundances in Dwarf Galaxies," *Astrophysical Journal*, vol. 832, p. 149, Dec. 2016.

[379] D. Kasen, B. Metzger, J. Barnes, E. Quataert, and E. Ramirez-Ruiz, "Origin of the heavy elements in binary neutron-star mergers from a gravitational-wave event," *Nature*, vol. 551, pp. 80–84, Nov. 2017.

[380] B. D. Metzger, "Welcome to the Multi-Messenger Era! Lessons from a Neutron Star Merger and the Landscape Ahead," *arXiv e-prints*, p. arXiv:1710.05931, Oct. 2017.

[381] D. M. Siegel and B. D. Metzger, "Three-Dimensional General-Relativistic Magnetohydrodynamic Simulations of Remnant Accretion Disks from Neutron Star Mergers: Outflows and r -Process Nucleosynthesis," , vol. 119, p. 231102, Dec. 2017.

[382] P. Beniamini, I. Dvorkin, and J. Silk, "Retainment of r-process material in dwarf galaxies," *Monthly Notices of the Royal Astronomical Society*, vol. 478, pp. 1994–2005, Aug. 2018.

[383] S. Rosswog, J. Sollerman, U. Feindt, A. Goobar, O. Korobkin, R. Wollaeger, C. Fremling, and M. M. Kasliwal, "The first direct double neutron star merger detection: Implications for cosmic nucleosynthesis," *Astronomy & Astrophysics*, vol. 615, p. A132, Jul. 2018.

[384] R. Barniol Duran, E. Nakar, T. Piran, and R. Sari, "The afterglow of a relativistic shock breakout and low-luminosity GRBs," *Monthly Notices of the Royal Astronomical Society*, vol. 448, pp. 417–428, Mar. 2015.

[385] A. Kathirgamaraju, R. Barniol Duran, and D. Giannios, "GRB off-axis afterglows and the emission from the accompanying supernovae," *Monthly Notices of the Royal Astronomical Society*, vol. 461, pp. 1568–1575, Sep. 2016.

[386] J. Granot, A. Panaitescu, P. Kumar, and S. E. Woosley, "Off-Axis Afterglow Emission from Jetted Gamma-Ray Bursts," *Astrophysical Journal Letters*, vol. 570, pp. L61–L64, May 2002.

[387] L. Nava, G. Vianello, N. Omodei, G. Ghisellini, G. Ghirlanda, A. Celotti, F. Longo, R. Desiante, and R. Barniol Duran, "Clustering of LAT light curves: a clue to the origin of high-energy emission in gamma-ray bursts," *Monthly Notices of the Royal Astronomical Society*, vol. 443, pp. 3578–3585, Oct. 2014.

[388] J. Granot and A. J. van der Horst, "Gamma-Ray Burst Jets and their Radio Observations," *Publications of the Astronomical Society of Australia*, vol. 31, p. e008, Feb. 2014.

[389] P. Beniamini, L. Nava, and T. Piran, "A revised analysis of gamma-ray bursts' prompt efficiencies," *Monthly Notices of the Royal Astronomical Society*, vol. 461, pp. 51–59, Sep. 2016.

[390] B.-B. Zhang, H. van Eerten, D. N. Burrows, G. S. Ryan, P. A. Evans, J. L. Racusin, E. Troja, and A. MacFadyen, "An Analysis of Chandra Deep Follow-up Gamma-Ray Bursts: Implications for Off-axis Jets," *Astrophysical Journal*, vol. 806, p. 15, Jun. 2015.

[391] P. Beniamini and A. J. van der Horst, "Electrons' energy in GRB afterglows implied by radio peaks," *Monthly Notices of the Royal Astronomical Society*, vol. 472, pp. 3161–3168, Dec. 2017.

[392] H. van Eerten, "Gamma-ray burst afterglow blast waves," *International Journal of Modern Physics D*, vol. 27, pp. 1 842 002–314, 2018.

[393] G. Hallinan, A. Corsi, K. P. Mooley, K. Hotokezaka, E. Nakar, M. M. Kasliwal, D. L. Kaplan, D. A. Frail, S. T. Myers, T. Murphy, K. De, D. Dobie, J. R. Allison, K. W. Bannister, V. Bhalerao, P. Chandra, T. E. Clarke, S. Giacintucci, A. Y. Q. Ho, A. Horesh, N. E. Kassim, S. R. Kulkarni, E. Lenc, F. J. Lockman, C. Lynch, D. Nichols, S. Nissanke, N. Palliyaguru, W. M. Peters, T. Piran, J. Rana, E. M. Sadler, and L. P. Singer, "A radio counterpart to a neutron star merger," *Science*, vol. 358, pp. 1579–1583, Dec. 2017.

[394] K. P. Mooley, D. A. Frail, D. Dobie, E. Lenc, A. Corsi, K. De, A. J. Nayana, S. Makhathini, I. Heywood, T. Murphy, D. L. Kaplan, P. Chandra, O. Smirnov, E. Nakar, G. Hallinan, F. Camilo, R. Fender, S. Goedhart, P. Groot, M. M. Kasliwal, S. R. Kulkarni, and P. A. Woudt, "A Strong Jet Signature in the Late-time Light Curve of GW170817," *Astrophysical Journal*, vol. 868, p. L11, Nov. 2018.

[395] Y. Wu and A. MacFadyen, "Constraining the Outflow Structure of the Binary Neutron Star Merger Event GW170817/GRB170817A with a Markov Chain Monte Carlo Analysis," *Astrophysical Journal*, vol. 869, p. 55, Dec. 2018.

[396] J. Zrake, X. Xie, and A. MacFadyen, "Radio Sky Maps of the GRB 170817A Afterglow from Simulations," *Astrophysical Journal*, vol. 865, p. L2, Sep. 2018.

[397] P. Kumar and J. Granot, "The Evolution of a Structured Relativistic Jet and Gamma-Ray Burst Afterglow Light Curves," *Astrophysical Journal*, vol. 591, pp. 1075–1085, Jul. 2003.

[398] J. D. Salmonson, "Perspective on Afterglows: Numerically Computed Views, Light Curves, and the Analysis of Homogeneous and Structured Jets with Lateral Expansion," *Astrophysical Journal*, vol. 592, pp. 1002–1017, Aug. 2003.

[399] P. Beniamini and E. Nakar, "Observational constraints on the structure of gamma-ray burst jets," *Monthly Notices of the Royal Astronomical Society*, vol. 482, pp. 5430–5440, Feb. 2019.

[400] J. G. Hills, "Possible power source of Seyfert galaxies and QSOs," *Nature*, vol. 254, pp. 295–298, Mar. 1975.

[401] M. J. Rees, "Tidal disruption of stars by black holes of 10 to the 6th-10 to the 8th solar masses in nearby galaxies," *Nature*, vol. 333, pp. 523–528, Jun. 1988.

[402] C. S. Kochanek, "The aftermath of tidal disruption: The dynamics of thin gas streams," *Astrophysical Journal*, vol. 422, pp. 508–520, Feb. 1994.

[403] E. S. Phinney, "Manifestations of a Massive Black Hole in the Galactic Center," in *The Center of the Galaxy*, ser. IAU Symposium, M. Morris, Ed., vol. 136, 1989, p. 543.

[404] G. Lodato, A. R. King, and J. E. Pringle, "Stellar disruption by a supermassive black hole: is the light curve really proportional to t$^{-5/3}$?" *Monthly Notices of the Royal Astronomical Society*, vol. 392, pp. 332–340, Jan. 2009.

[405] J. Guillochon and E. Ramirez-Ruiz, "Hydrodynamical Simulations to Determine the Feeding Rate of Black Holes by the Tidal Disruption of Stars: The Importance of the Impact Parameter and Stellar Structure," *Astrophysical Journal*, vol. 767, p. 25, Apr. 2013.

[406] A. Ulmer, "Flares from the Tidal Disruption of Stars by Massive Black Holes," *Astrophysical Journal*, vol. 514, pp. 180–187, Mar. 1999.

[407] L. E. Strubbe and E. Quataert, "Optical flares from the tidal disruption of stars by massive black holes," *Monthly Notices of the Royal Astronomical Society*, vol. 400, pp. 2070–2084, Dec. 2009.

[408] G. Lodato and E. M. Rossi, "Multiband light curves of tidal disruption events," *Monthly Notices of the Royal Astronomical Society*, vol. 410, pp. 359–367, Jan. 2011.

[409] J. S. Bloom, D. Giannios, B. D. Metzger, S. B. Cenko, D. A. Perley, N. R. Butler, N. R. Tanvir, A. J. Levan, P. T. O'Brien, L. E. Strubbe, F. De Colle, E. Ramirez-Ruiz, W. H. Lee, S. Nayakshin, E. Quataert, A. R. King, A. Cucchiara, J. Guillochon, G. C. Bower, A. S. Fruchter, A. N. Morgan, and A. J. van der Horst, "A Possible Relativistic Jetted Outburst from a Massive Black Hole Fed by a Tidally Disrupted Star," *Science*, vol. 333, p. 203, Jul. 2011.

[410] D. N. Burrows, J. A. Kennea, G. Ghisellini, V. Mangano, B. Zhang, K. L. Page, M. Eracleous, P. Romano, T. Sakamoto, A. D. Falcone, J. P. Osborne, S. Campana, A. P. Beardmore, A. A. Breeveld, M. M. Chester, R. Corbet, S. Covino, J. R. Cummings, P. D'Avanzo, V. D'Elia, P. Esposito, P. A. Evans, D. Fugazza, J. M. Gelbord, K. Hiroi, S. T. Holland, K. Y. Huang, M. Im, G. Israel, Y. Jeon, Y.-B. Jeon, H. D. Jun, N. Kawai, J. H. Kim, H. A. Krimm, F. E. Marshall, P. Mészáros, H. Negoro, N. Omodei, W.-K. Park, J. S. Perkins, M. Sugizaki, H.-I. Sung, G. Tagliaferri, E. Troja, Y. Ueda, Y. Urata, R. Usui, L. A. Antonelli, S. D. Barthelmy, G. Cusumano, P. Giommi, A. Melandri, M. Perri, J. L. Racusin, B. Sbarufatti, M. H. Siegel, and N. Gehrels, "Relativistic jet activity from the tidal disruption of a star by a massive black hole," *Nature*, vol. 476, pp. 421–424, Aug. 2011.

[411] S. B. Cenko, H. A. Krimm, A. Horesh, A. Rau, D. A. Frail, J. A. Kennea, A. J. Levan, S. T. Holland, N. R. Butler, R. M. Quimby, J. S. Bloom, A. V. Filippenko, A. Gal-Yam, J. Greiner, S. R. Kulkarni, E. O. Ofek, F. Olivares E., P. Schady, J. M. Silverman, N. R. Tanvir, and D. Xu, "Swift J2058.4+0516: Discovery of a Possible Second Relativistic Tidal Disruption Flare?" *Astrophysical Journal*, vol. 753, p. 77, Jul. 2012.

[412] D. R. Pasham, S. B. Cenko, A. J. Levan, G. C. Bower, A. Horesh, G. C. Brown, S. Dolan, K. Wiersema, A. V. Filippenko, A. S. Fruchter *et al.*, "A multiwavelength study of the relativistic tidal disruption candidate swift j2058. 4+ 0516 at late times," *Astrophysical Journal*, vol. 805, no. 1, p. 68, 2015.

[413] A. Tchekhovskoy, B. D. Metzger, D. Giannios, and L. Z. Kelley, "Swift J1644+57 gone MAD: the case for dynamically important magnetic flux threading the black hole in a jetted tidal disruption event," *Monthly Notices of the Royal Astronomical Society*, vol. 437, pp. 2744–2760, Jan. 2014.

[414] L. Z. Kelley, A. Tchekhovskoy, and R. Narayan, "Tidal disruption and magnetic flux capture: powering a jet from a quiescent black hole," *Monthly Notices of the Royal Astronomical Society*, vol. 445, pp. 3919–3938, Dec. 2014.

[415] B. J. Shappee, J. L. Prieto, D. Grupe, C. S. Kochanek, K. Z. Stanek, G. De Rosa, S. Mathur, Y. Zu, B. M. Peterson, R. W. Pogge, S. Komossa, M. Im, J. Jencson, T. W.-S. Holoien, U. Basu, J. F. Beacom, D. M. Szczygieł, J. Brimacombe, S. Adams, A. Campillay, C. Choi, C. Contreras, M. Dietrich, M. Dubberley, M. Elphick, S. Foale, M. Giustini, C. Gonzalez, E. Hawkins, D. A. Howell, E. Y. Hsiao, M. Koss, K. M. Leighly, N. Morrell, D. Mudd, D. Mullins, J. M. Nugent, J. Parrent, M. M. Phillips, G. Pojmanski, W. Rosing, R. Ross, D. Sand, D. M. Terndrup, S. Valenti, Z. Walker, and Y. Yoon, "The Man behind the Curtain: X-Rays Drive the UV through NIR Variability in the 2013 Active Galactic Nucleus Outburst in NGC 2617," *Astrophysical Journal*, vol. 788, p. 48, Jun. 2014.

[416] T. W.-S. Holoien, C. S. Kochanek, J. L. Prieto, K. Z. Stanek, S. Dong, B. J. Shappee, D. Grupe, J. S. Brown, U. Basu, J. F. Beacom, D. Bersier, J. Brimacombe, A. B. Danilet, E. Falco, Z. Guo, J. Jose, G. J. Herczeg, F. Long, G. Pojmanski, G. V. Simonian, D. M. Szczygieł, T. A. Thompson, J. R. Thorstensen, R. M. Wagner, and P. R. Woźniak, "Six months of multiwavelength follow-up of the tidal disruption candidate ASASSN-14li and implied TDE rates from ASAS-SN," *Monthly Notices of the Royal Astronomical Society*, vol. 455, pp. 2918–2935, Jan. 2016.

[417] J. S. Brown, T. W.-S Holoien, K. Auchettl, K. Z. Stanek, C. S. Kochanek, B. J. Shappee, J. L. Prieto, and D. Grupe, "The Long Term Evolution of ASASSN-14li," *ArXiv e-prints*, Sep. 2016.

[418] K. D. Alexander, E. Berger, J. Guillochon, B. A. Zauderer, and P. K. G. Williams, "Discovery of an Outflow from Radio Observations of the Tidal Disruption Event ASASSN-14li," *Astrophysical Journal Letters*, vol. 819, p. L25, Mar. 2016.

[419] J. L. Prieto, T. Krühler, J. P. Anderson, L. Galbany, C. S. Kochanek, E. Aquino, J. S. Brown, S. Dong, F. Förster, T. W.-S. Holoien, H. Kuncarayakti, J. C. Maureira, F. F. Rosales-Ortega, S. F. Sánchez, B. J. Shappee, and K. Z. Stanek, "MUSE Reveals a Recent Merger in the Post-starburst Host Galaxy of the TDE ASASSN-14li," *Astrophysical Journal Letters*, vol. 830, p. L32, Oct. 2016.

[420] K. D. French, I. Arcavi, and A. Zabludoff, "The Post-Starburst Evolution of Tidal Disruption Event Host Galaxies," *ArXiv e-prints*, Sep. 2016.

[421] G. F. Kennedy, Y. Meiron, B. Shukirgaliyev, T. Panamarev, P. Berczik, A. Just, and R. Spurzem, "Star-disc interaction in galactic nuclei: orbits and rates of accreted stars," *Monthly Notices of the Royal Astronomical Society*, vol. 460, pp. 240–255, Jul. 2016.

[422] I. Arcavi, A. Gal-Yam, M. Sullivan, Y.-C. Pan, S. B. Cenko, A. Horesh, E. O. Ofek, A. De Cia, L. Yan, C.-W. Yang, D. A. Howell, D. Tal, S. R. Kulkarni, S. P. Tendulkar, S. Tang, D. Xu, A. Sternberg, J. G. Cohen, J. S. Bloom, P. E. Nugent, M. M. Kasliwal, D. A. Perley, R. M. Quimby, A. A. Miller, C. A. Theissen, and R. R. Laher, "A Continuum of H- to He-rich Tidal Disruption Candidates With a Preference for E+A Galaxies," *Astrophysical Journal*, vol. 793, p. 38, Sep. 2014.

[423] K. D. French, I. Arcavi, and A. Zabludoff, "Tidal Disruption Events Prefer Unusual Host Galaxies," *Astrophysical Journal Letters*, vol. 818, p. L21, Feb. 2016.

[424] V. Springel, T. Di Matteo, and L. Hernquist, "Modelling feedback from stars and black holes in galaxy mergers," *Monthly Notices of the Royal Astronomical Society*, vol. 361, pp. 776–794, Aug. 2005.

[425] C. Bonnerot, E. M. Rossi, and G. Lodato, "Bad prospects for the detection of giant stars' tidal disruption: effect of the ambient medium on bound debris," *Monthly Notices of the Royal Astronomical Society*, vol. 458, pp. 3324–3330, May 2016.

[426] N. I. Shakura and R. A. Sunyaev, "Black holes in binary systems. Observational appearance." *Astronomy & Astrophysics*, vol. 24, pp. 337–355, 1973.

[427] R. Narayan, I. V. Igumenshchev, and M. A. Abramowicz, "Self-similar Accretion Flows with Convection," *Astrophysical Journal*, vol. 539, pp. 798–808, Aug. 2000.

[428] E. Quataert and A. Gruzinov, "Convection-dominated Accretion Flows," *Astrophysical Journal*, vol. 539, pp. 809–814, Aug. 2000.

[429] R. Narayan and I. Yi, "Advection-dominated accretion: A self-similar solution," *Astrophysical Journal Letters*, vol. 428, pp. L13–L16, Jun. 1994.

[430] J. Guillochon, M. McCourt, X. Chen, M. D. Johnson, and E. Berger, "Unbound Debris Streams and Remnants Resulting From the Tidal Disruptions of Stars by Supermassive Black Holes," *ArXiv e-prints*, Sep. 2015.

[431] D. Kasen and E. Ramirez-Ruiz, "Optical Transients from the Unbound Debris of Tidal Disruption," *Astrophysical Journal*, vol. 714, pp. 155–162, May 2010.

[432] J. Guillochon, H. Manukian, and E. Ramirez-Ruiz, "PS1-10jh: The Disruption of a Main-sequence Star of Near-solar Composition," *Astrophysical Journal*, vol. 783, p. 23, Mar. 2014.

[433] J. H. Lacy, C. H. Townes, and D. J. Hollenbach, "The nature of the central parsec of the Galaxy," *Astrophysical Journal*, vol. 262, pp. 120–134, Nov. 1982.

[434] A. R. Choudhuri, *The physics of fluids and plasmas : an introduction for astrophysicists /*, Nov. 1998.

[435] D. Giannios and B. D. Metzger, "Radio transients from stellar tidal disruption by massive black holes," *Monthly Notices of the Royal Astronomical Society*, vol. 416, pp. 2102–2107, Sep. 2011.

[436] J. K. Cannizzo, H. M. Lee, and J. Goodman, "The disk accretion of a tidally disrupted star onto a massive black hole," *Astrophysical Journal*, vol. 351, pp. 38–46, Mar. 1990.

[437] A. J. Levan, N. R. Tanvir, G. C. Brown, B. D. Metzger, K. L. Page, S. B. Cenko, P. T. O'Brien, J. D. Lyman, K. Wiersema, E. R. Stanway, A. S. Fruchter, D. A. Perley, and J. S. Bloom, "Late Time Multi-wavelength Observations of Swift J1644+5734: A Luminous Optical/IR Bump and Quiescent X-Ray Emission," *Astrophysical Journal*, vol. 819, p. 51, Mar. 2016.

[438] A. J. Levan, N. R. Tanvir, S. B. Cenko, D. A. Perley, K. Wiersema, J. S. Bloom, A. S. Fruchter, A. d. U. Postigo, P. T. O'Brien, N. Butler, A. J. van der Horst, G. Leloudas, A. N. Morgan, K. Misra, G. C. Bower, J. Farihi, R. L. Tunnicliffe, M. Modjaz, J. M. Silverman, J. Hjorth, C. Thöne, A. Cucchiara, J. M. C. Cerón, A. J. Castro-Tirado, J. A. Arnold, M. Bremer, J. P. Brodie, T. Carroll, M. C. Cooper, P. A. Curran, R. M. Cutri, J. Ehle, D. Forbes, J. Fynbo, J. Gorosabel, J. Graham, D. I. Hoffman, S. Guziy, P. Jakobsson, A. Kamble, T. Kerr, M. M. Kasliwal, C. Kouveliotou, D. Kocevski, N. M. Law, P. E. Nugent, E. O. Ofek, D. Poznanski, R. M. Quimby, E. Rol, A. J. Romanowsky, R. Sánchez-Ramírez, S. Schulze, N. Singh, L. van Spaandonk, R. L. C. Starling, R. G. Strom, J. C. Tello, O. Vaduvescu, P. J. Wheatley, R. A. M. J. Wijers, J. M. Winters, and D. Xu, "An Extremely Luminous Panchromatic Outburst from the Nucleus of a Distant Galaxy," *Science*, vol. 333, p. 199, Jul. 2011.

[439] E. Berger, A. Zauderer, G. G. Pooley, A. M. Soderberg, R. Sari, A. Brunthaler, and M. F. Bietenholz, "Radio Monitoring of the Tidal Disruption Event Swift J164449.3+573451. I. Jet Energetics and the Pristine Parsec-scale Environment of a Supermassive Black Hole," *Astrophysical Journal*, vol. 748, p. 36, Mar. 2012.

[440] D. Lin, J. Guillochon, S. Komossa, E. Ramirez-Ruiz, J. A. Irwin, W. P. Maksym, D. Grupe, O. Godet, N. A. Webb, D. Barret, B. A. Zauderer, P.-A. Duc, E. R. Carrasco, and S. D. J. Gwyn, "A likely decade-long sustained tidal disruption event," *Nature Astronomy*, vol. 1, p. 0033, Feb. 2017.

[441] G. C. Brown, A. J. Levan, E. R. Stanway, N. R. Tanvir, S. B. Cenko, E. Berger, R. Chornock, and A. Cucchiaria, "Swift J1112.2-8238: a candidate relativistic tidal disruption flare," *Monthly Notices of the Royal Astronomical Society*, vol. 452, pp. 4297–4306, Oct. 2015.

[442] F. De Colle, J. Guillochon, J. Naiman, and E. Ramirez-Ruiz, "The Dynamics, Appearance, and Demographics of Relativistic Jets Triggered by Tidal Disruption of Stars in Quiescent Supermassive Black Holes," *Astrophysical Journal*, vol. 760, p. 103, Dec. 2012.

[443] B. A. Zauderer, E. Berger, R. Margutti, G. G. Pooley, R. Sari, A. M. Soderberg, A. Brunthaler, and M. F. Bietenholz, "Radio Monitoring of the Tidal Disruption Event Swift J164449.3+573451. II. The Relativistic Jet Shuts Off and a Transition to Forward Shock X-Ray/Radio Emission," *Astrophysical Journal*, vol. 767, p. 152, Apr. 2013.

[444] R.-F. Shen and C. D. Matzner, "Evolution of Accretion Disks in Tidal Disruption Events," *Astrophysical Journal*, vol. 784, p. 87, Apr. 2014.

[445] J. Guillochon and M. McCourt, "Simulations of Magnetic Fields in Tidally-Disrupted Stars," *ArXiv e-prints*, Sep. 2016.

[446] R. D. Saxton, A. M. Read, S. Komossa, P. Lira, K. D. Alexander, and M. H. Wieringa, "XMMSL1 J074008.2-853927: a tidal disruption event with thermal and non-thermal components," *Astronomy & Astrophysics*, vol. 598, p. A29, Jan. 2017.